

UNCLASSIFIED

AD NUMBER

AD326487

CLASSIFICATION CHANGES

TO: unclassified

FROM: confidential

LIMITATION CHANGES

TO:

Approved for public release, distribution
unlimited

FROM:

Controlling DoD organization Dept. of the
Navy, Washington, DC.

AUTHORITY

ONR ltr dtd 20 Sep 1967; SAME

THIS PAGE IS UNCLASSIFIED

UNCLASSIFIED

AD 326487

DEFENSE DOCUMENTATION CENTER

FOR

SCIENTIFIC AND TECHNICAL INFORMATION

CAMERON STATION ALEXANDRIA, VIRGINIA

CLASSIFICATION CHANGED
TO UNCLASSIFIED
FROM CONFIDENTIAL

ACRONYM

C. A. H. LITR

EXT D 18, AUGUST 1966



UNCLASSIFIED

NOTICE: When government or other drawings, specifications or other data are used for any purpose other than in connection with a definitely related government procurement operation, the U. S. Government thereby incurs no responsibility, nor any obligation whatsoever; and the fact that the Government may have formulated, furnished, or in any way supplied the said drawings, specifications, or other data is not to be regarded by implication or otherwise as in any manner licensing the holder or any other person or corporation, or conveying any rights or permission to manufacture, use or sell any patented invention that may in any way be related thereto.

CONFIDENTIAL

DOWNGRADED AT 5-YEAR INTERVALS
DECLASSIFIED AFTER 12 YEARS
DOD DIR 5200.10

NAVEXOS P-2329

July 1961

35

IRIA State-of-the-Art Report

INFRARED QUANTUM DETECTORS



Institute of Science and Technology
THE UNIVERSITY OF MICHIGAN

ASTIA

NOV 27 1961

Contract NOnr 1224/12

DOWNGRADED AT 5-YEAR INTERVALS;
DECLASSIFIED AFTER 12 YEARS
DOD DIR 5200.10

CONFIDENTIAL

CONFIDENTIAL

75190
2389-50-T

IRIA State-of-the-Art Report

INFRARED QUANTUM DETECTORS (U)

Edited by
W. WOLFE
T. LIMPERIS

July 1961

Infrared Laboratory
Institute of Science and Technology
THE UNIVERSITY OF MICHIGAN
Ann Arbor, Michigan

53100
CONFIDENTIAL

This document contains information affecting the national defense of the United States within the meaning of the Espionage Laws, Title 18, U.S.C., Sections 793 and 794, the transmission or revelation of its contents in any manner to an unauthorized person is prohibited by law.

NOTICES

Reproduction Permission. Reproduction in whole or in part is permitted for any purpose of the United States Government.

Sponsorship. The work reported herein was conducted by the Institute of Science and Technology for the Office of Naval Research, Physics Branch, Contract NONr 1224(12). Contracts and grants to The University of Michigan for the support of sponsored research by the Institute of Science and Technology are administered through the Office of the Vice-President for Research.

ASTIA Availability. Qualified requesters may obtain copies of this document from:

Armed Services Technical Information Agency
Arlington Hall Station
Arlington Hall, Virginia

Final Disposition. After this document has served its purpose, it may be destroyed in accordance with provisions of the Industrial Security Manual for Safeguarding Classified Information. Please do not return it to the Institute of Science and Technology.

PREFACE

IRIA (Infrared Information and Analysis Center) at the Infrared Laboratory of The University of Michigan's Institute of Science and Technology is responsible for the collection, analysis, and dissemination to authorized recipients of all information concerning military infrared research and development. To this end, IRIA prepares annotated bibliographies, subject bibliographies, state-of-the-art reports, and miscellaneous publications; IRIA also sponsors symposiums and provides advice and assistance to visitors.

IRIA is supported by a tri-service contract, Nonr 1224(12) administered by the Office of Naval Research, Physics Branch. A steering committee consisting of representatives of the three military services assists in the technical direction of the work. Contracts and grants to The University of Michigan for the support of sponsored research by the Institute of Science and Technology are administered through the Office of the Vice-President for Research.

This report presents the results of a two-year effort to compile and analyze data. In addition to the authors of each section, the following individuals contributed significantly to the report. Professors Levinstein and Cashman criticized the contents of the entire report and made valuable contributions to its scope and accuracy. Dr. George Morton of the Radio Corporation of America criticized and made contributions to Section 5.4; Werner Beyen of Texas Instruments Incorporated contributed to Section 5.7; and Dr. Philip Cholet contributed to Section 5.6. Finally, David Anding and John Duncan assisted in many of the calculations, in the compilation and in some of the writing.

Since the material presented here represents this country's state of the art in infrared quantum detectors, the report is classified confidential in its entirety. Also, those paragraphs which contain confidential data are so labeled.

CONTENTS

Notices	ii
Preface	iii
List of Figures	vii
List of Tables	xiv
Abstract	1
1. Introduction, by William L. Wolfe	3
1.1. Purpose	3
1.2. Limitations	3
1.3. References	5
2. Physics of the Detection Process, by Gwynn H. Suits	5
2.1. Summary of the Energy-Band Model	6
2.2. Thermal Excitation of Electrons	7
2.3. The Concept of "Holes"	8
2.4. Flow of Charge Carriers	8
2.5. Impurities in Semiconductors	6
2.6. Interaction with Radiation	10
3. Theoretical Description of Detectors, by Sol Nudelman	14
3.1. Signal Generation in Quantum Detectors	14
3.2. Noise	14
3.3. Speed of Response	19
3.4. Spectral Response	40
3.5. References	42
4. Detector Evaluation from Theoretical Considerations, by Sol Nudelman	44
4.1. Noise Equivalent Power	44
4.2. Detector Classification	52
4.3. References	72
5. Detailed Description of Detectors	73
5.1. Introduction to Detector Enumeration, by Thomas Limperis	73
5.2. The Lead Salts, by Thomas Limperis	78
5.3. Impurity-Activated Germanium Detectors, by Henry Levinstein, Syracuse University	112
5.4. Impurity-Activity Germanium-Silicon Alloys, by Thomas Limperis	134
5.5. Tellurium, by Thomas Limperis and Gwynn H. Suits	147
5.6. Indium Arsenide, by Thomas Limperis	159
5.7. Indium Antimonide, by Joseph Mudar, Thomas Limperis, and William L. Wolfe	165
5.8. References	196

CONTENTS (Continued)

6. Unusual Detectors, by Gwynn H. Sufts, Thomas Limperis, and William L. Wolfe	203
6.1. The Image-Position Indicator	203
6.2. Infrared Detectors Based on Microwave Techniques	207
6.3. Optical-Pumping Techniques	210
6.4. References	214
Appendix A: Test Procedures, by Sol Nudel'man	216
Appendix B: Immersion Lenses for Infrared Instruments, by William L. Wolfe and John Duncan	243
Appendix C: Cooling Devices for Infrared Detectors, by Paul R. Barker and William L. Brown	255
Appendix D: Peltier Cooling, by Robert H. Vought, General Electric Company	276
Appendix E: Semiconducting Materials, by Thomas Limperis, John Duncan, and David Anding	319

FIGURES

2-1. The Band Picture of an Ideal Semiconductor	6
2-2. The Band Picture of an Ideal Semiconductor with Impurities	9
3-1. Photoconductive Detector Circuit	15
3-2. Detector Geometry	15
3-3. p-n Junction	16
3-4. Circuit Configurations	23
3-5. Effective Circuit Charge as a Function of Charge Displacement	26
3-6. Relative Intensity and Fluctuation of Photons as a Function of Wavelength and Temperature	35
3-7. Periodic Pulse Photoexcitation and Detector Response	37
3-8. Intrinsic Detector Response to a Constant Density of Photons, as a Function of Wavelength	41
3-9. Intrinsic Detector Response to Constant Energy Exposure, as a Function of Wavelength	41
3-10. Impurity Detector Response to a Constant Density of Photons, as a Function of Wavelength	41
4-1. NEP as a Function of Wavelength for Different Background Temperatures	55
4-2. Peak D^* vs. Background Temperature for Three Detectors in the Background-Limited Condition	62
4-3. D^* as a Function of Angular Field of View	62
4-4. D^{**} and D^* as Functions of Angular Field of View	63
4-5. Information Capacity and Information Efficiency as Functions of Signal-to-Noise Ratio	68
4-6. Frequency Compensation	71
5-1. D^* vs. λ for Available Detectors	74
5-2. Change in Band Gap with Temperature for the PbS Family	80
5-3. Possible Energy-Band Developments	80
5-4. Optical Absorption of Very Thin Crystals of PbS	82
5-5. Variation of Refractive Index with Temperature	82
5-6. PbS-Cell Configurations	83

FIGURES (Continued)

5-7. Effect of Background Radiation on PbS-Cell Resistance	83
5-8. Typical Relative Response of PbS	84
5-9. Typical Noise Spectrum of PbS	84
5-10. Immersed PbS Film	85
5-11. Summary of Data on the Effect of Nuclear Flux on PbS Characteristics	85
5-12. Histogram of D^* Values for PbS Detectors	86
5-13. Absolute Spectral Response of PbS Cells at 300°K	87
5-14. Peak D^* vs. Year of Manufacture of PbS Cells	91
5-15. Sensitivity Contours of PbS Cells	94
5-16. Absorption-Coefficient Measurements on PbSe Crystals	95
5-17. Effect of Background Radiation on PbSe-Cell Resistance	96
5-18. Noise-Power Spectrum of an Evaporated PbSe Photoconductor	96
5-19. Absolute Spectral Response of Evaporated PbSe Cells at 80°K	99
5-20. Absolute Spectral Response of Chemically Deposited PbSe Cells at 300°K	99
5-21. Absolute Spectral Response of Chemically Deposited PbSe Cells at 80°K	100
5-22. Absolute Spectral Response of Evaporated PbSe Cells at 300°K	100
5-23. Peak D^* vs. Year of Manufacture of PbSe Cells	102
5-24. Spectral Response of Early PbSe Cells	103
5-25. D^* for a $6\text{-}\mu$ Long-Wavelength Cutoff Background-Limited Photoconductive Detector as a Function of the Field of View	103
5-26. Two SBRC PbSe Detectors at 190°K	104
5-27. Two IRI PbSe Detectors at 78°K	104
5-28. Absorption of PbTe Crystal	105
5-29. Photovoltaic Spectrum for p-n Junctions in PbTe at Room Temperature	105
5-30. Resistance vs. Background for PbTe Detectors	106
5-31. PbTe Noise Spectrum	106
5-32. Influence of Background Radiation on Detector Noise in PbTe	107
5-33. Relative Response of PbTe at 77°K	107
5-34. NEP vs. Area for PbTe, $f = 90$ cps	108
5-35. NEP vs. Area for PbTe, $f = 800$ cps	111
5-36. Absorption Spectrum in Pure Ge	113
5-37. Absorption Coefficient in In-Doped p-Type Ge	113

FIGURES (Continued)

5-38. Lattice Absorption in Ge	115
5-39. Energy Level Diagram for Impurity Atoms in Ge	115
5-40. Noise Spectrum of p-Type Au-Doped Ge at 77°K	118
5-41. Peak D^*_λ vs. Long-Wavelength Cutoff for Background-Limited Detectors	119
5-42. Variation of D^* with Acceptance Angle	119
5-43. Ge Detector Assembly	121
5-44. Double Dewar Flask	121
5-45. Spectral Response of n- and p-Type Au-Doped Ge	122
5-46. Absolute Spectral Response of Cu, ZnI, AuI, and AuII Ge Detectors	122
5-47. Time Constant vs. Temperature of n-Type Ge	123
5-48. Histogram of D^* Values for n-Type Ge:Au	124
5-49. Signal and Noise Variation with Frequency for an n-Type Au, Sb-Doped Ge Detector at 90°K	124
5-50. Histogram of D^* Values for p-Type Ge:Au	127
5-51. S/N Ratio vs. Temperature for Ge:Cd, Ge:Hg, and Ge:Au Detectors	127
5-52. Histogram of D^* Values for the Ge:ZnI Detector	130
5-53. Histogram of D^* Values for the Ge:Cu Detector	131
5-54. Absolute Spectral Response of Experimental Ge:Cd and Ge:Hg Detectors	132
5-55. Composition Dependence of the Energy Gap of Si-Ge Alloys	134
5-56. Intrinsic Absorption Spectra in a Series of Ge-Rich Ge-Si Alloys at 78°K	135
5-57. Simple Band Picture	136
5-58. Impurity Ionization Energies as Functions of Alloy Composition	136
5-59. Ionization Energy of Au in Ge-Si Alloys	137
5-60. Typical Integrating-Chamber Assembly	138
5-61. Cell Element	138
5-62. Spectral-Response Curve for Ge-Si:AuI	139
5-63. Impurity Ionization Level vs. Percent Si for ZnII	141
5-64. Optical Absorption Coefficient of a Zn-Activated Alloy	141
5-65. Spectral-Response Curve for Ge-Si:ZnII	142
5-66. Absolute Spectral Response of Ge-Si:AuII	146
5-67. Relative Spectral Response of Ge-Si:Zn:AuII	146
5-68. Schematic Representation of the Te Crystal	147

FIGURES (Continued)

5-69. Single Crystal Te Boules Prepared by the Czochralski Method	146
5-70. Optical Transmission of a Te Sample as a Function of Photon Energy	150
5-71. Transmission of a Typical Te Crystal vs. Angle between the c-Axis and E Vector of the Incident Polarized Radiation	150
5-72. Spectral Dependence of the Refractive Index in Te Crystals	152
5-73. Frequency Response of Te	153
5-74. Noise Spectrum of Te	154
5-75. Absolute Spectral Response of Te	155
5-76. Blackbody NEP Distribution for 1/2 x 1/2-mm Te Detectors	157
5-77. Te Response and Sky Emission vs. Wavelength	158
5-78. Absorption Coefficient of InAs	159
5-79. Refractive Index of InAs	159
5-80. Energy Gap vs. Temperature for InAs	160
5-81. Absorption Spectrum of InAs with Temperature as a Parameter	160
5-82. Relative Spectral Response of InAs (Zn Alloy)	161
5-83. Relative Spectral Response of InAs (Cd Diffused)	161
5-84. Noise Spectrum for a Typical InAs Cell	163
5-85. S/N Ratio vs. Cell Temperature	164
5-86. Absorption in InSb	166
5-87. Apparent Optical Energy Gap of InSb as a Function of Electron Concentration	166
5-88. Band Structure vs. Lattice Spacing	167
5-89. Energy Gap as a Function of Temperature for InSb	167
5-90. Refractive Index of InSb	167
5-91. S/N Ratio vs. Bias Current for LAS Cell No. PV-52	169
5-92. Grown Junction	170
5-93. Noise Spectra of Grown-Junction InSb Detectors	171
5-94. Spectral Response of a Grown-Junction InSb Detector	171
5-95. Sensitivity Profile across p-n Junction of a Typical Grown Junction Detector	172
5-96. Histogram of Grown-Junction Cells	174
5-97. Typical Spectral Response for Diffused-Junction Cells	175
5-98. InSb Photovoltaic Diffused-Junction Noise Spectrum	176

FIGURES (Continued)

5-99. D* vs. Background Radiation in Diffused-Junction Cells	177
5-100. Histogram of Diffused-Junction Cells	178
5-101. Spectral Response of InSb Photoconductive Cells	183
5-102. Response of InSb to a Square Radiation Pulse	183
5-103. Noise Spectrum of Photoconductive InSb	184
5-104. S/N Ratio vs. Temperature for High- and Low-Impedance Cells	185
5-105. Histogram of Photoconductive Cells	188
5-106. Schematic Representation of the PEM Effect	190
5-107. Typical Spectral Response of an InSb PEM Cell at 300° K	191
5-108. Noise Spectrum for PEM Cells	191
5-109. Histogram of D* Values for PEM Detectors	193
5-110. Induced Impurity Levels in InSb	194
6-1. Lateral Photoeffect	204
6-2. Spot-Position Location in Two Dimensions	206
6-3. Variation of V_x with Spot Position	207
6-4. General Bronze Infrared Detector	208
6-5. Block Diagram of Test Setup	208
6-6. Possible Energy Levels	210
6-7. Energy-Level Diagram for an Infrared Quantum Counter	214
A-1. Block Diagram of System To Measure NEP	217
A-2. Determination of Optimum Bias	218
A-3. Test Circuitry for Infrared Detectors	219
A-4. Photoconductive Detector Circuits	220
A-5. Detector Frequency Response	224
A-6. Simple Spinning Mirror for Periodic Light-Pulse Generation	225
A-7. Spinning Mirror System for Periodic Light-Pulse Generation in the Millimicrosecond Time Domain	226
A-8. Signal, Noise, and Gate Relationship in Wave-Shape Recorder	228
A-9. Schematic of Wave-Shape Recorder	229
A-10. Block Diagram of Wave-Shape Recorder	230
A-11. Block Diagram of System To Measure Detector Response	231
A-12. Detector Relative Spectral Response	232

FIGURES (Continued)

A-13. Determination of Absolute Spectral Response	233
A-14. Blackbody Spectral Radiant Emittance	235
A-15. Detector Noise Spectrum	239
A-16. Detector Sensitivity Contour	240
A-17. A Typical Data Sheet	241
B-1. Aplanatic Sphere	246
B-2. Solid-Angle Geometry	247
B-3. Immersion-Lens Geometry	247
B-4. Detector Height vs. Distance from Original Focal Point	248
B-5. Normalized Detector Height vs. Angle δ	249
B-6. Distance of Detector Surface from Original Focal Plane vs. Angle δ	250
B-7. Comparative Fields of View of Immersed and Unimmersed Detectors in Barnes 4-Inch OptiTherm Radiometer	253
C-1. Spectral Response of PbS Detector	256
C-2. Variation of Detectivity of Spectral Peak with Chopping Frequency for PbS	256
C-3. Basic Direct-Contact Cooling System	257
C-4. Modified Direct-Contact Cooling System	258
C-5. Joule-Thomson Cooler	259
C-6. Joule-Thomson Pore-Plug Experiment	259
C-7. Isenthalpic Curves and Inversion Curve for a Gas	261
C-8. Isenthalpic Curves Superimposed upon Phase Diagram	263
C-9. Schematic Diagram of Gifford-McMahon Expansion Engine	265
C-10. Engine Cycle	266
C-11. Gifford-McMahon Cooler	267
D-1. Schematic Construction of a Peltier Heat Pump	278
D-2. Energy-Level Diagram of a Peltier Couple	279
D-3. Peltier Couple with Notation and Definitions	283
D-4. Maximum Rate of Heat Pumping, Current Required for Maximum Heat- Pumping Capacity, and Coefficient of Performance for Maximum Heat Pumping as Functions of T_c (or ΔT) for $T_h = 300^\circ \text{K}$	286
D-5. Maximum Coefficient of Performance, Current Required for Maximum Coefficient of Performance, and Heat-Pumping Rate for Maximum Coefficient of Performance for the Couple of Figure D-4	288

FIGURES (Continued)

D-6. Rate of Heat Pumping and Coefficient of Performance as Functions of current for Various Temperature Differences	289
D-7. Nomograph I	290
D-8. Nomograph II	291
D-9. Nomograph III	292
D-10. Nomograph IV	293
D-11. Nomograph V	294
D-12. Nomograph VI	295
D-13. Nomograph VII	296
D-14. Nomograph VIII	297
D-15. Nomograph IX	298
D-16. Nomograph X	299
D-17. Flow Diagram for Design of Peltier Cooler	301
D-18. Form-Factor Dependence of Optimum Currents (I_c and I_Q) and Maximum Temperature Difference (ΔT_m)	310
D-19. Form-Factor Dependence (for Different $\Delta T/\Delta T_m$) of Coefficient of Performance at Maximum Heat Pumping (ζ_Q) and Heat-Pumping Rate at Maximum Coefficient of Performance (Q_c)	310
D-20. Form-Factor Dependence (for Different $\Delta T/\Delta T_m$) of Maximum Heat-Pumping Rate (Q_m) and Maximum Coefficient of Performance (ζ_m)	310
D-21. Cascaded Couples with $\Delta T/\Delta T_m$ approximately 0.9 for Each Stage	314
D-22. Exploded View of Detector and Cooler	315
D-23. Peltier Cooler for Gunsight Detector	316
D-24. Performance Enhancement of AN/ASG-14 Infrared Gunsight due to Peltier Cooler	316

TABLES

4-1. Minimum Detectable Power for Ideal Quantum Detector	54
5-1. Photoelectric Properties of Available Detectors	76
5-2. Summary of PbS Data	88
5-3. Summary of PbSe Data	98
5-4. Summary of PbTe Data	109
5-5. Au-Doped Ge (n-Type)	126
5-6. Au-Doped Ge (p-Type)	129
5-7. Zn-Doped Ge	131
5-8. Cu-Doped Ge	132
5-9. D^* (500°K, —, 1) for Several Ge-Si:ZnII Cells	144
5-10. Ge-Si:AuII at 80°K	145
5-11. Physical Properties	148
5-12. Summary of InAs Data	156
5-13. InSb Cell Data (Photovoltaic, Grown-Junction)	173
5-14. InSb-Cell Data (Photovoltaic, Diffused-Junction)	179-181
5-15. InSb-Cell Data (Photoconductive)	188, 189
5-16. InSb-Cell Data (PEM)	192
5-17. D^* Values Calculated from Blunt's Data	194
A-1. Figures of Merit	217
A-2. Evaluation of $D^*_{\lambda, \text{peak}}$	237, 238
C-1. Parameters of Optimum Available Coolers	269
C-2. Direct-Contact Coolers	270, 271
C-3. Joule-Thomson Cryostats	272
C-4. Complete Systems	274, 275
D-1. Comparison of Coolers Designed for Maximum Cooling Rate with Coolers Designed for Maximum Coefficient of Performance	305
E-1. Elements	319, 320
E-2. Binary Compounds	320-323
E-3. Ternary and Quaternary Compounds	323, 324
E-4. Mixed Crystals	324
E-5. Impurity-Activated Semiconductors	325, 326
E-6. Organic Semiconductors	327-329

INFRARED QUANTUM DETECTORS

ABSTRACT

Unclassified

→ The theory of the detection process is described, and data such as ~~NEP, etc.~~ noise spectrum, time constant, and resistance are given for the following infrared detectors: the lead salts, impurity-activated germanium, germanium-silicon alloys, tellurium, indium arsenide, and indium antimonide. ~~Appendices include a~~ description of test procedures, immersion techniques, and cooling devices. *are appended.* →

1 INTRODUCTION

William L. Wolfe

1.1. PURPOSE

The design of an infrared detection, mapping, or tracking device is predicated on a knowledge of the quantity and quality of radiation at the entrance aperture. When such information is known, the design is then based on considerations involving the collecting optics, the scanning system, the transducer, and the electronics. The transducer, or the detector as it is usually called by infrared workers, is the heart of the system. Its characteristics usually govern such things as the permissible information rate, the required bandpass, the size of the instantaneous field of view, and the limits of the total field of view. The detector is also a prime determinant of the least radiation difference detectable by the equipment.

A detector is usually chosen for a system first on the basis of its spectral sensitivity, and next on the length of time it takes to respond to a signal, the available areas, noise characteristics, cooling requirements, and mounting. Additional considerations are its characteristics as a circuit element—principally its impedance—and such things as microphonics, availability, and cost. Certainly, it is not possible to place these characteristics in order of importance for all applications, but the general arrangement indicated above is probably representative.

The purpose of a state-of-the-art report on detectors is at least two-fold. First, all the above-mentioned characteristics of detectors should be presented in a clear and readily accessible form. The system designer can then use the data he needs. Second, there should be included enough theory for the engineer to estimate the characteristics of detectors of the future for his systems. This theory should also provide a basis for the detector workers to advance the state of the art.

The first four chapters of this report introduce and describe the ways that solid-state devices are used to transduce a flux of incident, infrared photons into an electrical signal. Chapters 5 and 6 describe the properties of present photodetectors and some possibilities for the future. The appendixes include descriptions of test procedures, immersion techniques, and cooling devices.

1.2. LIMITATIONS

There are two ways to classify infrared detectors. They may be classified according to whether they integrate all the power falling on their surface or whether they respond to local power densities

throughout their surface, thereby creating an image. They may also be classified according to the physical mechanism that is the basis of the transduction. The latter classification scheme is probably the more fundamental, but the former is of more use in instrumentation problems. Imaging detectors, for the purposes of this report, are such things as photoemissive tubes, the Evaporograph, the Edgegraph, and the Thermicon. In general, the latter three devices are presently not satisfactory for use in infrared military equipments because they have not reached sufficiently advanced stages of development. Photoemissive tubes have a fundamental wavelength limit of sensitivity which is short; they are therefore not useful in most modern systems which are based on detecting radiation emitted by targets. Such radiation is usually concentrated in the longer-wavelength regions. Therefore, the imaging detector is not considered in this report.

The two principal methods of detecting infrared radiation and transducing it into an electrical signal are thermal detection and quantum (photo) detection. All infrared detectors are ultimately quantum detectors since radiation occurs in this form; the distinguishing feature, however, lies in the method by which the detector transduces the radiant power. Since transduction in the thermal-detection case is primarily a simple power conversion in which the radiant power is converted into the increased heat of the detector, these detectors have a flat spectral response. On the other hand, the quantum or photodetectors which respond to incident photons by changing their electronic state do not exhibit an appreciable temperature rise; they have a very strong wavelength dependence.

Thermal detectors have been used for many years. Some examples are bimetallic strips, thermocouples, thermopiles, metal bolometers, and thermistor bolometers. Generally, thermocouples, thermopiles, and bimetallic strips are relatively insensitive to thermal radiation and quite sluggish in their response. Metal bolometers have not shown much promise to date, although the work of L. Davis at the Hughes Aircraft Company indicates that such a bolometer in modern form might be competitive in sensitivity and response with some photodetectors (Reference 1-1). Thermistor bolometers, first developed by W. W. Brattain (Reference 1-1), have been the workhorse of military detection systems in the 3- to 13- μ region of the spectrum (although recent, extrinsic detectors should surpass thermistors in time constant and sensitivity). However, since the present knowledge of thermistor bolometers has already been summarized, their properties are not included in this report (Reference 1-2).

Thus, this report is limited to photodetectors, indeed it will be concerned primarily with those detectors whose operation is based on the photoconductive, photovoltaic, and photoelectromagnetic properties of materials.

1.3. REFERENCES

- 1-1. W. H. Brattain and J. A. Becker, "Thermistor Bolometers," J. Opt. Soc. Am., 1946, Vol. 36, p. 354.
- 1-2. R. de Waard and E. Wormser, Thermistor Infrared Detectors, Part I: Properties and Developments, NAVORD Report Number 5495, Barnes Engineering Co., Stamford, Conn., 30 April 1958 (UNCLASSIFIED).

PHYSICS of the DETECTION PROCESS

Gwynn H. Suits

An understanding of the behavior of electrons in solids forms the foundation for the description of the interaction of radiation with quantum detectors. Therefore, a summary of the energy-band model of solids is presented to provide this foundation.

2.1. SUMMARY OF THE ENERGY-BAND MODEL

A very useful, though not fully rigorous, picture of the behavior of electrons in solids is currently used in most engineering literature on semiconducting devices, and a number of good references exist. The theory is best expounded by the use of an energy-level diagram such as that of Figure 2-1.

Electrons move about in a crystalline solid. The constants of motion are described by four quantum numbers for each electron. Three quantum numbers specify the three components of momentum, and one quantum number specifies the orientation of the electron spin. Within the solid, the momentum quantum numbers describing the electron motion have only discrete and usually closely consecutive values. The total energy is a function of these discrete quantum numbers and hence will also have only discrete values, which are closely consecutive (forming energy bands) except in a few important instances as illustrated by the gap in energy in Figure 2-1.

For the purpose of this discussion the Pauli exclusion principle applies; that is, in any isolated atomic system (a semiconducting crystal in this discussion), no two electrons may take a motion which

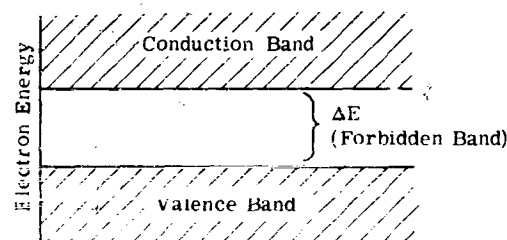


FIGURE 2-1. THE BAND PICTURE OF AN IDEAL SEMICONDUCTOR

is specified by the same four quantum numbers. For every permissible set of four quantum numbers there is a value of energy which the electron must have. For an electron to "occupy" an energy level means that an electron has a motion described by the only four quantum numbers that correspond to that energy value.

In a crystal at absolute zero temperature, electrons tend to fall into the motion which provides the lowest total energy. Because of the Pauli exclusion principle, however, all electrons cannot move at the lowest energy levels, so some electrons must then move at higher energies. In the case of an ideal semiconductor illustrated in Figure 2-1, the "valence band" is fully occupied. There are exactly as many electrons as valence-band energy levels to be occupied. A gap of forbidden energies exists between the lower-energy valence band and the higher-energy empty conduction band. This simply means that no combination of the four quantum numbers corresponds to energies in the gap range so that electrons cannot move through the material with total energies which are forbidden.

2.2. THERMAL EXCITATION OF ELECTRONS

The smooth motion of electrons through a crystal lattice depends upon the perfect spatial periodicity of the electrical potential energy. Any abrupt change from periodicity may provide a possible disruption of the motion. Even at low temperatures (e.g., liquid-nitrogen temperature) the atoms in crystals are in constant, agitated, thermal motion. The motion is also quantized and can be represented by the superposition of many quantized plane waves of strain moving through the crystal. Each quantum of strain energy is given the appropriate name "phonon." This mechanical agitation tends to disrupt the periodicity and hence the smooth motion of electrons. However, a disruption of the motion can occur only to those electrons which can change their motion or quantum numbers by such amounts that the change in electron energy is equal to the energy to be transferred by collision with the atoms. Here the influence of the Pauli principle is important since the electron cannot absorb such energy if the resulting change in energy would bring the electron to an energy level which is already occupied. In this random, agitated motion there is an important though infrequent chance that a fairly large energy exchange between electron and lattice atoms will occur so that electrons with energies near the top of the valence band can take on energies near the bottom of the conduction band where the levels are not likely to be occupied. Once conduction-band motion is established, the electron is free to accept even small additional energy increments from lattice atoms because of the low probability that adjacent energy levels in the conduction band will be occupied. The resulting motion of the electron is then equivalent to Brownian motion as long as it moves with conduction-band energies.

2.3. THE CONCEPT OF "HOLES"

When an electron in the valence band is excited into conduction-band energy levels, a vacancy occurs in the energy level which it has left. This vacancy can be occupied by other electrons in the valence band by means of small changes in energy which can easily be supplied by the lattice motion. The net result is that the vacant level becomes occupied and a new vacancy develops at a slightly different energy. This wandering vacancy acts physically as if a positively charged particle were undergoing Brownian motion with a tendency to rise on the energy-level diagram to the highest occupied energy level (in contradistinction to the electron which tends to fall to the lowest unoccupied energy level). The hypothetical particle is called a "hole" or p-type charge carrier because of the positive effective charge. The electrons in the conduction band in parallel nomenclature are called n-type charge carriers.

2.4. FLOW OF CHARGE CARRIERS

If the energy levels of the valence band were completely filled, there would be as many electrons moving in the +x direction as in the -x direction so that no net current would flow. The application of an external electric field does not alter this situation since the electrons cannot increase in energy by sufficiently small steps to accept acceleration by the field. The Pauli principle forbids small jumps to levels already occupied, and the gap of forbidden energies is too large.

However, as soon as a pair of n- and p-type carriers are formed by the excitation of an electron from valence-band energy to conduction-band energy, current can flow, but only as much current as the motion of two charge carriers can provide. The conductivity is proportional to the number of such carriers and to their mobility in the crystal so that

$$\sigma = e(n\mu_n + p\mu_p)$$

where e is the magnitude of the electronic charge, and μ_n and μ_p are the mobilities or the average drift velocity per unit electric field, respectively; n and p are the carrier concentrations in the mobile condition.

2.5. IMPURITIES IN SEMICONDUCTORS

In most cases, impurities in semiconducting materials are detrimental to the properties desirable in infrared detectors, but under controlled conditions traces of impurities in otherwise pure semiconductors can provide certain desirable changes in the energy-band structure. Concentrations of the order of 1 part in 10^6 to 10^9 of selected materials are sometimes intentionally introduced for particular effects.

Like any defect in the perfect periodicity of a crystal potential, an atom of an impurity in the crystal tends to disrupt the smooth motion of p- or n-type carriers which might otherwise be free to accelerate. In addition, impurities can alter the energy-band picture in various ways as indicated in Figure 2-2.

The energy levels due to impurities which are of interest fall within the large forbidden-energy gap. These levels are indicated as short in spatial extension, indicating that the electron is localized in space in the neighborhood of the impurity atom causing this change.

It should be noted that for substitutional impurities (those which take the same lattice position as the atoms of the pure material), the dashed lines are not additional levels but represent an alteration of what was there before.

Two important types of alterations may occur. The level marked D, called a donor level, is normally filled at low temperature, while the level marked A, called an acceptor level, is normally empty at low temperature.

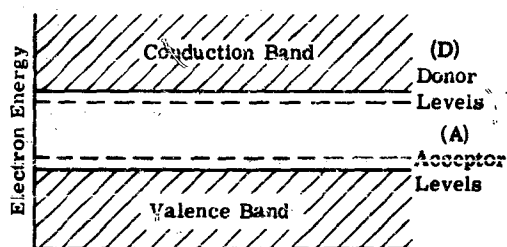


FIGURE 2-2. THE BAND PICTURE OF AN IDEAL SEMICONDUCTOR WITH IMPURITIES

At higher temperatures the thermal excitation is sufficient to excite electrons from donor levels to the conduction band in such numbers that the population of the donor levels is significantly depleted. A semiconductor in this condition will exhibit impurity conductivity having carriers of predominantly n-type. A similar picture applies to p-type conduction and acceptor levels. The empty localized donor level may be thought to contain a trapped hole, and the excitation of a valence-band electron to that level may be viewed as the excitation of a p-type carrier from the localized level to the valence band. In any real crystal there are both types of impurity, although one type usually predominates.

2.6. INTERACTION WITH RADIATION

The excitation of electrons in a solid may be brought about by the mechanical agitation of atoms (phonons) or by the absorption of photons which strike the crystal. While both types of excitation are important in infrared detectors, the excitation by photons plays a central role.

Suppose a pure crystal is held at low temperature so that the number of excited carriers (electrons in the conduction band and holes in the valence band) is small. Let the gap of forbidden energy be E_g . Now when a photon of frequency f , such that $hf \geq E_g$, is absorbed in the crystal by a valence-band electron, the electron will be excited to the conduction band, creating an n- and p-type carrier pair which would not normally be there in thermal equilibrium. This extra pair increases the conductivity of the crystal slightly as long as it exists. The rate at which pairs are created will be proportional to the number of suitable quanta incident upon the crystal. Usually the extra electrons and holes do not stay separated for long. They recombine by the aid of at least two mechanisms, but the end result is the same regardless of the mechanism, i.e., a conduction-band electron finds a hole in the valence band and loses energy so that it returns to the original lower energy level. The rate at which extra n- and p-type carriers recombine will determine the average time extra carriers can spend in the conducting state of motion.

In a pure crystal the average time spent by the charge carriers in the conducting condition and the average time required for recombination are the same. However, if spatially localized energy levels called traps exist in an impure crystal, then the charge carriers will spend a portion of their time in these nonconducting levels and will be free to conduct only intermittently. The "lifetime" of the carriers is defined as the average time which the charge carrier spends in the conducting condition, while the "recombination time" is defined as the average time the charge carriers stay in the excited states of motion, which includes the time spent in temporary localized positions at traps. Thus the recombination time is always greater than or equal to the lifetime.

In many cases, a trap energy level can be "occupied" by only one charge carrier so that the average population of carriers in all trap levels can never exceed a certain maximum number. As the population of carriers in trap levels increases, the number of unoccupied traps becomes significantly sparse so that the influence of traps tends to become insignificant. The rate at which charge carriers are trapped depends upon the "cross section" for capture by the traps for a particular charge carrier. Hence

$$\begin{aligned} R_n &= \sum_N v_n T_n \Delta n, & R_p &= \sum_p \bar{v}_p T_p \Delta p \\ R_n &= \sum_N \bar{u}_n T_n \Delta n, & R_p &= \sum_p \bar{u}_p T_p \Delta p \end{aligned}$$

where R = the number per cubic centimeter per second of extra carriers trapped

Σ = the capture cross section of the trap

\bar{u} = the average speed of the charge carrier

T_n or T_p = the concentration of the respective empty traps

Δn or Δp = the concentration of the respective extra charge carriers in the conducting state of motion

Subscripts n and p are used to indicate electrons and holes, respectively.

The rate at which extra carriers are re-emitted into the conducting state of motion depends mainly upon the size of the energy jump required to get away and the concentration of occupied traps. The dependence upon the size of the required energy is a statistical one governed approximately by Maxwell-Boltzmann statistics. Therefore one can say that the probability of a transition is proportional to $\exp(-E/kT)$, where E is the required energy and kT represents the thermal energy. When the thermal energy kT becomes very large compared to the required energy, the probability of a transition approaches 1; when $kT \ll E$, the probability approaches 0. Hence,

$$G_n = F_n T'_n \exp(-E_n/kT)$$

$$G_p = F_p T'_p \exp(-E_p/kT)$$

where G = the number of carriers per cubic centimeter per second which break free of traps

F = a constant characteristic of the trap

T'_n and T'_p = the concentrations of occupied traps

E = the required energy

k = the Boltzmann constant

T = the absolute temperature

n and p subscripts indicate "electrons" and "holes," respectively.

If the semiconductor is placed in a field of incident radiation, extra charge carriers can be generated by absorbed photons. If J represents the number of photons per unit area per unit time incident on the semiconductor, and if a is the absorption coefficient, then a relation for the rate of change of extra free carriers can be written

$$\frac{d}{dt}(\Delta n) = aJ - \Delta n/\tau_n + F_n T'_n \exp(-E_n/kT) - \sum_n \bar{u}_n T_n \Delta n$$

$$\frac{d}{dt}(\Delta p) = aJ - \Delta p/\tau_p + F_p T'_p \exp(-E_p/kT) - \sum_p \bar{u}_p T_p \Delta p$$

Although the further analysis of this model will not be covered here, certain important consequences should be pointed out. Notice that the lifetimes of the two types of carriers need not be the same, and, in fact, are usually significantly different. The extra charge-carrier concentrations need not be equal, and, in general, are significantly different. Recall that by definition Δn and Δp are the extra carriers which are in the conducting state. Those stuck temporarily in traps are not counted. Since the crystal is expected to be electrically neutral at all times, the balance of extra charge carriers must reside in traps when $\Delta p \neq \Delta n$.

In the simple trap model which is discussed here only one carrier is required for occupation. Hence the concentration of empty traps plus the concentration of traps occupied by extra carriers must just equal the concentration N_0 , P_0 , of traps normally unoccupied during thermal equilibrium—i.e.,

$$T_n + T'_n = T_{no}$$

$$T_p + T'_p = T_{po}$$

Thus the above relations may be written as

$$\frac{d\Delta n}{dt} = aJ - \frac{\Delta n}{\tau_n} + F_n T'_n \exp\left(\frac{-E_n}{kT}\right) - \sum_n \bar{u}_n (T_{no} - T'_n) \Delta n$$

$$\frac{d\Delta p}{dt} = aJ - \frac{\Delta p}{\tau_p} + F_p T'_p \exp\left(\frac{-E_p}{kT}\right) - \sum_p \bar{u}_p (T_{po} - T'_p) \Delta p$$

In thermal equilibrium all quantities of Δn , Δp , N' , and P' are zero by definition. Hence, Δn and Δp will both increase at the rate of aJ when proper illumination is abruptly started. When the steady state has been reached under illumination

$$\frac{d\Delta p}{dt} = 0$$

$$\frac{d\Delta n}{dt} = 0$$

Moreover, it can be demonstrated by straightforward reasoning that the terms on the right must balance in pairs.

$$aJ - \frac{\Delta n}{\tau_n} = 0$$

$$F_n T'_n \exp\left(\frac{-E_n}{kT}\right) - \sum_n (T_{no} - T'_n) \Delta n = 0$$

and similarly for the p-type carrier. Since there is no net trapping now, the population of extra carriers is simply $\Delta n = \tau_n aJ$ and $\Delta p = \tau_p aJ$.

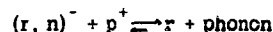
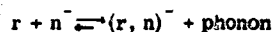
The effect of shallow temporary traps on the response time is usually to lengthen the rise and the decay times. In order to establish a steady state, additional carriers must be generated to populate the traps as well as to supply the usual loss of carriers through recombination. The decay time is also delayed by the time required to empty the population in temporary traps.

The final recombination of carriers can occur by the direct collision of p and n carriers so that the process can be written as

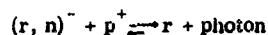


The reaction rate of the reverse reaction is very small. Some traps reside in semiconductors which have energy levels with relatively large energy differences from the valence band or conduction band. In this case, the probability that a trapped carrier may be re-emitted to the conducting condition by thermal agitation is small compared to the probability that recombination with the opposite carrier will occur at that trap. The traps at which recombination can occur are sometimes called "recombination centers."

The following reaction can take place:



where r represents the recombination site, and the phonon represents the mechanical motion of the lattice atoms. Actually reactions other than that listed above can also occur. If the energy levels and energies of reaction are proper, the reaction described by the second line above could be a reaction described by



where the photon which is emitted is of lower frequency. In general, combinations of these and other reactions take place simultaneously.

Since the lifetime of a carrier is measured only by the average time extra carriers remain in the conducting condition, the trapping of a carrier by a recombination center ends the life of the carrier even though that carrier may have to wait for a carrier of opposite type to complete the recombination reaction; so it is not unexpected to find the lifetimes of the two carrier types differing by significant amounts. One type of carrier usually waits for the other in a recombination center.

The operation of infrared quantum detectors in the photoconducting, photovoltaic, and photoelectromagnetic modes is based upon the monitoring of the extra carriers generated in the above fashion. The means by which this monitoring is performed determine the mode of operation of the detector.

3

THEORETICAL DESCRIPTION OF DETECTORS

Sol Muddelman

This chapter deals primarily with the processes of signal and noise generation in quantum and thermal detectors. In addition, a detector's speed of response and its spectral-response characteristics are described. However, additional information pertinent to these last two parameters is found in Appendix A.

The mechanisms involved in signal and noise generation will be described in substantial detail, accompanied generally by quantitative treatments that hopefully exemplify appropriate analysis procedures. The intention here is to establish the necessary background for Chapter 4, which deals with theoretical concepts for evaluating the performance capabilities of detectors.

3.1. SIGNAL GENERATION IN QUANTUM DETECTORS

The quantum detector absorbs electromagnetic radiation (or photons), and thereby generates internal charge carriers. The mechanism of this process requires that the quantum of energy associated with the photons ($E_{ph} = h\lambda/c$) be greater than some critical energy corresponding to allowed transitions between energy levels in the forbidden-energy region, the conduction band, and/or the valence band of the semiconducting detector. This process is carried out without any significant temperature change. The carriers so generated appear in a form suitable for measurement as a voltage or a current.

3.1.1. PHOTOCONDUCTIVE DETECTORS. The photoconductive detector is generally operated with the simple circuitry of Figure 3-1. The voltage drop V_C across the detector is given by

$$V_C = \frac{V}{r_L + r_C} \cdot r_C \quad (3-1)$$

where V is the bias battery voltage

r_L is the load resistor

r_C is the resistance of the photoconductive detector.

The signal voltage is the variation in the voltage drop caused by the change in r_C when the detector is exposed to signal radiation.

Therefore

$$\Delta V_C = I \cdot \Delta r_C + \Delta I \cdot r_C = I \cdot \Delta r_C$$

where I (the bias current) $= V/(r_L + r_C)$, and $\Delta I = 0$, since photoconductive detectors are generally operated under constant-current conditions.

The change in resistance is due to the change in the number of carriers created by the absorption of signal photons. The simplest case is the intrinsic photoconductor whose hole and electron mobilities are approximately equal. The geometrical configuration shown in Figure 3-2, where the electrodes are placed across the wd end faces and the ℓw surface is exposed to radiation, will be used for all discussions that follow, unless otherwise indicated. The cell resistance is given by

$$r_C = \rho \frac{\ell}{dw} = \frac{\ell}{\sigma dw} = \frac{\ell}{2ne\mu dw}$$

where ρ is the electric resistivity

$$\sigma \text{ is the electric conductivity} = ne\mu_n + pe\mu_p = 2ne\mu$$

μ is the mobility and $\mu_n = \mu_p$

n is the concentration of electrons

p is the concentration of holes

ℓ is detector length

w is detector width

d is detector thickness

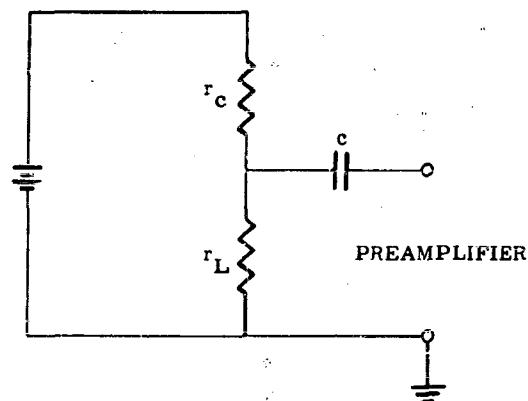


FIGURE 3-1. PHOTOCONDUCTOR DETECTOR CIRCUIT

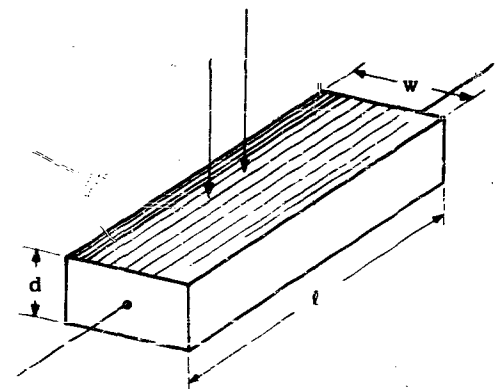


FIGURE 3-2. DETECTOR GEOMETRY

When radiation strikes the detector, it causes a change in the density of carriers, and therefore a change in conductivity. The change in resistance is then given by

$$\Delta r = \frac{dr}{dn} \cdot \Delta n_S = -\frac{\rho \ell}{dw} \cdot \frac{\Delta n_S}{N} \quad (3-2)$$

where $N_S = nwl$, N is "total number of carriers," and the subscript S means "due to signal radiation." The signal voltage is then

$$V_S = I \cdot \Delta r_C = \frac{V}{r_L + r_C} \cdot \frac{\rho \ell}{dw} \cdot \frac{\Delta n_S}{n} \quad (3-3)$$

or

$$V_S = \frac{V}{r_L + r_C} \cdot \frac{\rho \ell}{dw} \cdot \frac{\Delta N_S}{N} \quad (3-4)$$

The photodetector's small-signal properties are governed by (Reference 3-1):

$$\frac{d}{dt} \cdot \Delta N_S = A \eta_S J_S - \frac{\Delta N_S}{\tau} \quad (3-5)$$

where $\Delta N_S = N(t) - N$, A is the area $w\ell$, N is the equilibrium number of electrons in the absence of the signal photon flux density J_S , η_S is the responsive quantum efficiency, $N(t)$ is the number of electrons at time t , and τ is the electron-hole lifetime. The solution of this equation for a sinusoidal signal of modulation frequency, $f = \omega/2\pi$, is

$$|\Delta N_S(f)| = \frac{A \eta_S J_S \tau}{\sqrt{1 + (\omega \tau)^2}} \quad (3-6)$$

The fractional change in conductivity is

$$\frac{|\Delta N_S(f)|}{N} = \frac{\eta_S J_S \tau}{nd \sqrt{1 + (\omega \tau)^2}} \quad (3-7)$$

The signal voltage is

$$V_S = \frac{V}{r_L + r_C} \cdot \frac{\rho \ell}{dw} \cdot \frac{\eta_S J_S \tau}{nd \sqrt{1 + (\omega \tau)^2}} \quad (3-8)$$

It is clear that signal response improves with longer lifetimes, improved quantum efficiencies, and decreasing equilibrium density of carriers.

3.1.2. PHOTOVOLTAIC DETECTORS. The infrared photovoltaic detector is usually a single crystal of some semiconductor, with distinctive n and p regions. These regions are separated by a barrier called the "depletion" layer, across which a strong electric field exists. Similar layers can also be formed at a metal-semiconductor contact, at a p-type surface on an n-type bulk crystal, and at a junction between two semiconductors with unequal band gaps. All of them can be used to generate photovoltages.

Consider two crystals which are identical except that one crystal has impurities which make it n type and the other has different impurities which make it p type. The first crystal has a greater density of mobile or free electrons; the second has a greater density of holes. If these two crystals are connected together with perfect alignment of the atoms so as to make one large single crystal, then the higher concentration of free electrons in the n region causes a diffusion of electrons into the p region, and vice versa for holes. Each region of the crystal is initially independently neutral (even though the two regions have opposite types of conductivity). Thus when an electron diffuses from the n to the p side of the crystal, it gives the p side a negative charge. The next charge to diffuse over does so with more difficulty since the first charge has created an opposing electric field. Each successive charge that diffuses over experiences increased opposition and requires more energy to get over to the p side. Those that do get over have an increased potential energy corresponding to the charge build-up. Exactly the opposite situation prevails for holes. A negative charge layer is built up on the p side, while a positive charge layer is built up on the n side. This is shown in Figure 3-3. Finally, an equilibrium situation is reached where electrons diffusing from the n- to the p-type region are balanced by a flow of carriers drifting in the opposite direction because of the electric field. A corresponding situation applies to holes. This explains why a current flow is not observed when the two regions of the crystal are connected to an ammeter. At first glance, an examination of Figure 3-3 would lead to the impression that the charge distribution should cause the crystal to behave like a battery, since clearly an electric potential difference exists. However, the total current is the sum of the currents caused by this potential difference and that due to the imbalance in the charge densities of the two regions. At equilibrium, these currents are equal and opposite, resulting in a net current flow equal to zero. Mathematically, this situation can be described for the one-dimensional case as follows:

$$i_n = \sigma E = -ne\mu_n \frac{dV}{dx} \quad (3-9)$$

$$i_d = D_n \frac{dn}{dx} = \frac{kT}{e} \mu_n \frac{dn}{dx} \quad (3-10)$$

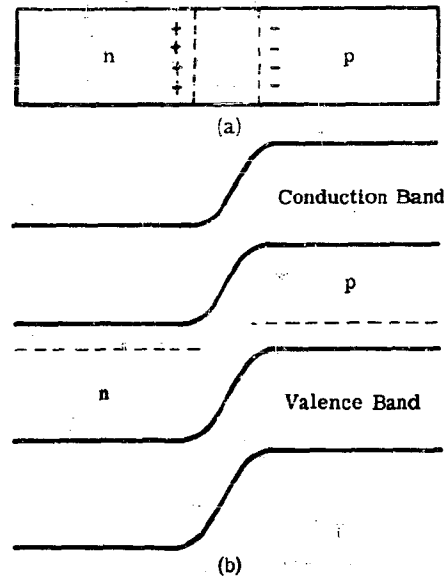


FIGURE 3-3. p-n JUNCTION. (a) Simplified charge distribution across the barrier. (b) Energy-level diagram.

where E is the electric field, the p-n junction is taken perpendicular to the x direction, i_n and i_d are the electronic drift and diffusion current densities, respectively, D_n is the diffusion coefficient for electrons, given by the Einstein relationship

$$D_n = \frac{kT}{e} \cdot \mu \quad (3-11)$$

and the other quantities are as noted earlier. At equilibrium, these two current densities are equal and opposite, so that

$$ne\mu_n \frac{dV}{dx} = D_n e \frac{dn}{dx} \quad (3-12)$$

This expression can be integrated to relate charge density and potential distribution in the barrier layer as

$$n(x) = A \exp \left[\frac{\mu_n}{D_n} V(x) \right] \quad (3-13)$$

where A is an integration constant. A similar derivation applies for holes.

When photons are continually absorbed in the region of the p-n junction, electron-hole pairs are created. This added concentration of carriers alters the diffusion and drift processes established when no photons are incident and results in a new equilibrium condition. A new, lower potential difference exists across the barrier. The electric field causing electrons to drift toward the n type region and the holes in the opposite region create negative and positive charges in the n and p regions, respectively. This results in the generation of a photovoltage measured across the junction. Thus a voltage generator has been created by causing a new distribution of charge carriers, which exists only as long as new carriers are continually being generated by the absorption of photons.

Another approach to understanding the basic process is to think of the device as a kind of current generator in which the new carriers generated are forced by the new nonequilibrium conditions to move out of the crystal junction. The n side of the crystal, now with too many electrons, becomes the negative electrode and electrons exit through its electrode. The situation is reversed for holes on the p type side, with the understanding that the departure of holes corresponds to electrons entering in p crystal.

A quantitative treatment describing this situation can be arrived at by utilizing the theory of the p-n junction diode. We shall not try to develop this theory here, but only to describe its results and the physical mechanisms involved.

The p-n junction is a diode whose voltage-current characteristic depends on the bias direction and the magnitude of the bias. The modern theory of the p-n junction derives from Shockley (Reference 3-2). The evolution of the theory is described by Moll (Reference 3-3). According to Shockley, the current-voltage relationship in the simplest case (low applied field and steep concentration gradients in going from the n- to the p-type regions) is given by:

$$I = I_s [\exp(eV/kT) - 1] \quad (3-14)$$

where

$$I_s = \frac{p_n D_p}{L_p} + \frac{n_p D_n}{L_n} \quad (3-15)$$

where L_p and L_n are the diffusion lengths of minority carrier electrons and holes in p- and n-type materials, respectively, and D_p and D_n are the corresponding diffusion constants. The diffusion constant and diffusion length are related by:

$$L = \sqrt{D\tau} = \sqrt{\frac{kT}{e} \cdot \mu \tau} \quad (3-16)$$

where τ is the minority carrier lifetime (References 3-4 and 3-5) and D is the diffusion coefficient for either holes or electrons, as indicated by a subscript. In this treatment, the current of holes flowing in one side of the junction is the same as that flowing out the other, while the current of electrons is also equal at both surfaces of the junction but moving of course in the opposite direction. The net current flow is then simply the sum of the hole and electron currents. One assumes further that the flow of electrons into the p region and holes into the n region (after passing through the junction) is essentially a diffusion process; that is, the n and p regions are more highly conductive than the junction; therefore practically all of the voltage drop is across the junction.

It is clear, from examination of Equation 3-12 in the case of an applied voltage sufficiently large, that I is exponentially dependent on the voltage. When the applied voltage is negative, the current flow approaches the saturation value I_s . The first case exists when the n region is attached to the negative electrode of a d-c supply, while the p region is made positive. This reduces the potential difference across the junction from its original equilibrium value and facilitates current flow. When the bias is applied in the reverse direction, and the current reaches its saturation value, the current flow is due entirely to the number of minority carriers able to cross the junction. It is now the electrons originating in the p material, within a diffusion length of the barrier L_p , and the holes in the n material, within a diffusion length of the barrier L_n , which constitute the carriers for current flow. These carriers are created by the G-R (generation-recombination) process whereby electron-hole pairs are created in the lattice from phonon (thermal) interaction between atoms that make up the lattice. The saturation arises when all possible minority carriers from either side of the junction region are contributing to the current flow.

The theory and experimental results, however, differ somewhat, even after all sources of error such as surface leakage and crystalline imperfections are included in the analysis. To resolve this difference an extra current component is distinguished, which is attributed to charge carrier generation by the absorption of photons in the barrier region. The p-n junction equation then becomes

$$I = I_s \left[\exp \left(\frac{eV}{kT} \right) - 1 \right] - I_{SC} \quad (3-17)$$

where I_{SC} is the current induced by the incident background radiation. Derivations of I_{SC} are given by Cummrow (Reference 3-6) and Rittner (Reference 3-7) in treatments of the solar battery.

The treatment of the p-n junction is still not complete in that account has not yet been taken of the facts that carriers are created by phonon interaction in the generation-recombination process within

the barrier region, and that there is a shunt-conductance leakage for practical diodes. The equation has to be further modified in the form

$$I = I_s \left[\exp\left(\frac{eV}{\beta kT}\right) - 1 \right] - I_{SC} + G_{sh} V \quad (3-18)$$

where β is a constant that provides the measure of the extra charge carriers, and G_{sh} is the conductance in shunt with the diode. The factor β is unity for an ideal diode, but in practice is about 2 to 3.

" This last equation can be used to derive either an expression for the output open-circuit voltage generated from a p-n junction photodetector, or an expression for the short-circuit current. When used as a photodetector, without any biasing, V in Equation 3-18 becomes simply the generated voltage. For the open-circuit case no current can flow, and the output voltage becomes

$$V = \frac{\beta kT}{e} \ln \left(\frac{I_{SC} - G_{sh} V}{I_s} + 1 \right) \quad (3-19)$$

while for the short-circuit case, where $V = 0$,

$$I = I_{SC} \quad (3-20)$$

In the case where

$$\frac{I_{SC} - G_{sh} V}{I_s} \ll 1$$

the logarithm above reduces to

$$\frac{I_{SC} - G_{sh} V}{I_s}$$

and

$$V = \frac{\beta kT}{e} \cdot \frac{I_{SC}}{I_s} \cdot \left[\frac{1}{1 + (\beta kT/e) \cdot (G_{sh}/I_s)} \right] \quad (3-21)$$

For the case where a periodically modulated signal is superimposed on a steady background, a correspondingly modulated voltage of amplitude V_M and current I_M are added to the background V_B and I_B . The modified expression is

$$I = I_s \left\{ \exp \left[\frac{e}{\beta kT} (V_B + V_M \exp i\omega t) \right] - 1 \right\} - (I_B + I_M \exp i\omega t) + G_{sh} (V_B + V_M \exp i\omega t) \quad (3-22)$$

Consider only the simple case where the total voltage generated is sufficiently small so that

$$\exp \frac{e}{\beta k T} [V_B + V_M \exp i\omega t] - 1 = \frac{e}{\beta k T} [V_B + V_M \exp i\omega t]$$

Then

$$I = I_s \left[\frac{e}{\beta k T} (V_B + V_M \exp i\omega t) \right] - [I_B + I_M \exp i\omega t] + G_{sh} [V_B + V_M \exp i\omega t]$$

The short-circuit current becomes

$$I_{SC} = - (I_B + I_M \exp i\omega t) \quad (3-23)$$

The open-circuit voltage becomes

$$V_B + V_M \exp i\omega t = \frac{I_B + I_M \exp i\omega t}{I_s e / \beta k T + G_{sh}} \quad (3-24)$$

The steady voltage is given by

$$V_B = \frac{I_B}{I_s e / \beta k T + G_{sh}} \quad (3-25)$$

and the a-c component is

$$V_M = \frac{I_M}{I_s e / \beta k T + G_{sh}} \quad (3-26)$$

Often, the p-n junction photodetector is operated in a manner similar to that of the photoconductive detector. A bias voltage is applied to the detector in series with a load resistance, with the photosignal picked off using the same kind of circuitry as for the photoconductive detector. The bias is applied to the junction diode in the reverse direction and effectively shows increased impedance to the pre-amplifier circuit. Radiation is absorbed creating carriers that reach the junction region, causing changes in the value of I_{sc} . As pointed out by Pruett and Petritz (Reference 3-8), the response of the photodiode to a small radiation signal ΔJ_S is obtained from the differential of Equation 3-18:

$$\Delta I = \left[- \frac{dI_{SC}}{dJ_S} + \frac{e}{\beta k T} \left(I_s \exp \frac{eV}{\beta k T} \frac{dV}{dJ_S} \right) + G_{sh} \frac{dV}{dJ_S} \right] \cdot J_S \quad (3-27)$$

The small-signal short-circuit current generator for a Norton representation is found by holding V constant:

$$I_S = \Delta I_{V = \text{constant}} = - \frac{dI_{SC}}{dJ_S} \cdot J_S$$

This term represents the increase in current due to signal superimposed on background radiation photons. Thus

$$\frac{dI_{SC}}{dJ_S} = e\eta A$$

and

$$I_S = -e\eta A J_S \quad (3-28)$$

where J_S is the number of photons per unit area per unit time falling on the detector of area A , and where the efficiency of conversion to electron-hole pairs is given by η . Thus the signal current is directly proportional to signal radiation.

3.1.3. THE PHOTOELECTROMAGNETIC DETECTOR. The electromagnetic (PEM or PME) effect may be described with reference to the more familiar Hall effect; see Figure 3-4. In both effects, a sample of the semiconducting material (usually in the form of a parallelepiped) is placed in a magnetic field and oriented so that its length is perpendicular to the direction of the magnetic field. The sides are arranged so that the magnetic field is perpendicular to another pair of parallel faces. In the Hall effect Figure 3-4(b), a current is made to flow through the sample by the application of a potential

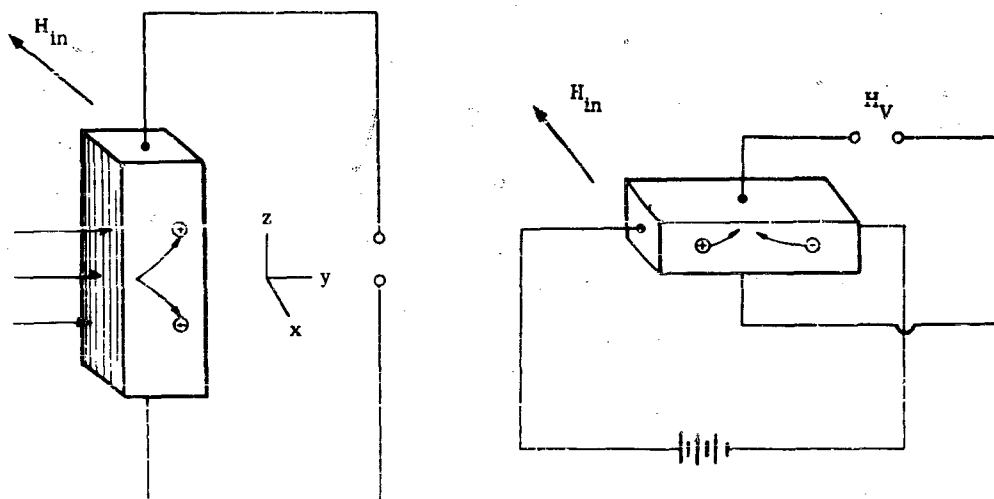


FIGURE 3-4. CIRCUIT CONFIGURATIONS. (a) PEM effect, (b) Hall effect.

difference across its ends. The magnetic-field causes electrons and holes to drift in opposite directions while they travel along the length of the sample. In the PEM effect, Figure 3-4(a), photon absorption creates an excess concentration of electrons and holes. The existence of extra carriers at the front surface and their absence at the rear leads to a diffusion of carriers from the front to the rear to equalize the inhomogeneous distribution. This diffusion process obeys the same law as described above for the photovoltaic detector (Equation 3-10).

The motion of the carriers in both samples is influenced by their interaction with the magnetic field. In the Hall effect, electrons and holes usually of different densities drifting along in opposite directions, and under the influence of the magnetic field, tend to accumulate a net charge on one side of the sample. This results in a potential difference between this side and the opposite face. Electrodes placed on these surfaces permit the measurement of this Hall voltage. The diffusion current in the PEM effect has both electrons and holes moving from the front to the rear faces of the sample. Charge carrier interaction with the magnetic field causes the holes and electrons to be deflected in opposite directions, and a potential difference between the sample ends develops. Electrodes placed across the ends permit the measurement of the PEM voltage. This voltage persists as long as the diffusion current flows, which in turn persists as long as the detector is irradiated.

Another phenomenon that might be noted here is the Dember effect. Consider Figure 3-4(a) without the magnetic field. Electron-hole pairs created at the front surface move toward the rear surface, in a manner dependent not only upon the carrier concentration at the front surface but also upon their mobilities. If the mobilities are significantly different, one type of carrier moves ahead of the other. This results in a potential difference between the front and rear surfaces, referred to as the Dember voltage. The resulting electric field creates a force in opposition to the diffusion force. The equation expressing this relationship for holes is

$$\frac{I}{e} = -D_p \frac{dp}{dy} + \mu_p p E_y \quad (3-29)$$

Under equilibrium conditions, the electric-field current component equals the diffusion current and $I = 0$.

$$E_y = -\frac{D_p}{\mu_p} \cdot \frac{dp}{dy} = \frac{kT}{e p} \cdot \frac{dp}{dy} \quad (3-30)$$

since $D_p = (kT/e) \mu_p$. A similar expression applies for electrons. It is clear that if electrons and holes move with equal mobilities, the net charge displacement is zero, and the Dember voltage ceases to exist. This field effect as noted by Moss (Reference 3-9) causes the slower carrier to accelerate and the faster one to slow down, tending to equalize their path lengths.

The theory of the PEM effect has been investigated in recent years by a number of authors, who have contributed to its continuous refinement (References 3-10 through 3-18). Moss suggests a readily understandable approach which provides a useful expression for the PEM signal voltage (Reference 3-9). Assume that the mobilities are sufficiently alike so that no appreciable electric field develops. The charges created at the front surface diffuse inward a distance given by their diffusion length.

$$L_n = \sqrt{D_n \tau} \quad (3-31)$$

where τ is the average carrier lifetime. The distance moved by the carrier toward the electrodes is given (for small θ) by

$$L \sin \theta \approx L \tan \theta \approx \theta$$

An estimate of the angle θ can be derived using the force components acting on the carrier. The diffusion force per carrier is given by

$$F_D = \frac{kT}{e\mu_p} \cdot \frac{dp}{dy}$$

The force created by carrier interaction with the magnetic field is given by

$$F_B = e[u \times B] = e\mu B$$

where

$$u = \frac{kT}{e\mu_p} \cdot \frac{dp}{dy} \cdot \mu_p$$

Therefore

$$F_B = \frac{kT}{p} \frac{dp}{dy} \mu_p B$$

and

$$\tan \theta = \frac{F_B}{F_D} = e\mu_p B \quad (3-32)$$

Hence the displacement toward the electrodes is given by

$$\sqrt{D_p \tau} e\mu_p B \quad (3-33)$$

The effective charge recorded by the meter in the circuit is

$$\frac{1}{\epsilon} \sqrt{D_p \tau} e\mu_p B \quad (3-34)$$

The factor $1/\epsilon$ can be explained simply by considering that one lead of the crystal is attached to an electrometer, and that the other is attached to ground as in Figure 3-5. Consider a "hole" of charge

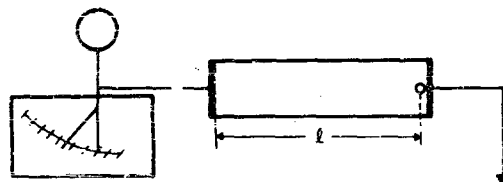


FIGURE 3-5. EFFECTIVE CIRCUIT CHARGE AS A FUNCTION OF CHARGE DISPLACEMENT

infinitesimally close to the grounded electrode. The potential energy recorded at the electrometer is given by

$$\phi_{\ell} = \frac{p}{\kappa \ell}$$

where κ is the dielectric constant. Displace the charge a distance r toward the electrometer, so that

$$\phi_{\ell-r} = p / \kappa (\ell - r)$$

The increase in potential energy at the electrometer due to the charge movement is given by

$$V = \phi_{\ell-r} - \phi_{\ell} = p r / \kappa \ell (\ell - r)$$

The charge P induced in the electrometer can be expressed in terms of V by

$$V = P / C$$

The capacity between two points in space is given by the distance between them. Thus

$$V = P / \kappa (\ell - r) = p r / \kappa \ell (\ell - r)$$

$$P = p r / \ell \quad (3-35)$$

A similar contribution arises from the electrons so that if both electrodes were placed directly across an ammeter the net current derived would be

$$i_s = \frac{\eta e B J_S}{\ell} \left(\mu_e \sqrt{D_e \tau} + \mu_h \sqrt{D_h \tau} \right) \quad (3-36)$$

where J_S is the number of photons per unit time absorbed by the detector element, and η gives the efficiency for conversion of photons to electron-hole pairs. The equivalent open-circuit voltage can be obtained by multiplying i_s by the magnetoresistance of the detector.

The mobilities μ_e and μ_h determine the complexity of the PEM signal. For the simplest case, where $\mu_e = \mu_h$, i_s reduces to

$$i_s = \frac{\eta e B J_S}{\ell} \cdot \mu^{3/2} \cdot \left(\frac{kT}{e} \tau \right)^{3/2} \quad (3-37)$$

The more complicated general cases, where μ_e , μ_h , p , and n are independent variables, have been treated by many authors including Pincherle (Reference 3-14), Kurnick and Zitter (Reference 3-12), and Kruse (Reference 3-18). Zitter (Reference 3-17) has been shown that the short-circuit PEM current can be expressed as

$$i_{\text{PEM}} = \left(1 + \frac{1}{b}\right) e \mu B J_S L_D^* \quad (3-38)$$

where

$$L_D^* = \left\{ \frac{D \tau_{\text{PEM}} (1 + C)}{1 + \mu^2 B^2 + bC \left[1 + (\mu^2 B^2)/b^2\right]} \right\} \quad (3-39)$$

and L_D^* is the effective ambipolar diffusion length, which for zero magnetic field reduces to the diffusion length of the minority carrier in an extrinsic semiconductor

C is the ratio of electron to hole densities for the crystal in the dark

b is the ratio of electron to hole mobilities

τ_{PEM} is the time constant for the PEM effect

For small values of μB it is clear that

$$L_D^* = \left[\frac{kT}{e} \cdot \frac{(\mu_e + \mu_h) (1 + C) \tau}{1 + bC} \right]^{1/2}$$

and that for $\mu_e \approx \mu_h \approx \mu$ and $b \approx 1$,

$$L_D^* = \sqrt{\frac{kT}{e} \mu \tau_{\text{PEM}}}$$

and that i_{PEM} is proportional to $\mu^{3/2}$. Therefore, in these limits, Zitter's equation (3-38) reduces to the form suggested by Moss (Reference 3-9).

In the case of μB large

$$L_D^* = \left[\frac{kT}{e} \cdot \frac{(\mu_e + \mu_h) \tau_{\text{PEM}} (1 + C)}{\mu^2 B^2 (1 + C/b)} \right]^{1/2}$$

such that $\mu^2 B^2 \gg b^2$. Then i_{PEM} approaches a value given by

$$i_{\text{PEM}} = \left(1 + \frac{1}{b}\right) J_S \left[kT e \left(\frac{1 + C}{1 + C/b} \right) \right]^{1/2} \cdot \left[\tau (\mu_e + \mu_h) \right]^{1/2} \quad (3-40)$$

and it is clear that the PEM signal is proportional to the square root of the effective mobility.

The time constant appearing in the PEM effect is a complicated quantity. It is defined by Zitter (Reference 3-17) and compared with the time constant for the photoconductive effect as

$$\tau_{\text{PEM}} = \frac{\tau_n + C\tau_p}{1 + C} \quad (3-41)$$

$$\tau_{\text{PC}} = \frac{\tau_n + \tau_p/b}{1 + 1/b} \quad (3-42)$$

In extrinsic material τ_{PEM} is just the lifetime of the minority carrier, which corresponds to the fact that minority carriers control the diffusion process in this kind of material. However, τ_{PC} is based on the fact that both carriers contribute to photoconductivity, regardless of the type of material. Since the time constant τ_{PEM} appears as a part of L_D in the expression for the short-circuit, i_{PEM} , it is clear that

$$i_{\text{PEM}} \sim \sqrt{\tau_{\text{PEM}}} \quad (3-43)$$

A comparison of the signal generated by the PEM effect to the photoconductive effect can well be made here. The photoconductive current density i_{PC} can be expressed in the form

$$i_{\text{PC}} = \left(1 + \frac{1}{b}\right) e J_s \mu E_x \tau_{\text{PC}} \quad (3-44)$$

where E_x is the applied electric field along the crystal. An examination of the dependence on the time constant reveals for the simple intrinsic case (assuming negligible trapping of excess carriers, where $\tau_n = \tau_p = \tau_{\text{PC}} = \tau_{\text{PEM}} = \tau$) that the PEM signal is proportional to the square root of τ , whereas i_{PC} is proportional to τ . Thus the fast, short-time-constant detector provides a larger signal in the PEM mode. Also, the magnetic field increases the effective resistance of the detector. Thus for the low resistivity, short-time-constant ($\tau < 10^{-6}$ sec) detector such as InSb, these two factors favor the PEM effect in improving signal output and the ability to match detector impedance to a preamplifier. There are other factors which favor the PEM detector. The PC detector is thinner than the PEM detector and therefore is generally more difficult to fabricate. In the fabrication of detectors care has to be exercised to avoid damaging their surfaces; otherwise an increase in the surface recombination velocities will result. Yet in mounting the detector, the back surface is almost always made to adhere to a cell mount. Thus the back surface is likely to have an increased recombination velocity compared to the front. This affects the PC detector adversely in that the effective density of carriers is reduced, whereas the PEM detector benefits because the diffusion force increases as the concentration gradient of carrier densities from front to back is made steeper.

A complete comparison of the different photodetectors cannot be made until their noise properties are understood. Further discussion is included in Chapter 4, where all the necessary factors are examined.

3.2. NOISE

There are essentially five sources of electric noise that appear in the output of semiconducting photodetectors. They are called:

1. Johnson Noise
2. Current, $1/f$, Modulation, or Excess Noise
3. Generation-Recombination (G-R) Noise
4. Shot Noise
5. Background Radiation

These noise types are treated in the order listed; the basic mechanisms contributing to the noise sources are described, and generally accepted analytic expressions that apply to them are given.

3.2.1. JOHNSON NOISE. This type of noise is often referred to as Nyquist noise, since both Nyquist (Reference 3-19) and Johnson (Reference 3-20) treated this problem in 1928. An ohmic resistance can be pictured as a material which contains a number of free charge carriers which move about in a crystalline lattice bumping into one another and into the atoms which make up the lattice. The motion of these carriers is random in nature; the average kinetic energy is a function of temperature, the greater the temperature, the greater their average kinetic energy. If a sufficiently sensitive ammeter or voltmeter were placed across a resistor, it would indicate fluctuating voltages or currents corresponding to the motion of the charge carriers. These fluctuations represent a noise whose behavior is evolved purely from thermodynamic considerations and not from the nature of charge carriers.

Johnson or Nyquist noise can be expressed as

$$\overline{v^2} = 4kTr\Delta f \quad (3-45)$$

where k is Boltzmann's constant, T is the absolute temperature Δf is the electrical bandwidth, r is the ohmic resistance, and v is the voltage fluctuation given by the difference between the instantaneous and average values of the voltage, where

$$v = v(t) - \bar{v} \quad (3-46)$$

3.2.2. CURRENT, 1/f, MODULATION, OR EXCESS NOISE. All of the above terms have been used at various times as names for the same kind of noise. It is a noise that appears commonly in photo-detectors in addition to the Johnson noise already discussed, and is generally found to have characteristics that can be described by the expression (Reference 3-21)

$$\overline{i^2} = C \frac{I_{d-c}^2}{fAd} \cdot \Delta f \quad (3-47)$$

where I_{d-c} is the total current through the sample

f is the frequency

C is a constant

Actually Equation 3-47 is not universal in that cases have been cited where the current exponent has been found as small as 1.25 and as large as 4 (Reference 3-22), while the frequency exponent has ranged from 1 to 3 (Reference 3-23). However, these extreme exponential variations are not particularly common, and can usually be associated with a particular material, or to some unique treatment and physical condition of a material (Reference 3-22).

The physical mechanism of this noise is the least understood of all the noise types found to date. Petritz (Reference 3-24) introduced the name "modulation" noise to identify the mechanism as something quite different from the carrier-density fluctuations described in the G-R process (see Section 3.2.3). An effect is assumed that causes the occurrence of a magnitude of conductivity modulation far larger than that obtained from simple carrier density fluctuations. This effect might well be related, however, to the electronic transitions involved in the G-R process. A simple mechanism that has been proposed involves the falling of electrons (while they are undergoing the transitions involved in the G-R process) into electrical lattice pits or wells called "traps" where they are temporarily immobilized. While the electrons are in this trapped condition, the local electronic structure of the crystal lattice is changed. This may well result from some shuffling about of lattice particles to some new equilibrium conditions and a resulting new electric field pattern. The net effect is presumed to be a marked change in the mobility of the carriers through the localized lattice, and/or a change in recombination velocity, and therefore conductivity modulation. The electronic traps are represented in the band picture as energy levels located in the forbidden energy gap. They are usually due to impurities in the crystal lattice and to crystalline imperfections from edge dislocations and plastic deformation. Thus a conduction-band electron or valence-band hole moving in the vicinity of an electron or hole trap, respectively, is suddenly caught and immobilized in a bound state. Escape is then possible by absorption of phonon energy. The probability of escape increases with increasing temperature, but decreases with the depth of the trap.

The modulation suggestion offered by Petritz, however, can still be only a part of the picture. Brophy and Rostocker (Reference 3-25), Brophy (Reference 3-26), and Bess (Reference 3-27) found with direct experimental evidence that the noise fluctuations in Hall voltage followed the same frequency dependence pattern as the noise from a conductivity measurement. It must be concluded therefore that, like conductivity, $1/f$ noise follows the fluctuation in the density of the majority current carriers.

The location of a major source of $1/f$ noise (at least in the case of germanium filaments) has been found to be the surface of the crystal. Recent studies by MacRae and Levinstein (Reference 28) noted that a surface inversion layer (a p-type surface on an n-type crystal, or vice versa) is sufficient to generate significant $1/f$ noise. A qualitative picture of what is happening involves assuming a set of two surface states, one fast and the other slow. The slow states are associated with the majority carrier traps discussed above, and located in the outermost surface layer of the filament. The fast states are assumed to exist in the interface region between the surface and bulk materials and are primarily responsible for the recombination velocity of the carriers at the surface. Corresponding to the fluctuating density of majority carriers, there is a fluctuating population of slow traps which causes the enhanced conductivity modulation in the bulk.

Although the surface provides $1/f$ noise, it is quite clear that this kind of noise can also be generated in the bulk material. Brophy (Reference 3-29) finds that, by plastic deformation, he can create noise sources and cause an increase of excess noise by orders of magnitude. These sources are uniformly distributed throughout the crystal, and also contribute an unusual I^4 dependence. Bess (Reference 3-30) assumed that the noise was due to edge dislocations with impurities diffusing along the edges of the dislocations. Such distributions throughout the bulk can provide noise spectra similar to that obtained by inversion surface layers (Reference 3-31).

When surfaces are treated so that their noise contribution is minimized, residual ($1/f$) noise may still exist. This noise has been associated with nonohmic contact regions, probably due to minority-carrier drift across the contacts. It appears that the fluctuating population of traps causes the capture cross section of the surface recombination centers to be modulated, in turn causing a fluctuating current of minority carriers, resulting in current modulation.

The discussion of $1/f$ noise has shown that the sources of this noise can be found at the surface, in the bulk, and at the contacts. A suitable theory has yet to be found which will provide a quantitative expression for the carrier-density fluctuation and the modulation efficiency.

3.2.3. GENERATION-RECOMBINATION (G-R) NOISE. This type of noise is inherent in the electronic system of semiconducting materials. The basic mechanism responsible for it can be described easily in terms of the band picture of solids.

All atoms in a lattice vibrate in a well-organized manner to the extent that their vibrations are quantized and can be described in particle terminology as "phonons". The energy of the phonon is given by

$$E = \hbar\omega$$

where $\hbar = h/2\pi$

h is Planck's constant

Valence-band electrons are continually jostled by the vibrations of the lattice atoms. Every so often, the nature and phasing of vibrations between atoms is such that an electron in their midst is able to gain enough energy to be freed from its bound (valence-band) state, and to move about in the conduction band. The electron is said to have suffered phonon collision, and to have undergone an energy change according to:

$$E(k') - E(k) = \hbar\omega$$

where k and k' define the energy states before and after phonon absorption.

When electrons leave the valence band for the conduction band, charge carriers (electrons and holes) become available for the purposes of current flow. The number of carriers created increases with material temperature, and for any one temperature will be greater for diminishing energy gap. The thermal (phonon) excitation process is statistical in nature, and the rate at which electrons are excited to the conduction band fluctuates.

In addition to the statistical pulses of generation, a similar situation holds for the recombination of carriers. The electrons and holes wander about the crystal lattice with some thermal motion, and during a "lifetime" characteristic of the semiconductor, get close enough together to recombine directly, or indirectly through a recombination center. The lifetime is a statistically fluctuating quantity, as is the instantaneous number of electrons and holes. Current-carrier fluctuations are therefore inherent in any semiconductor. These fluctuations give rise to G-R noise. When a sample is placed in a constant-current electric circuit one may observe conductivity fluctuations causing electric noise completely described by the G-R process.

Since this noise is a bulk property of the crystal and is due to conductivity fluctuations caused by carrier-density changes, it follows that (from Equation 3-2)

$$\Delta r = \frac{dr}{dn} \Delta n = \frac{\rho}{dw} \cdot \frac{\Delta n}{n} = \frac{\rho}{dw} \cdot \frac{\Delta n}{N}$$

and

$$\overline{v^2} = I_{d-c}^2 \cdot (\Delta r)^2 \quad (3-48)$$

It can be shown that (References 3-1 and 3-21)

$$\frac{(\Delta N)^2}{N} = \frac{2\tau}{1 + (\omega\tau)^2} \cdot \Delta f \quad (3-49)$$

Therefore

$$\overline{v^2} = I_{d-c}^2 \cdot r^2 \cdot \frac{2\tau}{N[1 + (\omega\tau)^2]} \quad (3-50)$$

or

$$\overline{i^2} = I_{d-c}^2 \cdot \frac{2\tau}{N[1 + (\omega\tau)^2]}$$

as shown by Van Vliet (Reference 3-32).

3.2.4. SHOT NOISE. This noise is usually associated with vacuum tubes; it is described as the electric noise that appears in the output of a vacuum tube when the grid, if any, is held at a fixed potential. It is more carefully described in what is usually called the temperature-limited condition. "Temperature limited" means that the anode voltage on the tube is sufficient to collect all of the electrons emitted from the cathode. Consider a temperature-limited diode connected to a resistance r . Because of the discreteness of the electronic charge, the number of electrons emitted at equal time intervals will fluctuate around an average value. The fluctuating current causes a fluctuating voltage across r which can be amplified and measured. The mean-square current fluctuation turns out to be constant up to frequencies of the order of the reciprocal of the transient time, and can be described by (Reference 3-33)

$$\overline{i^2} = 2eI_{d-c}\Delta f \quad (3-51)$$

where e is the electronic charge and I_{d-c} is the average current. Semiconductor photovoltaic detectors also exhibit shot-type noise. In the case of the vacuum tube, the electrons are taken as independent in the temperature-limited case, and it follows that the current through the resistance will consist of a series of short pulses, each pulse corresponding to the passage of an electron from cathode to anode. In the case of the semiconductor, a similar situation prevails. In a p-n junction diode, a space-charge region is developed across the barrier and an associated electric field. Electrons or holes created by photons or background photons, and diffusing into the barrier region, are swept from the n-type

material to the p-type material, or vice versa. This results in current pulses appearing across the diode with the same characteristics that are observed for the vacuum tube.

Petriz (Reference 3-21) has developed a theory applicable to the lead-chalcogenide (PbS, PbSe, PbTe) photoconductive films, which is suitable for discussion here. These films are composed of a system of tiny crystallites separated by intercrystalline barriers. Where space-charge regions exist. The barrier regions contribute both Johnson and shot noises, while the crystallites generate the usual Johnson noise. For barriers which are thin compared to carrier diffusion length, the barrier noise contribution can be determined by using the expression noted by Weisskopf for the short-circuit noise generator:

$$\overline{i^2} = \left(\frac{4kT}{r_B} + 2eI_B \right) \Delta f \quad (3-52)$$

The total noise due to the aggregate of crystallites that make up the film is found by properly summing the contributions from each of them. Petriz finds that the short-circuit current generator provides a noise given by

$$\overline{i^2} = \left(\frac{4kT}{r} + \frac{2eI_{d-c}}{n_f l} \right) \Delta f \quad (3-53)$$

where n_f is the number of crystallites per unit length of the detector, r_B is the resistance of a barrier, and r is the macroscopic detector resistance. The corresponding voltage expression is

$$\overline{v^2} = 4rkT + \frac{2er^2 I_{d-c}}{n_f l} \quad (3-54)$$

3.2.5. BACKGROUND RADIATION. Background radiation can be thought of as a stream of photons originating from the detector environment. The cell walls surrounding the detector, its window, and the media viewed by the detector through the cell window all contribute to this radiation. The extent of the individual contributions is determined by their respective temperatures, emissivities, and geometry.

Photons originating from the background and impinging on the detector arrive in a statistically fluctuating manner. In addition, the detector radiates in a manner dependent on its temperature and emissivity, obeying the same statistical law that applies to the background. The net fluctuation in radiant energy exchange causes a corresponding fluctuation in temperature and provides the mechanism for the limiting noise process in thermal detectors. This limiting process is called "tem-

perature noise." The photodetector is insensitive to this temperature effect. However, the radiation fluctuation causes charge carriers to be liberated in varying amounts, causing corresponding changes in the photoelectric effect utilized. When the cause of the electric noise observed in a photodetector is due to this radiation, the detector is said to be "background-radiation-noise limited."

Photons obey Bose-Einstein statistics (Reference 3-34), and their fluctuation can be described by

$$\overline{\Delta n^2} = n \left\{ 1 + \left[\exp\left(\frac{h\nu}{kT}\right) - 1 \right]^{-1} \right\} \quad (3-55)$$

This expression reduces to the classical case

$$(\Delta n)^2 = n \quad (3-56)$$

for values of

$$\exp h\nu/kT \gg 1$$

Substituting $\nu = c/\lambda$, and considering a room-temperature condition ($\approx 300^\circ\text{K}$), reveals that the exponential becomes sufficiently large for photons of wavelength less than 10 microns so that classical statistics can be applied. Fellgett (Reference 3-35) shows the relationship between the number of photons and their fluctuation; his result is shown in Figure 3-6.

Contribution to G-R Noise. In the derivation of the expression of G-R noise, it was assumed that the thermal generation of carriers followed the same statistical process as carrier generation from

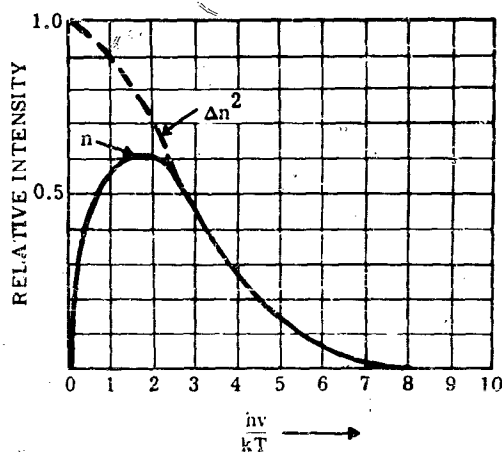


FIGURE 3-6. RELATIVE INTENSITY AND FLUCTUATION OF PHOTONS AS A FUNCTION OF WAVELENGTH AND TEMPERATURE. (From Reference 37.)

the absorption of background photons. Therefore the expressions in Equations 3-49 and 3-50 are applicable here. The only difference is in the calculation of N_r , that is, the contribution to N by the radiation. The complete expression used to derive Equation 3-49 is given by Petritz (References 3-1 and 6-21) as

$$\frac{\Delta N^2}{N^2} = \frac{4\tau^2 \cdot \Delta f \cdot A(\eta_r J_r + \eta_\ell J_\ell)}{1 + (\omega\tau)^2} \quad (3-57)$$

where J_ℓ is the lattice phonon flux

J_r is the background radiation photon flux incident on the detector

η_r, η_ℓ are the efficiency factors for conversion of photons and phonons to carriers.

The number of carriers created by the absorption of photons is of the form

$$N_r \propto A \eta_r J_r \tau$$

where

$$\eta_r J_r = \frac{c}{4} \int_0^\infty \frac{\eta(\nu) n_r(\nu, T_r)}{E_g/h} d\nu \quad (3-58)$$

where $\eta(\nu)$ is the responsive quantum efficiency at frequency ν ; c is the velocity of light; $\eta_r(\nu, T_r)$,

the density of photons in the background = $\frac{8\pi\nu^2}{c^3 [\exp(h\nu/kT) - 1]}$

Similar expressions hold for lattice processes. It is clear then that reducing the temperature of the background or of the detector causes a reduction in N and the carrier fluctuation. When N_r is greater than the number contributed by phonon processes, the detector is G-R-background noise limited.

3.3. SPEED OF RESPONSE

The speed of response of a photodetector depends upon the mechanism by which charge carriers recombine after their generation by the absorption of radiation. Various recombination mechanisms are possible and are described by Smith (Reference 3-4) and Bube (Reference 3-36). Generally these mechanisms fall into two categories: (1) Radiative recombination, or recombination of electrons and holes by transitions of electrons from the conduction band directly to the valence band; (2) recombination of electrons and holes through "recombination centers." The decay rate depends upon the type of mechanism, the concentration of carriers generated by the signal, the concentration of recombination centers, and often the existence of electron and hole traps whereby the carriers are temporarily immobilized and unable to participate in the kinetics of recombination.

In simple processes such as (1) above, the photosignal decay after the removal of signal radiation follows a simple exponential decay law. For more complicated mechanisms, the decay might be described by a sum of exponential terms, or possibly a power law. Frequency-response measurements follow a similar pattern of complexity.

3.3.1. PULSE RESPONSE. When the photon-generated carriers in the semiconductor decay in an exponential manner, the photoresponse to a pulse of light can be described as follows.

During the time of exposure to the light pulse, the detector signal will increase according to

$$v = v_0 [1 - \exp(-t/\tau)] \quad (3-60)$$

where v_0 is the maximum value of the signal obtained for a light pulse sufficiently long so that $\exp(-t/\tau) \ll 1$. For a pulse of short time duration, t_0 , the rise of the signal will follow Equation 3-60 to a maximum value of

$$v_{t_0} = v_0 [1 - \exp(-t_0/\tau)] \quad (3-61)$$

The decay that follows the end of the light pulse is given by

$$v = v_{t_0} \left[\exp\left(-\frac{t - t_0}{\tau}\right) \right] \quad (3-62)$$

or

$$v = v_0 [1 - \exp(-t_0/\tau)] \cdot \left[\exp\left(-\frac{t - t_0}{\tau}\right) \right] \quad (3-63)$$

The signal rise and fall are shown in Figure 3-7. Notice the asymmetry in the rise and decay parts of the trace. The rise is shorter in time than the decay, and the initial slopes of rise and decay are

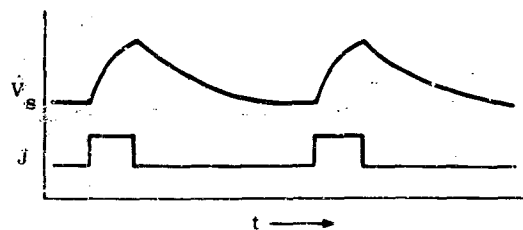


FIGURE 3-7. PERIODIC PULSE PHOTOEXCITATION AND DETECTOR RESPONSE

significantly different in their absolute magnitude. To illustrate the latter, differentiate Equations 3-60 and 3-63 and examine their slopes at time $t = 0$, and t_0 , respectively.

$$\left. \frac{dv}{dt} \right|_{t=0} = \frac{v_0}{\tau} \left[\exp \left(-\frac{t}{\tau} \right) \right] = \frac{v_0}{\tau} \Big|_{t=0} \quad (3-64)$$

$$\left. \frac{dv}{dt} \right|_{t=t_0} = -\frac{v_0}{\tau} \left[1 - \exp \left(-\frac{t_0}{\tau} \right) \right] \Big|_{t=t_0} \quad (3-65)$$

It is clear that the decay and rise curves cannot look alike unless the light pulse $t_0 \gg \tau$. The time constant τ can be obtained from a semilogarithmic plot of Equation 3-63 (the decay curve), whereas it cannot be obtained readily from Equation 3-60.

3.3.2. FREQUENCY RESPONSE. When the detector response is observed for excitation by sinusoidally modulated radiation, rather than pulses of light, the response is frequency dependent and behaves as

$$v(\omega) = \frac{v_0}{[1 + (\omega\tau)^2]^{1/2}} \quad (3-66)$$

where $\omega = 2\pi f$, f is the frequency of the exciting signal, and τ is the time constant for the decay mechanism. Fortunately many of the detectors in present usage follow the exponential law of decay, and an effective time constant is easily reported. The measurement techniques used to determine the time constant are described in Appendix A. From a responsivity vs. frequency plot, τ can be calculated easily from the selection of ω when the response is down by $1/\sqrt{2}$, for then

$$\frac{v}{v_0} = \frac{1}{\sqrt{2}} = \frac{1}{\sqrt{1 + (\omega\tau)^2}} \quad (3-67)$$

when $\omega\tau = 1$ or $\tau = (2\pi f)^{-1}$.

Another approach is to measure the response at two different chopping frequencies, and take the ratio of the two signals as follows:

$$\frac{v_1}{v_2} = \left[\frac{1 + (\omega_2\tau)^2}{1 + (\omega_1\tau)^2} \right]^{1/2} \quad (3-68)$$

and solving for τ , obtain

$$\tau = \frac{1}{2\pi} \left[\frac{v_1^2 - v_2^2}{(f_2 v_2)^2 - (f_1 v_1)^2} \right] \quad (3-69)$$

for the time constant. From this relationship and assuming that small signal changes (about 10%) can be recorded, a chopping frequency of about 100 kcps permits a determination of time constant to about 1 μ sec.

3.3.3. MULTIPLE TIME CONSTANTS. When the speed of response does not depend on frequency in a manner described by Equation 3-66, there does not appear to be any clear definition of the time constant. This situation prevails particularly when multiple electronic transitions of a carrier are involved so that two or more time constants exist. The decay may follow two or more successive exponential processes, or possibly combinations of power and exponential laws. The frequency-response characteristic curves will then show two or more peaks (or plateaus), while the decay following a pulse of light will exhibit sections which will follow different decay laws. The time constant has been defined in different ways. Generally, the definition is that $\tau = 1/2\pi f$, where f is the frequency at which the responsivity is 0.707 times the zero-frequency responsivity, or at which the high- and low-frequency asymptotes intersect, or at which the slope of the responsivity vs. frequency curve is -6 db per octave, or sometimes at which the phase lag is 45° (Reference 3-37). All of these definitions are equal when the photosignal decay follows a simple exponential decay law or the process is described in terms of the frequency response by an equation in the form of Equation 3-66. The time constant can be estimated by noting the time required for the detector response to decay 67% or 90% from its maximum value (it is understood that the pulse of radiation is sufficient for the phot signal to reach its maximum value).

A frequency-dependent measurement will follow an expression of the form

$$v = \frac{K_1 \sin(\omega\tau_1 - \phi_1)}{[1 + (\omega\tau_1)^2]^{1/2}} + \frac{K_2 \sin(\omega\tau_2 - \phi_2)}{[1 + (\omega\tau_2)^2]^{1/2}}$$

A general solution permitting an evaluation of the two time constants is possible, but is a complicated matter. According to Levinstein (Reference 3-38), a completely general solution requires solving for four unknowns: K_1 , K_2 , ϕ_1 , and ϕ_2 . It is necessary to measure response at four different fre-

quencies to obtain sufficient information for a solution. If the frequencies are chosen properly, then the two time constants are given by an equation of the form

$$\tau_1, \tau_2 = \left\{ \frac{(ed - ah)^2 + [(ed - ah)^2 \pm 4(bh - fd)(eb - af)]}{2(bh - fd)} \right\}^{1/2}$$

where a, b, d, e, f, and h are obtained from lengthy frequency-dependent measurements. The expression is complicated but does offer recourse when exact analysis from frequency-response data becomes necessary.

The selection of a universal time constant for this complicated case is necessary but is not likely to be made in the near future. Therefore, the reader is advised to understand the different definitions noted above.

3.4. SPECTRAL RESPONSE

A discussion of the fundamental mechanisms responsible for photodetector response is presented in Section 3.1. However, a summary of the important aspects relating to spectral response is presented here for continuity. Detailed discussions of the experimental procedures and the calculations required to determine a detector's spectral response are found in Appendix A.

The spectral response of a photodetector depends upon the photon energy required to free a charge carrier. If the photon energy is sufficiently large, additional charge carriers can be generated in proportion to the photon flux.

A plot of responsivity versus wavelength may be drawn in two ways, depending upon the units used in the evaluation of responsivity. It may be expressed as the amount of signal voltage obtained per unit of incident photon flux at a given wavelength, or as the amount of signal voltage obtained per unit of incident power at a given wavelength. The former is the equivalent of a plot made directly with a monochromator capable of providing detector illumination with a constant unit flux density of photons at all wavelengths, while the latter is that for a constant unit of power exposure. Since a photodetector responds directly to the number of photons per second that are absorbed, an idealized detector would provide a spectral responsivity plot like Figure 3-8. Usually, however, the radiation output of monochromators is measured by a "black" detector such as a thermocouple. The thermocouple has a constant responsivity as a function of wavelength (at least in the wavelengths of interest here), and is a device which responds to the radiation power. Thus the photodetector responsivity is usually measured in terms of power rather than photon flux density, and the resultant ideal plot is shown in

Figure 3-9. The difference in the shapes of the curves in Figures 3-8 and 3-9, is readily explained on examining the expression for a photon's energy

$$h\nu = hc/\lambda \quad (3-70)$$

The photons of shorter wavelengths have higher energies. Therefore, fewer photons per second are required to maintain a constant unit of power with decreasing wavelength. Since a photodetector signal is proportional to the photon flux, the detector signal falls off with decreasing wavelength.

The sharp dropoff point, at the position indicated as λ_m , determines the minimum energy a photon must have to free a charge carrier. If the energy is in electron volts and the wavelength in microns, then the relationship between them is

$$\lambda_m = \frac{1.24}{\text{Energy (ev)}} \quad (3-71)$$

Impurity-type photoconductors such as gold-doped germanium are designed to extend the spectral response of the material to longer wavelengths than possible with the pure material. The impurities introduce new energy levels in the forbidden gap region of the intrinsic material, and therefore permit lower energy carrier transitions corresponding to longer wavelength response. An idealized spectral response curve for the impurity photodetector is shown in Figure 3-10. The short wavelength response up to λ_{1m} is associated with intrinsic absorption and carrier transitions across the complete energy gap; λ_{2m} refers to the extrinsic wavelength cutoff point. The long wavelength response between λ_{2m} and λ_{1m} is attributed to the carrier transitions involving the "impurity levels"; λ_{2m} refers to the wavelength at which impurity photoresponse ceases. The difference in the response magnitudes of these two spectral regions corresponds to the high absorption of the lattice for photons in the intrinsic region, as compared to the weak absorption by low density impurities in the extrinsic region. In order to improve the magnitude of the latter region, it is customary to house the detector in a small integrating chamber with a hole to admit the signal radiation. This causes the photons to make multiple passes through the detector, improving the probability of their absorption.

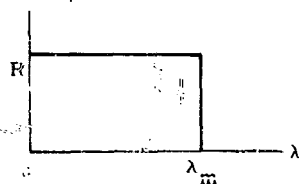


FIGURE 3-8. INTRINSIC DETECTOR RESPONSE TO A CONSTANT DENSITY OF PHOTONS, AS A FUNCTION OF WAVELENGTH

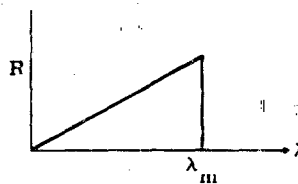


FIGURE 3-9. INTRINSIC DETECTOR RESPONSE TO CONSTANT ENERGY EXPOSURE, AS A FUNCTION OF WAVELENGTH

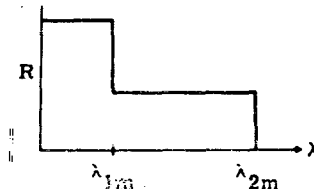


FIGURE 3-10. IMPURITY DETECTOR RESPONSE TO A CONSTANT DENSITY OF PHOTONS, AS A FUNCTION OF WAVELENGTH

3.5. REFERENCES

- 3-1. R. L. Petritz, Proc. IRE, 1959, Vol. 47, p.1458.
- 3-2. W. Shockley, Bell System Tech. J., 1949, Vol. 28, p. 435.
- 3-3. J. L. Moll, Proc. IRE, 1958, Vol. 46, p. 1076.
- 3-4. R. A. Smith, Semiconductors, Cambridge, New York, 1959.
- 3-5. G. Goudet and C. Meuleau, Semiconductors, MacDonald & Evans, London, 1957.
- 3-6. R. L. Cummertow, Phys. Rev., 1954, Vol. 95, p. 16.
- 3-7. E. S. Rittner in R. G. Breckenridge, B. R. Russell, and E. E. Hahn (eds.) Photoconductivity Conference, Wiley, New York, 1956.
- 3-8. G. R. Pruett and R. L. Petritz, Proc. IRE, 1959, Vol. 47, p. 1524 (1959).
- 3-9. T. S. Moss, Proc. Phys. Soc., London, 1953, Vol. B66, p. 999.
- 3-10. P. Aigrain and H. Bulliard, Compt. rend., 1953, Vol. 236, pp. 595 and 672.
- 3-11. Moss, Pincherle and Woodward, Proc. Phys. Soc. London, 1953, Vol. B66, p. 743.
- 3-12. S. W. Kurnick and R. N. Zitter, J. Appl. Phys., 1956, Vol. 27, p. 278.
- 3-13. S. W. Kurnick and R. N. Zitter, Photoconductivity Conference, Wiley, New York, 1956.
- 3-14. L. Pincherle, Photoconductivity Conference, Wiley, New York, 1956.
- 3-15. O. Garreta and J. Grosvalet, Progress in Semiconductors, Heywood, London, 1956, Vol. 1, p. 167.
- 3-16. W. van Roosbroeck, Phys. Rev., 1956, Vol. 101, p. 1713.
- 3-17. R. N. Zitter, Phys. Rev., 1958, Vol. 112, p. 852.
- 3-18. P. W. Kruse, J. Appl. Phys., 1959, Vol. 30, p. 770.
- 3-19. H. Nyquist, Phys. Rev., 1928, Vol. 33, p. 110.
- 3-20. J. B. Johnson, Phys. Rev., 1928, Vol. 32, p. 97.
- 3-21. R. L. Petritz, Phys. Rev., 1956, Vol. 104, p. 1508.
- 3-22. J. J. Brophy, J. Appl. Phys., 1957, Vol. 27, p. 1383.
- 3-23. T. G. Maple, L. Bess, and H. A. Gebbie, J. Appl. Phys., 1955, Vol. 26, p. 490.
- 3-24. R. L. Petritz, Proc. IRE, 1952, Vol. 40, p. 1440.
- 3-25. J. J. Brophy and N. Rostoker, Phys. Rev., 1955, Vol. 100, p. 754.
- 3-26. J. J. Brophy, Phys. Rev., 1957, Vol. 106, p. 675.
- 3-27. L. Bess, J. Appl. Phys., 1955, Vol. 26, p. 1377.
- 3-28. A. U. MacRae and H. Levinstein, Phys. Rev., 1960, Vol. 119, p. 62.
- 3-29. J. J. Brophy, J. Appl. Phys., 1956, Vol. 27, p. 1383.
- 3-30. L. Bess, Phys. Rev., 1956, Vol. 103, p. 72.
- 3-31. J. R. Morrison, Phys. Rev., 1956, Vol. 104, p. 619.

- 3-32. K. M. van Vliet, Proc. IRE, 1958, Vol. 46, p. 1004.
- 3-33. A. van der Ziel, Proc. IRE, 1958, Vol. 46, p. 1019.
- 3-34. R. C. Tolman, Principles of Statistical Mechanics, Clarendon, Oxford, 1938, p. 512.
- 3-35. P. B. Fellgett, J. Opt. Soc. Am., Vol. 39, p. 970.
- 3-36. R. H. Bube, Photoconductivity of Solids, Wiley, New York, 1960.
- 3-37. Proposed Standard for Testing and Describing Infrared Detectors, Working Panel "J-1," in press.
- 3-38. H. Levinstein et al., Interim Report on Infrared Detectors, Syracuse University under Air Force Contract AF 33(616)-3859, September 1958, p. 13.

4 DETECTOR EVALUATION from THEORETICAL CONSIDERATIONS

Sol Nudelman

The equations for signal voltage and noise voltage derived in Chapter 3 indicate that detector parameters such as size, time constant, and bandwidth of operation are important factors in evaluating a detector's capability. Detectors are made of many different materials, and differ in size and time constants. The engineer is thus faced with the problem of selecting the best one for his purpose. On the basis of the analysis of Section 3.1, he has the basic ingredients for such a selection. However, an examination of the signal and noise equations would involve him in a tedious and nonprofitable task of juggling these equations to fit his immediate problem. What is needed is a simple number which provides a detector "rating" independent of the bothersome parameters, from which he can make a quick, proper detector selection. The purpose of this chapter is to describe and discuss the substantial effort that has been put forth to provide this "universal" number for rating detectors.

The treatment that follows begins with a general discussion of NEP, Noise Equivalent Power. It then continues with detailed analyses of the photoconductive detectors in their various noise-limited conditions. These serve as examples of treatments applicable to the quantum and thermal classes of detectors. Detector classification schemes based on NEP are presented thereafter.

4.1. NEP (NOISE EQUIVALENT POWER)

Consider an infrared detector exposed to some incident radiation, in a circuit which provides an electric signal voltage proportional to the radiant power. Assume also that the dominant electric noise in the circuit is generated by the detector (not the preamplifier). Let the radiant power P be expressed as $H \cdot A$, where H is the irradiance and A is the area of the detector. The absorption of power P by the detector results in a signal voltage, V_S , in the circuit. When the power source is removed or masked, and the detector allowed to see only the background, then a noise voltage, V_N , is obtained. The predominant mechanism causing this noise might be internal to the detector, such as from Johnson, shot, and/or lattice-governed-G-R noise sources. In the case of the best detectors, this noise might well be governed by the fluctuations in photon flux irradiating the detector,

that is, the background-noise-limited condition. A simple proportionality can be set up, relating these voltage readings and the power P .

$$\text{NEP}/V_N = H \cdot A/V_S \quad (4-1)$$

Thus, if Johnson noise is responsible for V_N , then NEP represents the amount of power that would have to fall onto the detector to generate an equivalent voltage V_N . This relationship is more usually observed in the form

$$\text{NEP} = H \cdot A/V_S/V_N \quad (4-2)$$

Clearly, NEP is also the power exposure required by the detector to obtain a signal-to-noise voltage ratio of unity.

A relatively simple analysis can be attempted for the purpose of providing some insight into the problem. Assume a simple detector in a circuit, from which is obtained a signal voltage, V_S , and a noise voltage, V_N . The noise voltage is assumed to be due to a uniform distribution of noise sources throughout the bulk of the detector. Consider two of these detectors connected electrically in series. The total signal voltage is simply $V_{S1} + V_{S2}$, since the signals are coherent; and the noise voltages add as their mean squares, since they are incoherent. The noise voltage of each unit is the rms value of the voltage fluctuation, or $V_N = \sqrt{v^2}$ where $v = v(t) - \bar{v}$, $v(t)$ is the instantaneous value of the noise voltage, and \bar{v} is the average value. The signal-to-noise ratio from the combined units, V_{ST}/V_{NT} , is

$$\frac{V_{ST}}{V_{NT}} = \frac{V_{S1} + V_{S2}}{[V_{N1}^2 + V_{N2}^2]^{1/2}} \quad (4-3)$$

If the two detectors are identical in area and thickness, $V_{S1} = V_{S2}$, and equal noise is generated from each of them, then

$$\frac{V_{ST}}{V_{NT}} = \frac{2V_{S1}}{\sqrt{2} V_{N1}} = \sqrt{2} \frac{V_{S1}}{V_{N1}} \quad (4-4)$$

Suppose these two detectors are now connected electrically in parallel. Since currents can be added in a straightforward manner when dealing with parallel circuits, consider the noise sources as current generators. The total noise becomes (similar to the noise-voltage analysis)

$$I_T^2 = I_{N1}^2 + I_{N2}^2 \quad (4-5)$$

and for identical detectors

$$I_{NT} = \sqrt{2 I_{N1}^2} \quad (4-6)$$

The signal current is now

$$I_{ST} = I_{S1} + I_{S2} = 2 I_{S1} \quad (4-7)$$

The signal-to-noise current ratio becomes

$$\frac{I_{ST}}{I_{NT}} = \frac{2 I_{S1}}{\sqrt{2} I_{N1}} = \sqrt{2} \frac{I_{S1}}{I_{N1}} \quad (4-8)$$

The noise current can be expressed as a noise voltage by simply multiplying the total noise current by the effective resistance of the circuit. Therefore

$$r_t = \frac{r_1 r_2}{r_1 + r_2} = \frac{r_1}{2} \quad \text{for } r_1 = r_2 \quad (4-9)$$

and

$$V_{NT}^2 = I_{NT}^2 r_t^2 = \frac{I_{N1}^2 r_1^2}{2}$$

or

$$V_N = \frac{1}{\sqrt{2}} \cdot I_{N1} r_1 \quad (4-10)$$

The signal voltage is $V_{ST} = V_{S1} = V_{S2}$, since the circuit is now equivalent to two identical batteries placed in parallel.

$$\frac{V_{ST}}{V_{NT}} = \frac{I_{S1} \cdot r_1}{\frac{1}{\sqrt{2}} \cdot I_{N1} r_1} = \sqrt{2} \frac{V_{S1}}{V_{N1}} \quad (4-11)$$

The analysis can readily be extended to three or more detector units. It is immediately apparent from the treatment with two units, however, that with either the series or parallel arrangement the signal-to-noise ratio depends on the square root of the total detector area. This then indicates that the NEP of a detector should also depend on the square root of the area by insertion in Equation 4-2.

4.1.1. ANALYSIS OF NEP FOR THE PHOTOCONDUCTIVE DETECTOR. A detailed analysis of the dependence of NEP on area for the various noise-limited cases can be developed starting with the definition of NEP, Equation 4-2.

The procedure followed is to substitute appropriate expressions for the signal and noise voltages in this equation and to generate an equation which delineates the geometry, time constant, and bandwidth-dependence of NEP. The photoconductive detector is the only photodetector type treated here, since the procedure is straightforward and can be applied by the reader to any other types of detectors.

The factor for the incident power will be $H \cdot A$, where H is the irradiance, and the signal voltage as given by Equation 3-8. Therefore

$$NEP = \frac{V_N}{(I_{d-c} \rho l / wd) [\eta_S J_S \tau / nd \sqrt{1 + (\omega \tau)^2}]} \quad (4-12)$$

where $I_{d-c} = V / (r_C + r_L)$

4.1.1.1. Johnson Noise. In Section 3.2.1, the Johnson noise voltage was given by

$$V_N = \sqrt{v^2} = \sqrt{4kTr\Delta f}$$

Inserting Equation 3-45 into Equation 4-12 provides

$$NEP = HA \frac{\sqrt{4kTr\Delta f}}{(I_{d-c} \rho l / wd) \cdot [\eta_S J_S \tau / nd \sqrt{1 + (\omega \tau)^2}]} \quad (4-13)$$

where $r = \rho l / wd$ and $I_{d-c} = iwd$. In the last term, i = current density = σE , where E = electric field strength and $\sigma = 2ne\mu$ ($\mu = \mu_n = \mu_p$). Using Equation 3-11 and 3-18, Equation 4-13 can be simplified by first rewriting σ in the form

$$\sigma = 2ne \frac{D_n}{kT/e} = \frac{2ne^2}{kT} \cdot \frac{L_n^2}{\tau} \quad (4-14)$$

Simplifying so that all factors other than area, time constant, and bandwidth are lumped together provides

$$NEP = K_1 \frac{\sqrt{A \cdot \Delta f}}{\tau} \cdot \sqrt{1 + (\omega \tau)^2}$$

where

$$K_1 = \frac{kT \sqrt{2nd}}{e \eta_S J_S E} \cdot H$$

Thus the relationship between NEP, area, time constant, and bandwidth is clearly spelled out for the Johnson-noise-limited case by

$$\text{NEP} \propto \sqrt{A \cdot \Delta f / \tau} \quad (4-15)$$

Notice that the Johnson noise exists without current flow, while the photoconductive signal requires a bias current. Even though a basic difference exists between processes responsible for signal and noise generation, a \sqrt{A} dependence results; this is compatible with the discussion of Section 4.1.

4.1.1.2. Current, 1/f Modulation, or Excess Noise. In section 3.2.2, this noise was described by the equation

$$V_N = I_{d-c} r \sqrt{CAf/wdf}$$

Inserting Equation 3-47 into Equation 4-12 provides

$$\text{NEP} = HA \frac{I_{d-c} r \sqrt{CAf/wdf}}{I_{d-c} (\rho f/wd) \cdot [\eta_S J_S \tau / nd \sqrt{1 + (\omega \tau)^2}]} \quad (4-16)$$

$$\text{NEP} = K_2 \sqrt{A \Delta f / \tau} \sqrt{1 + (\omega \tau)^2} / \tau \quad (4-17)$$

where

$$K_2 = (n \sqrt{Cd} / \eta_S J_S) H \quad (4-18)$$

In this instance, both the signal and noise are associated with bias currents. However, even though a complete understanding of the source of 1/f noise is not yet available, it is clear that, for a uniform generation of noise throughout the bulk and/or surface of the detector, the NEP will depend upon the square root of the detector area. In addition, NEP will vary as $f^{-1/2}$.

4.1.1.3. Generation-Recombination Noise. In Section 3.2.3, G R noise was described by Equation 3-48 as

$$V_N = I_{d-c} r \sqrt{\Delta N^2 / N}$$

The signal-to-noise voltage ratios then become

$$\frac{V_S}{V_N} = \frac{I_{d-c} \tau \Delta N_S / N}{I_{d-c} \tau \sqrt{\Delta N_N^2} / N} = \frac{\Delta N_S}{\sqrt{\Delta N_N^2}} \quad (4-19)$$

from Equation 3-49.

$$\sqrt{\Delta N^2} = \sqrt{2\tau\Delta f / [1 + (\omega\tau)^2]} \cdot \sqrt{N}$$

Consider here only the background-noise-limited condition, where N is the number of carriers arising from J_T photons per unit time impinging on the detector. Therefore

$$N = 2J_B A \eta_B \tau \quad (4-20)$$

where each photon absorbed creates two carriers (an electron and a hole). The change in the number of carriers due to signal radiation is given by Equation 3-7.

$$\Delta N_S = \frac{A \eta_S J_S \tau}{\sqrt{1 + (\omega\tau)^2}}$$

therefore

$$\frac{V_S}{V_N} = \frac{\eta_S J_S}{\sqrt{4J_B \eta_B}} \sqrt{\frac{A}{\Delta f}} \quad (4-21)$$

$$NEP = HA \frac{\sqrt{4J_B \eta_B \Delta f}}{\eta_S J_S \sqrt{A}}$$

$$NEP = K_3 \sqrt{A \Delta f} \quad (4-22)$$

where

$$K_3 = \left(\sqrt{4J_B \eta_B} / \eta_S J_S \right) H$$

In this instance, as for current (1/f) noise, the signal and noise are associated with bias-current flow. Here the dependence of NEP on square root of area arises from the averaging process required in arriving at the value for the mean square fluctuation in carriers generated at random by the background photons. Notice that NEP in this case does not depend upon the time constant. This

is due to the behavior of the detector now being controlled by the same processes for signal and noise. Both the quantities ΔN_S and $\sqrt{\Delta N_N^2}$ are linearly dependent on τ . Their ratio is independent of τ in the sense that the detector will respond equally well in time to background photons and signal photons.

4.1.1.4. Shot Noise. In Section 3.2.4, the shot-noise contribution to photoconductive-film noise was given by Equation 3-54:

$$V_N = r \sqrt{2eI_{d-c} \Delta f / n_f \tau}$$

Substitute Equation 3-54 into Equation 4-12; the NEP becomes

$$NEP = HA \frac{r \sqrt{2eI_{d-c} \Delta f / n_f \tau}}{I_{d-c} r \eta_{SJ} S \tau / nd \sqrt{1 + (\omega\tau)^2}} \quad (4-23)$$

Substitute as before in Equation 4-14 to get

$$I_{d-c} = \sigma Ewd = 2ne\mu^* Ewd \quad (4-24)$$

where μ^* is an average reduced mobility for carriers in the film, and from Equation 3-16; μ^* is given by

$$\mu^* = \frac{L^2}{kT} \cdot \frac{e}{\tau} \quad (4-25)$$

to obtain

$$NEP = K_4 \sqrt{\frac{A\Delta f}{\tau}} \cdot \sqrt{1 + (\omega\tau)^2} \quad (4-26)$$

where

$$K_4 = \sqrt{\frac{ndkT}{eEn_f L^2}} \cdot \frac{H}{\eta_{SJ} S} \quad (4-27)$$

4.1.1.5. Summary for Photoconductive Detectors. In all four noise-limited conditions examined here, NEP is clearly dependent on the square root of the product of the bandwidth and the area of the detector. The time constant and frequency dependencies of shot- and of Johnson-noise-limited detectors are identical. This should be expected since both noise spectra are essentially flat. The factor in the NEP expression denoting this identical condition is

$$\sqrt{\frac{1 + (\omega\tau)^2}{\tau}}$$

The case of $1/f$ noise provides a factor given by

$$\frac{1 - (\omega\tau)^2}{f} \cdot \frac{1}{\tau}$$

while G-R noise leads to an expression independent of the frequency and time constant. Finally the G-R background-noise-limited NEP does not contain any factors associated with a detector mechanism of operation. This should be expected since a detector measuring background noise is limited by that external noise, and thereby loses its identity. In other words, any number of different detectors operating with the same spectral characteristics could not be distinguished from one another in terms of NEP, if they were all limited by background noise. If the detectors are G-R phonon noise limited, then J_B in Equation 4-22 must be replaced by J_F . In that event charge carriers produced by the detector lattice dominate as the noise source, and the noise can be identified by the temperature dependence.

4.1.2. PHOTOVOLTAIC AND PEM DETECTORS. As noted above, detailed analysis of NEP for the photovoltaic and PEM detectors will not be carried out here. From the discussion of signal generation in Sections 3.1.2 and 3.1.3, together with the treatment of noise in 3.3, it is easy to follow the same procedure used in 4.1.1 to obtain the NEP properties of these two detectors. However, some of this work has already been carried out, and will be summarized here.

Pruett and Petritz (Reference 4-2) derive the signal-to-noise ratio, and NEP for the back-biased photovoltaic detector. This detector is limited by shot noise (Reference 4-3), and the NEP is given by

$$NEP = HA \sqrt{\Delta f} \sqrt{N_N} / e \eta A J_S \quad (4-28)$$

where the noise is given by

$$\begin{aligned} N_N &= i_n^2 / \Delta f \\ &= 2e \left[I_{SC} - \frac{I_S}{\beta} \left(\exp \frac{eV}{\beta kT} + 1 \right) \right] + 4kTG_{sh} \cdot \left[\frac{k_1 G_{sh}^2 V^2 + k_2 (1 - G_{sh} V)^2 + k_3 I^2}{f} \right] \end{aligned} \quad (4-29)$$

The signal-to-noise ratio is maximized by operating V slightly negative, but almost zero. This permits the elimination of the $1/f$ noise term, and

$$I_{sc} \gg \frac{I_S}{\beta} \left[\exp (eV / \beta kT) + 1 \right] \quad (4-30)$$

4.1.3. COMPARISON OF DETECTORS. C. Hilsum and O. Simpson (Reference 4-4) have treated all three types of photodetectors in an extensive manner, examining particularly the dependence of the NEP for the Johnson-noise-limited case. Some of their conclusions are as follows:

The PEM mode is favored for a semiconductor with high carrier mobility and short lifetime (e.g., InSb), while the PC mode is favored for a semiconductor of long lifetime and low density of carriers. This is apparent from the factor $\sqrt{n_i/\mu_n\mu_p}$ which appears explicitly in the PEM formula, compared with n_i/τ in the PC formula. Reducing the crystal thickness below the diffusion length of the carriers results in no advantage for the PEM mode, but a proportionate advantage can be gained in the PC mode, provided that the surface recombination velocity is sufficiently low. The p-n junction is preferred for semiconductors with low carrier density and low mobility; the depth of the junction below the surface is not critical so long as it is less than the minority carrier diffusion length.

For values of μB small compared to 1, it is clear from the earlier discussion of the PEM signal that the observation of high carrier mobility favoring a PEM detector is appropriate. However, some modification appears necessary for increasing values of μB , since the dependence of the PEM signal on mobility changes. Values suggested by Kruse for the InSb PEM detectors indicate detector operation is in a region where the PEM signal depends upon μ^* for $*$ less than 1.5 (Reference 4-5). This causes NEP to depend inversely on μ raised to a power less than 1.

In principle, it appears that the best detector obtainable should be the photovoltaic, G-R background-noise-limited detector. This is so because the other two detectors in this noise-limited condition have a G-R noise that depends upon fluctuations induced by both the generation and recombination processes. However, the photovoltaic detector does not suffer from this statistical fluctuation on recombination, since the process here is essentially a minority carrier moving back to its majority carrier status on crossing the barrier. Thus the background noise fluctuation observed for this detector is $1/\sqrt{2}$ less than for the photoconductive and PEM detectors.

4.2. DETECTOR CLASSIFICATION

Detector classification schemes generally start with NEP and modify it in some way to obtain a convenient comparison of any detector with the best possible performance that the detector might offer. Optimum performance is usually judged with reference to the limiting background-radiation-noise condition. Detector rating is then expressed in terms of its spectral response and/or its response to a blackbody at some reference temperature, compared to the best possible values obtainable. In this section, the dependence of NEP on λ and T is discussed first, and the classifications suggested by various contributors to improve the rating method follows.

4.2.1. DEPENDENCE OF NEP ON WAVELENGTH AND BACKGROUND TEMPERATURE. Consider the expression for NEP in the background-limited case, given by Equation 4-22:

$$\text{NEP} = \frac{\sqrt{2\eta_B}}{\eta_S} \frac{\sqrt{J_B}}{J_S} H \sqrt{A\Delta f}$$

Assume for simplicity that the quantum efficiencies for background and signal are equal to unity. Then

$$\text{NEP} = \frac{\sqrt{J_B}}{J_S} H \sqrt{2A\Delta f} \quad (4-31)$$

The irradiance H can be expressed in terms of the number of photons per unit (area · time) multiplied by appropriate photon energies and summed up. However, of particular interest here is the detector which is illuminated by a monochromatic beam of photons. The wavelength of the beam is the same as the cutoff wavelength of the detector. Suppose then that J_S is restricted to a wavelength λ_c so that the signal photon flux may be specified $J_{S\lambda_c}$ then H is given by

$$H = J_{S\lambda_c} \frac{hc}{\lambda_c} \quad (4-32)$$

Therefore

$$\text{NEP}_{\lambda_c} = \frac{hc}{\lambda_c} \sqrt{2J_B A\Delta f} \quad (4-33)$$

A plot of the noise equivalent power NEP_{λ_c} as a function of cutoff wavelength can be obtained by substituting different values of λ_c and corresponding photon flux densities J_B for the black background at temperature T . J_B is the flux of all photons with wavelengths between $\lambda = 0$ and $\lambda = \lambda_c$. Celinas and Genoud (Reference 4-6) obtained Table 4-1 by following this procedure for a 300°K background, a detector of unit area, and a 1-cps bandwidth of operation.

A standard of reference in calibrating a detector is its detection ability in responding to a 500°K blackbody source against a room temperature background. Therefore, it would be useful to know the minimum amount of 500°K radiant power necessary to equal background fluctuations. This can be determined by rewriting the expression for NEP in the form

$$\text{NEP} = \frac{HA}{J_S \sqrt{A} \sqrt{2J_B}} \quad (4-34)$$

TABLE 4-1. MINIMUM DETECTABLE POWER FOR IDEAL QUANTUM DETECTOR*

λ_c Cutoff Wavelength (μ)	N_B Photons/Sec on 1-Cm ² Area	$P_{B \min \lambda_c}$ (watts)
1.0	6.6	$(5 \times 10^{-19})^\dagger$
2.0	4.2×10^{10}	2.0×10^{-14}
3.0	5.8×10^{13}	5.0×10^{-13}
4.0	1.9×10^{15}	2.2×10^{-12}
5.0	1.3×10^{16}	4.5×10^{-12}
6.0	4.9×10^{16}	7.3×10^{-12}
8.0	2.2×10^{17}	1.2×10^{-11}
10.0	5.0×10^{17}	1.4×10^{-11}
∞ §	4.15×10^{18}	3.9×10^{-11}

* Area = 1 cm²; background = 300°K, solid angle $\approx 2\pi$.

† The expression for $P_{B \min}$ breaks down for very small values of N_B . This number is included only to show the rapid variation of $P_{B \min}$ between 1 and 2 μ .

§ Ideal thermal detector.

for unit bandwidth and efficiency. Therefore

$$NEP = \sqrt{2A} H \sqrt{J_B / J_S}$$

However

$$J_B = \int_0^{\lambda_c} J_\lambda(T_B) d\lambda$$

$$J_S = \int_0^{\lambda_c} J_\lambda(500^\circ) d\lambda$$

(4-35)

for detectors whose cutoff wavelength is λ_c . Therefore

$$NEP = \sqrt{2A \cdot H} \cdot \sqrt{\frac{\int_0^{\lambda_c} J_{\lambda}(T_B) d\lambda}{\int_0^{\lambda_c} J_{\lambda}(500^\circ) d\lambda}} \quad (4-36)$$

where $J_{\lambda}(T)$ is the background photon density as a function of body temperature. Figure 4-1 shows the dependence of NEP for a 500°K source, for background temperatures ranging from 200°K to 500°K ,

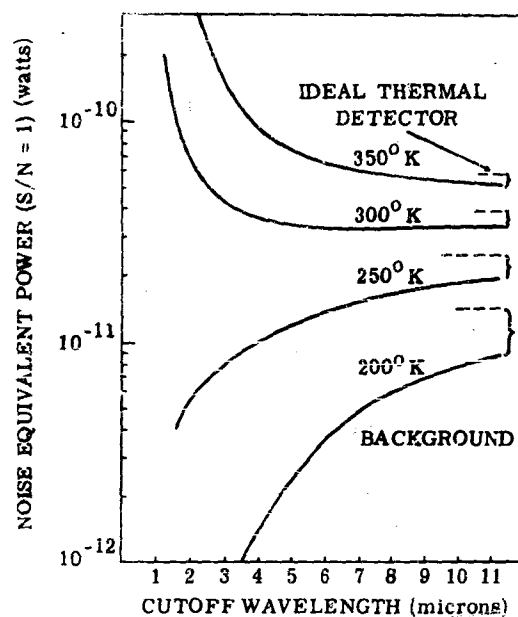


FIGURE 4-1. NEP AS A FUNCTION OF WAVELENGTH FOR DIFFERENT BACKGROUND TEMPERATURES

and for detectors of different cutoff wavelengths λ_c . This figure is taken from a report by Gellinas and Genoud (Reference 4-6), who also note the following:

For a 300°K background there is a wide range of λ_c for which $P_{Bmin500}$ remains almost constant. In other words, for an ideal quantum detector looking at a 500°K blackbody against a 300°K background, it makes essentially no difference what cut-off wavelength is chosen (beyond 1 μ): the increased response to background by raising λ_c is almost exactly compensated by the increased signal. For blackbody radiation it can be shown in general that P_{Bmin} is insensitive to λ_c for a target temperature approximately twice the background temperature.

For background temperature less than 300°K (and a 500°K source) it is advantageous to use as short a cut-off wavelength as possible, while the opposite conclusion holds for background temperatures higher than 300°K.

4.2.2. JONES SYSTEM OF CLASSIFICATION. Jones has contributed a substantial effort to the understanding and categorizing of infrared detectors (References 4-7 and 4-8). He suggested that the reciprocal of NEP, denoted as "detectivity, D" was a more suitable quantity for rating detectors. The advantage of D is a psychological one, in that larger detectivities, rather than smaller NEP's, represent better detectors. Jones considers "detectivity" particularly desirable because it also avoids usage of the word "sensitivity," which has a variety of meanings in technical language.

Jones observed that data taken from thermal and photodetectors, could be distinguished or classified by the way in which their detectivity is related to time constant and frequency response. He noted that their behavior in one case is like the detectivity obtained for an ideal thermal detector, while in another case it behaves like an estimated best-obtainable thermal detector. Accordingly, two classes of detectors were set up, the first based on the detectivity obtained for the ideal detector (capable of seeing background thermal or photon noise), while the second was based on the best obtainable heat detector from Havens' limit.

In establishing this system of classification, a reference condition of detector measurement is designated. It defines a reference or detective time constant and a bandwidth according to

$$\tau = \left[D_1(f_m) \right]^2 / 4 \int_0^\infty \left[D_1(f_m) \right]^2 df \quad (4-37)$$

$$\Delta f = \int_0^\infty \left[D_1(f) / D_1(f_m) \right]^2 df \quad (4-38)$$

and

$$\Delta f = 1/4\tau \quad (4-39)$$

where $D_1(f_m)$ is the detectivity in a unit bandwidth for a modulation frequency that maximizes the detectivity. The motivation behind these reference conditions is to provide a measurement of the detectivity for the important special case where the bandwidth of the noise is the same as the bandwidth of the detector. The classifications then become

$$\text{Class I} \quad D = k_1 \sqrt{\tau}/\sqrt{A} \quad (4-40)$$

$$\text{Class II} \quad D = k_2 \tau/\sqrt{A} \quad (4-41)$$

Detectors limited by a flat spectrum such as Johnson noise, have a detectivity in a unit bandwidth classified as

$$\text{Class Ia} \quad D_1(f) = k_1/2\sqrt{A} \sqrt{1 + (\omega\tau)^2} \quad (4-42)$$

$$\text{Class IIa} \quad D_1(f) = k_2 \sqrt{\tau}/2\sqrt{A} \sqrt{1 + (\omega\tau)^2} \quad (4-43)$$

In the case of the $1/f$ -noise-limited detector, Jones then finds it necessary to redefine the reference time constant and bandwidth as

$$\Delta f = 4f_m \quad (4-44)$$

$$\tau = \frac{1}{4} \tau_p \quad (4-45)$$

where τ_p is the detector time constant. The detectivity for a unit bandwidth has a maximum at the frequency f_m defined by

$$f_m = 1/2\pi\tau_p \quad (4-46)$$

Therefore

$$\Delta f = 4/2\pi\tau_p = 1/2\pi\tau \quad (4-47)$$

From this it follows that

$$\text{Class Ib} \quad D_1(f) = \frac{2k_2 \sqrt{\pi} \sqrt{f\tau}}{A \sqrt{1 + 16(\omega\tau)^2}} \quad (4-48)$$

$$\text{Class IIb} \quad D_1(f) = \frac{2k_2 \sqrt{\pi} \sqrt{f} \cdot \tau}{A \sqrt{1 + 16(\omega\tau)^2}} \quad (4-49)$$

In Section 4.1.1, analytical expressions were derived for NEP in the various noise-limited conditions. They can now be compared with Jones' system of classification. In the analysis that follows, various constants (K_1, K_2, K_3, K_4) appear; also, k_1 is equal to $1/K_1$, etc. These constants are not set equal to Jones constants k_1 and K_2 , since the purpose here is to show only how the NEP relationships from Section 4.1.1 led to Jones' system of classification.

A problem arises for the G-R noise-limited case. Equation 4-22 shows that the NEP for this noise is independent of frequency. Therefore, the detective bandwidth by Equation 4-38 must be infinite, and the detective time constant must equal zero. To avoid this dilemma and because the purpose here is only to derive expressions for detectivities from NEP's in forms suitable for comparison with the expressions of Jones, the responsive time constant and bandwidth are used. These are defined as

$$(\Delta f)_\gamma = \int_0^\infty \frac{[\gamma(f)]^2}{[\gamma_{\max}]^2} df \quad (4-50)$$

$$\tau_\gamma = 1/4(\Delta f)_\gamma \quad (4-51)$$

where γ is the relative response.

4.2.2.1. Johnson-Noise-Limited Detectivity. The detectivity for this noise limitation is derived from Equation 4-15

$$D = \frac{1}{\text{NEP}} = \frac{1}{K_1} \frac{\sqrt{\tau}}{\sqrt{A \cdot \Delta f}} \cdot \frac{1}{\sqrt{1 + (\omega\tau)^2}} \quad (4-52)$$

in a unit bandwidth; therefore

$$D_1 = k_1 \sqrt{\tau} / \left(\sqrt{A} \sqrt{1 + (\omega\tau)^2} \right) \quad (4-53)$$

which is the form of a class IIa detector and so defined by Jones. If the bandwidth $\Delta f = 1/4\tau$, the detectivity becomes at zero frequency

$$D = k_1 \tau / \sqrt{A} \quad (4-54)$$

which is the form of the class II detector.

4.2.2.2. Excess- or "1/f"-Noise-Limited Detectivity. This detectivity is derived from Equation 4-1b

$$D = \frac{1}{\text{NEP}} = \frac{1}{K_2} \cdot \frac{\tau_p}{\sqrt{1 + (\omega\tau_p)^2}} \cdot \sqrt{\frac{f}{A \cdot \Delta f}} \quad (4-55)$$

for a unit bandwidth,

$$D_1 = \frac{1}{K_2} \cdot \frac{\tau_p}{\sqrt{1 + (\omega\tau_p)^2}} \cdot \sqrt{\frac{f}{A}} \quad (4-56)$$

The constant τ_p is the detector response time constant. Jones defines a reference time constant $\tau = \tau_p/4$. Using this time constant, it follows that

$$D_1 = k_2 \cdot \frac{\tau\sqrt{f}}{\sqrt{1 + 16(\omega\tau)^2}} \cdot \frac{1}{\sqrt{A}} \quad (4-57)$$

which is the form of the class IIb detector.

4.2.2.3. Generation-Recombination-Noise-Limited Detectivity. In this case, both signal and noise depend on the frequency in the same manner. Thus the expression for NEP was found to be independent of the factor $\sqrt{1 + 16(\omega\tau)^2}$. The detectivity is derived from Equation 4-22

$$D = \frac{1}{K_3} \cdot \frac{1}{\sqrt{A \cdot \Delta f}} \quad (4-58)$$

The detectivity in the reference bandwidth takes the form

$$D = k_3 \cdot \sqrt{\tau/A} \quad (4-59)$$

which is a class I detector.

4.2.2.4. Shot-Noise-Limited Detectivity. This detectivity is derived from Equation 4-26

$$D = \frac{1}{K_4} \cdot \frac{\sqrt{\tau}}{\sqrt{1 + (\omega\tau)^2}} \cdot \frac{1}{A \cdot \Delta f} \quad (4-60)$$

Shot noise has a flat frequency spectrum, and provides a detectivity in a unit bandwidth similar to Johnson noise:

$$D_1 = \frac{k_4}{\sqrt{1 + (\omega\tau)^2}} \cdot \sqrt{\frac{\tau}{A}} \quad (4-61)$$

and in the responsive bandwidth

$$D = \frac{k_4}{\sqrt{1 + (\omega\tau)^2}} \frac{\tau}{\sqrt{A}} \quad (4-62)$$

$$D = k_4 \frac{\tau}{\sqrt{A}} \quad (4-63)$$

for zero frequency, which is the form of a class II detector.

4.2.2.5. Figures of Merit. By taking the ratio of the detectivity of class I detectors with that of the perfect thermal detector (limited by photon noise), Jones derives a figure of merit called M_1 , expressed as

$$M_1 = 2.76 \times 10^{-11} \times D\sqrt{A}/\sqrt{\tau} \quad (4-64)$$

A figure of merit for the class II detector was derived using Havens' limit as the reference detector. Havens arrived at his estimate by treating thermal detectors as heat engines, considering their operation from a theoretical analysis of the efficiency of such engines, and arriving at an ultimate limit of performance capability by including considerations of limiting noise, available materials, and techniques. On this basis, the class II figure of merit becomes

$$M_2 = 3 \times 10^{-11} \times D\sqrt{A}/\tau \quad (4-65)$$

4.2.2.6. D-Star (D^*). The expressions for detectivity for the different limiting noise types always contain the factor $1/\sqrt{A \cdot \Delta f}$. Therefore, they are a function of detector size and the electrical bandwidth of operation. A more useful number is one that establishes the performance of the detector independent of these quantities. Jones suggested that the quantity D^* , defined as

$$D^* = \sqrt{A \Delta f} / \text{NEP} = D\sqrt{A \cdot \Delta f} \quad (4-66)$$

serves to characterize the detector in terms of the intrinsic properties of the material of which it is made (Reference 4-9).

The wavelength dependence of D^* for the background-limited condition can be obtained by inserting the expression for NEP from Equation 4-33 in Equation 4-66;

$$D_{\lambda}^* = \lambda_c / hc \cdot \sqrt{2J_B}$$

A sample calculation for the evaluation of D^* at 6μ for a 6μ -cutoff detector follows (Reference 4-10).

$$J_B = 4\pi c \int_0^\phi \int_0^{\lambda_m} \frac{1}{\lambda^4} \frac{d\lambda}{\exp(hc/\lambda kT) - 1} \sin \phi \cos \phi d\phi$$

$$= 2\pi c \sin^2 \phi \int_0^{\lambda_m} \frac{1}{\lambda^4} \frac{d\lambda}{\exp(hc/\lambda kT) - 1}$$

where J_B is expressed in photons per square centimeter per second, $\phi = \theta/2$ is one-half the angular field of view, θ , and λ_m is the long-wavelength threshold of the detector. The quantity after the integral sign may be determined from a radiation slide rule or the Lowan and Blanch tables (Reference 4-11). For $\phi = \pi/2$ (2π steradian field of view) and $\lambda_m = 6\mu$, $J_B = 4.8 \times 10^{16}$ quanta/cm²/sec, $\lambda/hc = 10^{20}/3.3$ joules⁻¹. Thus, D_λ^* at 6μ is

$$\frac{10^{20}}{2 \times 3.3 \times (4.8 \times 10^{16})^{1/2}} = 7 \times 10^{10} \text{ cm/watt} \cdot \text{sec}^{1/2}$$

Figure 5-1 shows the variation of D_λ^* at the spectral peak as a function of the long-wavelength threshold for ideal photoconductive and photovoltaic detectors.

D_λ^* can be improved by reducing the magnitude of J_B . From Equation 3-58 it is clear that this reduction can be accomplished by decreasing the temperature of the background radiation sources. This can be done by cooling the walls of the cell surrounding the detector, using a cooled filter to reduce the background radiation from a spectral region not present in the signal, and using the detector against a cooler background outside the cell. Figure 4-2 shows the variation of D_λ^* at spectral peak as a function of background temperatures for three different values of detector cutoff. A further decrease in J_B can be achieved by reducing the angular field of view observed by the detector, as shown in Figure 4-3. Thus it appears well worth while to restrict the field of view of a detector to that value required for a particular application.

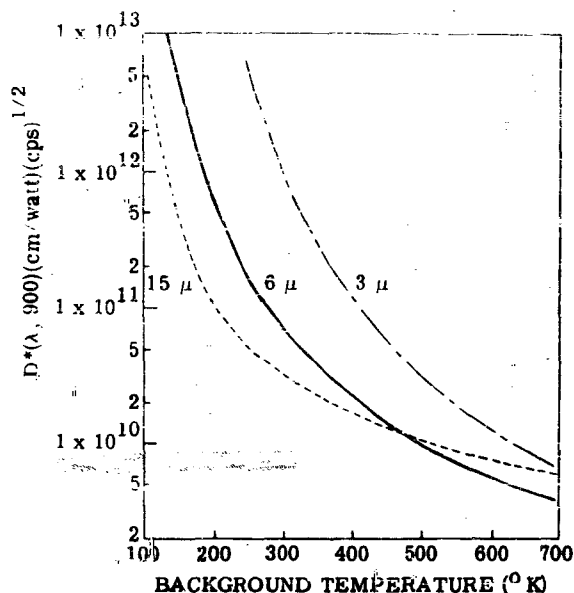


FIGURE 4-2. PEAK D^* VS. BACKGROUND TEMPERATURE FOR THREE DETECTORS IN THE BACKGROUND-LIMITED CONDITION

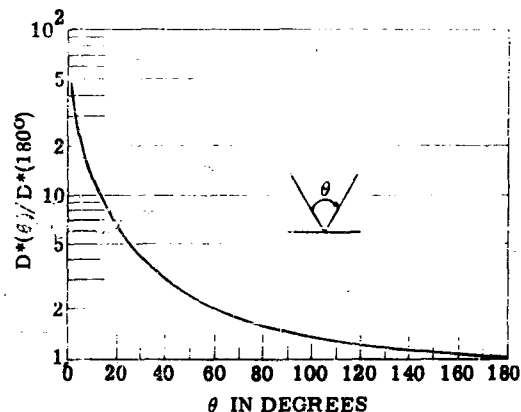


FIGURE 4-3. D^* AS A FUNCTION OF ANGULAR FIELD OF VIEW

4.2.2.7. D-Double Star (D^{**}). It is shown in Section 4.2.2.6 that D^* for the background-limited case is dependent on the angular field of view observed by the detector. Jones suggested that a quantity independent of this factor would be (Reference 4-12)

$$D^{**} = (\mathcal{Q}/\pi)^{1/2} D^*(A\mathcal{Q}\Delta f/\pi)^{1/2} \cdot D \quad (4-67)$$

where \mathcal{Q} is an effective weighted solid angle, referred to a solid angle of π steradians, which the detector element sees through the aperture in a cell's radiation shield. If the detector has circular symmetry, and the solid angle can be represented as a cone with the half angle θ_0 , then

$$\mathcal{Q} = \pi \sin^2 \theta_0 \quad (4-68)$$

The effect of this concept is shown in Figure 4-4, where D^{**} is shown to be substantially independent of the angle.

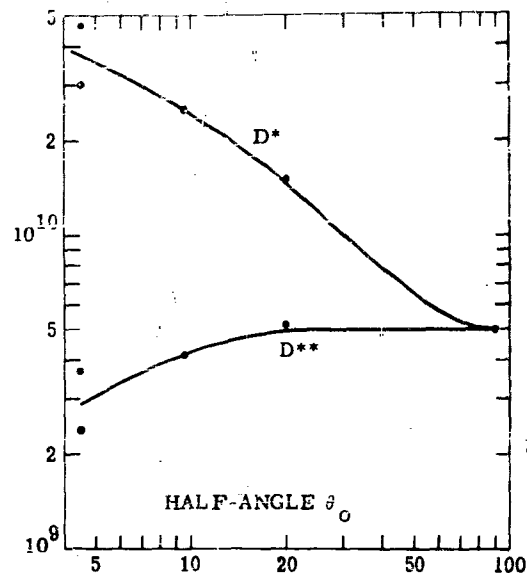


FIGURE 4-4. D^{**} AND D^* AS FUNCTIONS OF ANGULAR FIELD OF VIEW

4.2.2.8. Discussion. The analysis carried out in Sections 4.2.2.1 through 4.2.2.5 indicates the following:

- (1) Class I detectors are limited by background and G-R noise.
- (2) Class II detectors are limited by all other sources of noise.
- (3) A class II detector can become a class I detector if its performance is improved to the point that background or G-R noise predominates over any other noise source. This can be done by cooling a detector. It appears that when a detector becomes background limited, it loses its identity. Its NEP as shown by Equation 4-22 is governed by the rms fluctuation in background photons striking the detector. Thus the performance of the detectors is completely described by the condition of the background. If a number of different detectors, all having the same spectral response characteristics, were background limited, they could not be identified individually on the basis of NEP, D , D^* , or a class I designation. This would be so even though they might be made of different materials and/or have different time constants.

(4) The significance of the figures of merit M_1 and M_2 is not clear, particularly in reference to Havens' limit. Since a detector can go from class II to class I, the reference might well be to the background-limited condition in both cases.

(5) The units of D^* have received considerable attention and at one time were a matter of controversy. Jones' original definition of D^* appeared in the form

$$D^* = \sqrt{\frac{A}{1 \text{ cm}^2} \cdot \frac{\Delta f}{1 \text{ cps}}} \cdot \frac{1}{\text{NEP}}$$

Thus it appeared that the definition normalized D^* to a unit area and bandwidth, and that the unit of D^* was reciprocal watts. This unit seemed appropriate since D^* was an intrinsic measure of a material's ability to detect radiation power. However, considerable opposition arose to the normalization procedure adopted by Jones, and the units ultimately accepted were those that appear in a straightforward examination of dimensions, namely, $\text{cm} \cdot (\text{cps})^{1/2} \cdot \text{watt}^{-1}$. These units might appear somewhat peculiar in that D^* is supposed to provide a measure of the intrinsic ability of a detector material to respond to radiation power, and yet contains the dimensions of size and frequency. Nevertheless, D^* appears to do its job on the basis of data available to date. An explanation of this seeming contradiction appears to come from an examination of the equations derived earlier for NEP in the various noise-limiting cases.

Consider the G-R case where

$$\text{NEP} = \frac{\sqrt{2J_B \eta_B}}{\eta_S J_S} \cdot H \cdot \sqrt{A \cdot \Delta f}$$

The factor $\sqrt{A \cdot \Delta f}$ cancels in the computation of D^* , so that the remaining factors provide the units. The quantities η_B and η_S are efficiency factors. Therefore, the dimensional analysis is simplified to

$$\begin{aligned} D^* &= \frac{J_S}{\sqrt{J_B}} \cdot H = \frac{\# \text{ Photons}_S \cdot \text{cm}^2 \cdot \text{sec}}{\sqrt{\# \text{ Photons}_B \cdot \text{cm}^2 \cdot \text{sec}}} \cdot \frac{\text{cm}^2}{\text{watt}} \\ &= \frac{\text{cm}}{\sqrt{\text{sec}}} \cdot \frac{1}{\text{watts}} = \frac{\text{cm} \sqrt{\text{cps}}}{\text{watts}} \end{aligned}$$

since the numbers of photons are dimensionless, and the reciprocal of time is equivalent here to a frequency. The derived units of D^* becomes $\text{cm} \cdot (\text{cps})^{1/2} \cdot \text{watts}$, consistent with accepted usage.

An interpretation of the meaning of the units of D^* can now readily be put forth. In the measurement of NEP, radiation power from a blackbody illuminates a detector to generate a signal voltage

V_N . A noise voltage V_N is obtained when the detector views an ambient black background. V_N may result from background fluctuations or noise sources internal to the detector. In the background-limited case, it is shown above that D^* is dependent only on J_S , J_B , and H , while being explicitly independent of area and bandwidth. These are all factors in the measurement procedure, and the units of D^* can be attributed to J_S , J_B , and H . Since these quantities represent the numbers of photons and watts per unit area, it is clear that the measurement is inherently normalized. Thus if one wishes to perform a series of measurements in which the bandwidth and/or the area are variables, the experiment would be carried on with constant J_S , J_B , and H . The evaluation of D^* in this situation is truly independent of detector area. It appears, therefore, that Jones' intuition and experience leading to his judgment of the significance of D^* were correct.

It is fruitful to examine the units of D^* in the Johnson- and shot-noise-limited cases. The appropriate expressions can be obtained by inserting Equations 4-14 and 4-26 into Equation 4-63. They are for D^* limited by Johnson noise:

$$D^* = \frac{\eta_S J_S eEL}{\sqrt{2ndkTH}} \cdot \sqrt{\frac{\tau}{1 + (\omega\tau)^2}}$$

and for D^* limited by shot noise

$$D^* = \sqrt{\frac{L^2 eEn_t}{ndkT}} \cdot \frac{\eta_S J_S}{H} \cdot \sqrt{\frac{\tau}{1 + (\omega\tau)^2}}$$

In the Johnson noise case, the quantities eEL and kT represent electric and thermal energies, and have the same basic units. Let us separate out these factors in the dimensional analysis.

$$D^* = \frac{eEL}{kT} \cdot \frac{1}{\sqrt{nd}} \cdot \frac{J_S}{H} \cdot \sqrt{\tau}$$

treating the case where $\omega\tau \ll 1$, and omitting all numerical factors. Substituting units provides

$$D^* = \frac{\text{Energy}_{\text{elec}}}{\text{Energy}_{\text{therm}}} \cdot \frac{1}{\sqrt{\frac{1}{\text{cm}^2}}} \cdot \frac{\text{Photons/Area} \cdot \text{Time}}{\text{watts/Area}} \cdot \sqrt{\text{Time}}$$

$$\frac{\text{Energy}_{\text{elec}}}{\text{Energy}_{\text{therm}}} \cdot \frac{\text{cm}}{\text{watts}} \cdot \frac{1}{\text{Time}}$$

$$D^* = \frac{\text{cm} \cdot \text{cps}}{\text{watts}}$$

In the case of shot noise, the quantity $n_f \cdot L$ is unitless, eEL is an electric energy, and D^* can be expressed dimensionally as

$$D^* = \sqrt{\frac{\text{Energy}_{\text{elec}}}{\text{Energy}_{\text{therm}}}} \cdot \text{cm} \cdot \frac{\# \text{ Photons/Area} \cdot \text{Time}}{\# \text{ watts/Area}} \cdot \sqrt{\text{Time}}$$

for the case of $\omega \tau \ll 1$. On simplifying

$$D^* = \sqrt{\frac{\text{Energy}_{\text{elec}}}{\text{Energy}_{\text{therm}}}} \cdot \frac{\text{cm}}{\text{watts}} \cdot \frac{1}{\sqrt{\text{Time}}}$$

$$D^* = \frac{\text{cm} \sqrt{\text{cps}}}{\text{wat}^{1/2}}$$

It is clear that units are consistently maintained for D^* in the different noise-limited cases. An interesting feature of this examination is that the ratio of an electric energy to a thermal energy appears as a factor for the Johnson noise-limited case, and that the square root of this quantity appears in the shot noise case. This is consistent with different mechanisms responsible for the two cases. In both cases, an increasing bias voltage and a decreasing temperature should result in increasing D^* . The density of carriers n is also dependent on T , and decreases with reduced temperature. However, reduced T can also affect the magnitude of the energy gap, changing the cutoff wavelength, and also affects the time constant τ . These apparently are the factors that are adjustable. In particular, when seeking the optimum bias for a photoconductive detector, it may well be a matter of raising the bias until an increased temperature from Joule heating results. Further biasing could cause adverse temperature effects, and therefore a reduced D^* .

(6) In a recent statistical analysis of the NEP's reported on lead-compound film detectors, Limperis (Reference 4-13) reported that these excess-noise-limited detectors follow an $A^{1/2}$ dependence, confirming the treatment of Section 4.1.1.2. Until recently, data did not clearly indicate a consistent geometry dependence for NEP. There were two factors which prevented obtaining consistent data:

(a) Limiting detector noise sources were not uniformly distributed through the detector. That is, most of the noise was generated at the electrodes, around the detector periphery, at localized regions on the crystal's surface and within the bulk. Detector technology has now reached the stage where uniform sources of noise from the crystal's surface and bulk are becoming the dominant factors.

(b) The photoresponse was generally nonuniform across a detector surface. The film detectors were particularly difficult to deal with in this regard, as shown in Figure A-16. Therefore, an effective detector area has to be defined, which Jones suggested as

$$A_e = \frac{\iint_A \gamma(x, y) dx dy}{\gamma_{\max}}$$

where $\gamma(x, y)$ is the local responsivity of a detector at position x, y on the surface, γ_{\max} is the maximum value of $\gamma(x, y)$ obtained on scanning a small light spot over the surface.

It appears that detector technology has improved to the point where uniformity of noise generation and response is sufficiently advanced to provide reliable data for analysis.

4.2.3. PETRITZ SYSTEM OF CLASSIFICATION

4.2.3.1. Information Capacity and Efficiency. Efforts to establish the performance capability have concentrated on NEP and its meaning in terms of a reference number such as D^* . Petritz suggested that to properly select or evaluate a detector, additional information is required. In particular, it is important to know not only an rms quantity such as NEP, but in addition the rate at which the detector is able to collect and provide information, and how efficiently it is able to convert absorbed signal photons to "bits" of information. Petritz applied information theory to establish a complete system that would describe a detector, and provide a systematic approach to the selection of an optimum detector for a given application. The treatment is somewhat detailed, and can only be summarized here. The interested reader is referred to two publications which apply (References 4-14 and 4-15), and from which the following material is drawn.

The basic equation of information theory states that the maximum attainable information capacity or rate, C , of a channel of infinitesimal bandwidth, df , is given by (References 4-16 and 4-17)

$$C(df) = df \log_2 \left[1 + (V_S/V_N)^2 \right] \text{ bits/sec} \quad (4-69)$$

while the capacity for a finite bandwidth $\Delta f = f_2 - f_1$ is

$$C(\Delta f) = \int_{f_1}^{f_2} \log_2 \left[1 + (V_S/V_N)^2 \right] df \quad (4-70)$$

The unit of information, 1 bit, is the information gained in a measurement where there are two equally probable results. Thus 1 bit of information is obtained when a particular value is measured. For the case where the signal to noise ratio is independent of frequency (as for G-R noise), the information capacity is given by

$$C(\Delta f) = \Delta f \log_2 \left[1 + (V_S/V_N)^2 \right] \quad (4-71)$$

The dependence of $C(\Delta f)$ on V_S/V_N is shown in Figure 4-5. Notice that when the signal-to-noise ratio is unity,

$$C_N = \Delta f \quad (4-72)$$

or the number of bits of information per second is equal to the bandwidth. For the case

$$\Delta f = 1/\tau$$

the reciprocal of the time constant is also the information capacity. The information efficiency is defined as

$$\psi = \frac{C \text{ (bits/sec)}}{P \text{ (watts)}} = \frac{C}{P} \text{ bits/joule} \quad (4-73)$$

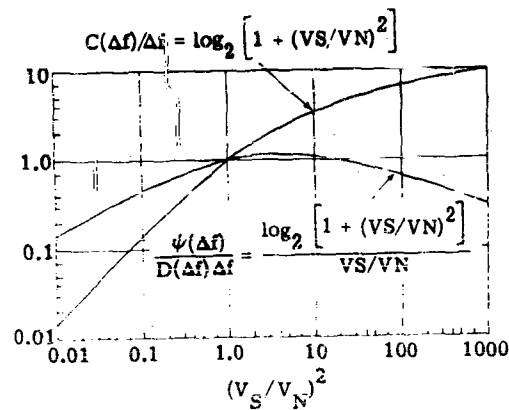


FIGURE 4-5. INFORMATION CAPACITY AND INFORMATION EFFICIENCY AS FUNCTIONS OF SIGNAL-TO-NOISE RATIO

or expressed in terms of quanta

$$\psi = \frac{C}{P/h\nu} \text{ bits/quantum}$$

where P is the power flow to the detector.

The dependence of ψ on the signal-to-noise ratio for the narrowband condition is obtained from equation 4-69, and the definition of NEP:

$$\psi = \frac{\log_2 [1 + (V_S/V_N)^2] \cdot \Delta f}{(V_S/V_N) \text{ NEP}}$$

$$\psi = \frac{\log_2 [1 + (V_S/V_N)^2] D \cdot \Delta f}{V_S/V_N}$$

where D is independent of the signal-to-noise ratio. Figure 4-5 shows a plot of $\psi/D\Delta f$ versus V_S/V_N . A maximum appears at a ratio of signal to noise of unity, indicating that the detector is achieving an optimum number of bits of information per incident photon. This simple treatment provides a meaning for information capacity and efficiency. Petritz then goes on to systematically examine these quantities and signal, noise, NEP, and detectivity for the Johnson-, excess-, and G-R-noise-limiting cases, as well as for the general bandwidth case.

The result of this analysis provides a series of normalized expressions and curves suitable for evaluating NEP, C_N , and ψ_N (subscript N refers to case where $V_S/V_N = 1$), when experimental data for the detector's noise spectrum, signal spectrum, and responsivity are provided. In addition it was found that a detector generally achieves an optimum information efficiency in or near the reference condition $\Delta f = 1/4\tau$ (where τ is the responsive time constant rather than the reference time constant of Jones); that it is generally costly in NEP, C_N , and ψ_N to use $\Delta f \gg 1/4\tau$; and finally that NEP is improved at the expense of C_N and ψ_N when $\Delta f \ll 1/4\tau$.

In conclusion, information efficiency was shown to be a measure of the performance of a detector in that it expresses how efficiently a cell converts radiation energy into bits of information. Furthermore, it expresses how NEP and information rates are exchangeable. It can be used to compare cells under the condition of equal information rates, under the condition of maximum information efficiencies, and in fact under any arbitrary conditions. Petritz recommends therefore that information efficiency be considered as a figure of merit for radiation detectors.

4.2.3.2. Frequency Compensation. From the remarks made above in Section 4.2.3.1 regarding the relationship between Δf and τ , it is clear that an exact relationship between Δf and τ is not sacred. If one needed improved NEP, and if information efficiency or capacity were not important factors, a reduced bandwidth of operation could be used at the expense of increased measuring time to obtain a desired result. Ultimate performance along these lines would be obtained using a synchronous detector technique, where $\Delta f \ll \Delta f_c$ and signals well below noise levels become detectable. Very little has been said up to this point, however, about the possibility of using a bandwidth greater than that suggested by $1/4\tau$. It is clear from the subsections of Section 4.1, that the responsivity in our general, simple case decreases as $[1 + (\omega\tau)^2]^{-1/2}$ and that the noise may fall off in the same manner (G-R) or $1/f$ (excess), or be essentially flat (Johnson). It will be worth while to determine whether there is anything to be gained by an extended bandwidth operation for these limiting cases, where the signal-to-noise ratio is greater than unity. We shall consider here a G-R noise-limited condition, referring the reader to Petritz for a detailed treatment of all cases (Reference 4-14). In this particular case any frequency compensation techniques must boost the detector's signal and noise to the same extent. Therefore, any compensation that applies effectively must relate to the flat Johnson and shot noises of the preamplifier system as an effective limiting condition. In the analysis that follows, the responsivity will have the frequency spectrum associated with a simple exponential type photodecay, and the limiting noise will be treated as flat and associated with the preamplifier.

Consider Figure 4-6, where we are interested first in responsivity curves B and D. These two different responsivities are related to detector time constants τ_1 and τ_3 by

$$\gamma_1 = \frac{\beta_S \tau_1}{\sqrt{1 + (\omega \tau_1)^2}}$$

$$\gamma_3 = \frac{\beta_S \tau_3}{\sqrt{1 + (\omega \tau_3)^2}}$$

where β_S is a constant relating signal volts to watts independent of frequency and time constant. Finally there is also a flat noise spectrum V_N given by F. Thus for detector 1, the detectivity is given by

$$D_1 = \frac{\gamma}{V_N} = \frac{\beta_S \tau_1}{V_N} \cdot \frac{1}{\sqrt{1 + (\omega \tau_1)^2}}$$

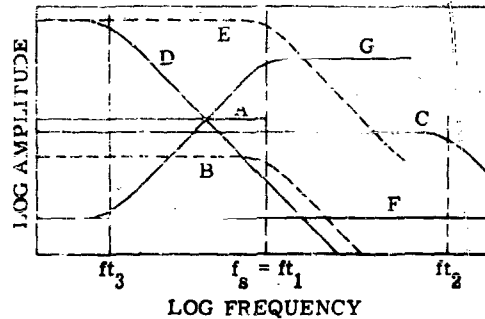


FIGURE 4-6. FREQUENCY COMPENSATION

Let us see if it is possible to apply frequency compensation to detector 3, so that its performance at extended frequency can be made comparable or better than detector 1. Consider a compensation system that has a frequency response

$$\gamma_f = \left[\frac{1 + (\omega\tau_3)^2}{1 + (\omega\tau_1)^2} \right]^{1/2}$$

The compensated response of detector 3 is

$$\gamma_{3C} = \gamma_3 \gamma_f = \frac{\beta S_3 \tau_3}{\sqrt{1 + (\omega\tau_3)^2}}$$

which extends the frequency response curve out to f_{T1} as shown by E. The flat noise F spectrum is also modified by compensation to

$$V_{NC} = V_N \left[\frac{1 + (\omega\tau_3)^2}{1 + (\omega\tau_1)^2} \right]^{1/2}$$

as described by curve G. The new detectivity of detector 3 is

$$\gamma_{3C} / V_{NC} = \beta S_3 \tau_3 / \sqrt{1 + (\omega\tau_3)^2}$$

which is the same as for the uncompensated detector. Comparing this with detector 1,

$$\frac{\gamma_{3C}/V_N}{\gamma_1/V_N} = \frac{\gamma_3}{\gamma_1} \frac{\tau_3}{\tau_1} \frac{\sqrt{1 + (\omega\tau_1)^2}}{\sqrt{1 + (\omega\tau_3)^2}} \geq 1$$

for all frequencies. Thus the compensated slow detector has at least as good a responsivity as the fast uncompensated detector. This results basically from the dependence of responsivity on lifetime. Thus in this G-R case compensation is profitable.

4.3. REFERENCES

- 4-1 R. L. Petritz, Proc. IRE, 1958, Vol. 47, p. 1465.
- 4-2 G. R. Pruett and R. L. Petritz, Proc. IRE, 1958, Vol. 47, p. 1524.
- 4-3 A. van der Ziel, Proc. IRE, 1958, Vol. 46, p. 1019.
- 4-4 C. Hilsum and O. Simpson, Proc. Inst. Elec. Engrs. (London), 1959, Vol. 106, Pt. B, Supp. 1, No. 15, p. 398.
- 4-5 P. W. Kruse, J. Appl. Phys., Vol. 30, p. 770.
- 4-6 R. W. Gelinas and R. H. Genoud, Report of the RAND Corporation, Santa Monica, California, p. 1697, 1959, p. 8.
- 4-7 R. C. Jones, J. Opt. Soc. Am. 1949, Vol. 39, p. 344.
- 4-8 R. C. Jones, Proc. IRE, 1958, Vol. 47, p. 1495.
- 4-9 R. C. Jones, Proc. IRIS, June 1957, Vol. 2, p. 9.
- 4-10 P. Bratt, W. Engeler, H. Levenstein, A. MacRae, and J. Pehek, Germanium and Indium Antimonide Infrared Detectors, Syracuse University, under WADD contract Nr. AF 33(616)-3859, February 1960.
- 4-11 A. N. Lowan and G. Blanch, J. Opt. Soc. Am. 1940, Vol. 30, p. 70.
- 4-12 R. C. Jones, Proc. IRIS, 1960, Vol. 5, No. 4, p. 35.
- 4-13 T. Limperis and W. Wolfe, Proc. IRIS, 1960, Vol. 5, No. 4, p. 141; also presented to Optical Society of America, March 2-5, 1961.
- 4-14 R. L. Petritz, Proc. IRIS, 1957, Vol. 2, No. 1, p. 18.
- 4-15 R. L. Petritz, Photoconductivity Conference, Wiley, New York, 1956, p. 49.
- 4-16 D. A. Bell, Information Theory, Pitman, London, 2nd ed., 1956.
- 4-17 Leon Brillouin, Science and Information Theory, Academic, New York, 1956.

5
DETAILED DESCRIPTION of DETECTORS
Confidential

5.1. (Confidential) INTRODUCTION TO DETECTOR ENUMERATION, by Thomas Limperis

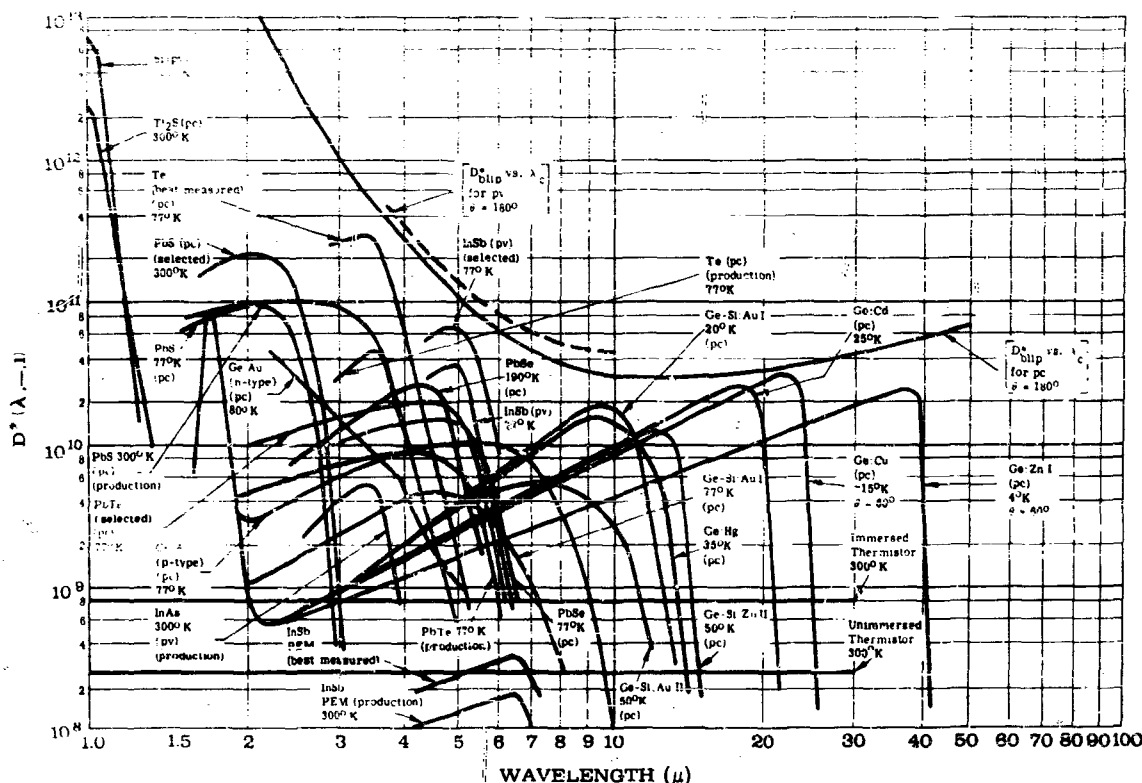
The fundamental problem which faces the infrared scientist or engineer regarding detectors is choosing the best cell for his application from the many different kinds of detectors available. Many of the detector parameters must be taken into consideration before the final judgment can be made. They include:

- (1) spectral response
- (2) detectivity
- (3) resistance
- (4) noise spectrum
- (5) relative response
- (6) time constant
- (7) parameter linearity
- (8) sensitivity contour
- (9) cooling temperature
- (10) availability
- (11) magnitude of signal and noise

Usually the most important of these is the absolute spectral response, for the detector must be sensitive in the wavelength region of interest. Perhaps the next most important parameter is the time constant, since it provides a measure of the information capacity of the detector. The magnitude of signal and noise and the resistance are good measures of the simplicity or difficulty of the electronic design required, and the cell operating temperature tells something of installation difficulties.

In this section most of the above-mentioned parameters are discussed individually for all the commonly used detectors. Composite curves of the spectral response and a table of the other pertinent parameters are included so that a ready comparison may be made. These summaries follow immediately.

The spectral responses, or detectivities as a function of wavelength, of most of the detectors treated in this report and all of the currently used detectors are shown in Figure 5-1. Values for immersed and unimmersed thermistors are given for comparison. Unless indicated otherwise, the curves are for representative detectors - those that would be delivered by the appropriate manufacturers most of the time. For lead sulfide, lead telluride, lead selenide, and tellurium, values for

FIGURE 5-1. D^* VS. λ FOR AVAILABLE DETECTORS

Confidential

selected cells are also given. The details of the averaging process, values of standard deviation, and other details are given in the appropriate subsequent sections.

A theoretical curve for D^* is also shown in Figure 5-1. These theoretical values were determined by assuming that the detector's spectral response has a saw-tooth configuration. For this type of response, the wavelength at peak detectivity and the cutoff wavelength are the same. The calculations were based on the assumption that the ultimate noise limitation was caused by random arrival of photons from the background. (See Chapter 3 for a detailed discussion of noise.) Present-day quantum detectors often have spectral responses which differ considerably from the assumed saw-tooth shape. For example, the impurity-activated germanium detectors have a spectral response

which is more accurately approximated by a superposition of two saw teeth, one corresponding to the intrinsic absorption region and the other to the extrinsic absorption region. More exact approximations to the actual curves can also be used. Smith, Jones, and Chasmar (Reference 5-1) did this for lead salts. A brief explanation of how to compare the theoretical limit with the curve for any given detector is in order. The theoretical limit of peak D^* (for a 300°K background and 180° field of view) is plotted as a function of the detector long-wavelength cutoff. The cutoff is defined as that wavelength at which D^* has decreased by a factor of 2 from the maximum D^* . To find the theoretical limit of detectivity, one simply determines the cell cutoff wavelength and reads off the D^* peak value from the curve. By comparing this value with the peak D^* of a representative cell one may observe how close detectors approach the theoretical limit for that material. In cases where the material is relatively new, one can expect the difference to be large; and, conversely, when the state of the art is quite close to the theoretical limit (a factor of an order of magnitude or less), little improvement should be expected in D^* . However, increases in detectivity can be obtained by limiting the detector field of view with cooled shields (see Chapters 3 and 4 for a detailed discussion of this). Improvements might also be expected in terms of reproducibility and parameter stability. For example, the lead salts have average detectivities about an order of magnitude from the theoretical limit, but much is desired in the way of parameter stability.

Other parameters of detectors are presented in Table 5-1. Ranges are given for the impedance and time constant for each material. One should keep in mind that for oxygen-sensitized film-type detectors, either impedance or time constant may be optimized at the expense of the other, often with some sacrifice in NEP.

In many detector applications, high levels of background radiation exist. Consequently some measure of the photosaturation (or nonlinear effects) is needed. We propose a figure of merit, H_s , which is defined as follows: H_s is that level of effective background¹ irradiance incident on the detector which causes a degradation of a factor of 5 over noise equivalent power which was measured with a background temperature of 300°K . The factor of 5 has no significance except to indicate the level of background radiation where photosaturation is appreciable. This degradation can be caused by an increased noise level or decreased responsivity. H_s gives the equipment designer a measure of the cell performance in high-temperature environments such as exist in infrared-guided, high-velocity missile systems. The figure of merit reported in Table 5-1 was calculated from the data generated by Molitor et al. (References 5-2 to 5-5), who made measurements on PbS, PbSe, PbTe, InSb, and

¹Effective background irradiance implies only those background photons which have wavelengths in the spectral region to which the detector is sensitive.

TABLE 5-1. PHOTOELECTRIC PROPERTIES OF AVAILABLE DETECTORS
Confidential

Material	Mode	Resistance	Time Constant (μ sec)	H_s (w/cm^2)	D^* Peak ($cm \cdot cps^{1/2} \cdot w^{-1}$)	λ Peak (μ)	Cell Temp. ($^{\circ}K$)
PbS	PC	0.5-1.5 M Ω	150-500	1.3×10^{-3}	1×10^{11}	2	300
	PC	1-10 M Ω	800-1500		6×10^{10}	2.5	77
PbSe	PC	50K-5 M Ω	1-10		5×10^8	3.4	300
	PC	0.2-20 M Ω	10-20		4.5×10^{10}	3.4	228
	PC	5-100 M Ω	10-30	2×10^{-2}	8×10^9	4.7	77
PbTe	PC	0.1-10 M Ω	1-10		2×10^7	3.2	300
	PC	50-100 M Ω	~ 15	5×10^{-3}	8×10^9	4.5	77
Tl ₂ S	PC	1-10 M Ω	300-1000		2.5×10^{12}	0.9	300
Te	PC	500-2 K Ω	~ 60		4.8×10^{10}	3.5	77
	PC	1.0-100 Ω	<1		1.3×10^9	5.8	193
	PC	$\sim 200\Omega$	<1		4×10^{10}	5.3	77
InSb	PV	200-2000 Ω	<1	1.5×10^{-2}	4×10^{10}	5.3	77
	PEM	2-50 Ω	<1		1×10^8	6.4	300
InAs	PV	30-200 Ω	~ 2		8×10^9	3.5	300
Ge:AuI	PC	0.1-5 M Ω	<1		8×10^9	5.0	77
Ge:AuII	PC	1-40 M Ω	30-1000	3.5×10^{-4}		1.5	80
Ge:Cd	PC		<1		2.7×10^{10}	17	28
Ge:Cu	PC	30K Ω -20 M Ω	<1		3×10^{10}	25	~ 15
Ge:Hg	PC				2×10^{10}	9	35
Ge:Zn	PC	~ 0.5 M Ω	<0.1		1×10^{10}	34	4.2
Ge-Si:Au	PC	~ 0.6 M Ω	<1		2×10^9	9	60
Ge-Si:Zn	PC	~ 30 M Ω	<1		2×10^9	10	60
Si	PV	770 M Ω	~ 4		9.6×10^{12}	0.9	300
Thermistor	PC	0.5-2.5 M Ω	1-15 msec		2.9×10^8	—	300

Ge.Au. Resistance, noise (90, 1), responsivity, and NEP were determined as functions of background illumination. For PbTe the value of I_g is an average over the three cells; for the others only one detector was measured. Unfortunately, these data are not available for all detector types.

In some detector applications (i.e., infrared systems in interplanetary space), the detector is subject to high-energy particle bombardment. Consequently, some knowledge of the behavior of detector response to high-energy particle flux is of value. Unfortunately, the majority of work (References 5-6 to 5-11) in this area has been directed towards observing these effects in the lead-salt detectors only. This may be because room-temperature cells are so convenient in these applications.

Immediately following are detailed descriptions of the individual detectors. The first of these sections describes the lead chalcogenides (PbS, PbSe, and PbTe). This is followed by discussions of impurity-activated germanium, impurity-activated germanium-silicon alloys, tellurium, indium arsenide, and indium antimonide.

5.2. THE LEAD SALTS, by Thomas Limperis

The lead chalcogenides were the first most highly developed, highly reproducible infrared quantum detectors available for scientific and military application. The early work on these materials dates back to World War II, when German scientists developed two methods for producing a new type of lead-salt detector which was composed of a thin polycrystalline film. One method of preparation was to deposit the film by chemical means. It is interesting to note that chemical methods for depositing lead sulfide films have been well known in the mirror industry for nearly half a century, but such reflecting films exhibit little or no photoconductivity. The other method is an evaporation technique. The film-type lead sulfide detector was first produced in the United States in 1944 by Casman at Northwestern University (Reference 5-12). Subsequently, in 1945, Sosnowski et al. (Reference 5-13) of the Admiralty Research Laboratory (now the Services Electronics Research Laboratory) produced the first lead sulfide film-type detector in England. More detailed information on the history of these cells may be obtained from a special issue of the Proceedings of the Institute of Radio Engineers (References 5-14 and 5-15).

The detectors which are available today are on the average far better than those used during and immediately after World War II, although some of the old detectors are as good as any today. Although more is understood today about the operation of these detectors, there is still a reasonable amount of cut and try and "do-it-cause-it-works."

Three photoelectric properties of the lead salts have been used for the purpose of detecting infrared radiation. They are the photovoltaic, photoelectromagnetic, and photoconductive effects. Photoconductivity in polycrystalline films has been the most frequently used effect, since the photovoltaic and photoelectromagnetic modes require single crystals. These crystals are still relatively difficult to make, and, since their carrier-recombination time is very short, only extremely small photocurrents can be obtained.

The spectral response of the three types of detector has been measured and reported in the literature. Moss (Reference 5-16) has measured the PEM (photoelectromagnetic) response in Wisconsin galena of high purity. Fischer et al. (Reference 5-17) measured the photovoltaic response in Sardinian galena. The long-wavelength limit of response for these modes in the galena crystals was 3.0μ . Scanlon and Lieberman (Reference 5-18), using synthetic single crystals of PLS, PbSe, and PbTe, measured the room-temperature photovoltaic response, and determined the long-wavelength limits as approximately 3.3μ , 5.08μ , and 4.0μ respectively. The long-wavelength limit is defined as the wavelength at which the response falls to 1/2 the peak value. The carrier lifetime in single crystals was found by these and other workers to be several orders of magnitude shorter than the lifetime in thin films.

Models for Photoconductive Detection with Thin Films

When thin films of the lead salts are examined under a microscope they appear to be composed of small single crystals 0.1 to 1.0 μ long (Reference 5-19), separated by barriers 0.001 μ wide. These barriers are probably composed of PbO and/or PbO \cdot PbSO₄ (Reference 5-20). The lengths of the microcrystals are dependent on the amount of film oxidation (page 1869 of Reference 5-21 and Reference 5-22), where longer oxidation periods result in smaller microcrystals.

Optical absorption (Reference 5-23) and electrical conductivity (Reference 5-24) measurements on single crystals of the lead salts have shown that the energy gap of the single crystal corresponds to the long-wavelength limit of photoconductivity of the film. Thus, the photoelectric process in which free carriers are generated by absorption of photons involves a main-band transition in which an electron is raised from the full band to the conduction band, thereby leaving a hole in the full band. The role that oxygen plays in the photoconductive process therefore must be found in the recombination of charge carriers. Recombination processes are discussed generally in terms of the carrier lifetime or importance (References 5-20 and 5-25 to 5-27). Three models will be discussed briefly.

In the intrinsic-carrier model (Reference 5-25) oxygen acts as a p-type compensator impurity to balance the n-type impurities in the film. Both the lifetime and the number of free holes and electrons are equal. Recombination occurs between electrons and holes either directly or via recombination centers. Maximum response is obtained by minimizing the electron and hole densities by compensation and by maximizing the lifetime of hole-electron pairs.

In the minority-carrier model (References 5-25 and 5-28), the film is visualized as a composite of microscopic n-p-n junctions. The crystallites are n-type with a thin layer of p-type material in between, presumably produced by the oxidation treatment. Barrier modulation plays an important role in this model. The diffusion of minority carriers across the p-n junctions results in lowering the space-charge barrier at the junction, thereby allowing more current to flow across the junction. A long minority-carrier lifetime and a low minority-carrier charge density are again necessary for high responsivity.

The majority-carrier model (References 5-29 and 5-30) depends on the presence of minority-carrier traps in the film, which are due to oxygen or oxygen-containing molecules. The traps may be of either the surface or the bulk type. The free minority carrier created initially by the photon, when trapped, leaves the majority carrier free to conduct. The increase in the majority-carrier lifetime is proportional to the time the minority carrier spends in the trap. High responsivity is obtained by optimizing the ratio of the majority-carrier lifetime to the majority-carrier density.

Secondary amplification is also possible through lowering of the intercrystalline-barrier potential by the trapped minority carriers.

Many of the properties of photoconducting films have been explained by the last two models. It is not unlikely that both these processes and other mechanisms are present in the various photoconductive films.

Band Gap

In 1952, Gibson (Reference 5-31) and Clark and Cashman (Reference 5-32) reported that the location of the absorption edge (and therefore the band gap) is a function of the temperature of the lead-salt crystal or film upon which the measurements are being made. An examination of this dependency revealed that the edge shifts towards longer wavelengths with decreasing temperature by the amount of $9.5 \times 10^{-3} \mu/\text{°C}$, this corresponds to a decrease in the energy gap of $4 \times 10^{-4} \text{ eV}/\text{°C}$ (Figure 5-2). This shift is anomalous since the absorption edge in most semiconductors moves towards shorter wavelengths with decreasing temperature.

One method for theoretically determining the energy levels in solids is to consider the lattice sites widely separated and to observe the behavior of the discrete atomic energy levels as the atoms are brought closer together to form the crystal lattice. Because of their charge interaction, when the atoms are brought closer together these discrete energy levels broaden into bands. Two possible behaviors are shown in Figure 5-3. The normal spacing is a room-temperature condition. If the lattice spacing is decreased slightly from the room-temperature position by decreasing temperature

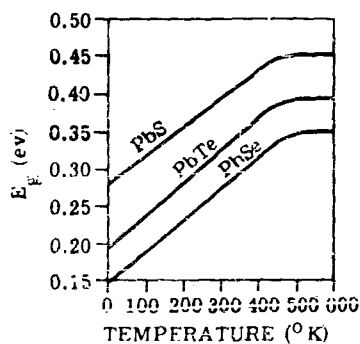


FIGURE 5-2. CHANGE IN BAND GAP WITH TEMPERATURE FOR THE PbS FAMILY

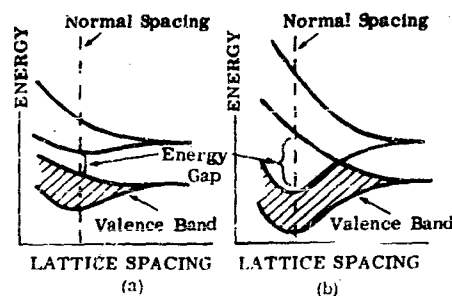


FIGURE 5-3. POSSIBLE ENERGY-BAND DEVELOPMENTS

or increasing pressure, the band gap decreases as in Figure 5-3(a) and increases as in Figure 5-3(b). Presumably the lead chalcogenides behave in a manner similar to that shown in Figure 5-3(a). Electron lattice interaction (a broadening of allowed energy levels by phonon-electron interaction) also affects the size of the band gap. With decreasing temperature there is less interaction between the electrons and the lattice; this results in narrowing the widths of the valence and conduction bands, and therefore a wider band gap. The net result of the two effects described above (electron-lattice interaction and change in lattice spacing) is a band-gap change of 4×10^{-4} ev/°C.

5.2.1. LEAD SULFIDE. Lead sulfide in single-crystal form has a blue, metallic appearance and a cubic (sodium chloride) structure (Reference 5-33). It melts at 1114°C and has a specific gravity of 7.5. The primary impurities found in the natural crystals are zinc, copper, and silver. The synthetic crystals are plagued with nonstoichiometry which strongly influences the electrical and optical properties; however, synthetic crystals with resistivities up to 1 ohm-cm (almost the intrinsic value at room temperature) have been prepared by Scanlon and Lieberman (Reference 5-18) by growing crystals in a controlled vapor pressure of sulfur.

Many of the optical and other physical properties of this material are reported in a recent IRIA publication (Reference 5-34).

5.2.1.1. Absorption. The long-wavelength absorption edge of lead sulfide has been determined by Scanlon (Reference 5-18) with high-resolution optical transmission measurements on very thin crystals (Figure 5-4). For present purposes, the absorption edge will be defined as that point on the absorption curve where the slope is a maximum. The edge, according to Figure 5-4, for room-temperature lead sulfide occurs at 3.0μ (about 0.4 ev) with a corresponding absorption coefficient of about 2000 cm^{-1} . Since the spectral response and the optical absorption are related, the position of this edge is important. In fact, it lies at the same wavelength as the single-crystal photovoltaic-response cutoff and the polycrystal photoconductive-response cutoff, indicating that these responses are due to absorption resulting in main-band transitions.

5.2.1.2. Refractive Index. In 1953, Avery (Reference 5-35) determined the index of refraction for lead sulfide in the wavelength region beyond the absorption edge ($\lambda > 3.0 \mu$). The refractive index was found to change with the type of material and variations in applied oxygen pressure in a manner not easily explained. It varied linearly, however, with changes in sample temperature. The temperature dependence is illustrated in Figure 5-5.

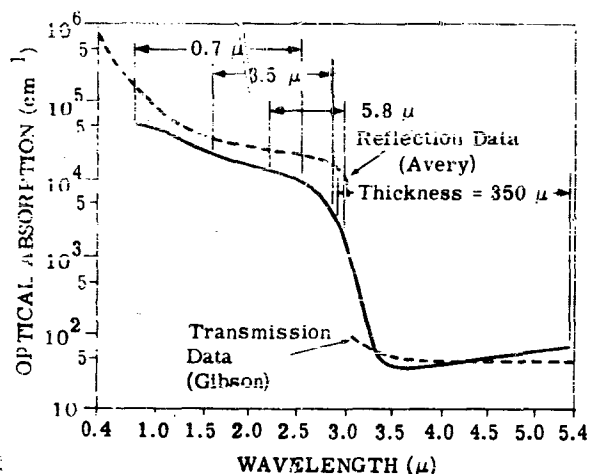


FIGURE 5-4. OPTICAL ABSORPTION OF VERY THIN CRYSTALS OF PbS. Thicknesses of the samples used for different parts of the curve are shown.

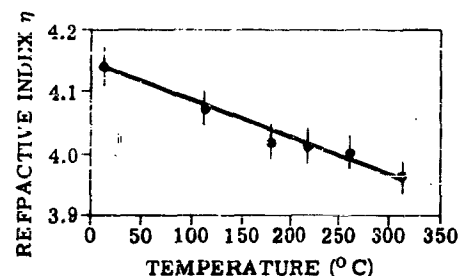


FIGURE 5-5. VARIATION OF REFRACTIVE INDEX WITH TEMPERATURE

5.2.1.3. Resistance. The dark resistance of a lead sulfide cell is independent of its sensitive area as long as it has a square geometric configuration. This is true since the resistance is defined as $R_c = \ell / \sigma wd$, where ℓ is the length, w is the width, and d is the cell thickness. A typical detector made specifically for room-temperature operations will have an impedance value of 1.0 megohm at room temperature. Upon cooling, the impedance will increase to 30 megohms at dry ice temperature and 60 megohms at liquid-nitrogen temperature. The impedance can be controlled during the manufacturing process (probably by controlling the amount of oxygen sensitization) within the range of 1.0 kohm to 100 megohms (Reference 5-36) for detectors at any temperature. A wide range of cell impedance can also be obtained by varying the cell geometry (varying the ratio of ℓ/w). The Eastman Kodak Company (Reference 5-37) has reported an impedance variation from 6×10^3 to 10^7 ohms for room-temperature cells. Figure 5-6 illustrates three possible cell configurations to obtain this latitude. Figure 5-6(a) shows the geometry of the conventional cell where ℓ is the length, w is the width, and d is the film thickness. The cross hatching represents the gold electrodes, and the dark portion is the sensitive film. The configuration in Figure 5-6(b) leads to high impedances since $\ell \gg w$. Conversely, a configuration such as Figure 5-6(c) results in low impedances since $w \gg \ell$. One of the problems incurred when using cells with these geometries is the loss of a portion of the energy from the target since the image may overlap the sensitive area.

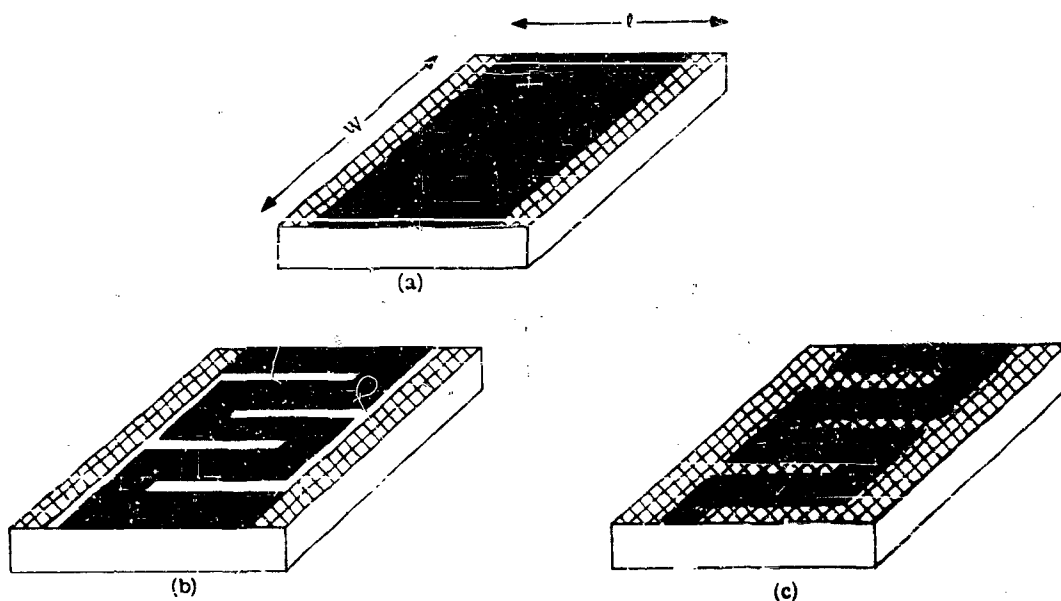


FIGURE 5-6. PbS-CELL CONFIGURATIONS

The cell resistance is also a function of the level of background illumination incident on the cell. This dependence has been determined by using an Eastman Kodak PbS detector. These data (Reference 5-2) are presented in Figure 5-7.

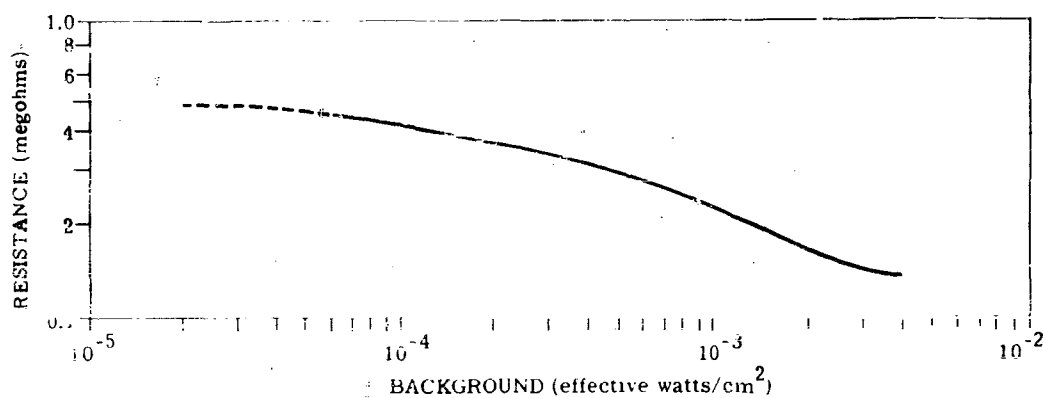


FIGURE 5-7. EFFECT OF BACKGROUND RADIATION ON PbS-CELL RESISTANCE

5.2.1.4. Noise. Figures 5-8 and 5-9 show the noise spectrum and frequency response of a typical cooled PbS cell which was selected as representative of PbS cells in general. This selection was made from one of the NOLC (Naval Ordnance Laboratory Corona) reports on PbS (Reference 5-38).

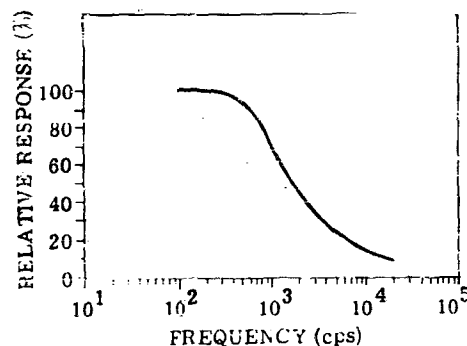


FIGURE 5-8. TYPICAL RELATIVE RESPONSE OF PbS

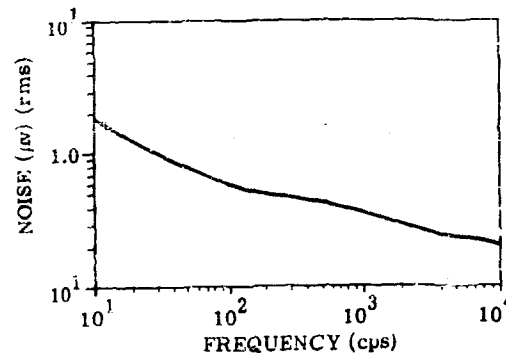


FIGURE 5-9. TYPICAL NOISE SPECTRUM OF PbS

The noise power spectrum appears to be approximately $1/f$ (corresponding to a noise-voltage spectrum of approximately $1/f^{1/2}$) in a range between 0 and 100 cps. In the range from 100 to 1000 cps G-R noise predominates, and beyond 4000 cps, the major contributor is Johnson noise.

If both the frequency response and the noise spectrum are examined simultaneously, it may be noted that, if the chopping frequency is in the $1/f$ region of the power spectrum, the relative response of the cell is at a maximum. The cell still yields maximum response if the chopping frequency is increased to approximately 150 cps where generation-recombination noise begins to dominate. If one attempts to chop in a region where Johnson noise is limiting, beyond 4000 cps, the relative response will have decreased because of time-constant considerations, and the signal-to-noise ratio will have dropped significantly. It appears from the foregoing discussion that one would hope to obtain a maximum signal-to-noise ratio by chopping at frequencies just beyond the $1/f$ -noise region, where the noise has decreased significantly and the cell still yields maximum response. The optimum chopping frequency may be determined by plotting NEP or detectivity as a function of chopping frequency.

The variation of 90 cps noise voltage with the level of background radiation has been determined by Molitor et al. (References 5-2 to 5-5). These results indicate that the noise voltage in PbS is constant for background illumination levels from 10^{-5} to 4×10^{-3} watt/cm².

5.2.1.5. Immersion. Several manufacturers have reported successful immersion of PbS films (Figure 5-10). Infrared Industries, Inc., has available PbS detectors immersed in either sapphire or strontium titanate which allow temperature cycling from -196°C to 100°C, implying that temperature changes in this region will not seriously effect the cell characteristics.

The Eastman Kodak Company is presently using Kodak selenium glass and "other materials" (presumably SrTiO₃ or pressed compacts of the Irtran series) as immersion materials. These lenses are available with radii ranging from 2.5 to 13 mm. (Note Appendix B on immersion techniques.)

5.2.1.6. Radiation Effects. The effects of nuclear radiation (gamma, fast neutrons, and protons) on PbS-detector parameters have been studied by several researchers (References 5-6 through 5-11). A summary of the recent measurements by Billups and Gardner (Reference 5-11) is presented in Figure 5-11. Their work was directed towards recreating the environment believed to exist in the Van Allen radiation belt (References 5-39 and 5-40). Radiations of 7.5, 133, and 450 Mev were used in the experiments. Changes in the parameters of responsivity and resistance were observed as a function of total flux dosage (integrated flux); the results are presented in Figure 5-11. Integrated

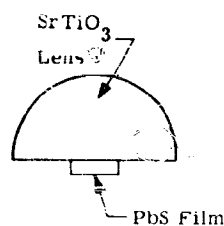


FIGURE 5-10. IMMERSED PbS FILM

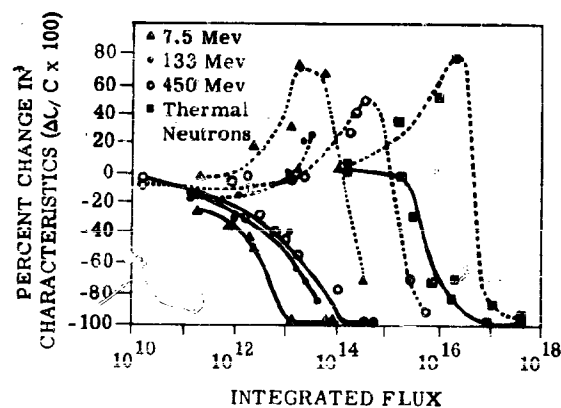


FIGURE 5-11. SUMMARY OF DATA ON THE EFFECT OF NUCLEAR FLUX ON PbS CHARACTERISTICS.
----- resistance ——— responsivity

fluxes of 10^{12} correspond to 2 years in the heart of the Van Allen belt. It was found that cells whose responsivities degraded by 50% or less recovered rapidly (in a matter of hours). For degradations larger than this the recovery time is longer.

5.2.1.7. Detectivity. Over the past nine years, NOLC has disseminated a large amount of data on the photoelectric properties of photoconductive detectors (a few detectors of the photovoltaic and photoelectromagnetic type have also been reported) which have been constructed from a large variety of materials. The detectors used in these measurements were sent to NOLC from the cell manufacturers. They represent, in some cases, the contractor's best effort at that time, and, in others, the average detector from a large batch. The room-temperature PbS data reported since 1956 were used statistically in this section. Slightly over 100 cells are represented in this statistical study. The results are shown in Table 5-2 and Figures 5-12 and 5-13. These presentations are described individually below.

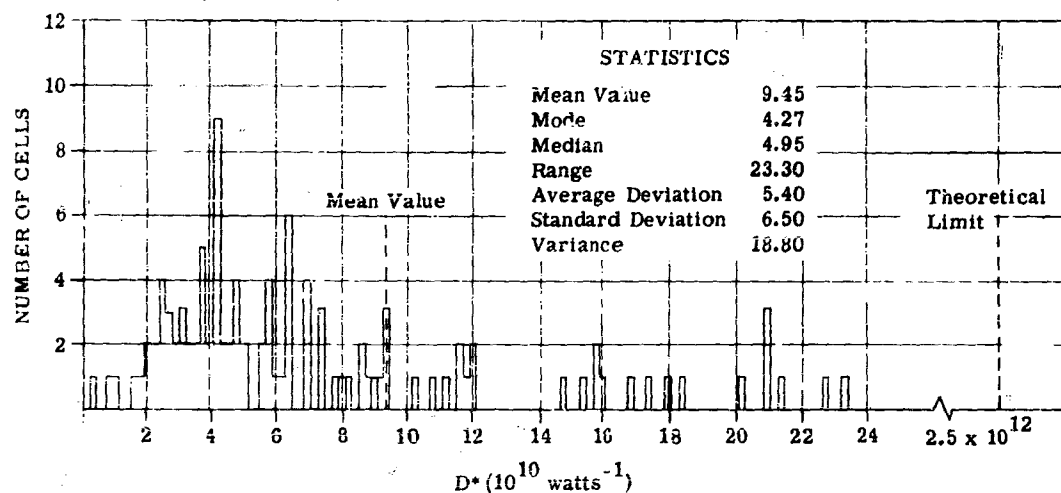


FIGURE 5-12. HISTOGRAM OF D^* VALUES FOR PbS DETECTORS

Table 5-2 contains a list of all the reports from which the data were obtained. Included in the table are the pertinent cell parameters along with the name of the cell manufacturers and a reference to the report. For example, the first line presents the parameters from 39 cells manufactured by IRI (Infrared Industries, Inc.). All of these cells had sensitive areas of 25 mm^2 . The average value of NEP, τ , dark resistance, cell temperature, wavelength of peak detectivity, cell noise voltage, and cell current are given. The standard deviations from the average values are also given for each

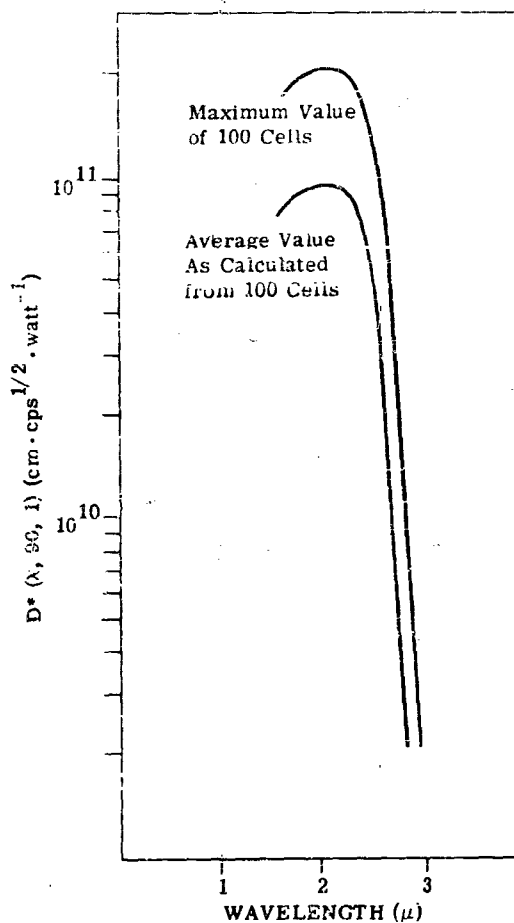


FIGURE 5-13. ABSOLUTE SPECTRAL RESPONSE
OF PbS CELLS AT 300°K

parameter to indicate the spread of values. Two cells from NOLC Reports No. 397 and 400 were omitted from the study because their characteristics deviated greatly from the rest of the cells. The time constants were determined by shining a square-wave pulse of light on the cell and determining the length of time it took the signal voltage to reach 63 % of its maximum value. In the last line of the table the time constant is listed as τ -effective (the effective time constant). This is determined by observing the cell response as a function of chopping frequency.

TABLE 5-2. SUMMARY OF PBS DATA

Year	Age	Sex	Height (cm)	Weight (kg)	Body fat (%)	Maximal heart rate (b/min)	Maximal oxygen uptake (l/min)	Maximal power (W)	Maximal speed (m/min)	Maximal force (N)	Maximal torque (Nm)	Maximal power (W)	Maximal speed (m/min)	Maximal force (N)	Maximal torque (Nm)
1990	18	M	175	65	12	180	3.5	1200	1.5	1000	150	1200	1.5	1000	150
1991	19	F	165	55	15	170	3.0	1100	1.4	900	140	1100	1.4	900	140
1992	20	M	180	70	10	190	3.8	1300	1.6	1100	160	1300	1.6	1100	160
1993	21	F	170	60	13	185	3.2	1250	1.5	1050	155	1250	1.5	1050	155
1994	22	M	185	75	9	200	4.0	1400	1.7	1200	170	1400	1.7	1200	170
1995	23	F	175	65	14	190	3.3	1300	1.6	1100	160	1300	1.6	1100	160
1996	24	M	190	80	8	210	4.2	1500	1.8	1300	180	1500	1.8	1300	180
1997	25	F	180	70	16	200	3.5	1400	1.7	1200	170	1400	1.7	1200	170
1998	26	M	195	85	7	220	4.5	1600	1.9	1400	190	1600	1.9	1400	190
1999	27	F	185	75	17	210	3.7	1500	1.8	1300	180	1500	1.8	1300	180
2000	28	M	200	90	6	230	4.8	1700	2.0	1500	200	1700	2.0	1500	200
2001	29	F	190	80	18	220	3.9	1600	1.9	1400	190	1600	1.9	1400	190
2002	30	M	205	95	5	240	5.0	1800	2.1	1600	210	1800	2.1	1600	210
2003	31	F	195	85	19	230	4.1	1700	2.0	1500	200	1700	2.0	1500	200
2004	32	M	210	100	4	250	5.2	1900	2.2	1700	220	1900	2.2	1700	220
2005	33	F	200	90	20	240	4.3	1800	2.1	1600	210	1800	2.1	1600	210
2006	34	M	215	105	3	260	5.4	2000	2.3	1800	230	2000	2.3	1800	230
2007	35	F	205	95	21	250	4.5	1900	2.2	1700	220	1900	2.2	1700	220
2008	36	M	220	110	2	270	5.6	2100	2.4	1900	240	2100	2.4	1900	240
2009	37	F	210	100	22	260	4.7	2000	2.3	1800	230	2000	2.3	1800	230
2010	38	M	225	115	1	280	5.8	2200	2.5	2000	250	2200	2.5	2000	250
2011	39	F	215	105	23	270	4.9	2100	2.4	1900	240	2100	2.4	1900	240
2012	40	M	230	120	0	290	6.0	2300	2.6	2100	260	2300	2.6	2100	260
2013	41	F	220	110	24	280	5.1	2200	2.5	2000	250	2200	2.5	2000	250
2014	42	M	235	125	-1	300	6.2	2400	2.7	2200	270	2400	2.7	2200	270
2015	43	F	225	115	25	290	5.3	2300	2.6	2100	260	2300	2.6	2100	260
2016															

	1	2	3	4	5	6	7	8	9	10	11	12	13	14	15	16	17	18	19	20	21	22	23	24	25	26	27	28	29	30	31	32	33	34	35	36	37	38	39	40	41	42	43	44	45	46	47	48	49	50	51	52	53	54	55	56	57	58	59	60	61	62	63	64	65	66	67	68	69	70	71	72	73	74	75	76	77	78	79	80	81	82	83	84	85	86	87	88	89	90	91	92	93	94	95	96	97	98	99	100
1	1	2	3	4	5	6	7	8	9	10	11	12	13	14	15	16	17	18	19	20	21	22	23	24	25	26	27	28	29	30	31	32	33	34	35	36	37	38	39	40	41	42	43	44	45	46	47	48	49	50	51	52	53	54	55	56	57	58	59	60	61	62	63	64	65	66	67	68	69	70	71	72	73	74	75	76	77	78	79	80	81	82	83	84	85	86	87	88	89	90	91	92	93	94	95	96	97	98	99	100

Figure 5-12 is a histogram of D^* (λ_{pk} , 90, 1) values. The data for this histogram were obtained from the reports enumerated in Table 5-2. The theoretical limit of detectivity is included for comparison. This value was determined by using the theoretical limit of NEP for room temperature cells determined by Smith, Jones, and Chasmar (Reference 5-1). The calculations were made for the background-limited case (i.e., detectors whose noise limitation is due to the random arrival of background photons). It is interesting to note that several detectors differ from this theoretical limit by a factor of only 10. The mean value differs from the theoretical limit by a factor of 25, which indicates that the state of the art is good. The mode or D^* (λ_{pk} , 90, 1) value which occurs most frequently is $4.3 \times 10^{10} \text{ cm} \cdot \text{cps}^{1/2} \cdot \text{watt}^{-1}$. Today, all major PbS cell manufacturers guarantee a detectivity of around $10^{11} \text{ cm} \cdot \text{cps}^{1/2} \cdot \text{watt}^{-1}$, and they will provide cells with higher detectivities at extra cost.

The theoretical limits of D^* as determined from Smith, Jones, and Chasmar generally require some modification in order to make comparisons with the D^* values of actual cells. An examination of their analysis shows that the parameters are cell temperature; λ_m , the wavelength of peak response; λ_0 , the wavelength where the response is down 50%; and, λ_1 , the wavelength where the response is down down to 1/100 of its peak value. For lead sulfide detectors at room temperature, Smith et al. chose 2.5μ for the wavelength of maximum response (apparently based on some early data of Moss), whereas 2.1μ would be a more realistic choice based on the average of 100 cells. The shift of 0.4μ to shorter wavelengths will increase the value of D^* theoretical limit because a smaller number of room-temperature photons are involved in producing generation-recombination noise.

Petriz (Reference 5-41) has computed the detectivity, D^*_{Blip} as a function of energy gap and long-wavelength limit, λ_c , defined by $E = hc/\lambda_c$. Although his calculation assumes that the spectral response terminates abruptly at λ_c , his D^* values are only about a factor of 2 higher than those of Smith et al., provided Smith's λ_0 is used. Thus, from Smith's table with $\lambda_m = 2.5 \mu$ and $\lambda_0 = 2.9 \mu$, $D^* = 6.7 \times 10^{11} \text{ cm} \cdot \text{cps}^{1/2} \cdot \text{watt}^{-1}$. From Petritz's curves with $\lambda_c = 2.9 \mu$, $D^* = 1.4 \times 10^{12} \text{ cm} \cdot \text{cps}^{1/2} \cdot \text{watt}^{-1}$. The change in D^* with long-wavelength limit should be the same by either analysis, although detailed calculations by Smith's method have not been done with $\lambda_0 = 2.5 \mu$. From the average-value curve for 100 cells, $\lambda_m = 2.1 \mu$ and $\lambda_0 = 2.5 \mu$. From Petritz's curve

$$\frac{D^*(\lambda_c = 2.5)}{D^*(\lambda_c = 2.9)} = 2.5$$

The slope of the long-wavelength tail in Smith's analysis is determined by the values of λ_0 and λ_1 . It appears that the experimental curves of Figure 5-13 have about the same slope as the theoretical curve. In order to obtain a comparison with the experimental curves, it seems reasonable to

assume that Smith's curve should be shifted 0.4 μ to the left, and there the ordinates should be multiplied by the factor 2.5.

A few more remarks regarding the slope of the long-wavelength tail seem appropriate since an examination of the spectral response curves of PbS cells made by different manufacturers shows considerable difference in the slope. It is well known that the long-wavelength tail of the spectral response curve may be represented by a simple exponential function of λ .

$$S(\lambda) = \text{const} \exp [a(\lambda_0 - \lambda)]$$

The logarithm of S is generally plotted, which yields a straight line with slope a . In Smith's analysis a was established by the experimentally determined values of λ_0 and λ_1 . In order to compare actual cell detectivity with the theoretical limit for a given material, say lead sulfide, the experimental values of λ_0 and λ_1 should be determined, and a calculation similar to that of Smith et al. made to determine the D^* theoretical limit, provided of course that these wavelengths differ from those of Smith. Then slope a for IRI and ECA (Electronics Corporation of America) PbS cells is flatter, at least in recent years, than those of other companies. At longer wavelengths, the D^* values for these cells in some cases exceed the theoretical limit unless the Smith calculation is modified.

Figure 5-13 presents for comparison $D^*(\lambda, 90, 1)$ as a function of wavelength of the theoretical limit of D^* , the maximum value of the 109 cells used in the study described above, and the average value from the same study.

Figure 5-14 is an interesting plot; it illustrates the detectivity of room-temperature lead sulfide cells measured by NOLC since 1951. Each data point represents the D^* and vintage of one cell. The points are highly scattered, and consequently few inferences can be made. However, the figure does illustrate the results of the PbS effort in that time interval. The theoretical limit of D^* is included for comparison.

When judging the products of various manufacturers, more than one photoelectric property should be considered at one time. For example, cell detectivity may be increased and dark resistance decreased at the sacrifice of time constant, or vice versa. Most manufacturers today are able to construct these cells at either extreme. This may be illustrated by noting in Table 5-2 that the Eastman Kodak cells have a higher D^* value by a factor of approximately 4 than the others; however, the average time constant of these cells is longer than the time constants of the other cells by a factor of 4. This phenomenon has been observed by a number of researchers in the field and was

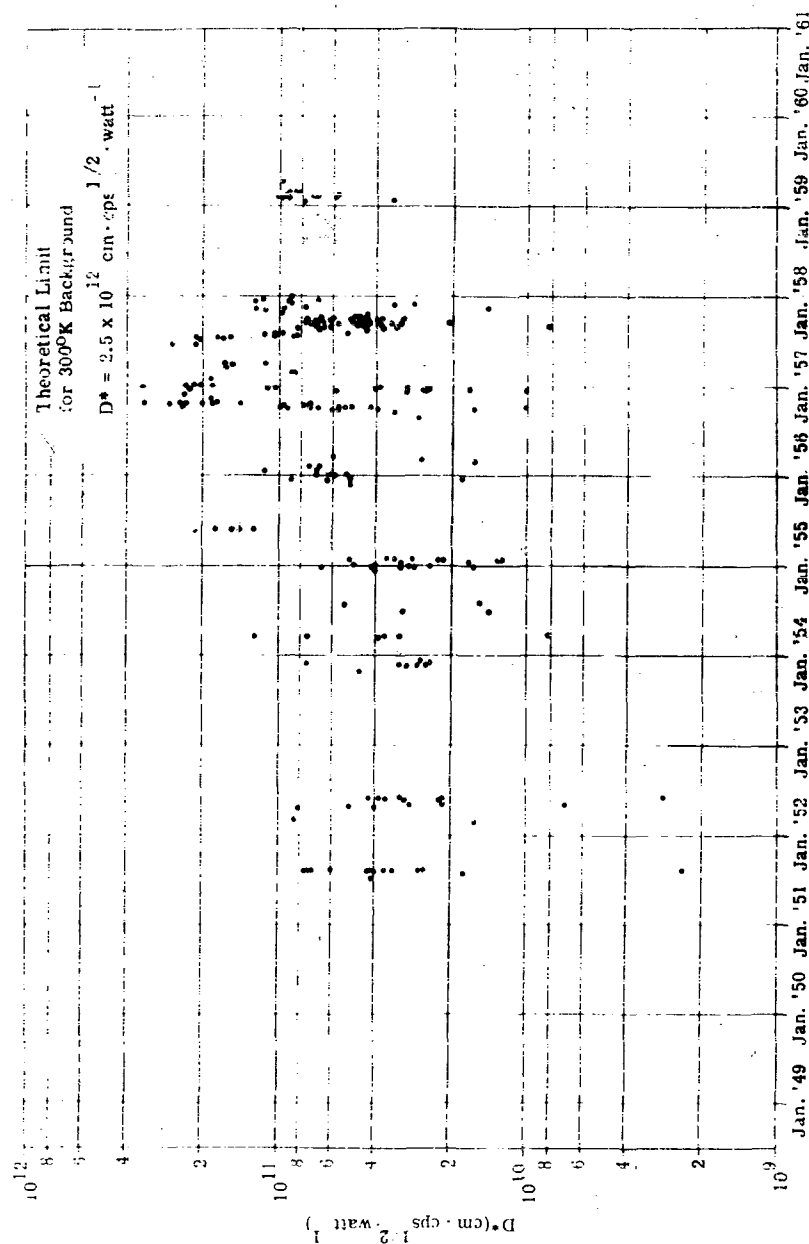


FIGURE 5-14. PEAK D^* VS. YEAR OF MANUFACTURE OF PbS CELLS, 25°C; $f = 90 \text{ cps}$.

first reported by McAlister (Reference 5-42). He noted that

$$S\tau \approx C$$

where τ is the time constant, S is Jones' S , and C is a constant. S is defined as

$$S \triangleq \frac{NEP\sqrt{f}}{\sqrt{A}\sqrt{\Delta f}}$$

where f is the chopping frequency and Δf the bandwidth. D^* is a better measure of detectivity; it is given by

$$D^* = \frac{\sqrt{A}\sqrt{\Delta f}}{NEP}$$

then,

$$D^* = \frac{\sqrt{f}}{S}$$

and finally

$$\frac{\sqrt{f}}{D^*} \approx \text{constant}$$

Since the chopping frequency is always 90 cps for MCLC data, \sqrt{f} may be incorporated in the constant.

It should be noted that evaporated types such as the French cells of Table 5-2 show shorter time constants at room temperature than those prepared by chemical deposition. Evaporated types which show poor long-wavelength response but which have time constant of 50 μsec or less are widely used in sound reproduction and in near-infrared communication systems.

All the cell properties presented in Table 5-2 are functions of temperature. A typical time constant for room-temperature lead sulfide films is around 500 μsec . This value increases to 5000 μsec when the cell is cooled to liquid-nitrogen temperature. The D^* value increases at roughly the same rate. Cooled FbS detectors were not treated statistically in this report since the data were meager. However, typical time constants, resistances, and D^* (λ , 90, 1) are presented in Section 5.1. Eastman Kodak has reported a production PbS detector² which exhibits a time constant of 9 μsec with little sacrifice in peak D^* at room temperature. These extraordinary cells, however, have extremely unstable characteristics.

²Private communications with George Koch of Eastman Kodak Company.

5.2.1.9. Summary. In view of the data presented above, one might say that PbS has an advanced state of the art and that little improvement should be expected in the way of detectivity. However, improvement is needed in other respects if this cell is to be the mainstay in the 1- to 3- μ region. These improvements should include stability of cell characteristics, shorter time constants, better sensitivity contours, and higher reproducibility.

Stability to cell environments was a problem for room-temperature cells in the early 1950's (Reference 5-43). The water and oxygen in the air was absorbed by the cell, thereby altering the photoelectric properties drastically. This problem has been overcome somewhat by isolating the detector surface from air by cementing a cover glass to the surface, applying a lacquer coating, or enclosing the detector in a potting compound. Stability of the characteristics in cooled PbS cells is still a problem. Cells which are mounted in an evacuated dewar have a tendency to outgas the oxygen and therefore alter their characteristics (since dark resistance, D^* , and other photoelectric properties depend on the degree of oxygenation). This cannot be solved as easily as the room-temperature stability problem, since potting compounds and lacquer coatings also outgas and eventually contaminate the dewar vacuum. Since room-temperature PbS cells are used primarily, this problem may be overlooked.

Since long-time-constant detectors are not adequate in systems where high information capacities are required, such as rapid-scanning devices, Eastman Kodak and others have been concerned with decreasing the time constant without degrading the detectivity.

The nonuniformity of response across the sensitive surface is also a problem. To illustrate this, typical sensitivity contours are displayed in Figure 5-15 (Reference 5-44). The numbers appearing in the figure represent the relative response values for the areas enclosed by the contour lines. These sensitivity contours were selected from NOLC reports and to the authors' knowledge closely represent the average chemically deposited and evaporated PbS cell.

On the other hand, since these detectors are constructed by depositing sensitive films on non-conducting surfaces, it is apparent that many geometrical configurations are possible, and in fact this is the case. Geometries such as linear arrays, mosaics, spherical substrates, annular sensitive areas, and many others are available from manufacturers today. In view of this, and the fact that parameters such as NEP, τ , and resistance may be tailor-made to fit the system (though at the expense of other parameters), one can say that this detector is quite versatile.

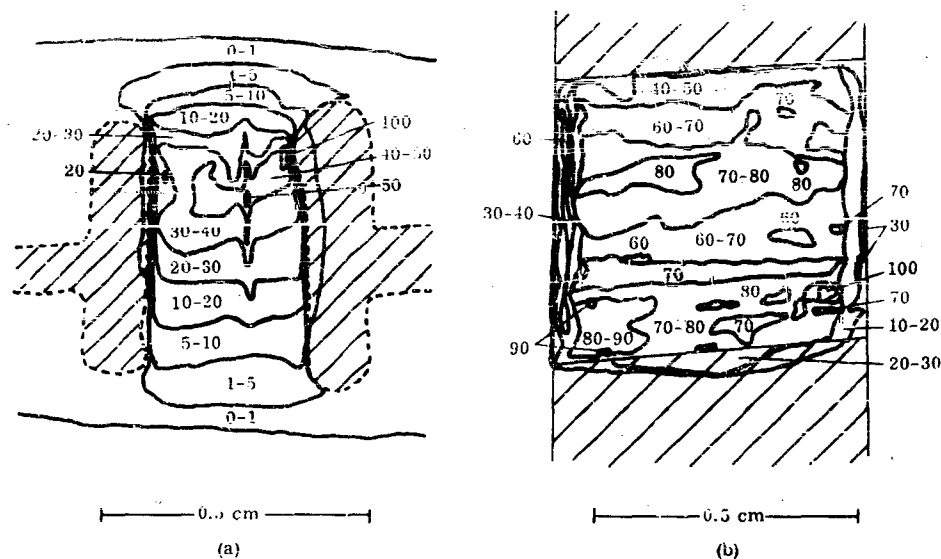


FIGURE 5-15. SENSITIVITY CONTOURS OF PbS CELLS. (a) Evaporated. (b) Chemically deposited.

A list of PbS-detector manufacturers is given below.

U. S. Manufacturers

1. Bulova Research and Development Laboratories, Inc.
2. Continental Electronic Company
3. Eastman Kodak Company
4. Electronics Corporation of America
5. General Electric Company
6. Infrared Industries, Inc.
7. Santa Barbara Research Center
8. Minneapolis-Honeywell Regulator Company

Foreign Manufacturers

1. Admiralty Research Laboratories
2. British Thompson-Houston Company
3. Electro A. G. Zurich
4. Societe Anonyme de Telecommunications
5. Mullard Electronics Products, Ltd.
6. Observatory of Paris
7. Services Electronics Research Establishment
8. Royal Radar Establishment

5.2.2. LEAD SELENIDE. Crystalline lead selenide has a shiny, gray appearance. It is found in nature in the form of small single crystals called clausthalite. Its structure is that of rock salt with a binding believed to be partially ionic and partially covalent. Solid lead selenide melts at 1065°C. It has a density of 8.1 g cc.

5.2.2.1. Absorption. The room temperature absorption spectrum of lead selenide has been determined by Avery (Reference 5-35) by measuring the reflection coefficient of single crystals. Gibson (Reference 5-31) and Scanlon and Lieberman (Reference 5-18) determined the absorption spectrum at various temperatures using transmission measurements on single crystals. The results are presented in Figure 5-16. These data indicate that the absorption edges for this material at room, dry-ice, and liquid-nitrogen temperatures are located at 5.0μ , 5.6μ , and 7.0μ , respectively.

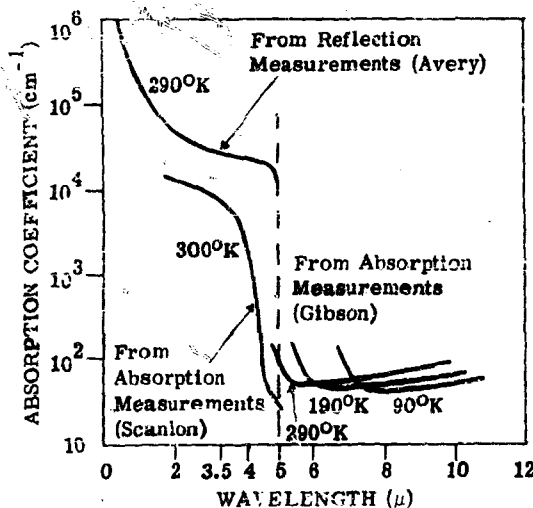


FIGURE 5-16. ABSORPTION-COEFFICIENT MEASUREMENTS ON PbSe CRYSTALS

5.2.2.2. Refractive Index. Values of the refractive index and the real and imaginary parts of the dielectric constant have been determined by Avery (Reference 5-45). He shows that the index of refraction varies from about 3.5 to 4.5 in the region of 1.0μ to 2.2μ , and from 4.5 to 4.6 in the region of 2.2μ to 3.5μ .

5.2.2.3. Resistance. The dark resistance of the detector increases as the cell temperature decreases: it is also dependent upon the amount of oxygenation the film receives during preparation. Room-temperature evaporated cells with square geometric configurations have dark resistances of around 1 megohm, while the room-temperature chemically deposited detectors have resistances of around 50 kohm. When the chemically deposited detectors are cooled, the resistance increases from 2 to 30 megohms.

Just as in the case of PbS, PbSe cells may be constructed in a wide range of geometrical configurations to furnish a latitude in resistances for different applications. The resistance is also a function of the level of background illumination as in the case of PbS. On a log-log plot (cell resistance versus background flux density) the resistance falls from 30 megohms at a background level of 10^{-4} watt/cm² to a resistance of 10 megohms at a background level of 10^{-2} watt/cm². The data are presented in Figure 5-17. The background flux reported includes only those quanta which produce charge carriers via band-to-band transitions.

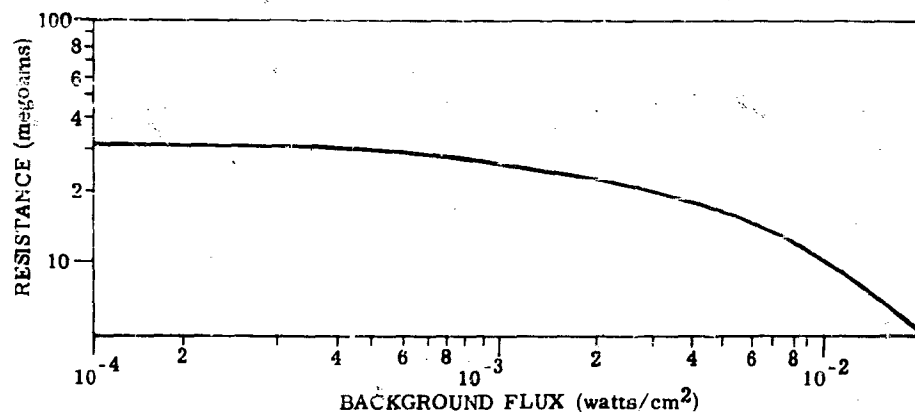


FIGURE 5-17. EFFECT OF BACKGROUND RADIATION ON PbSe-CELL RESISTANCE

5.2.2.4. Noise. Evaporated room-temperature PbSe cells have a noise spectrum similar to that shown in Figure 5-18 (Reference 5-14); $1/f$ noise dominates at frequencies below 100 cps. In the fre-

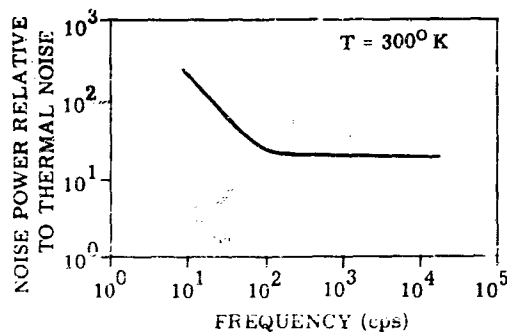


FIGURE 5-18. NOISE-POWER SPECTRUM OF AN EVAPORATED PbSe PHOTOCONDUCTOR

quency range of 100 cps to around 10^5 cps the limiting noise is caused by the random generation and recombination of charge carriers induced by the thermal agitation of lattice. At frequencies above 10^5 cps Johnson noise dominates.

In the region of G-R (generation-recombination) noise the S/N ratio is independent of frequency, even though at the high-frequency end of the G-R region the absolute value of the noise and signal voltages may be decreasing. This is true because the noise and signal have similar frequency dependencies.

In the case of chemically deposited cells the noise spectrum is similar to that in Figure 5-18; however, at the lower frequencies the decrease in noise power is less rapid than $1/f$.

As the cell temperature is decreased, the total noise power across the spectrum decreases, but the limiting noise mechanisms in the different frequency regions remain the same. There might be a slight change of the frequency at which each becomes dominant.

Noise in PbSe detectors is also a function of the level of background illumination. The total noise power at 90 cps was determined as a function of background illumination level (References 5-2 to 5-5). This noise power was found to be constant for background illumination levels up to 10^{-3} watt/cm²; and for higher illumination levels the noise power increased slowly.

5.2.2.5. Immersion. Optical gain by immersing the detector in a material with high index of refraction has been obtained by SBRC (Santa Barbara Research Center). The material they use is strontium titanate. The cell material is actually deposited upon the planar surface of the hemisphere (see Appendix B).

5.2.2.6. Detectivity. As in the case of PbS, data presented in the NOLC reports have been used statistically in this study. Table 5-3 is a comprehensive chart which lists the reports from which the data were taken. Also included in the table are the various pertinent parameters which describe a detector. For example, the first line in the table tells something about the 16 SBRC detectors which appeared in NOLC Report No. 398, December 1957. The average value of τ , D^* , NEP, cell noise voltage, dark resistance, and other parameters are listed along with their standard deviation.

When considering the application of statistics to PbSe, one finds it necessary to treat the following kinds of cells individually.

- | | |
|--|--|
| (1) Evaporated PbSe (liquid-nitrogen-cooled) | (3) Evaporated PbSe (uncooled) |
| (2) Chemically deposited PbSe (liquid-nitrogen-cooled) | (4) Chemically deposited PbSe (uncooled) |

TABLE 5-3. SUMMARY OF PbSe DATA

[illegible][illegible]

These cells are treated in groups as described above because of the considerable difference in peak D^* and spectral response characteristics among the different detector types. The average value of $D^*(\lambda, 90, 1)$ and maximum value of $D^*(\lambda, 90, 1)$ are presented in Figures 5-19 to 5-22. The theoretical limit of detectivity (assuming the noise limitation is due to the random arrival of background photons) is also included for comparison. These theoretical curves were obtained by determining the threshold wavelength (λ_c) in each case and reading off the peak D^* value from Figure 5-1. A spectral response similar to the measured response was then drawn such that its locus passed through the determined theoretical peak value. The resulting curve is acceptable for comparative purposes; however, it should be emphasized that the theoretical peak value was determined originally by assuming

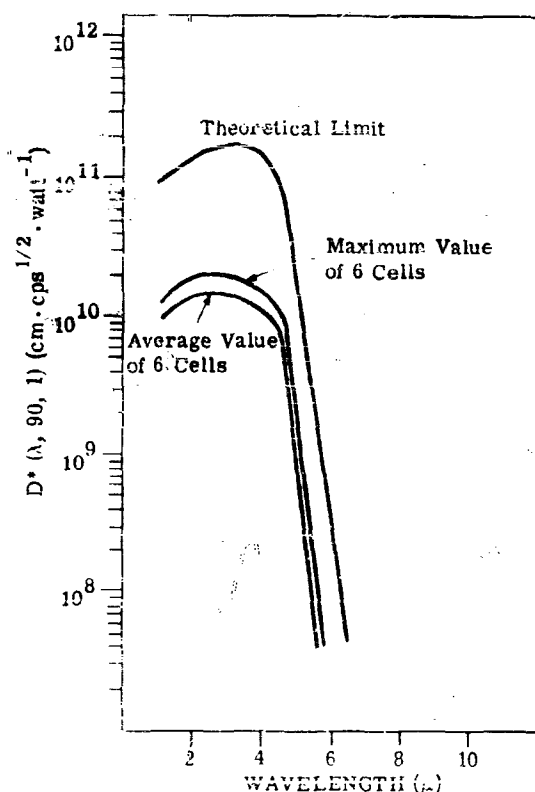


FIGURE 5-19. ABSOLUTE SPECTRAL RESPONSE OF EVAPORATED PbSe CELLS AT 80°K.

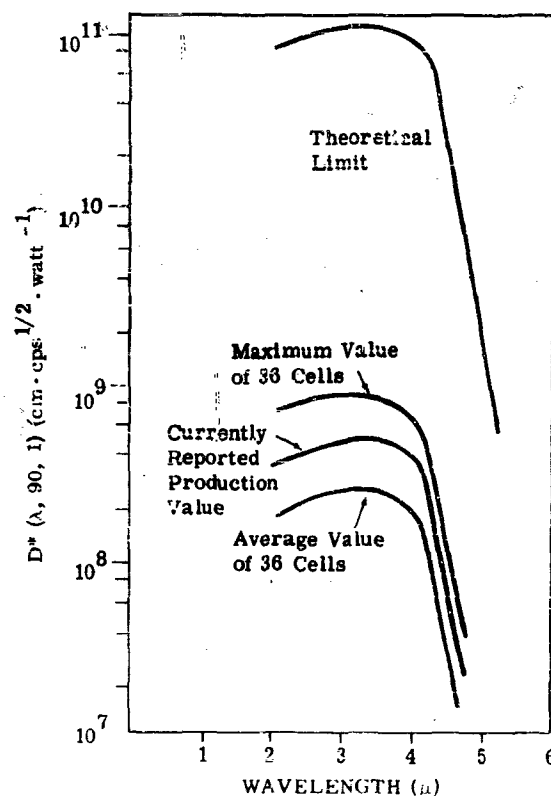


FIGURE 5-20. ABSOLUTE SPECTRAL RESPONSE OF CHEMICALLY DEPOSITED PbSe CELLS AT 300°K.

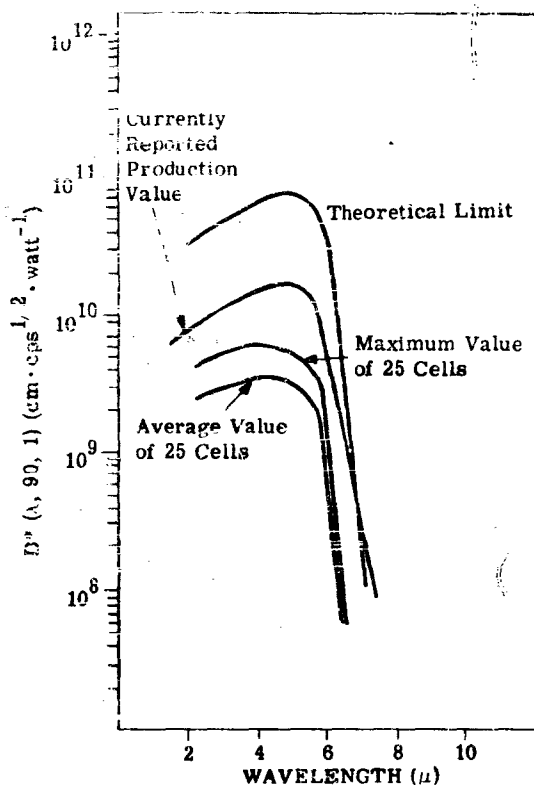


FIGURE 5-21. ABSOLUTE SPECTRAL RESPONSE OF CHEMICALLY DEPOSITED PbSe CELLS AT 80°K

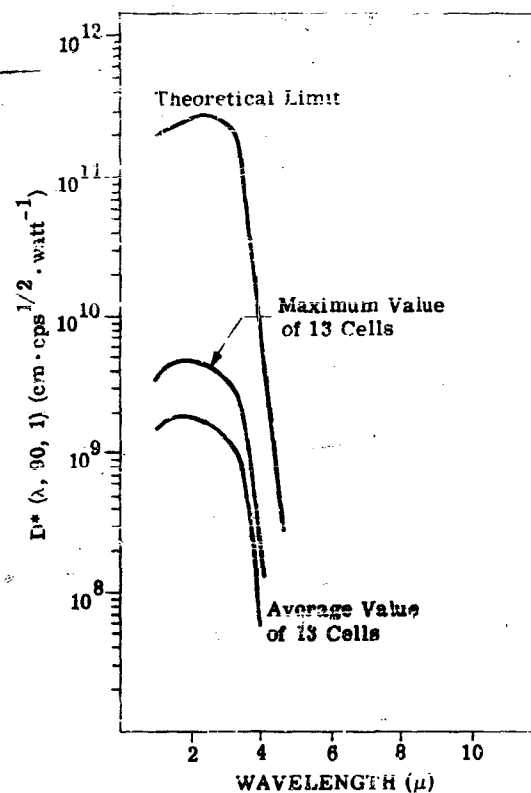


FIGURE 5-22. ABSOLUTE SPECTRAL RESPONSE OF EVAPORATED PbSe CELLS AT 300°K

a saw-tooth configuration of the response curve. The data used in this section are those reported by NOLC after 1956.

Figure 5-19 presents the results from these calculations on six cells of the evaporated PbSe liquid-nitrogen-cooled type along with the theoretical limit of detectivity. The results are quite interesting. The striking feature is the lack of long-wavelength response. The intrinsic band gap at 80°K is about 0.18 ev, which indicates a long-wavelength threshold of about 7 μ. In Figure 5-19 the long-wavelength threshold is 4.6 μ. A probable explanation for this discrepancy is that these evaporated films are prepared extremely thin to provide a high signal-to-noise level, and, as a result, these thin cells transmit the radiation beyond 4.6 μ. Experimental work at Eastman Kodak confirms this dependency, however, indications are that the problem is much more complex (Reference 5-46).

Figure 5-21 presents the results from 25 cells of the liquid-nitrogen-cooled chemically deposited type. Here, the departure of peak D^* from the theoretical limit is larger than that observed in the previous figure, but the long-wavelength limit occurs at a wavelength of about 6μ , in contrast to the limit of 4.5μ exhibited by their evaporated counterparts.

The results for room-temperature chemically deposited and room-temperature evaporated PbSe detectors are presented in Figures 5-20 and 5-22. Here we see again a difference in the long-wavelength limit of response.

It is interesting to observe the progress which was made over the years (since 1951) in the development of these detectors. A plot of all the data reported by NOLC in that time interval is presented in Figure 5-23. Each point represents the peak D^* value for one detector and its vintage. Although the data points are highly scattered, it seems apparent that liquid-nitrogen-cooled, chemically deposited cells have not shown much improvement in peak D^* (however, improvement has been made in the way of reduced aging effects, higher production yields, etc.). The same comment might be made regarding room-temperature evaporated cells. However, it should be pointed out that the spectral response in the case of early, uncooled, evaporated cells was similar to that in Figure 5-24, where the peak D^* occurs somewhere in the spectral region below 1μ , and so the peak D^* value plotted for these early years must be used with care.

On the other hand, uncooled chemically deposited cells and liquid-nitrogen-cooled evaporated cells have been improved, as indicated in Figure 5-24.

Detectors with limited fields of view (employing cooled shields) are available from Santa Barbara Research Center. The effect of limiting the field of view is to increase the D^* value as described in Chapters 3 and 4. The amount of increase depends on both the amount of change in field of view and on the percentage of the total detector noise which is caused by random fluctuations in photon arrival. At high chopping frequencies (about 1000 cps) and at liquid-nitrogen temperatures, the PbSe detector is limited mainly by generation-recombination noise, with the majority of this G-R noise being caused by the background irradiance. The relationship of $D^*(500^\circ\text{K}, \infty, 1)$ to the detector field of view is presented in Figure 5-25.

Recently SBRC has announced the development of a dry-ice-cooled PbSe cell which has a peak detectivity comparable to the liquid-nitrogen-cooled cell. The cutoff wavelength of this detector is shorter than that of the liquid-nitrogen cell due to the broadening of the band gap with increased temperature. The dry-ice cell cuts off at about 5μ , while the liquid-nitrogen cell has a detectivity extending to 6.2μ . Several of these dry-ice-cooled cells have been measured at Syracuse University (Reference 5-47). The resulting spectral response is presented in Figure 5-26.

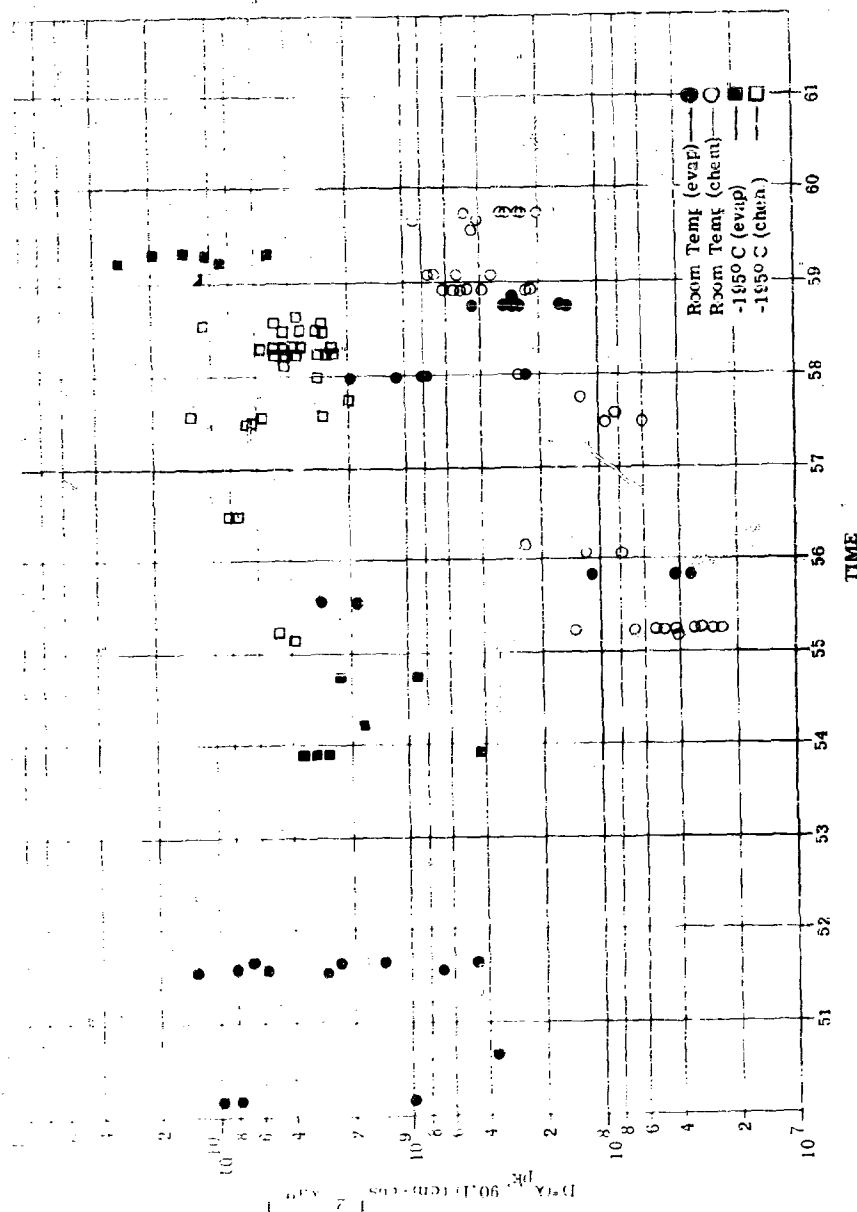


FIGURE 5-23. PEAK D* VS. YEAR OF MANUFACTURE OF F33e CELLS

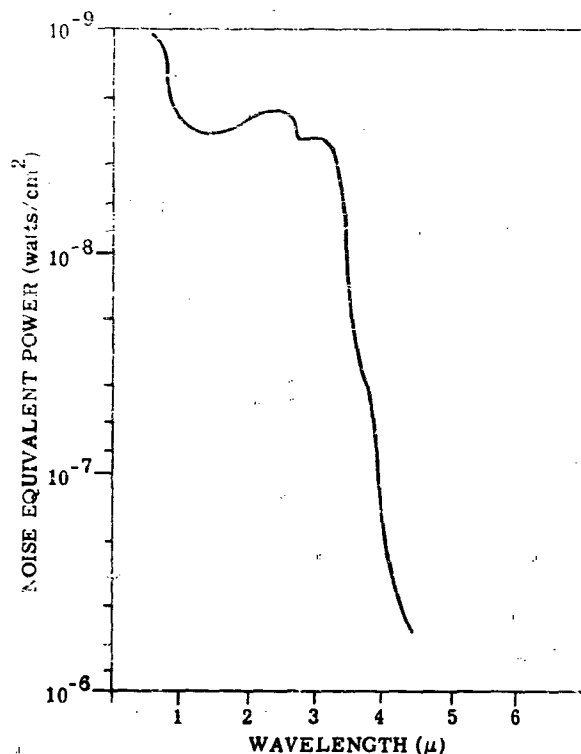


FIGURE 5-24. SPECTRAL RESPONSE OF EARLY PbSe CELLS

IRI has increased the liquid-nitrogen PbSe response for wavelengths shorter than two microns. However, the details of how this was done were not available at the time of this writing. Figure 5-27 presents the $D^*(\lambda, 90, 1)$ for two such cells.

The manufacturers of PbSe detectors are listed below.

U. S. Manufacturers

1. Avion Electronics Division, ACF Industries, Inc.
2. Eastman Kodak Company
3. Infrared Industries, Inc.
4. Librascope, Inc.
5. Santa Barbara Research Center

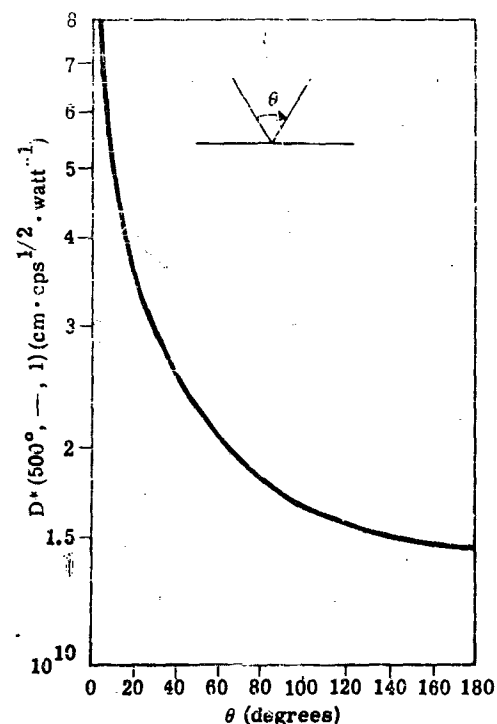


FIGURE 5-25. D^* FOR A 6- μ LONG-WAVELENGTH CUTOFF BACKGROUND-LIMITED PHOTOCONDUCTIVE DETECTOR AS A FUNCTION OF THE FIELD OF VIEW

Foreign Manufacturers

1. Admiralty Research Laboratory
2. Societe Anonyme de Telecommunications
3. Mullard Electronic Products, Ltd.
4. The Plessey Company
5. Royal Radar Establishment

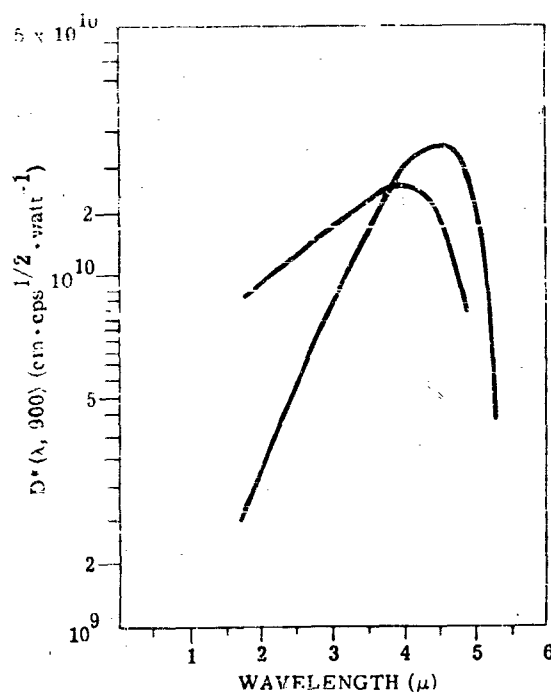


FIGURE 5-26. TWO SBRC PbSe DETECTORS AT 190°K

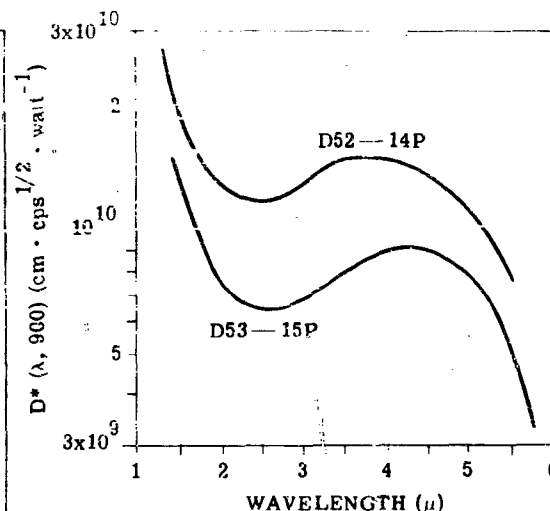


FIGURE 5-27. TWO IRI PbSe DETECTORS AT 78°K

5.2.3. LEAD TELLURIDE. Lead telluride is found in nature in the form of small single crystals called *aitate*. These natural crystals have a white appearance, a cubic (sodium chloride) structure (page 546 of Reference 5-33), a density of 8.16 g/cc, and a melting point of 912°C.

5.2.3.1. Absorption. The infrared absorption spectrum of lead telluride has been determined by Gibson (Reference 5-48) and Scanlon and Lieberman (References 5-18, 5-49, and 5-50). The results of these measurements are presented in Figure 5-28. These data indicate a long-wavelength absorption edge for room-temperature, dry-ice, and liquid-nitrogen detectors of 4 μ, 4.6 μ, and 5.4 μ, respectively.

The long-wavelength limit of photoconductivity in polycrystalline films and of photovoltaic response in single crystal p-n junctions (References 5-18, 5-49, and 5-50) (Figure 5-29) coincides well with the position of the absorption edge measured in single crystals. This indicates that these mechanisms involve main-band transitions (i. e., electrons with energy levels in the valence absorb the

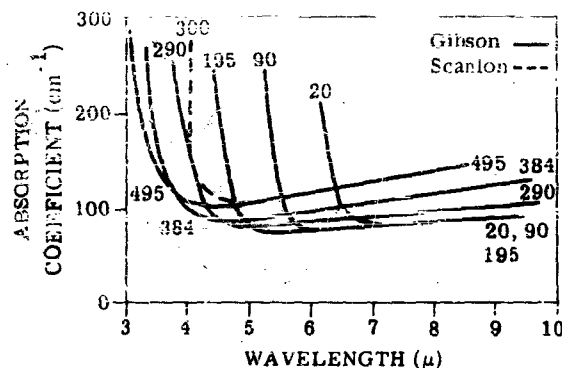


FIGURE 5-28. ABSORPTION OF PbTe CRYSTAL.
Temperatures in degrees Kelvin.

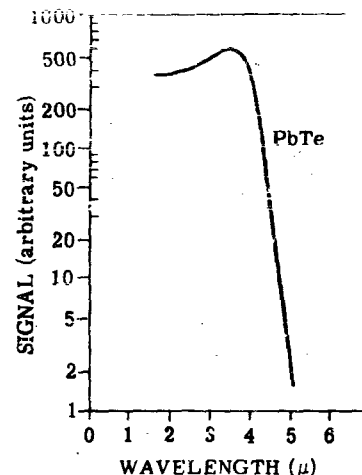


FIGURE 5-29. PHOTOVOLTAIC SPECTRUM FOR p-n JUNCTIONS IN PbTe AT ROOM TEMPERATURE. $\lambda_{1/2} = 4.05$; $\Delta E \approx 0.30$ eV; $\tau = 0.1$ μ sec.

photon energy and consequently make transitions directly to the conduction band, leaving a hole in the valence band and a free electron in the conduction band).

5.2.3.2. Refractive Index. The refractive index obtained for surfaces with different polish has been reported by Avery (Reference 5-46). It was found to vary from about 4.1 to 5.2 in the region of 1.0 to 2.0 μ , and from 5.2 to 5.3 in the region of 2.0 to 3.5 μ . Avery also reported the real and imaginary parts of the dielectric constant in the same article.

5.2.3.3. Resistance. Detectors made from this material have dark resistances which are much higher than their PbS and PbSe counterparts. Liquid-nitrogen-cooled PbTe cells have resistances of 50 to 100 megohms for square configurations. Room-temperature PbTe exhibits resistances of around 0.1 to 10 mehoohms; however, these detectors are seldom used due to the serious degradation in P^* . Various geometrical configurations such as those described in Section 5.2.1 are also possible with this material. In fact, to keep the cell resistance at a minimum, detectors are sometimes constructed in an annular shape with the electrodes located at the center and outer regions of the annulus. This configuration leads to an l/w ratio that is smaller than the one in the square-area cells, and therefore a smaller resistance value results.

The resistance is also a function of the level of background irradiance, since $R = e/\sigma\omega d$ and $\sigma = ne\mu$, where $n \propto H_{bb}$; therefore, $R \propto 1/H_{bb}$. Figure 5-30 presents the relation between these parameters. The measurements were made by Molitor et al. (References 5-2 to 5-5) using 3 PbTe detectors manufactured by Farnsworth Electronics Company (now ITT Laboratories).

5.2.3.4. Noise. The noise spectrum of PbTe has a $1/f$ component which dominates at frequencies up to 6×10^3 cps, as indicated in Figure 5-31. Beyond this frequency, generation-recombination noise is the dominant noise component out to the region where Johnson noise becomes significant. Due to the short time constant in PbTe (compared to PbS), the radiation may be chopped at a higher frequency in order to reduce the noise and still operate in a region of maximum response. Chopping frequencies of 800-1000 cps are common. A decrease in noise voltage by a factor of 3 would result

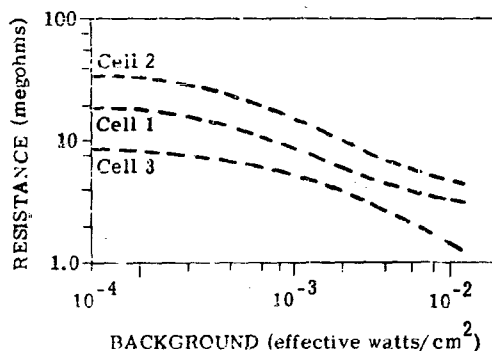


FIGURE 5-30. RESISTANCE VS. BACKGROUND FOR PbTe DETECTORS

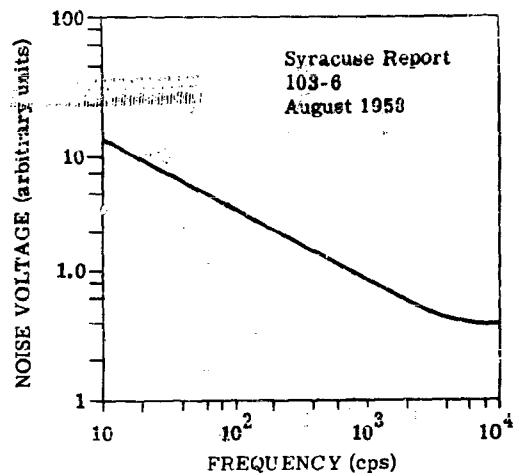


FIGURE 5-31. PbTe NOISE SPECTRUM

in an increase of detectivity by the same factor, since

$$D^* = \frac{\sqrt{A} \sqrt{\Delta f}}{NEP}$$

and

$$NEP = P_i \frac{V_n}{V_s}$$

Therefore,

$$D^* = \left(\frac{\sqrt{A} \sqrt{\Delta f}}{P_i} \right) \left(\frac{V_s}{V_n} \right)$$

The noise is also a function of the level of background radiation striking the detector surface. McIntire et al. have measured the dependence of noise upon background radiation at a chopping frequency of 90 cps for 3 Farnsworth cells. The results are presented in Figure 5-32.

These data indicate that the noise level is constant with background irradiance until about 2×10^{-3} effective watt/cm² are received at the detector from the background. The term effective implies an irradiance determined by considering only those photons which are energetic enough to cause electron transitions in the detector.

5.2.3.5. Relative Response. The relative response of lead telluride has the configuration shown in Figure 5-33. The response can, however, deviate radically from that shown in the figure. For example, if the sensitive films are very thin, the longer-wavelength photons will pass through the film without being absorbed and thereby cause the long-wavelength limit to occur at a wavelength shorter than 5.5μ . If the films are overoxidized, one finds a characteristic peak in the responsivity curve at about 1.5μ .

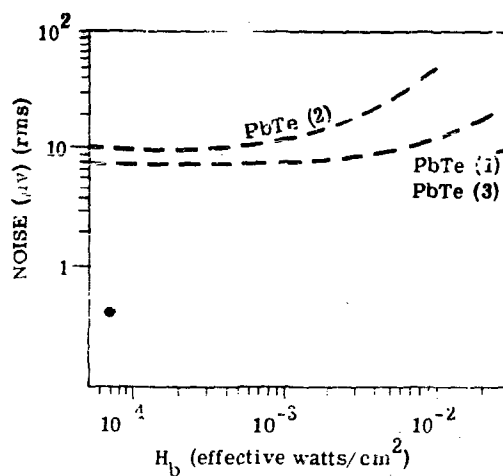


FIGURE 5-32. INFLUENCE OF BACKGROUND RADIATION ON DETECTOR NOISE IN PbTe

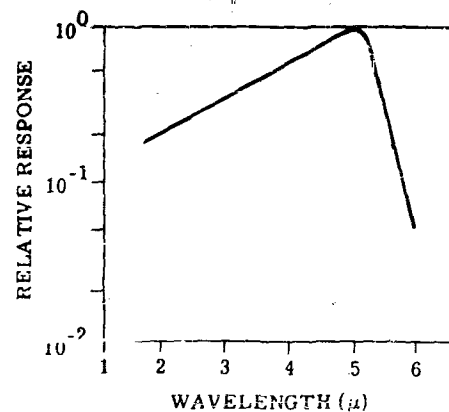


FIGURE 5-33. RELATIVE RESPONSE OF PbTe AT 77°K

5.2.3.6. Detectivity. Development of the PbTe cell was initiated by the Germans during the Second World War. In this country, Syracuse University, among others, began working on this material for infrared detection purposes around the latter part of 1949. This work continued for around ten years, and, during that time interval, several hundred cells have been constructed, tested, and reported by Syracuse. In the last eight years, the cell test facility, NOLC, has reported the characteristics of 28 PbTe detectors from various manufacturers. All of these latter cells are presented in Table 5-4. The manufacturer, report reference, and all the pertinent parameters are included. As indicated in the table, most of these data are quite old; consequently a statistical treatment of them would have little significance.

A statistical study of the data reported by Syracuse University since 1955 has been made. The study was carried out in a slightly different manner than in the cases of PbS and PbSe. Since Syracuse reported their data at two chopping frequencies (90 cps and 800 cps), a study was made for each frequency.

NEP (λ , 90 cps, 1) was plotted as a function of cell area (Figure 5-34). Each point represents a detector.

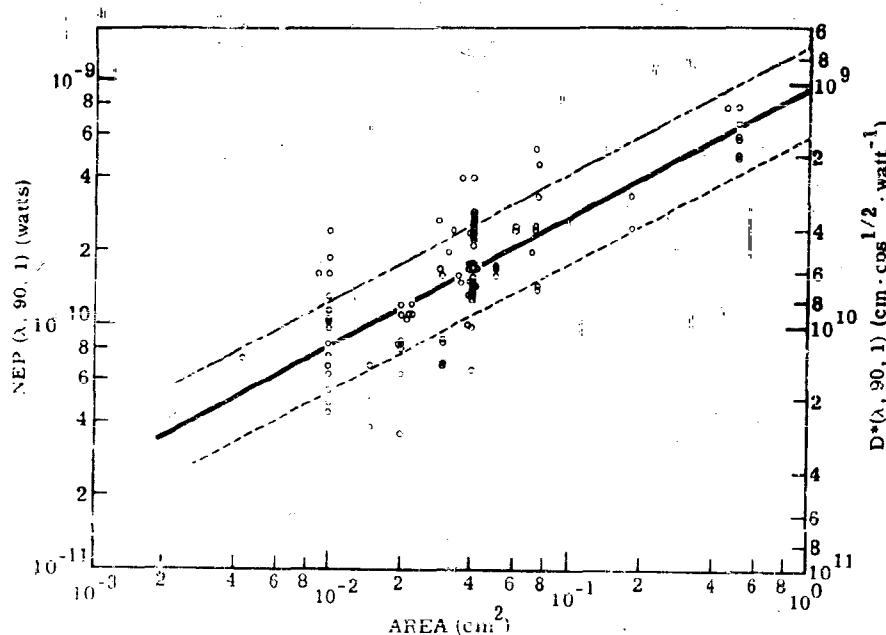


FIGURE 5-34. NEP VS. AREA FOR PbTe, $f = 90$ CPS

CONFIDENTIAL

[illegible]

1. The Naval Ordnance Department is the only one of the three which has a separate organization for the development of new weapons.

[illegible]

Four important parameters can be obtained from this chart. They are: the area dependence of the NEP, the latitude in cell area, the average value of D^* , and the best cell reported in that time interval. The area dependence of the NEP (λ_{pk} , 90 cps, 1) was determined by assuming the expression

$$NEP = KA^n$$

where K is a proportionality constant, n is the slope of the least square best fit line through the data points, and A is the cell area. The calculated value of n is 0.53 (Reference 5-51) for 30-cps chopping frequency, which is in good agreement with the assumed square-root relationship. At the 1-cm^2 equal-area line, the $D^*(\lambda_{pk}, 90, 1)$ scale was drawn so that one can see the average value of D^* by noting the intersection of the best-fit line with this axis. The dashed lines in Figure 5-34 are located one standard deviation from the best-fit line. The highest $D^*(\lambda_{pk}, 90, 1)$ value of the entire 83 cells is $4 \times 10^9 \text{ cm}^2 \text{ cps}^{1/2} \cdot \text{watt}^{-1}$.

The NEP's of most of the cells shown in Figure 5-34 were also determined for a 800-cps chopping frequency. These data are shown in Figure 5-35. The values of n ($n = 0.45$), average $D^*(\lambda_{pk}, 800, 1)$, standard deviation, and best D^* value are presented. Today's production $D^*(\lambda_{pk}, 900, 1)$ value is included along with the D^* value of a selected cell (Reference 5-14) for comparison. The theoretical limit is included to give some idea of the state of the art of PbTe.

Manufacturers of PbTe detectors are listed below.

U. S. Manufacturers

1. Electronics Corporation of America
2. ITT Laboratories
3. Minneapolis-Honeywell Regulator Company

Foreign Manufacturers

1. Societe Anonyme de Telecommunications
2. Mullard Electronics Products, Ltd.

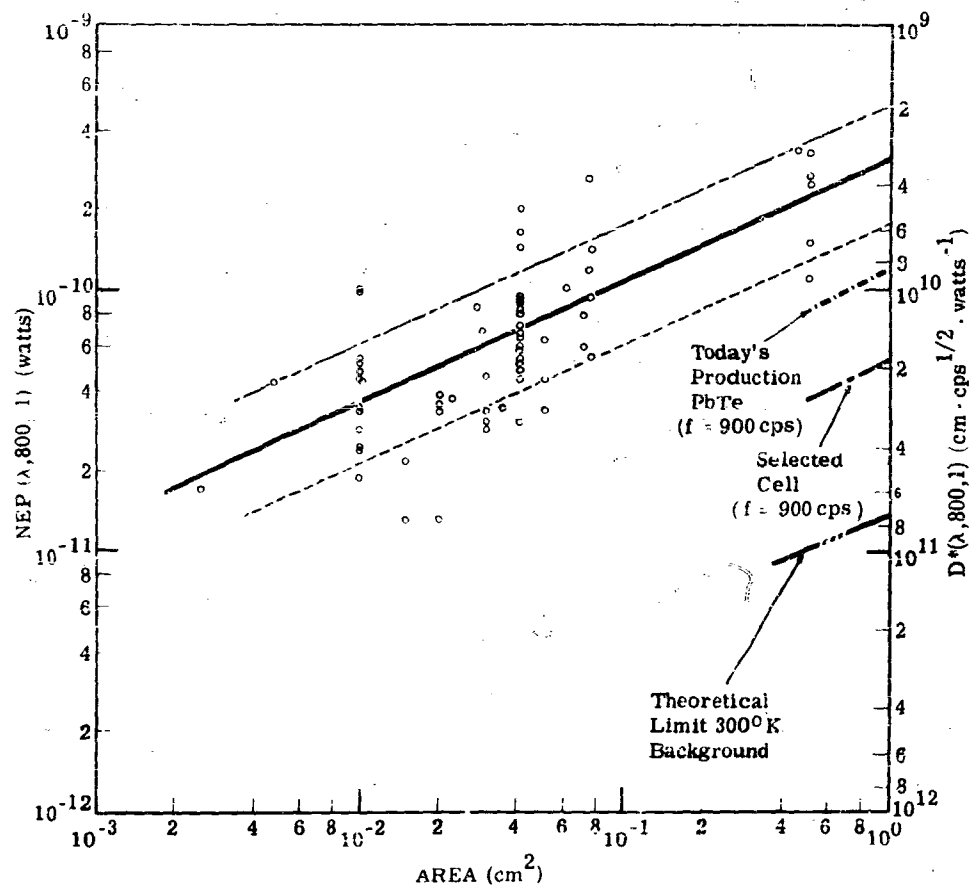


FIGURE 5-35. NEP VS. AREA FOR PbTe, $f = 800$ CPS

5.3 IMPURITY ACTIVATED GERMANIUM DETECTORS, by Henry Levinstein, Syracuse University

5.3.1. INTRODUCTION. Germanium is an element in group IV of the periodic table. It crystallizes in the diamond structure, each atom having 4 nearest neighbors. Since each atom has 4 valence electrons, covalent bonds are formed between each atom and its 4 nearest neighbors. The element was first studied extensively during World War II, when a germanium rectifier with high-peak inverse voltage was developed. Advances were made rapidly, since the element is not only chemically simple, but also because it appeared to have considerable practical value. Much of the early research was performed at Purdue University and at the Bell Telephone Laboratories.

The raw material is obtained from the flue dusts and slag of zinc and lead mining. It is first crudely refined, then converted to volatile GeCl_4 and fractionally distilled to separate other chlorides. The chloride is converted to pure GeO_2 by hydrolysis. GeO_2 is then reduced to Ge in a hydrogen furnace. Germanium so produced is further purified by zone refining, a technique whereby successive sections of a germanium bar are heated above the melting point. Impurities which prefer to remain in the melt are pushed to one extremity of the bar, the section which solidifies last. By removing this region and repeating the technique several times, impurities which may be detected by electrical measurements can be reduced to fewer than 1 in 10^{10} . Germanium so purified is polycrystalline. Single crystals may be obtained by the zone-leveling technique (Reference 5-52) or the Czochralski pulling technique (Reference 5-53).

The zone-leveling technique requires that a single-crystal seed be placed next to the polycrystalline bar. The region nearest the seed is then melted. By moving the source of heat slowly away from the seed, the molten zone solidifies, while adjoining regions begin to melt. As each region solidifies it becomes part of the single crystal which has its origin at the seed. In the pulling technique a single-crystal seed is immersed into the molten germanium very close to its freezing point. Upon slow withdrawal of the seed from the melt, germanium adhering to the seed forms a single crystal.

In its purest form, germanium is intrinsic at room temperature and has a resistivity of 47 ohm-cm at 25°C. Charge carriers are electrons in the conduction band and holes in the valence band. These are produced when lattice vibrations free an electron from the Ge-Ge bond, leaving behind a positive hole which acts as a carrier. Alternatively, free holes and electrons may be produced when incident photons of appropriate energy interact with the crystal. Figure 5-39 (References 5-54 and 5-55) shows the absorption spectrum of germanium when electrons are excited across the gap between valence and conduction bands. Shockley and Hall (Reference 5-56) showed that the temperature dependence of absorption could be explained by the existence of indirect transitions (direct and indirect transitions are different types of optical transition).

is one in which energy and momentum are conserved between electron and absorbed photon; and indirect (nonvertical) transition is defined as one in which an electron absorbs a photon and undergoes a change in its k vector, momentum being conserved by the absorption or emission of a phonon by interaction with the lattice. The high-absorption region to point A in Figure 5-36 is due to direct transitions; the absorption region between points A and B is due to indirect transitions.

In addition to the fundamental absorption, photons may be absorbed in p-type material by the transitions or holes between various bands composing the valence band (References 5-57 and 5-58). The top of the valence band consists of 2 bands, degenerate at $k = 0$ (k = electron wavenumber vector), with a third band split off by spin orbit coupling. Figure 5-37 (Reference 5-59 to 5-61) shows the absorption spectra of a typical p-type Ge sample at several temperatures. The absorption bands in the 4- μ regions arise from transitions between bands 1 and 2 and the third band. The band starting at 10 μ arises from transitions between the upper two bands.

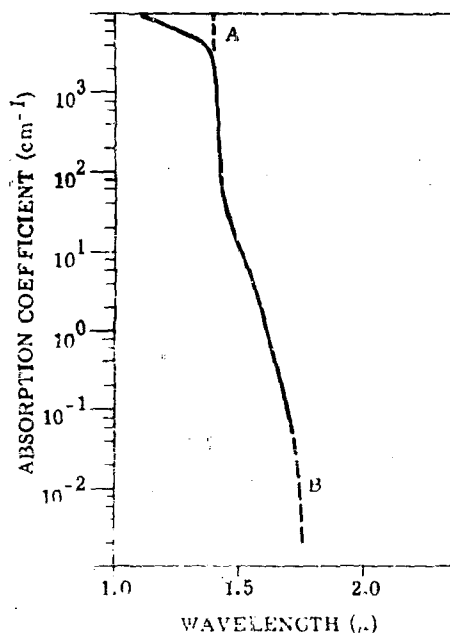


FIGURE 5-36. ABSORPTION SPECTRUM IN PURE Ge

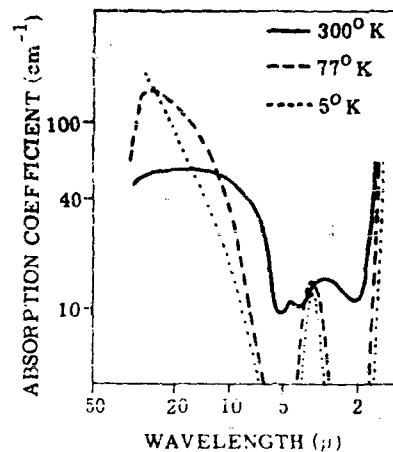


FIGURE 5-37. ABSORPTION COEFFICIENT IN In-DOPED p-TYPE Ge

Photons may be absorbed not only by electrons and holes, but they may also be absorbed by the crystal lattice. This leads to the absorption spectrum shown in Figure 5-38 (References 5-62 and 5-63).

The addition of impurities to Ge produces a drastic change in electrical properties. The addition of group V impurities (Sb, As, etc.) leads to n-type conductivity; the addition of group III impurities to p-type conductivity. When a group V impurity is added, an element with 5 valence electrons replaces Ge at a regular lattice position. Four of the 5 electrons form covalent bonds with adjoining Ge atoms. The fifth electron moves in a Bohr-like orbit, bound to the impurity element by the excess charge of its nucleus. A group III impurity when substituted for a Ge atom is able to complete only 3 of the 4 covalent bonds demanded by the Ge lattice. The fourth bond is completed by an electron from a nearby Ge atom. This leaves a positive hole bound to the impurity, moving in a Bohr-like orbit about the impurity. The energy to free the hole from the group III impurity or the electron from the group V impurity is given by an expression similar to that used in the calculation of the ionization potential of the hydrogen atom:

$$E = \frac{2\pi^2 m^* e^4}{h^2 K^2}$$

where m^* is the effective mass of electron or hole, e is the electronic charge, h is Planck's constant, and K is the dielectric constant of Ge (16.1). E turns out to be about 0.01 ev, a value in good agreement with experimental results (Reference 5-64). In view of this small activation energy, group III and group V impurities are completely ionized at room temperature. Electrons and holes are bound to their impurities only in the liquid-helium temperature region.

The use of Ge with impurities as an infrared detector was first suggested by Burstein (Reference 5-65). While the energy required to free holes and electrons from a covalent bond is about 0.75 ev and leads to a response to only 1.8μ , the response obtained by freeing charge carriers from group III or group V impurities would be expected to give a response to about 120μ . Because of the extremely low temperature required to prevent ionization of these impurities by lattice vibrations, a search has been conducted for impurities with greater activation energies. The effect of gold in Ge was reported by Dunlap (References 5-66 to 5-68) as well as Morton, Hahn, and Schultz (Reference 5-69). Because of the success achieved with gold-doped germanium, detectors have been constructed with many other impurities. Figure 5-39 shows a summary of the energy levels of various impurities in germanium.

For a review article on impurities in Ge see Reference 5-70.

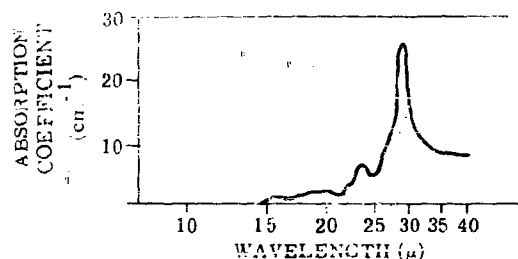


FIGURE 5-38. LATTICE ABSORPTION IN Ge

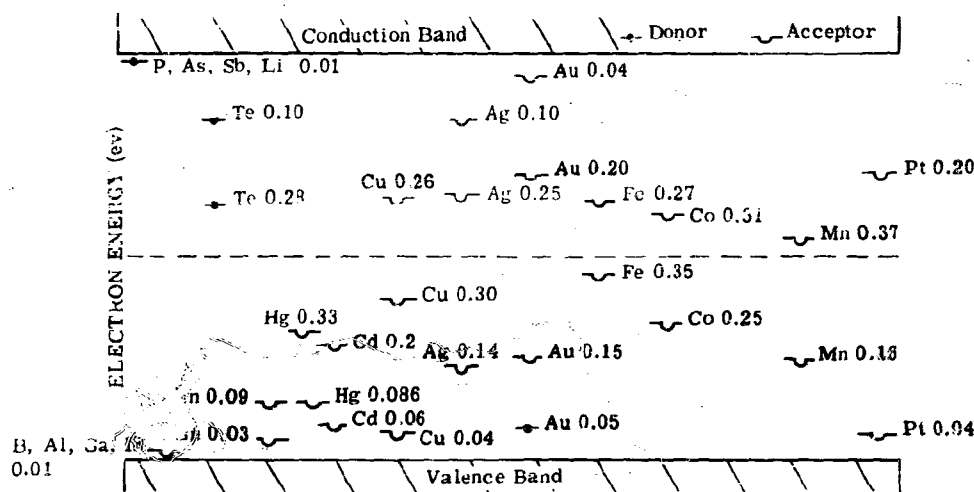


FIGURE 5-39. ENERGY LEVEL DIAGRAM FOR IMPURITY ATOMS IN Ge

Of particular interest are impurities with energy levels of about 0.1 ev or less; since detectors constructed from these materials have a long wavelength response extending through the 9- to 13- μ atmospheric window where no intrinsic detector material is currently available. Detectors have now been constructed from Ge:Zn, Ge:Cu, Ge:Cd, and Ge:Hg, in addition to Ge:Au.

5.3.2. PHYSICAL PARAMETERS OF IMPURITY-ACTIVATED GERMANIUM DETECTORS. In its application, a Ge-impurity detector is placed in a circuit containing also a load resistance and a bias battery. When photons with energy sufficient to free charge carriers (either electrons or holes) from

the impurities are incident upon the material, the resistance of the photoconductor decreases and the voltage across the load resistor increases. After the radiation is removed, the resistance of the photoconductor begins to increase again and reaches its original value when all the charge carriers have been captured by recombination centers, the same or similar impurities from which they were originally excited. The general physical principals governing the behavior of Ge detectors with various impurities are similar; only specific details are different and depend upon the type of impurity used.

5.3.2.1. Spectral Response. The spectral response consists of two regions. The region of intrinsic response with a peak at 1.5μ and a threshold at 1.8μ is the same for all germanium detectors. The long-wavelength response to 6μ for the Ge:AuII detector, to 9μ for the Ge:AuI, to 14μ for the Ge:Hg detector, to 15μ for Ge:ZnII, to 22μ for Ge:Cd, to 30μ for Ge:Cu, and 40μ for Ge:ZnI is characteristic of the type of impurity used and the particular energy level of the impurity from which charge carriers are excited. The relative magnitudes of the peaks of intrinsic and impurity response depend on the detector preparation and construction. In certain applications, the intrinsic peak is suppressed; in others, it is merely adjusted to the desired magnitude relative to the peak in the impurity response.

5.3.2.2. Time Constant. The time constant of the detectors in the impurity response region is given by

$$\tau = 1/N_D \Sigma u$$

where N_D represents the density of recombination centers, Σ their capture cross section, and u the thermal velocity of the charge carriers. Only N_D may be varied during the manufacture of the detector. Σ and its temperature dependence are characteristic of the particular type of impurity used. Time constants less than $1 \mu\text{sec}$ are always obtained from Ge:AuI, Ge:Zn, and Ge:Cu detectors. Ge:AuII ($6\text{-}\mu$) detectors have been constructed with time constants varying between $20 \mu\text{sec}$ and 2msec . In the intrinsic region, time constants depend on the length of time it takes for holes and electrons to recombine, either directly or by way of recombination centers. Since much of the intrinsic radiation is absorbed on the surface, the treatment of the surface plays an important role. Values varying from several μsec to several hundred μsec have been observed. Since the intrinsic response is generally suppressed, no great emphasis need be placed on these time constants.

5.3.2.3. Signal. The voltage change, V_s , produced when the detector with resistance r_C is connected in series with bias battery E and the load resistor r_L and is exposed to radiation, is given by:

$$V_s = \frac{E r_C r_L}{(r_C + r_L)^2} \frac{\Delta R_c}{R_c} = \frac{E r_C r_L}{(r_C + r_L)^2} \frac{\Delta N}{N} \quad (5-1)$$

where ΔR_C is the change in detector resistance, and ΔN the change in the number of free charge carriers produced by the action of the radiation. $\Delta R = G\tau$, where G is the rate at which charge carriers are freed by the radiation and τ represents the time they remain free. N , the number of charge carriers where no signal radiation is incident on the detector, is composed of two components: N_{TH} , the charge carriers which have been freed by vibrations of the crystal lattice, and N_B , those charge carriers freed by background radiation. Under ideal operating conditions, N_{TH} should be considerably smaller than N_B . This is accomplished by cooling the detector. The coolant temperature should be such that $kT \ll E_i$, the impurity activation energy. In general, it has been found that kT should be less than $1/30$ of the activation energy (k represents the Boltzmann constant — 1.38×10^{-23} joules/ $^{\circ}\text{K}$). N_B , the number of charge carriers produced by background radiation, is determined by the amount and temperature of the background. N_B may be most conveniently reduced by surrounding the photoconductive element by a cooled radiation shield whose aperture is determined by the field of view required in the application of the detector. It must be noted, however, that a reduction in N_B frequently requires further cooling of the detector if the condition $N_{TH} \ll N_B$ is to be satisfied.

When the radiation incident on the detector is modulated sinusoidally, the signal voltage varies as

$$\frac{1}{\sqrt{1 + \omega^2 \tau^2}}$$

For detectors with time constants of the order of 10^{-8} second, modulating frequencies to 1 mc produce no variation in signal. In general, the distributed capacitance of the detector and associated circuits cannot be reduced below $20 \mu\text{fd}$. Thus if full use is to be made of the short detector time constant, load resistors below 1000 ohms must be used. As may be seen from Equation 5-1, such a low value requires that the bias supply voltage E must be made larger if the signal is not to be so small that it is masked by the noise inherent in the succeeding amplifier. In general, the signal varies linearly with applied bias voltage. The maximum value of E which may be applied across the detector depends upon its construction and the type and quality of contacts which are made to the sensitive element. Maximum bias currents are specified for each detector. Values larger than 100 amp are found only in the best detectors and are not common. When the maximum specified current value is exceeded, the detector noise increases superlinearly without, however, damaging the detector. A reduction in bias current to its maximum permissible value restores the original characteristics of the detector.

5.3.2.4. Detector Noise. The noise spectrum of a typical detector is shown in Figure 5-40. It has two components: $1/f$ noise and noise due to fluctuations in generation and recombination of charge carriers (Reference 5-71). As the name implies, $1/f$ noise is a noise whose power varies inversely

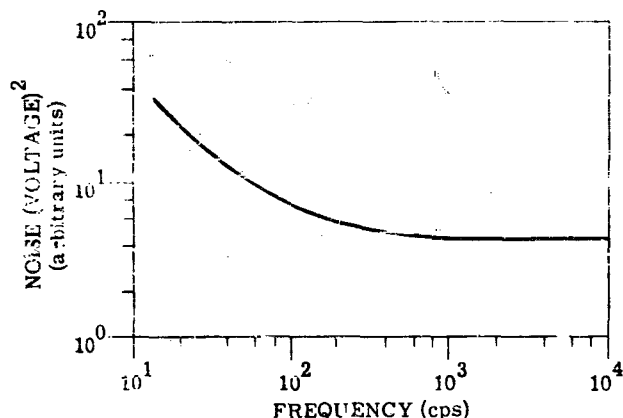


FIGURE 5-40. NOISE SPECTRUM OF p-TYPE Au-DOPED Ge
AT 77°K.

with frequency; it is predominant at low frequencies. It is not an inherent property of the detector material but depends on the techniques which are used in the construction of the contacts and the surface of the detector (Reference 5-72). In certain well-constructed detectors, the $1/f$ noise spectrum can usually be made negligible above 100 cps. Noise due to fluctuations in charge-carrier generation and to the recombination rate is important from 100 cps to where Johnson noise becomes dominant.

5.3.2.5. Detectivity. Since both signal and noise have the same frequency dependence in the region where $1/f$ noise is negligible, D^* is frequency invariant. Since, furthermore, the bias voltage enters in the same manner in both equations, the detectivity is generally constant until the optimum bias voltage has been exceeded. Above that point, the detectivity decreases rapidly with increasing bias voltage, since signal increases sublinearly and noise superlinearly. Under ideal conditions the detector is operated at a temperature where it is background-limited. If it is assumed that one charge carrier is liberated by each photon incident on the detector, both the detectivity when the detector is exposed to blackbody radiation and also the detectivity at spectral peak may be calculated. The detectivity $D^*(T)$ for a blackbody at temperature T is found by substituting Equations 5-1 and 3-50 in the defining equation for D^*

$$D^* = \frac{S}{N} (\Delta f)^{1/2} A^{-1/2} H_s^{-1}$$

where Δf is the bandwidth of the amplifying system, A the detector area, and H_s the incident power.

One can then obtain

$$D^*(T) = Q_B^{-1/2} Q_S / 2H_S$$

where Q_S represents the signal photon flux and Q_B the background photon flux. Since at a particular wavelength,

$$H_S = Q_S hc / \lambda$$

where h is Planck's constant and c is the velocity of light,

$$D^*_\lambda = Q_B^{-1/2} (2hc/\lambda) \cdot 1$$

Figure 5-41 shows the variation of D^* at spectral peak for photoconductive detectors as a function of long-wavelength threshold of the detector, if a 300°K background at a 180° angular field of view is assumed.⁴ The variation of detectivity with angular field of view is given in Figure 5-42.

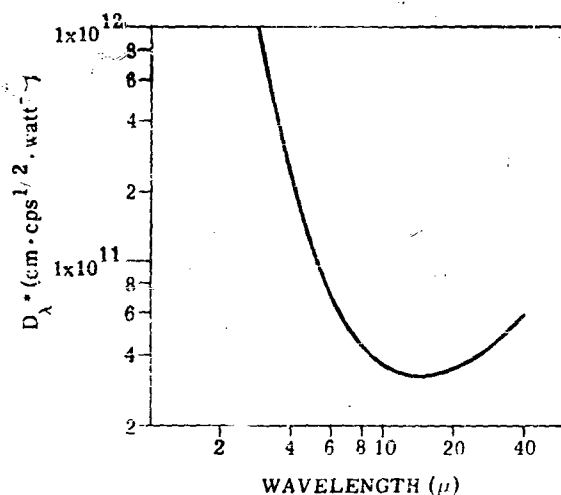


FIGURE 5-41. PEAK D^*_λ VS. LONG-WAVELENGTH CUT-OFF FOR BACKGROUND-LIMITED DETECTORS. Field of view = 180° ; background temperature = 300°K .

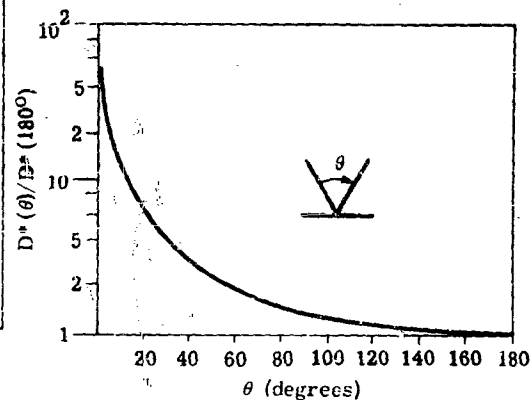


FIGURE 5-42. VARIATION OF D^* WITH ACCEPTANCE ANGLE

⁴ For a detailed discussion see Reference 5-73.

5.3.3. DETECTOR CONSTRUCTION. All presently available impurity-activated detectors require cooling. The detector envelope is therefore designed to permit the use of liquid nitrogen or a mini-cooler for detectors with a spectral response extending to 9 μ , and liquid hydrogen or helium for longer-wavelength detectors. A single dewar construction is generally sufficient for detectors cooled to liquid-nitrogen temperature. The dewar is constructed from either glass or metal. The type of window is determined by the spectral response of the sensitive material. The window is either fused or soldered to the cell envelope for best results. The Ge sample is generally cut from a large single crystal to which the desired impurity is added during the crystal-growing process. In certain cases, pure Ge is cut into sections of the desired dimension and the impurity is then diffused into the Ge section. Sections as large as 5 x 5 x 5 mm and as small as 0.2 x 1 x 1 mm have been used as sensitive elements for detectors. These sections are generally mounted in an integration chamber which serves a dual purpose. It limits the amount of background radiation which the sensitive element "sees," and it serves to reflect onto the sample radiation which has not been absorbed during the initial passage through the sample. The integration chamber is attached directly to the chamber containing the coolant. Thus the sensitive element and the integration chamber reach the temperature of the coolant.

Two leads are generally provided. In the case of metal envelopes, the envelope may replace one of the leads. The detectors are evacuated to pressures of less than 10^{-6} mm of mercury and gettered where necessary. Figures 5-43 and 5-44 show several particular types of detector construction. Modifications in size and shape of the detector envelope are possible and depend upon the particular application and the method for cooling. Dewar dimensions vary from 1 x 1/2 inch to 5 x 2 inches and larger. Double dewars as large as 5 x 20 inches have been constructed. The area of the sensitive element is determined by the size of the Ge sample and the size of the aperture in the radiation shield. Areas as small as 0.002 cm² and as large as 1 cm² have been prepared. Extremes in detector areas, either very large or very small, lead to detectors whose D^* is generally not as high as medium values of area (such as 0.04 cm²).

5.3.4. DETECTOR CHARACTERISTICS: Ge:Au^b

5.3.4.1. General. Ge:Au detectors are available in two forms, depending on which energy level of Au in Ge is used. When Au is the only major impurity in Ge, holes which are bound to the Au atoms at sufficiently low temperatures may be freed by incident photons with a resulting increase in conductivity. The photon energy required is 0.14 eV, resulting in a detector with a long wavelength threshold

^b For a detailed discussion of the effect of Au in Ge see Reference 5-55.

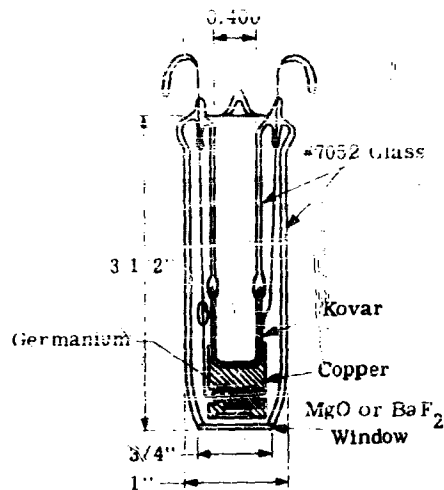


FIGURE 5-43. Ge DETECTOR ASSEMBLY

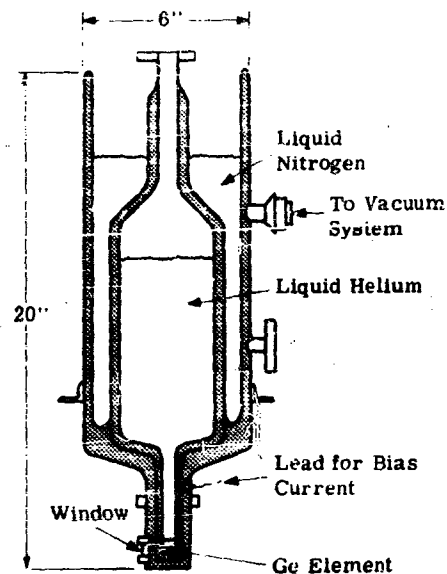


FIGURE 5-44. DOUBLE DEWAR FLASK

at 9μ . When an electron donor impurity such as Sb is added to the Ge which already contains Au, electrons from the donor atoms will neutralize the positive holes until, when Sb and Au concentrations are equal, all holes are neutralized, and the photoconductivity to 9μ disappears. Further addition of Sb provides an additional electron for each Au atom. The energy required to free this electron is 0.2 ev, leading to a detector with a long-wavelength threshold at 6μ .

5.3.4.2. The 6μ Ge:Au Detector (n-type Ge:Au). The spectral response of this detector is shown in Figures 5-45 and 5-46. It is composed of three regions: the response below 1.8μ is the response of pure Ge; the response beyond 2.5μ is due to electron excitation from the 0.2-ev gold level; and the response between 1.8 and 2.5μ is due to the excitation of holes and electrons from the various Au energy levels. The total response curve has a peak in the intrinsic region at 1.5μ , and no pronounced secondary peak. The speed of response depends on the wavelength of the incident radiation. From 2.5μ to the spectral cutoff, average detectors have time constants on the order of $50\mu\text{sec}$. However, time constants as long as 1 msec have been observed in some detectors. These time constants are temperature-sensitive, decreasing as the temperature rises above 78°K . Figure 5-47 shows the variation of time constants with temperature for several detectors. Between 1.8μ and 2.5μ no definite time constant may be defined. In that region, various transitions of charge carriers between energy

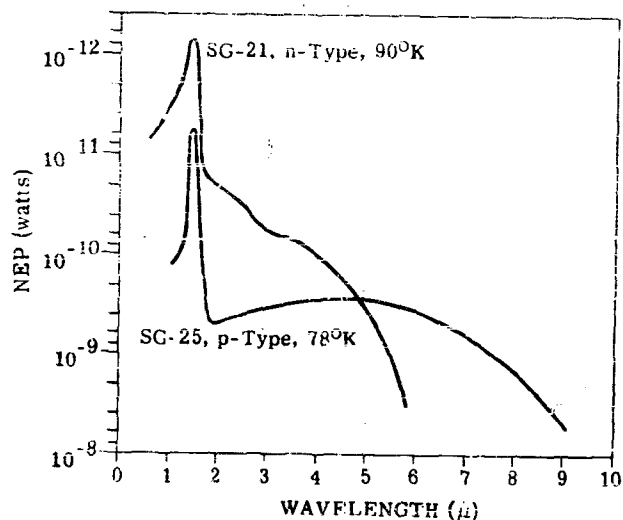


FIGURE 5-45. SPECTRAL RESPONSE OF n- AND p-TYPE Au-DOPED Ge

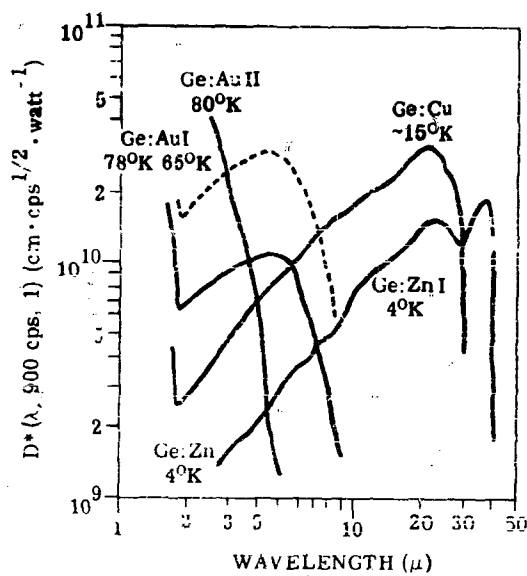


FIGURE 5-46. ABSOLUTE SPECTRAL RESPONSE OF Cu, ZnI, AuI, AND AuII Ge DETECTORS

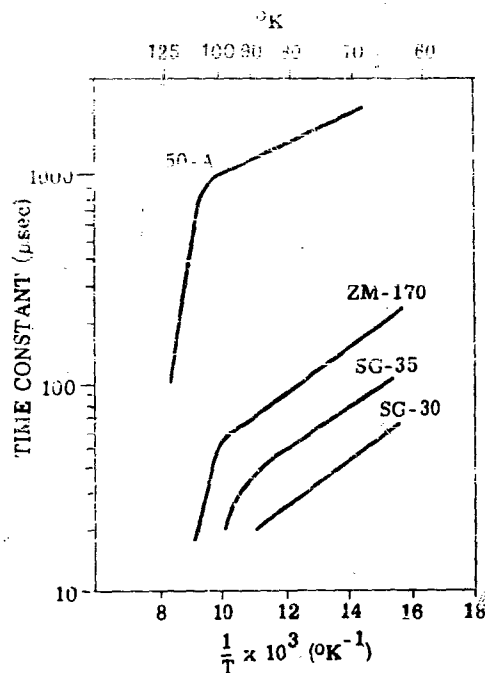


FIGURE 5-47. TIME CONSTANT VS. TEMPERATURE
OF n-TYPE Ge

levels and conduction and valence bands lead to quenching phenomena. The response time of the detector depends on the intensity of the incident signal, and, under certain conditions, illumination of the detector may lead to an increase instead of a decrease in resistance. If these effects are objectionable in actual use, the detector should be provided with a filter which eliminates the spectral region below 2.5μ . It is because of these effects that these detectors are more suitable for qualitative rather than quantitative work. Values of D^* (500, 900, 1 cps) are in the vicinity of 2×10^9 $\text{cm} \cdot \text{cps}^{1/2} \cdot \text{watt}^{-1}$. A histogram of the D^* values of a number of detectors is given in Figure 5-48. The detector is characterized by extremely large signal and noise values at operating bias currents, and is therefore useful in devices whose noise cannot be reduced sufficiently to allow use of detectors which have greater D^* but lower signal and noise voltages. Signal and noise variations with frequency for a typical detector are shown in Figure 5-49. Beyond 500 cps both signal and noise have the same frequency dependence. D^* thus stays constant with increasing frequency. Below about 500 cps, 1 noise becomes increasingly pronounced, while the signal changes only slightly. D^* thus decreases

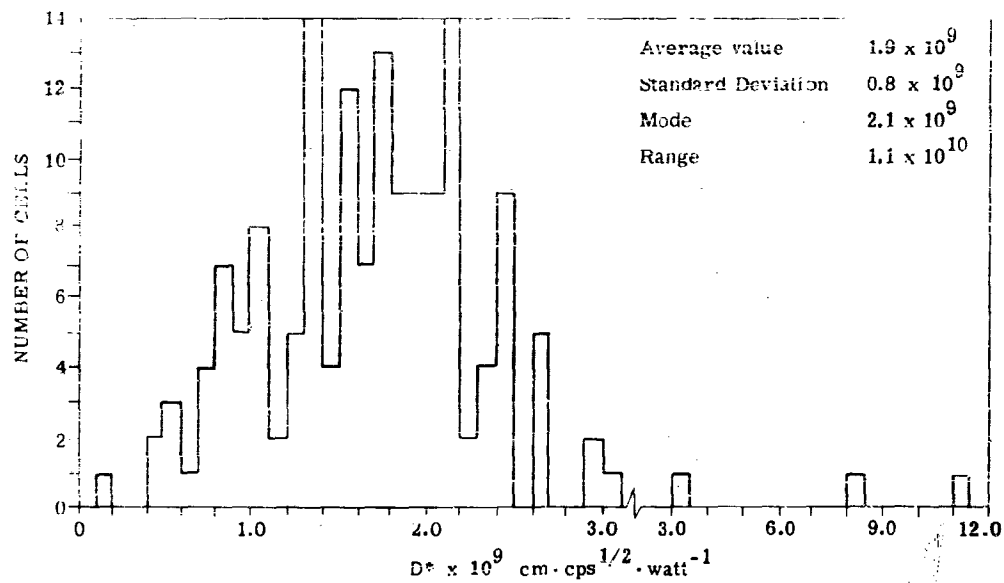


FIGURE 5-48. HISTOGRAM OF D^* VALUES FOR n-TYPE Ge:As

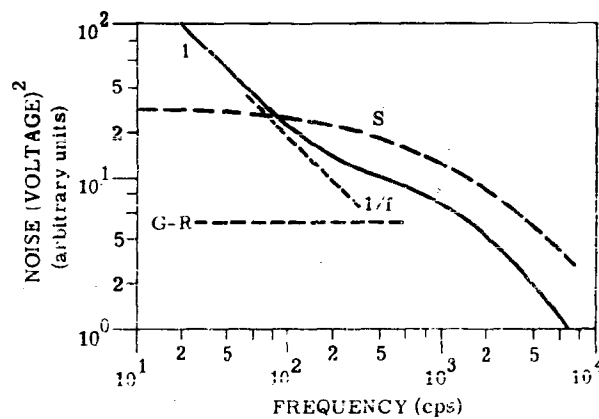


FIGURE 5-49. SIGNAL AND NOISE VARIATION WITH FREQUENCY FOR AN n-TYPE Au,Sb-DOPED Ge DETECTOR AT 90°K

for lower frequencies. Detector resistances vary between 1 and 40 megohms, depending on the dimensions and preparation of the sample and the amount of background radiation the sensitive element "sees". Parameters of D^* , resistance, time constant, etc., which have been reported in the literature are listed in Table 5-5. The detectors are provided with a sapphire window, although coated silicon windows are available. The Ge sample is prepared by adding both gold and antimony during the crystal growth process. Crystals are then cut into slices of the desired dimension and mounted in a dewar envelope. Contacts are soldered to the sample wire before or after mounting. The sensitive element is frequently embedded in sulfur to improve its stability. The dewar is evacuated to a pressure lower than 10^{-6} mm of Hg. A low pressure is desirable to prevent frosting of the detector window and to permit longer storage of the coolant. It is not essential for the actual operation of the detector element, and no loss in sensitivity is experienced when the element is exposed to atmospheric pressure and then re-evacuated. The only supplier for this type of detector is the Philco Corporation.

5.3.4.3. The 9- μ Ge: Au Detector (p-type Ge: Au). In contrast to the 8- μ Ge: Au detector, the 9- μ detector has well-behaved characteristics. The spectral response is shown in Figures 5-45 and 5-46. It consists of the intrinsic response extending to 1.8- μ (characteristic of pure germanium) superimposed on the response due to excitation of holes from the gold centers. This response has a peak in the vicinity of 5 μ . Time constants in the spectral region beyond 1.8 μ are less than 0.1 μ sec, as may be seen from the expression

$$\tau = \frac{1}{n\Sigma u}$$

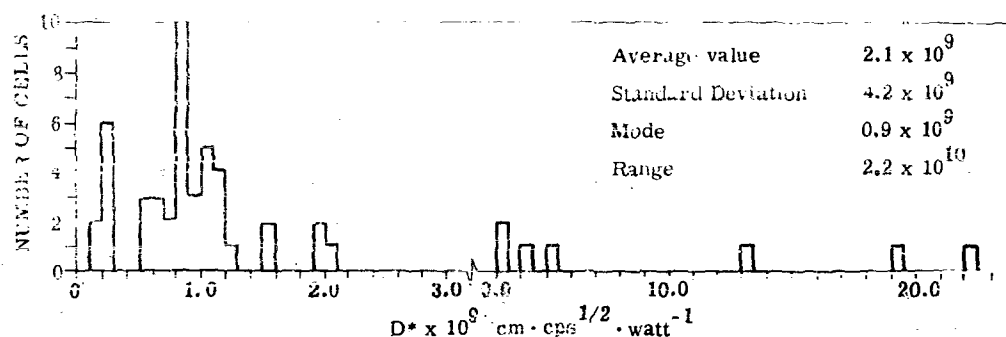
where n is the density of centers which capture charge carriers, Σ is the capture cross section of these centers, and u is the thermal velocity of the charge carriers. $u \approx 10^7$ cm/sec, Σ , unusually large in this case, is 10^{-13} cm². n is generally larger than 10^{13} centers/cc. This gives a value of $\tau \approx 0.1$ μ sec. Since it is not practical to reduce n below 10^{13} centers/cc, no larger value of τ may be contemplated. τ can, of course, be reduced by increasing the number of capturing centers, a matter which can be accomplished during the crystal growth process by the addition of Sb, whose donor electrons, when trapped by Au atoms, act to capture free holes. The Sb concentration, however, is generally held considerably lower than that of Au (1/10 or less).

The 9- μ Ge: Au detectors are generally operated at 78°K because of the ready availability of liquid nitrogen. At that temperature the average detectivity is 3×10^9 cm · cps^{1/2} · watt⁻¹. Detectors with values of D^* ranging between 10^9 and 6×10^{10} are commercially available. A histogram of the D^* values of a number of detectors is given in Figure 5-5C. If the detector is cooled to 60°K, the

TABLE 5-5. Au-DOPED Ge (n-TYPE)

Mfr.	Date of Production	Cell Temp. (°C)	Area (mm ²)	Current (μa)	Dark Resistance (m-ohms)	Blackbody Response		Time Constant (μsec)	Ch. Appl. Frequency (cps)	N
						NEP (watts)	10 ⁸ cm-cps (μa)			
Sylvania	8-55	-196	13.3	4.0	5.6	8.4×10^{-10}	3.1×10^8		90	2
Sylvania	12-55	-196	10.1	1.3	28.0	4.5×10^{-10}	7.9×10^8		90	2
Philco	12-57	-196	6.0	1.0	11.0	2.1×10^{-10}	9.0×10^8	1900	90	2
Philco	11-59	-195	12.3	1.2	4.6	2.2×10^{-10}	1.5×10^9	50	90	2
Philco	3-59	-195	1.3	0.8	19.0	1.6×10^{-10}	2.3×10^9	441	90	2
Sylvania	3-58	-196	11.2	4.5	15.1	4.0×10^{-11}	9.4×10^9		90	2
Philco	1-58	-195	9.3	1.0	9.1	2.0×10^{-10}	1.7×10^9	20	800	1:1

1. Inform Report on Infrared Detectors, Report Number 102-8, Syracuse University, Syracuse, N. Y., October 1955 (UNCLASSIFIED).
2. Inform Report on Infrared Detectors, Report Number 102-9, Syracuse University, Syracuse, N. Y., January 1956 (UNCLASSIFIED).
3. Inform Report on Infrared Detectors, Report Number 103-5, Syracuse University, Syracuse, N. Y., December 1957 (UNCLASSIFIED).
4. Properties of Photodetectors, NOLC Report Number 525, Naval Ordnance Laboratory, Corona, Calif., August 1960 (CONFIDENTIAL).
5. Properties of Photodetectors, NOLC Report Number 497, Naval Ordnance Laboratory, Corona, Calif., June 1960 (CONFIDENTIAL).
6. W. J. Siegen, P. R. Bratt, H. W. Davis, L. F. Johnson, H. L. Lammstein, and A. C. MacFarlane, Cooled Infrared Detectors, *Proc. IRE*, March 1959, Vol. 3, No. 1, p. 20 (UNCLASSIFIED).
7. Summary Report on Detector Development, Report Number 2140-01, Philco Corp., Philadelphia, Pa., September 1958 (UNCLASSIFIED).

FIGURE 5-50. HISTOGRAM OF D^* VALUES FOR p-TYPE Ge: Au

temperature at which it becomes background-limited, D^* may increase by as much as a factor of 4 over the value at 78°K . Since the shape of the spectral response is identical for all detectors of this type, the ratio of D^* , the detectivity at the $5\text{-}\mu$ spectral peak, to D^* (500°K), the blackbody detectivity, is identical for all these detectors. It is approximately 2.7. Large variations of D^* with temperature in the vicinity of its operating temperature (78°K) (Figure 5-51) require that special caution be exercised in the construction of the detector in order to reduce fluctuations in D^* with variations in coolant temperature. Thus unless the thermal capacity of the detector mounting is sufficiently large, fluctuations in coolant temperatures, such as are produced by the bubbling of liquid nitrogen, will produce undesirable fluctuations in detector resistance and lead to noise.

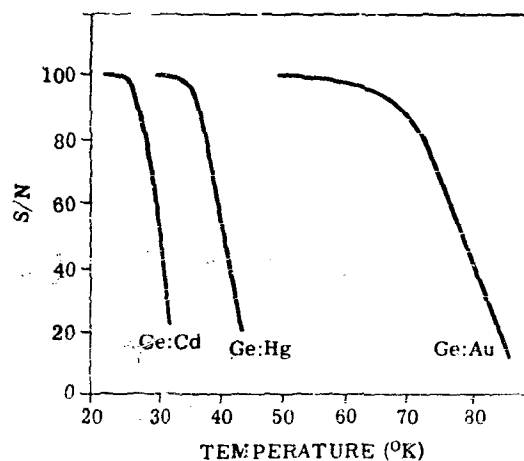


FIGURE 5-51. S/N RATIO VS. TEMPERATURE FOR Ge: Cd, Ge: Hg, AND Ge: Au DETECTORS

Because of the short time constant, the detector signal is frequency-invariant to at least 1 mc. Noise has $1/f$ and G-R noise components. Since for a well-constructed detector $1/f$ noise is negligible above 100 cps, D^* is essentially frequency-invariant above 100 cps. Both signal and noise voltages vary linearly with bias current until the designated maximum current is reached. For well-constructed detectors, this value may be as high as 100 amp. Values of the resistance, depending on sensitive-element dimensions, coolant temperature, and single-crystal preparation vary from 0.1 to 5 megohms. Parameters of D^* , resistance, time constant, etc., which have been reported in the literature, are listed in Table 5-6. Sensitive elements are mounted in an integration chamber whose aperture determines the detector size. In contrast to background limited detectors, Ge: Au (p), when operated at 78°K , shows only small increase in D^* as the angular field of view is narrowed.

Detectors mounted in various shapes and types of dewars are available from Philco, RCA, Westinghouse, Raytheon, and SBRC.

5.3.5. DETECTOR CHARACTERISTICS. Ge:Zn (References 5-74 and 5-75)

5.3.5.1. General. When zinc is added to Ge during crystal growth, holes may be excited from the 0.03-ev level to the valence band. This leads to a photoconductive response with a long-wavelength threshold at 40μ . Cooling to at least 10°K is required to produce optimum detectivity. If during crystal growth donor atoms such as antimony are added to the melt, electrons from these donor atoms will neutralize all holes if the number of donor atoms is exactly equal to the number of zinc atoms in the crystal. Holes may then be excited from a 0.09-ev level to the valence band. This detector has a spectral response extending to about 15μ and may be operated at temperatures in the vicinity of 40°K . While the 49μ detector (Ge:ZnI) has been produced and is at present in use in several systems, the 15μ Ge:ZnII detector is still in the experimental stage.

5.3.5.2. Ge:ZnI (40μ) Detector. Figure 5-46 shows the spectral response of the Ge:ZnI (ZIP) detector currently available. A histogram of the D^* values of a number of detectors is given in Figure 5-52. This particular detector has a 60° angular field of view. Peak response occurs at 36μ . The structure in the spectral curve beyond 14μ is due to absorption of photons by the crystal lattice. Measurements of the detector time constants indicate values less than $0.1\mu\text{sec}$. Thus the signal is frequency-independent in the useful operating range of the detector if precautions are taken to reduce circuit time constants. Detector noise is predominantly of the $1/f$ type up to 1000 cps. The detector can therefore be operated to great advantage at chopping frequencies beyond 1000 cps. The detector has nonlinear resistance characteristics when a bias voltage is applied. An average

CONFIDENTIAL

TABLE 5-6. AU-DOPED Ge (p-TYPE)

Mtr	Date of Production	Ce. Temp. (°C)	Area (mm ²)	Current (μA)	Dark Resistance (megohms)	Blackbody Response NEP (cm ⁻² sec ^{-1/2} W ^{-1/2})	Spectral Peak NEP (cm ⁻² sec ^{-1/2} W ^{-1/2})	Time Constant (μsec)	Operating Frequency (Hz)	Number of Cells	View Angle (°K)	Source
Syracuse	11-54	-156	18.3	18.3	3.1	1.1×10^{-8}		<1	90	5		1
Syracuse	8-54	-156	27.5	8.7	3.8	4.9×10^{-10}		<1	90	5		2
Syracuse	2-55	-156	33.5	7.0	7.0	3.4×10^{-10}		<1	90	4		3
Syracuse	5-54	-156	5.0	8.0	2.8	5.0×10^{-10}		<1	90	4		4
Syracuse	8-55	184	21.4	9.0	8.2	6.2×10^{-10}			90	5		5
Syracuse	12-55	186	8.4	37.0	0.7	3.3×10^{-10}			91	1		6
Syracuse	1-56	154	7.2	31.0	1.0	2.1×10^{-10}			91	1		7
Syracuse	5-59	191	3.4	60.0	0.2	6.0×10^{-11}		<1	90	1		8
Syracuse	3-58	189	4.0	29.0	1.6	1.0×10^{-11}		<1	96	1		9
Philco	2-55	-191	20.3	75.0	0.5	5.1×10^{-10}		<1	90	2		1
Philco	1-58	184	2.3				3×10^{-11}		750	1		10
PCA	2-56	191	5.0	3.3	4.7	8.3×10^{-10}		10	80	2		7
PCA	1-60	238	18.9	7.7	6.9	3.4×10^{-9}			90	1		11
Westinghouse	11-58	191	4.0	30.0	1.7	2.0×10^{-11}		<1	100	1	150	12
Westinghouse	12-57	191	4.0	60.0	1.0	8.0×10^{-11}		<1	90	1		13
Philco	1-58	191	1.8	2.5	5.0	1.7×10^{-10}		<1	90	1		14
SORC	5-58	-126	4.3	46.0	0.3	1.9×10^{-10}		<1	90	1		15

1. Interim Report on Infrared Detectors, Report Number 102-5, Syracuse University, Syracuse, N. Y., January 1955 (UNCLASSIFIED).

2. Interim Report on Infrared Detectors, Report Number 102-4, Syracuse University, Syracuse, N. Y., October 1954 (UNCLASSIFIED).

3. Interim Report on Infrared Detectors, Report Number 102-3, Syracuse University, Syracuse, N. Y., April 1955 (UNCLASSIFIED).

4. Interim Report on Infrared Detectors, Report Number 102-2, Syracuse University, Syracuse, N. Y., July 1954 (UNCLASSIFIED).

5. Interim Report on Infrared Detectors, Report Number 102-1, Syracuse University, Syracuse, N. Y., October 1953 (UNCLASSIFIED).

6. Interim Report on Infrared Detectors, Report Number 102-0, Syracuse University, Syracuse, N. Y., January 1953 (UNCLASSIFIED).

7. Interim Report on Infrared Detectors, Report Number 102-6, Syracuse University, Syracuse, N. Y., April 1955 (UNCLASSIFIED).

8. Interim Report on Infrared Detectors, Report Number 103-4, Syracuse University, Syracuse, N. Y., March 1956 (UNCLASSIFIED).

9. W. J. Byers, P. R. Brett, H. W. Davis, L. F. Johnson, H. Levinstein and A. J. MacRae, Colored Infrared Detectors, Proc. IRE, March 1958, Vol. 3, No. 1, p. 20 (UNCLASSIFIED).

10. Development of High-Sensitivity Infrared Detectors, Report Number H-2201-F, Philco Corp., Philadelphia, Pa., November 1955 (UNCLASSIFIED).

11. Properties of Photoconductive Detectors, NOLC Report Number 360, Naval Ordnance Laboratory, Corona, Cal., February 1957 (UNCLASSIFIED).

12. Technical cell, private communication with Dr. G. A. Merton of RCA.

13. Interim Report on Infrared Detectors, Report Number 103-7, Syracuse University, Syracuse, N. Y., December 1956 (UNCLASSIFIED).

14. Interim Report on Infrared Detectors, Report Number 103-3, Syracuse University, Syracuse, N. Y., December 1955 (UNCLASSIFIED).

15. Interim Report on Infrared Detectors, Report Number 103-5, Syracuse University, Syracuse, N. Y., June 1958 (UNCLASSIFIED).

CONFIDENTIAL

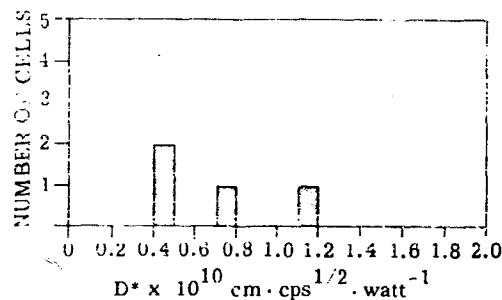


FIGURE 5-52. HISTOGRAM OF D^* VALUES FOR THE Ge:ZnI DETECTOR

detector has a resistance of about 2 megohms when an electric field of about 20 v/cm is applied across it. As the field is increased to 60 v/cm, the resistance begins to decrease rapidly with further increase in applied bias potential. This drastic resistance decrease is due to impact ionization. Both signal and noise increases linearly to the point where impact ionization takes place. While the detector can actually be used at higher bias voltage, optimum detectivity is obtained when 60 v/cm is applied across the sample. Parameters of D^* , resistance, time constant, etc., which have been reported in the literature, are listed in Table 5-7. The photosensitive sample is mounted in a double dewar, such as that shown in Figure 5-44. Dewars of this type are available from Hoffman Laboratories, The Linde Company, and The Vacuum Barrier Corporation. The inner chamber holds 1 liter of liquid helium. The outer chamber is cooled by liquid nitrogen. When so used, liquid helium may be maintained in the dewar for about 24 hours. In contrast to Ge:Au, where only about 10^{15} gold atoms/cc may be incorporated in the crystal, zinc may be added to concentrations of about 10^{16} . This greater density absorbs a higher fraction of the incident radiation, thus making the use of an integration chamber less essential. The dewar is provided with a potassium bromide window if the entire spectral response is desired. Appropriately coated Ge windows may be used if the response in certain spectral regions is to be enhanced or depressed. Detectors of this type have been manufactured by the Perkin-Elmer Corporation.

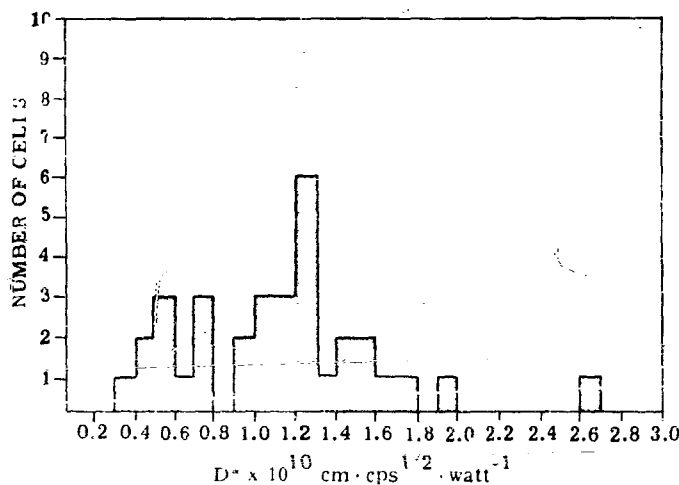
5.3.6. DETECTOR CHARACTERISTICS: Ge:Cu. Copper is most conveniently added to Ge after the crystal has been grown. This is accomplished by cutting the Ge single crystal into elements of the desired dimensions, plating a thin copper film on the sides of the elements, and then diffusing the copper into the Ge by heating at temperatures slightly below the melting point of Ge for several hours. Copper in Ge has an energy 0.64 ev above the valence band. Thus photons with energies greater than

TABLE 5-7. Zn-DOPED Ge

Mfr.	Date of Production	Cell Temp. (°K)	Area (mm ²)	Current (μA)	Dark Resistance (megohms)	Blackbody Response D* NEP (watts)	D* (cm·cps) ^{1/2} ·watt ⁻¹	Time Constant (μsec)	Chopping Frequency	Number of Cells	Data Source
PER	4-60	12	210			3.3×10^{-10}	4.9×10^9	<1	400	3	1
PER	12-60	12			2.7		1.1×10^{10}	<1	400	1	1

1. Data taken from NRI Zn-Detector, Report Number 5644, The Perkin-Elmer Corp., Norwalk, Conn., April 1960 (UNCLASSIFIED).

0.04 eV will excite holes from the copper centers, producing photoconductivity which extends to $30\ \mu$. Since the holes are bound to Cu with an energy of only 0.04 eV, the detector elements must be cooled to such temperatures that lattice vibrations cannot free the charge carriers. Temperatures in the vicinity of 15°K are sufficient. Since the detector is still in a stage of development, not much information is available about specific characteristics. A histogram of the D^* values of a number of detectors is given in Figure 5-53. Time constants are less than $1\ \mu\text{sec}$, possibly considerably less. D^* at $25\ \mu$, the spectral peak, is approximately $3 \times 10^{10}\ \text{cm} \cdot \text{cps}^{1/2} \cdot \text{watt}^{-1}$ for a detector with a 60° angular field of view (Figure 5-46). $1/f$ noise seems to be negligible above 500 cps, and from that point on to higher frequencies, D^* is frequently invariant. As is the case in other impurity-activated Ge detectors, the quality of the contact determines the maximum bias current and therefore

FIGURE 5-53. HISTOGRAM OF D^* VALUES FOR THE Ge-Cu DETECTOR

the maximum noise and the maximum signal-per-watt incident power. As in the case of the Ge:Zn detector, impact ionization determines the maximum bias voltage which may be applied. Since cooling to 15°K is required, a double dewar similar to that used for Ge:Zn may be used for mounting the detector. Detectors mounted in this or similar dewars are available commercially from Texas Instruments Incorporated, the Santa Barbara Research Center, and RCA. Parameters of D^* , resistance, time constant, etc., which have been reported in the literature, are listed in Table 5-8.

TABLE 5-8. Cu-DOPED Ge

Mfr.	Date of Production	Cell Temp. (°K)	Area A (mm ²)	Current I (μA)	Dark Resistance R_D (megohms)	Blackbody Response	Spectral Peak		Time Constant (cps)	Chopping Frequency (cps)	Number of Cells	View Angle (deg)	Data Source
						D^* (cm-cps ^{1/2} -w ⁻¹)	NEP (watts)	D^* (cm-cps ^{1/2} -w ⁻¹)					
TI	2-59	4.2	3.7	1825	21	9.7×10^9				900	13	66	1
SiPC	2-59	4.2	5.9	1577		1.2×10^{10}		6.4×10^{10}		1800	15	45	2
SiPC	2-61	4.2	10.4	1468	0.01	3.9×10^{10}	4.5×10^{-11}	7.5×10^{10}		1800	5	88	2

1. W. J. Beyers, G. R. Pruett, H. D. Adams, and L. Sloan, "Infrared Detector Research and Development at Texas Instruments," Proc. IRIP, 1960, Vol. 5, No. 4, p. 99 (CONFIDENTIAL).

2. Private communication with Donald Bode.

5.3.7. DETECTOR CHARACTERISTICS: Ge:Sb (Reference 5-76). Electrons may be freed from Sb atoms in Ge by a photon energy greater than 0.01 ev. This leads to detectors with a long-wavelength threshold at about 130 μ. While several experimental detectors of this type have been prepared, no commercial source presently exists.

5.3.8. DETECTOR CHARACTERISTICS: Ge:Cd (Reference 5-77). The Ge:Cd detection was originally developed to fill the need for an 8-14 μ detector which could be operated at liquid-hydrogen temperature. Cd is added during crystal growth by passing cadmium vapor over the molten Ge. The energy required to free charge carriers (holes) from the Cd atoms in the Ge lattice is 0.055 ev, giving a long-wavelength cutoff of the spectral response at about 22 μ. Figure 5-54 shows the spectral response of a Ge:Cd detector. The detection requires cooling to about 26°K; at 30°K the detectivity decreases by a factor 2 (Figure 5-51). The time constant of this detector, as for most of the other impurity-activated Ge detectors (except the 6-μ Ge:Au detector), is less than 1 μsec. Detectors of this type in conjunction with a liquid-hydrogen-cooling system are available from the Raytheon Manufacturing Company.

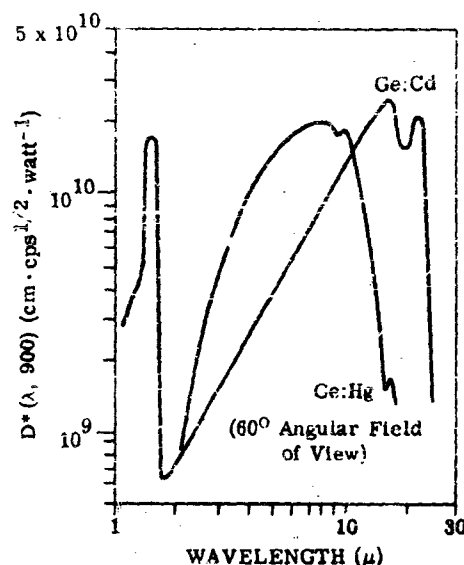


FIGURE 5-54. ABSOLUTE SPECTRAL RESPONSE OF EXPERIMENTAL Ge:Cd AND Ge:Hg DETECTORS

5.3.9. DETECTOR CHARACTERISTICS: Ge:Hg (Reference 5-78). The availability of liquid neon and other cooling systems which operate down to 35° K have led to the development of the Ge:Hg detector at Syracuse University. Mercury is introduced into Ge during crystal growth by passing a stream of hydrogen over mercury at a temperature of about 300°C. The hydrogen stream carries the Hg vapor over the molten Ge zone. Preliminary measurements have indicated mercury concentrations up to 5×10^{14} atoms/cc in the grown Ge crystal. The energy required to free charge carriers from the lower Hg level is 0.086 ev. A spectral response of Ge:Hg is shown in Figure 5-54. Since only a few crystals have been grown and mounted, considerable improvement may be expected when this detector is more fully developed. The temperature required for cooling is 35° K. At 40° K the detectivity has decreased by a factor 2 (Figure 5-51). The detector is not yet commercially available.

5.4. IMPURITY-ACTIVATED GERMANIUM-SILICON ALLOYS, by Thomas Limperis

Crystals of germanium-silicon alloys were first prepared around 1939 by Stohr and Klemm (Reference 5-79), who showed that Ge and Si formed a continuous series of solid solutions. They also showed that the lattice constant of this system, which has a diamond structure, varies linearly with compositions between the values for pure Ge and pure Si. Later, Levitas et al. (Reference 5-80) and Johnson and Christian (Reference 5-81) found that the width of the forbidden band in this semiconductor is also dependent upon the percentage of silicon in the alloy. This dependency is displayed in Figure 5-55.

According to Herman (Reference 5-82), the knee of the curve is probably due to the different rates of change in band gap in the [111] direction and the [100] direction with varying amounts of Si in the Ge lattice (the numbers in brackets are Miller indices, which represent a direction in the crystal lattice). As Si is added to Ge, the conduction bands in the [100] and [111] directions move away from the valence band. The [111] conduction band moves away at a faster rate than the [100] conduction band. From 0 to 15 mol percent silicon, the band gap in the [111] direction is smaller than the band gap in the [100] direction, and consequently the change in this band gap with the amount of added silicon will determine the variation of band gap for the system. In the range beyond 15 mol percent Si, the band gap in the [111] direction is larger than in the [100] direction, and consequently the rate at which the [100] minimum moves away from the valence band will determine the band gap of the system.

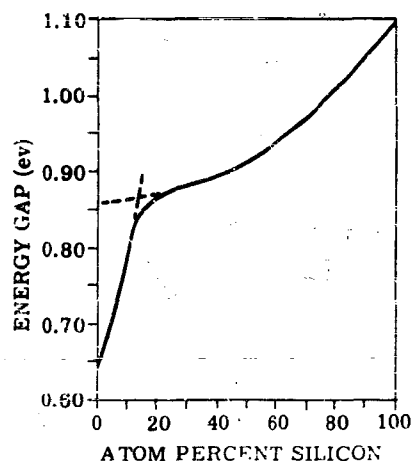


FIGURE 5-55. COMPOSITION DEPENDENCE OF THE ENERGY GAP OF Si-Ge ALLOYS

Since this dependency exists, one would expect a corresponding change in the absorption spectrum with varying amounts of silicon in the alloy, and, in fact, this is the case. The absorption spectrum (Reference 5-83) is presented in Figure 5-56 with the percentage of silicon as a parameter.

The smallest energy gap for the Ge-Si system (from Figure 5-55) is, of course, the band gap of pure germanium (about 0.7 eV), which corresponds to a long-wavelength cutoff of approximately 1.8μ . Band gaps of this order are not particularly interesting to the military infrared system designer today since the targets of interest emit radiation in the longer-wavelength atmospheric windows. However, the addition of impurities into the lattice of these alloys leads to some interesting results. For example, the elements gold, copper, indium, zinc, and boron introduce allowed electron energy levels in the forbidden band gap, which greatly affect the optical and electrical properties of the materials. These impurity-induced energy levels change the ionization energy (energy required to transport a hole to the valence band or electron to the conduction band). This is illustrated in Figure 5-57, where E_i is the ionization energy and E_g is the band gap. In this simple picture, the impurity centers are p-type or electron acceptors. Thus, an electron transition to one of these levels from the valence band results in a hole which is free to conduct in the valence band.

In the Ge-Si system, the impurity-induced levels move away from the valence band (E_i increases) with increasing silicon content. The resulting variation in ionization energy with varying amounts of silicon in the system is shown in Figure 5-58.

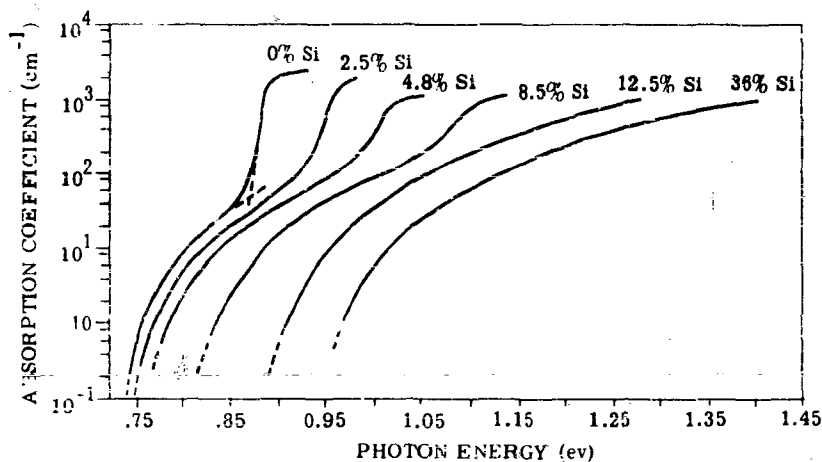


FIGURE 5-56. INTRINSIC ABSORPTION SPECTRA IN A SERIES OF Ge-RICH Ge-Si ALLOYS AT 78°K

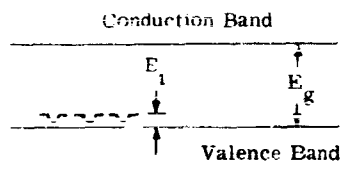


FIGURE 5-57. SIMPLE BAND PICTURE

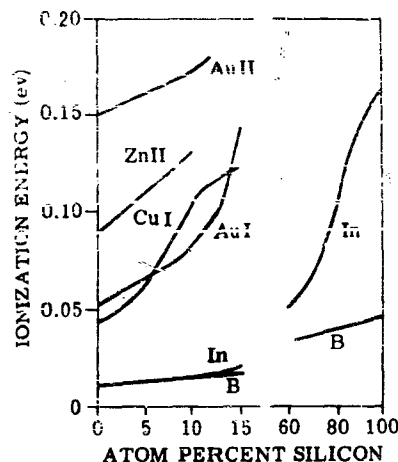


FIGURE 5-58. IMPURITY IONIZATION ENERGIES AS FUNCTIONS OF ALLOY COMPOSITION

The ionization energy necessary to provide a long-wavelength response of $14\ \mu$ (the long-wavelength edge of the far-infrared window) is about 0.09 eV. We can see from Figure 5-58 that energy levels introduced by boron lie closer to the valence band than 0.09 eV for all values of silicon concentration (Reference 5-84). Consequently, Ge-Si detectors using this impurity would have a photoconductive long-wavelength cutoff beyond $14\ \mu$. The indium impurity leads to ionization energies of 0.09 eV at silicon concentrations between 70% and 80%. Single crystals containing this silicon concentration and the indium activator have been grown and the characteristics measured; however, these crystals are extremely difficult to prepare and therefore further efforts in this area have been abandoned. Detectors have been constructed of Ge-Si doped with: zinc (employing the second zinc level), gold (using the first level), gold (using the second level), and zinc plus gold (using the second level of zinc and the first level of gold). Detectors of this type were developed primarily to provide long-wavelength photodetection at operating temperatures of approximately 50°K or pumped-over-liquid-nitrogen temperatures. The characteristics of these detector types represented by the symbols Ge-Si:ZnII, Ge-Si:AuI, Ge-Si:AuII, and Ge-Si:ZnAuI, respectively, are described below in detail.

5.4.1. (Ge-Si):AuI. The gold impurity introduces several levels in the forbidden gap. The position of these levels is greatly influenced by the percentage of silicon in the alloy as described above. Figure 5-59 (Reference 5-85) shows the variation of ionization energy in the first and second levels of gold in the germanium-silicon system.

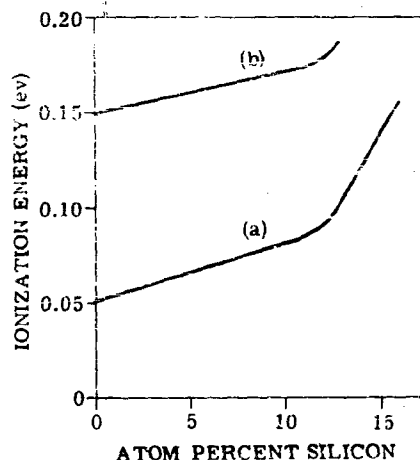


FIGURE 5-59. IONIZATION ENERGY OF Au IN Ge-Si ALLOYS. (a) First level. (b) Second level.

From this figure it may be seen that by choosing the first gold level and selecting the proper amount of silicon one can obtain an ionization energy sufficiently small (0.09 eV) to allow carrier generation by photons with wavelengths in the 8- to 13- μ region (the far-infrared window). The utility in being able to change the band gap by simply varying the percentage of silicon is obvious. The concentration of Si may be chosen so that the energy gap is sufficiently small for detection in the far-infrared window, but not so small that the long-wavelength limit of photoconductivity lies beyond 13 μ , where cell temperatures below 30°K are needed to reduce the number of thermally generated carriers. Detectors employing this material are commercially available today from the Electron Tube Division of RCA.

5.4.1.1. Absorption. The absorption coefficient for this detector type is quite small (about 1 cm^{-1}) (Reference 5-84) in the region of 8-13 μ . Since the detectivity is directly proportional to the percentage of absorbed quanta, it behooves the detector designer to somehow increase the absorption. For impurity-activated Ge-Si cells this is done in one of two ways. First, for small-area cells (smaller than $0.5 \times 0.5 \text{ cm}^2$) an integrating chamber with highly reflecting walls is used, as shown in Figure 5-60. This configuration insures multiple traversals of the incident photons through the sensitive element, thereby effectively increasing photon absorption. For detector areas around $0.5 \times 0.5 \text{ cm}^2$, the bottom of the sensitive element is slanted (Figure 5-61) to provide multiple internal reflections.

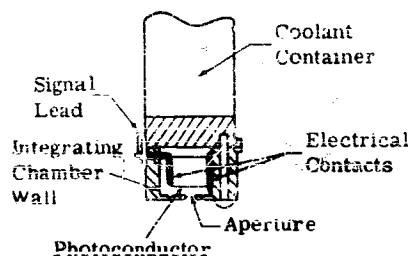


FIGURE 5-60. TYPICAL INTEGRATING-CHAMBER ASSEMBLY

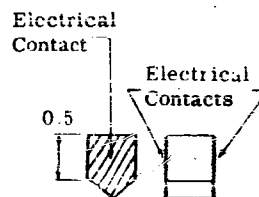


FIGURE 5-61. CELL ELEMENT

5.4.1.2. Resistance. The dark resistance of these cells is extremely high at liquid-hydrogen temperatures. Values of resistance around 170 megohms have been measured; however, it is believed⁶ that this is the resistance of the leakage path and that the actual cell resistance is much higher. For cell temperatures around 60°K or pumped over liquid nitrogen, the resistance is around 500 kohm. The resistance is exponentially dependent upon the reciprocal of the temperature, or $R \propto e^{1/T}$, where R is the resistance and T is the cell temperature.

5.4.1.3. Time Constant. The time constant of this detector is less than 1 μ sec.

5.4.1.4. Noise. The noise power spectrum has a $1/f$ component at chopping frequencies below 300 cps. and beyond that point the noise is white. In the white region, the noise is predominantly due to fluctuations in the generation and recombination of the charge carriers caused by either the background radiation or by lattice vibrations, depending upon the cell temperature. For cell temperatures of approximately 20°K and below, and background temperatures of around 300°K, the noise is predominantly background noise (noise caused by the random arrival of photons from the background). As the cell's operating temperature is increased, the random generation and recombination of carriers brought about by the thermal agitation of the lattice begins to predominate.

Since the time constant is very short, the radiation incident on the detector may be chopped at frequencies up to 10^5 cps. At frequencies above 300 cps, the noise is out of the $1/f$ region and the responsivity is at a maximum, which leads to a maximum signal-to-noise ratio.

⁶ Private communication with Dr. G. A. Morton and Dr. M. Schultz.

5.4.1.5. Detectivity. A typical spectral response for Ge-Si:AuI cells, which are available from RCA, is presented below. As mentioned earlier, the long-wavelength cutoff is dependent upon the amount of silicon which is added to the lattice. For the spectral response presented in Figure 5-62, the percentage of silicon is about 11%; this provides a long-wavelength cutoff of about 12μ . The detector described in Figure 5-62 has a coated Ge window. The peak value of D^* is dependent upon several parameters, including the cell temperature and the cell field of view. If the noise is predominantly background noise, then placing cooled shields adjacent to the detector to restrict its field of view will decrease the background noise and consequently increase D^* . For the detector to be background-noise limited, the operating temperature must be 50°K or less for backgrounds of about 300°K .

Unfortunately, no measurements on this type of cell have been published by the two cell test facilities, NOLC and Syracuse. RCA reports⁷ that for a 250-volt bias, a 120° field of view, a 21°K

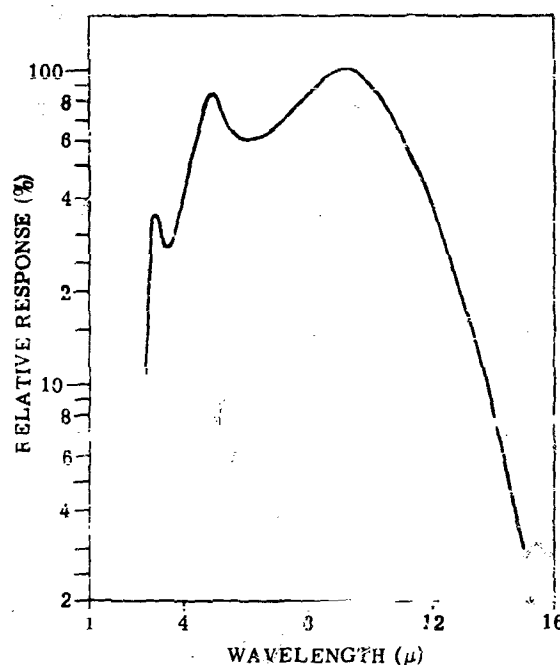


FIGURE 5-62. SPECTRAL-RESPONSE CURVE FOR Ge-Si:AuI

⁷Private communications with Dr. G. A. Morton.

operating temperature, and a 2.5-megohm load, D^* (500°K, 300, 1) is 6 to $10 \times 10^9 \text{ cm} \cdot \text{cps}^{1/2} \cdot \text{watt}^{-1}$, which corresponds to a peak D^* of 1.2 to $2 \times 10^{10} \text{ cm} \cdot \text{cps}^{1/2} \cdot \text{watt}^{-1}$. The 2°K temperature is obtained with liquid hydrogen in the cryostat. Dewar-cooler assemblies employing this coolant are available from RCA. When operating at pumped-over-liquid-nitrogen temperatures (about 50°K), the D^* (500°K, 100, 1) is $5 \times 10^9 \text{ cm} \cdot \text{cps}^{1/2} \cdot \text{watt}^{-1}$, and, at cell temperatures of 77°K, the D^* (500°K, 100, 1) is approximately $5 \times 10^6 \text{ cm} \cdot \text{cps}^{1/2} \cdot \text{watt}^{-1}$. These values of D^* may be converted to peak D^* by the following expression

$$D^*_{\text{peak}} = 2 D^* (500^\circ\text{K}, \text{---}, 1)$$

Photosaturation studies of this detector have not been reported up to the time of this report. Of course, when the cell is background-noise limited, one should expect the NEP to degrade with increasing background temperature because of the dependence of noise upon the level of background irradiance. When the cell is not background-noise limited, the NEP will be constant for increasing background irradiance until a level is reached where background noise is predominant.

5.4.2. Ge-Si:ZnII. Infrared detectors using the second level of Zn in the Ge-Si lattice are also available from RCA. As in the case of Ge-Si:AuI, the amount of Si added to the Ge lattice is chosen to obtain a long-wavelength cutoff which lies at about 13μ , which is the long-wavelength edge of the 8- to $13\text{-}\mu$ window. The variation of ionization energy (or band gap) with percentage of Si is presented in Figure 5-63. Generally speaking, around 4% of Si is used to provide the long-wavelength response described above.

When preparing these cells, a compensating n-type impurity such as antimony is used to fill all the acceptor levels which lie closer to the valence band than the second Zn level. The result is that electron transitions which do occur are between the valence band and the second zinc level. The hole which remains in the valence band is then free to produce a photocurrent.

5.4.2.1. Absorption. Transmission measurements (Reference 5-85) have been made on a zinc-activated Ge-Si lattice containing 7.5% silicon. From these measurements, the absorption spectrum was determined (Figure 5-64). The figure indicates that the absorption coefficient is only around 1 cm^{-1} in the range of 2 to 10.5μ . Such transparency in the region of interest is undesirable since

*These values were obtained from only one cell reported by RCA in Reference 5-85.

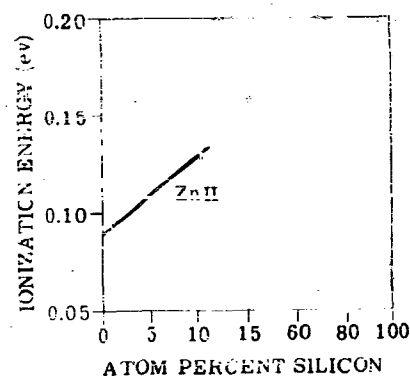


FIGURE 5-63. IMPURITY IONIZATION LEVEL VS. PERCENT SI FOR ZnII

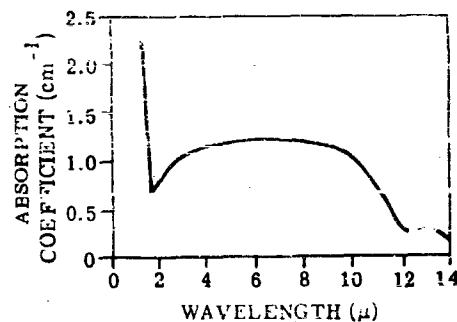


FIGURE 5-64. OPTICAL ABSORPTION COEFFICIENT OF A Zn-ACTII. ED ALLOY, Ge-Si:ZnII; 7.5% Si.

the signal voltage is directly proportional to the percentage of quanta absorbed. Methods have been devised to solve this problem in these detectors. They are described in the section on Ge-Si:Au I (Section 5.4.1).

5.4.2.2. Resistance. The dark resistance of detectors constructed from this material is reported to be about 70 megohms for cell temperatures around 21°K. However, indications⁹ are that this is the resistance of the leakage path and that the cell impedance is much higher. When temperatures of about 60°K are used, the resistance is around 30 megohms.

5.4.2.3. Time Constant. The time constant is less than 1 μsec.

5.4.2.4. Noise. The noise is the same as that reported for Ge-Si:Au.

5.4.2.5. Detectivity. A typical spectral response curve for Ge-Si:Zn is shown in Figure 5-65. As mentioned above, the long-wavelength cutoff is dependent upon the amount of silicon which is added to the lattice. For the spectral response shown in Figure 5-65, the percentage of silicon is around 4. The peak D^* value is dependent upon several parameters including the cell's temperature and its field of view.

⁹Private communication with Dr. G. A. Morton and Dr. M. L. Schultz.

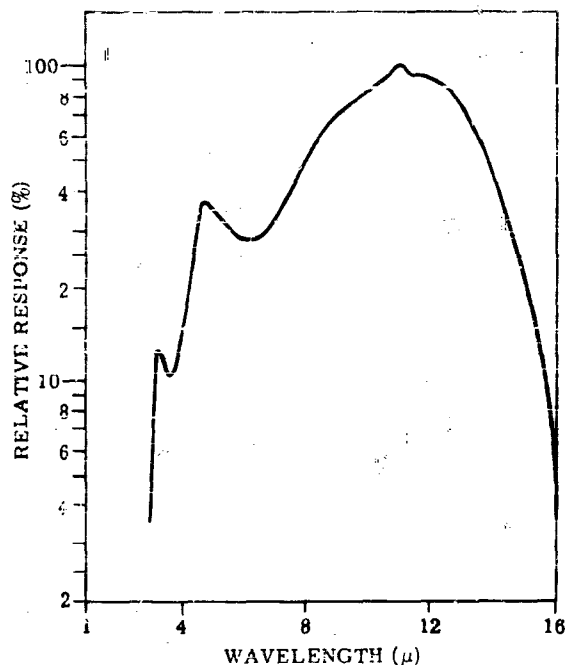


FIGURE 5-65. SPECTRAL-RESPONSE CURVE FOR
Ge-Si:ZnII

For cell temperatures of around 50°K or less and background temperatures of 300°K, the cell is background-noise limited. Therefore, placing cool shields adjacent to the sensitive element to restrict its field of view will effectively decrease the background noise and consequently increase the detectivity (the relationship between these variables is shown in Figure 5-42).

One Ge-Si:ZnII detector with a coated-Ge window was sent to NOLC for testing. The results were reported in a recent NOLC report (Reference 5-87). The measurements were made at a cell temperature of 50°K. A summary of the results is given below.

Dark Resistance	2.3×10^6
Cell Current	38 μ a
Cell Noise	0.96 μ volts
Load Resistance	2.5×10^6 ohms
Cell Area	$\sim 2.25 \text{ cm}^2$
$D^*(500^\circ\text{K}, 90, 1)$	$7.1 \times 10^9 \text{ cm} \cdot \text{cps}^{1/2} \cdot \text{watt}^{-1}$
$D^*(\lambda_{pk}, 90, 1)$	$1.5 \times 10^{10} \text{ cm} \cdot \text{cps}^{1/2} \cdot \text{watt}^{-1}$

The detector element consisted of nine 0.5 x 0.5-cm cubes arranged in a square mosaic. A metal cone mounted outside the window limited the field of view to about 70° .

For cell temperatures of 21°K ,¹⁰ a load of 2.5 megohms, a bias of 250 volts, and a 120° field of view, $D^*(500^\circ\text{K}, 900, 1)$ is $1.8 \times 10^{10} \text{ cm} \cdot \text{cps}^{1/2} \cdot \text{watt}^{-1}$, which corresponds to a D^* peak of $D^*(\lambda, 900, 1)$ equal to $3.6 \times 10^{10} \text{ cm} \cdot \text{cps}^{1/2} \cdot \text{watt}^{-1}$. As in the case of Ge-Si:AuI, the 21°K temperature is obtained by using liquid hydrogen. A cryostat-dewar package employing this coolant is available from RCA (with the cryostat furnished by Air Products Corporation, Allentown, Pennsylvania). At pumped-over-liquid-nitrogen temperature (about 50°K), the $D^*(500^\circ\text{K}, \text{---}, 1)$ value decreases to about $10^{10} \text{ cm} \cdot \text{cps}^{1/2} \cdot \text{watt}^{-1}$. $D^*(500^\circ\text{K}, \text{---}, 1)$ becomes about $1.5 \times 10^{10} \text{ cm} \cdot \text{cps}^{1/2} \cdot \text{watt}^{-1}$ at 60°K . $D^*(500^\circ\text{K}, \text{---}, 1)$ may be converted to peak D^* by the expression.

$$D^*(\lambda_{pk}, \text{---}, 1) = 2D^*(500^\circ\text{K}, \text{---}, 1)$$

These values of $D^*(500^\circ\text{K}, \text{---}, 1)$ were obtained from 7 cells reported by RCA in their quarterly progress reports during 1955 and 1960. The data are shown in Table 5-9.

Photosaturation studies have not been reported up to the time of this report. Of course, when the cell is background-noise limited, one should expect a degradation in NEP with increasing background temperature because of the dependence of noise upon the level of background irradiance. When the cell is not background-noise limited, the NEP will be constant for increasing background irradiance until a level is reached where background noise predominates. At this level the NEP will behave as described above.

The resistance and responsivity are also functions of background irradiance; however, the data are not yet available.

¹⁰Private communications with Dr. Morton of RCA.

TABLE 5-9. D^* (500°K, —, 1) FOR SEVERAL Ge-Si:ZnII CELLS

Cell Number	50°K	60°K	78°K	Ref.
AW283-5.2% Si	4×10^9	6×10^8	10^7	1
AW284-4.3% Si	10^{10} (f = 1500 cps)	2×10^9 (f = 1500 cps)	1.5×10^8 (f = 1500 cps)	2
AW285-3.5% Si	10^{10} (f = 1500 cps)	1.5×10^9 (f = 1500 cps)	5×10^7 (f = 1500 cps)	2
AW286-5.1% Si	8×10^9 (f = 1500 cps)	1.5×10^9 (f = 1500 cps)	5×10^7 (f = 1500 cps)	2
AW287-4.9% Si	10^{10} (f = 1500 cps)	1.5×10^9 (f = 1500 cps)		1
AW300-5.5% Si	1.5×10^{10} (f = 100 cps)	1.5×10^9 (f = 100 cps)	5×10^7 (f = 100 cps)	3
AW302-4.7% Si	7×10^9 (f = 100 cps)	10^9 (f = 100 cps)	2×10^7 (f = 100 cps)	3

1. K. S. Ling, Impurity Activated Alloy Infrared Detectors, Third Quarterly RCA Progress Report, Electron Tube Division, Radio Corporation of America, Harrison, N. J., January 1960 (UNCLASSIFIED).
2. G. A. Morton, Infrared Photoconductors, Eighth Interim RCA Report, David Sarnoff Research Center, Radio Corporation of America, Princeton, N. J.
3. K. S. Ling, Impurity Activated Alloy Infrared Detectors, Fourth Quarterly RCA Progress Report, Electron Tube Division, Radio Corporation of America, Harrison, N. J., January 1960 (UNCLASSIFIED).

5.4.3. Ge-Si:AuII. The variation of ionization energy of the second level of gold in the Ge-Si system is shown in Figure 5-59. Several detectors have been constructed from this material with peak detectivities around 4.5μ and long-wavelength photoconduction thresholds of about 6μ . The measurements on these cells are presented in Table 5-10. A typical relative response curve for this material (about 10% Si) is shown in Figure 5-66.

5.4.4. Ge-Si:Zn:AuII. Adding two activating materials to the Ge-Si system leads to some interesting results (Reference 5-86). First, the spectral response configuration differs considerably from that of the detectors described above. The resulting curve appears to be roughly the sum of the individual response curves for the two activating materials. The result, shown in Figure 5-67, is a response with two peaks. One lies at 4.0μ and the other around 11μ . Between the intrinsic edge at 1.8μ and around 11.5μ , the net response is constant within a factor of 2. The D^* (500°K, 100, 1) for this cell is about $1.5 \times 10^8 \text{ cm} \cdot \text{cps}^{1/2} \cdot \text{watt}^{-1}$ at 60°K and about $8 \times 10^8 \text{ cm} \cdot \text{cps}^{1/2} \cdot \text{watt}^{-1}$ at 50°K. Improvement in D^* by a factor of 2 may be achieved by chopping at higher frequencies (around 1500 cps).

CONFIDENTIAL

TABLE 5-10. Ge-Si: Au II at 80°K

Cell Number	λ (peak) (μ)	λ_c (10%) (μ)	D^* (500°K, 100, 1) (cm · cps ^{1/2} · watt ⁻¹)	D^* (λ_{pk} : 100, 1) (cm · cps ^{1/2} · watt ⁻¹)	Dark Resistance (ohms)	Reference
478 I 1			10^9	3.5×10^9	2×10^6	1
478 B 1	4.5		8.8×10^8	3×10^9	5×10^7	1
AW274-9.9% Si	4.5		1.4×10^9	5×10^9	$\rho = 5.3 \times 10^7$	2
AW1 3-10% Si	4.0		2.1×10^9	7.8×10^9		2
488E1-6.3% Si	5	8.6	1.4×10^9	4.3×10^9		3
488E2-6.3% Si	5	---	2.1×10^9	6.1×10^9		3
488F1-8.1% Si	4.5	8.3	2.8×10^9	9.5×10^9		3
488F2-8.1% Si	4.5	---	2.9×10^9	1.0×10^{10}		3
488F3-8.1% Si	4.5	7.9	1.9×10^9	6.5×10^9		3
488F4-8.1% Si	4.5	8.2	2.5×10^9	8.2×10^9		3
488G1-9.4% Si	4	7.4	3.4×10^9	1.5×10^{10}		3
488G2-9.4% Si	4	7.7	2.9×10^9	1.2×10^{10}		3
488G3-9.4% Si	4	7.2	3.7×10^9	1.6×10^{10}		3
488H2-10.0% Si	4	7.0	2.9×10^9	1.6×10^{10}		3

1. K. S. Ling, Impurity Activated Alloy Infrared Detectors, Fourth Quarterly RCA Progress Report, Electron Tube Division, Radio Corporation of America, Harrison, N. J., April 1960 (UNCLASSIFIED).

2. W. E. Harty, K. S. Ling, J. S. Martin, M. L. Schultz, and A. L. Smith, Impurity Activated Alloy Infrared Detectors, Second Quarterly RCA Progress Report, Electron Tube Division, Radio Corporation of America, Harrison, N. J., October 1959 (UNCLASSIFIED).

3. Private communications with Dr. G. A. Morton.

CONFIDENTIAL

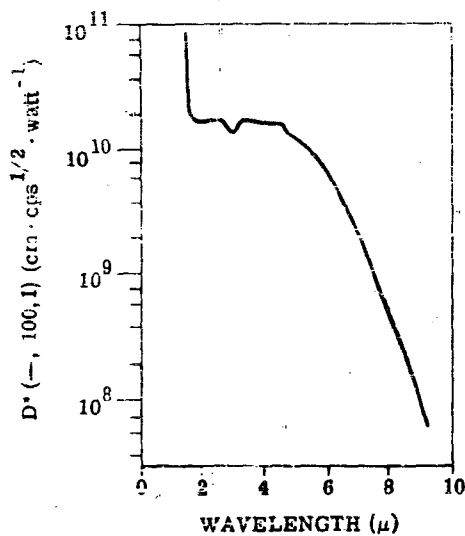


FIGURE 5-66. ABSOLUTE SPECTRAL RESPONSE OF Ge-Si:AuII. Cell No. 488G3; 9.4% Si; 80° K

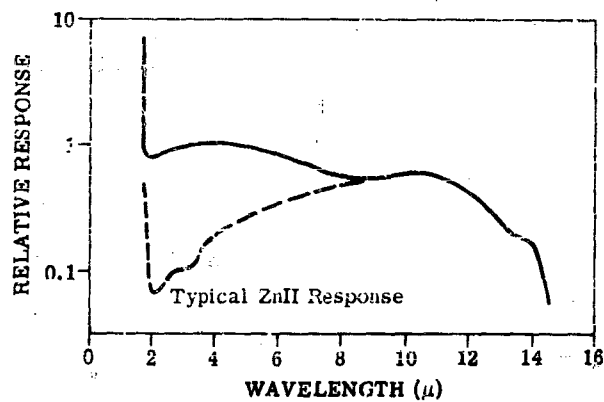


FIGURE 5-67. RELATIVE SPECTRAL RESPONSE OF Ge-Si:Zn:AuII. Cell No. AW299; 5.3% Si.

5.5. TELLURIUM, by Thomas Limperis and Gwynn H. Suits

5.5.1. INTRODUCTION. The element tellurium was discovered by Muller von Richenstern in 1782 and later named by Klaproth in 1798. It was found primarily in the form of tellurides of gold and other metals. In powder form it has a grayish-white, metallic appearance.

5.5.2. PHYSICAL PROPERTIES. Tellurium has a melting temperature of $449.5 \pm 0.3^\circ\text{C}$ (Reference 5-88) and a specific gravity of 6.24 at 20°C (References 5-33, 5-89, and 5-90). Single crystals of this material have a rhombohedral structure with a D_3^4 or D_3^6 space group as expressed in the Schoenflies notation. A schematic representation of the structure is shown in Figure 5-68. The atoms are bonded in such a way as to form helical structures. These helices, when placed adjacent to each other, make up the crystal. The strength of the bond between atoms in the helix is much stronger than the bonding between adjacent helices. Consequently, the physical, electrical, and optical properties display a strong anisotropy. Table 5-11 lists two physical properties for two orientations of the crystal; along the c-axis (in the direction of the helices), and perpendicular to the c-axis to show the degree of anisotropy.

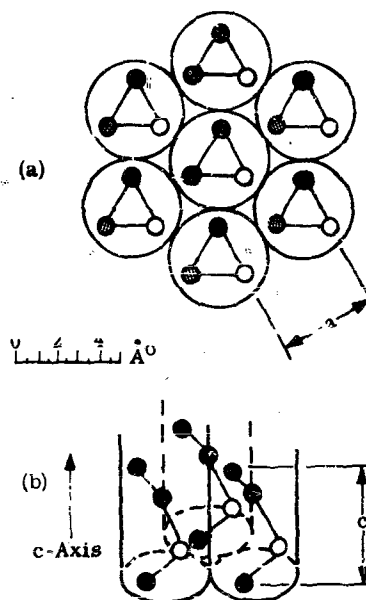


FIGURE 5-68. SCHEMATIC REPRESENTATION OF THE Te CRYSTAL.
(a) Top View. (b) Side View.

TABLE 5-11. PHYSICAL PROPERTIES

Crystal Orientation	Linear Expansion Coefficient (deg ⁻¹)	Compressibility (cm ² /dyne)
c-axis	-1.6×10^{-6}	-4.1×10^{-13}
⊥ c-axis	2.72×10^{-5}	2.8×10^{-12}

There are a number of ways of preparing tellurium single crystals, but the two most common techniques are those of Czochralski (Reference 5-91) and Bridgman (Reference 5-92). In the Czochralski method, a small, single crystal of tellurium is lowered into a crucible filled with the molten element. The temperatures are controlled very carefully so that the molten material begins to solidify slowly at the interface between the seed and the melt. The seed, while rotating slowly, is gradually raised until a large single crystalline boule develops. This technique has been used by Weidel (Reference 5-93), Keezer (Reference 5-94), and Davis (Reference 5-95). Boules 2 cm in diameter and 7 cm long (Figure 5-69) have been pulled, and a high degree of crystal perfection has been obtained. The difficulties encountered in this technique seem to be in properly controlling the temperatures and obtaining good seed material. In the Bridgman method, chunks of bulk tellurium are placed in a long, thin, horizontal, crucible boat. At one end of the boat a single crystal seed is inserted. Heat is applied at the seed-bulk interface until the material melts. The boat is then moved gradually so that the molten region travels from the seed-bulk interface to the opposite end. The degree of perfection of single crystals prepared in this manner has been relatively low. A third method used at WRL (The University of Michigan's Willow Run Laboratories, now the Institute of Science and Technology) is the vapor-deposition technique. Here the bulk tellurium is heated at one end of a long tube, containing low pressure H₂; it is condensed in some region farther along on the walls of the tube. This method requires good control of the temperature gradient along the tube. The crystals produced range from 1 mm x 5 mm to 2 mm x 8 mm and can be used directly as photo-detector elements or as seed material for the two methods described above.

The best crystals grown by the Czochralski method have as good detector properties as the crystals grown from the vapor phase. However, the growth of good crystals by the vapor-deposition technique is more easily accomplished and requires very little capital equipment in comparison to the Czochralski method. For the person who wishes to make a few of his own tellurium photodetectors without entering into large-scale production, the vapor-deposition method would be the quickest and would require the least commitment of time and money. On the other hand, controlled doping and large-scale preparation of good tellurium crystals are probably best done by the Czochralski method.

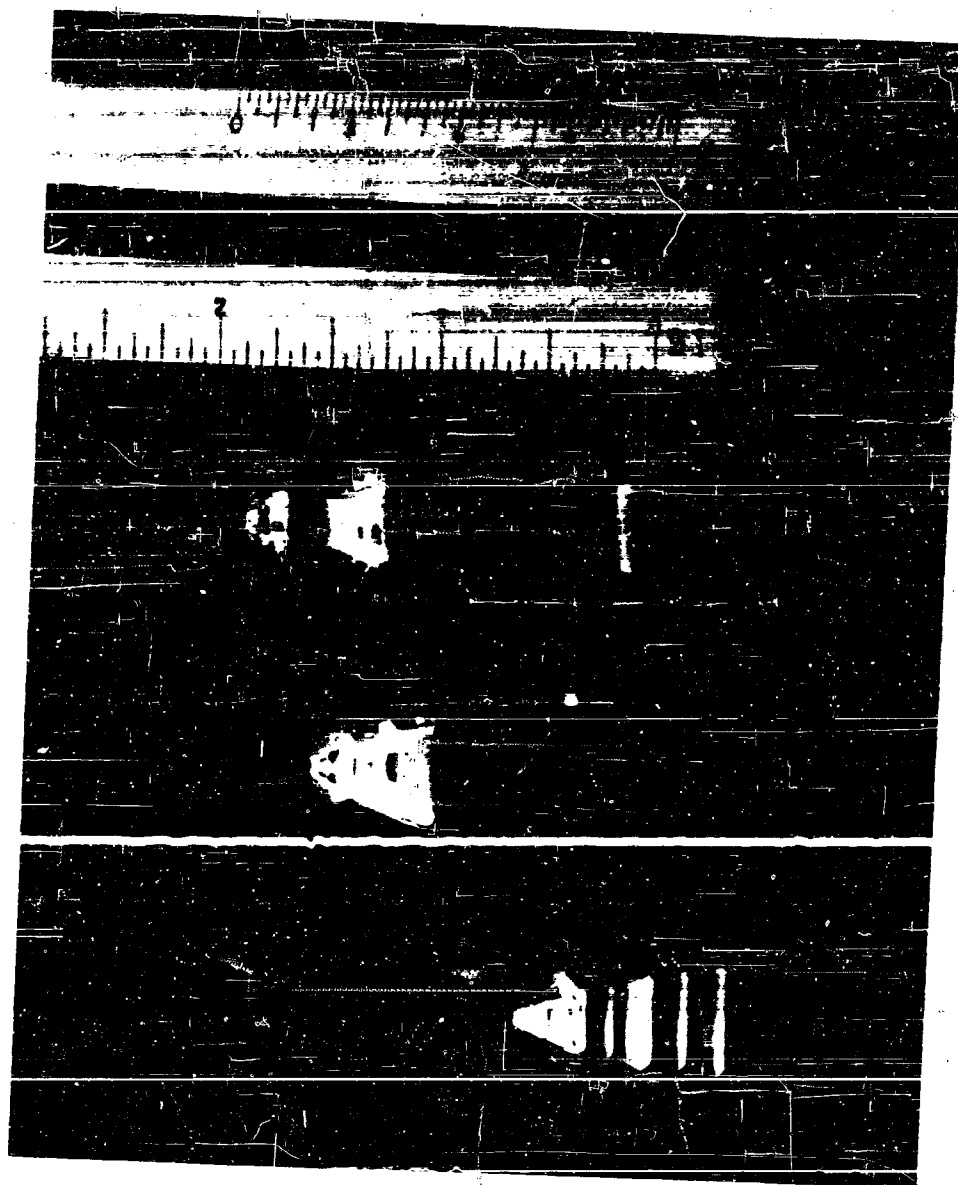


FIGURE 5-19. SINGLE-CRYSTAL Te BOULES PREPARED BY THE CZOCHRALSKI METHOD

Single-crystal tellurium is very soft. It is easily scratched and bent. It cleaves parallel to the c-axis, but it is difficult to cut or cleave perpendicular to the c-axis without inducing local fractures. Single crystals grown from vapor or the melt have a metallic lustre and a strong tendency to exhibit natural crystal faces.

Soldering to tellurium can be done by using an acid flux and bismuth metal followed by any good lead-tin solder. Welding wire leads is easily done by pressing hot wires against the tellurium crystal. Evaporated-gold contacts can be made to hold quite well by standard methods. Vacuum evaporation of tellurium is easily accomplished by standard means.

Because of the anisotropy of thermal expansion of tellurium, large sections (about 25 mm^2) of tellurium cannot be mounted rigidly against a thermal sink, but must be mounted by fixing only an edge or corner of the crystal to the thermal sink to avoid fracture of the crystal. Nonrigid mounting using silastic can be used for large area crystals.

5.5.3. ABSORPTION. Loferksi (Reference 5-96) and Nomura and Blakemore (Reference 5-97) have measured the infrared absorption of single crystals with two orientations of the electric vector of the incident light. Electric fields perpendicular and parallel to the c-axis were used. The results are given in Figure 5-70. The variation in percentage of transmission of $5\text{-}\mu$ radiation with the angle between the electric vector and the c-axis is given in Figure 5-71. The absorption coefficient for unpolarized incident light should lie somewhere between the two extreme values obtained with the

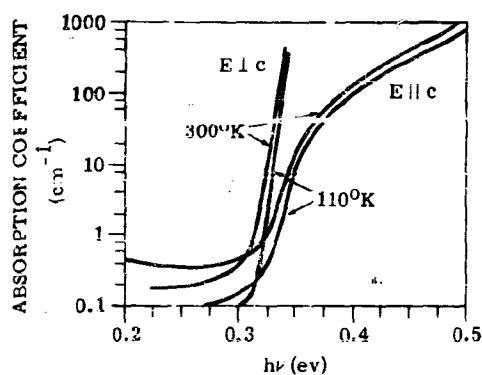


FIGURE 5-70. OPTICAL TRANSMISSION OF A Te SAMPLE AS A FUNCTION OF PHOTON ENERGY

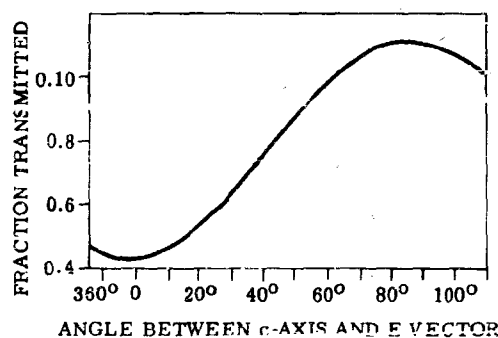


FIGURE 5-71. TRANSMISSION OF A TYPICAL Te CRYSTAL VS. ANGLE BETWEEN THE c-AXIS AND THE E VECTOR OF THE INCIDENT POLARIZED RADIATION. $\lambda = 5 \mu$.

perpendicular and parallel polarized light. Values of absorption constant between 10^4 and 10^5 cm^{-1} in the 1- to 3- μ spectral region have been obtained by Moss (Reference 5-98) by measuring the transmission through thin film.

The position of the absorption edge is a function of both the temperature and pressure. Loferski found a temperature dependence of $-7 \times 10^{-5} \text{ ev/}^\circ\text{C}$. The negative sign implies that the edge moves towards longer wavelengths with increasing temperature. Neuringer (Reference 5-99) has found a pressure dependence of the absorption edge (E_{II}^{C}) of $-1.9 \times 10^{-5} \text{ ev/atom}$.

5.5.4. BAND GAP. The band structure of Te cannot be described adequately by a simple band picture where a valence band is separated from a single conduction band by the forbidden zone (or band gap). The absorption spectrum suggest a more complex structure. Discussions of presently accepted band pictures of tellurium along with references to the original work are presented by Moss (Reference 5-100, pp. 173-175). No attempt will be made to discuss this point in detail here, since it is beyond the scope of this report. Reitz (Reference 5-101) has calculated the electronic band structure of tellurium and selenium. In his approach only nearest-neighbor interactions were considered important. Reitz started with a hypothetical chain having 90° bond angles and considered the transition to actual bond angles (102°) as a perturbation. In agreement with experiment, his calculations lead to two long-wavelength absorption edges, depending on the polarization of the incident light with respect to the c-axis.

Measurements on the temperature variation of conductivity and the Hall coefficient yield an energy gap value of $0.33 \pm 0.01 \text{ ev}$. This value, as described in the preceding section, is a function of the temperature and pressure of the crystal.

The addition of selenium to the tellurium has an effect of increasing the band gap; consequently, the photoconductive properties are also altered. An investigation of this work along with the effects of doping are presently being studied at The University of Michigan.

5.5.5. REFRACTIVE INDEX. The refractive index of tellurium films was investigated by Moss (Reference 5-102), while Hartig and Loferski (Reference 5-103) and Caldwell (Reference 5-104) investigated the refractive index of bulk crystals. The results of the crystal studies are shown in Figure 5-72. Here the anisotropic behavior in tellurium is again evident. The refractive index is relatively constant between 4 and 14 μ , but a considerable difference is seen between the refractive indices for the two polarizations of the electric vector.

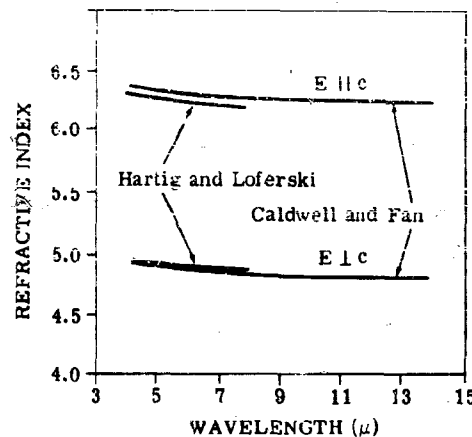


FIGURE 5-72. SPECTRAL DEPENDENCE OF THE REFRACTIVE INDEX IN Te CRYSTALS

5.5.6. **TELLURIUM AS A DETECTOR.** Early investigations of the photoconductive properties of this element were carried out on thin deposited films. In the latter part of 1948, Moss (Reference 5-105) prepared several of these films using a vacuum deposition technique. He found the films photoconductive when cooled to liquid-nitrogen temperatures. The measured NEP's (noise equivalent powers) were quite poor, with time constants ranging between 300 and 1000 μ sec. Fukuroi et al. (Reference 5-106) have made extensive measurements of the photoelectric properties of tellurium single crystals grown by the Bridgman method; however, the principal aim of this work was to measure the photoelectric properties and not necessarily to produce infrared detectors. In 1958, Suits (Reference 5-107) reported the fabrication and measurement of single-crystal-tellurium photoconductors. Later, in 1960, Butter and McGlaughlin (Reference 5-108) of the Honeywell Ordnance Division, Hopkins, Minnesota, reported fabrication of tellurium detectors as a military product. The properties of resistance, spectral response, time constant, noise spectrum, and detectivity of today's tellurium detector are described below in detail.

5.5.6.1. **Resistance.** Single-crystal-tellurium detectors are characterized by a rather low dark resistance. Values of 2000 ohms per square at liquid-nitrogen temperatures are considered average today. The term per square implies that the length of the crystal is equal to the width. Consequently, for geometries other than square, one needs only to multiply 2000 by the new length-to-width ratio to predict the dark resistance. Resistance values of this magnitude require crystals with a high degree

of perfection, and proper handling techniques to prevent stressing the crystal and introducing dislocations which affect the resistivity and carrier lifetime.

5.5.6.2. Time Constant. Measurements of the lifetime of charge carriers in single crystals of tellurium have been made by de Carvalho (Reference 5-109) using the PEM effect. He found values of time constant (τ) of around 10^{-8} second, and, upon cooling the crystal, a rapid increase in τ resulted. Near room temperature τ followed the relationship

$$\tau \propto \exp E/kT$$

where E is the energy gap which is about 0.33 ev. Time constants of tellurium photoconductive detectors are about $60 \mu\text{sec}$ at 77°K . Three tellurium detectors have been sent to NOLC for testing (References 5-87, 5-110, and 5-111). One was from WRL (1959) and the other two were from the Minneapolis-Honeywell Regulator Company. The detector from WRL utilized a p-por-phase crystal, while the other two were prepared by the Czochralski method. The relative response as a function of chopping frequency for these three cells is shown in Figure 5-73. The effective time constants of these cells can be calculated by the expression

$$\tau_{\text{eff}} = 1/2\pi f$$

where f is the frequency at which the response degrades 3 db from the maximum value. Butter and McGlaughlin report good agreement between τ_{eff} and the time constant measured by the radiation-pulse technique, where one observes the photocurrent decay time. The average detectors constructed at WRL display time constants of about $50 \mu\text{sec}$ at 77°K .

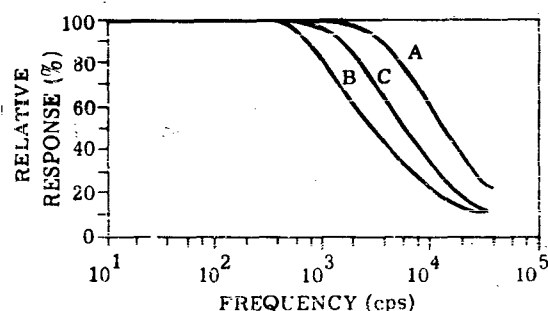


FIGURE 5-73. FREQUENCY RESPONSE OF T₂

5.5.6.3. Noise. The noise frequency spectrum of the three cells described above is shown in Figure 5-74. The noise is characterized by a $1/f$ power spectrum (except for cell A which follows $1/f^{2/3}$). Generation-recombination noise begins to dominate around 10^3 cps. Measurements (Reference 5-112) made on one selected cell from WRL indicated that the cell was background-noise limited when chopped at 5000 cps. Private communications with McGlaughlin of Minneapolis-Honeywell indicate that they have also constructed cells limited by background noise.

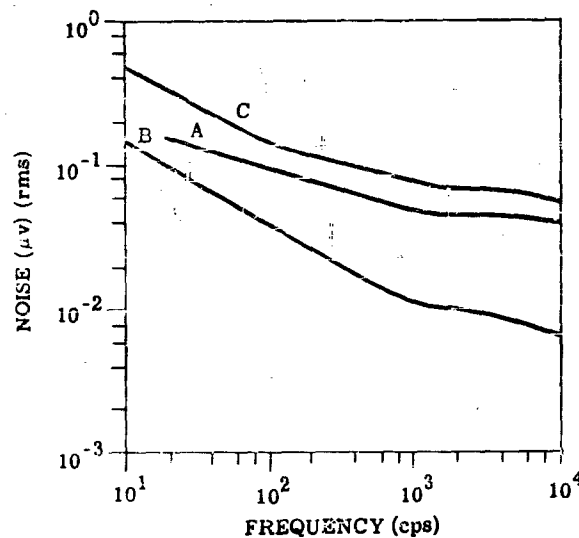


FIGURE 5-74. NOISE SPECTRUM OF Te

5.5.6.4. Detectivity. Shown in Figure 5-75 are the spectral dependence of $D^*(\lambda, 90, 1)$ for the three cells described above. Cell A is typical of the production model available from Minneapolis-Honeywell.¹¹ The other characteristics of these cells are given in Table 5-12. It should be noted here that the data shown in Figure 5-75 were taken at a chopping frequency of 90 cps. An examination of the relative response and noise (Figures 5-73 and 5-74, respectively) indicates that at 90 cps the noise limitation is $1/f$, and that chopping at higher frequencies will lead to a lower noise voltage without affecting the detector response. For cell A, increasing the chopping frequency from 90 cps to 2000 cps would decrease the noise from 10^{-7} volt to 4.5×10^{-8} volt (about a factor of 2). The

¹¹Private communications.

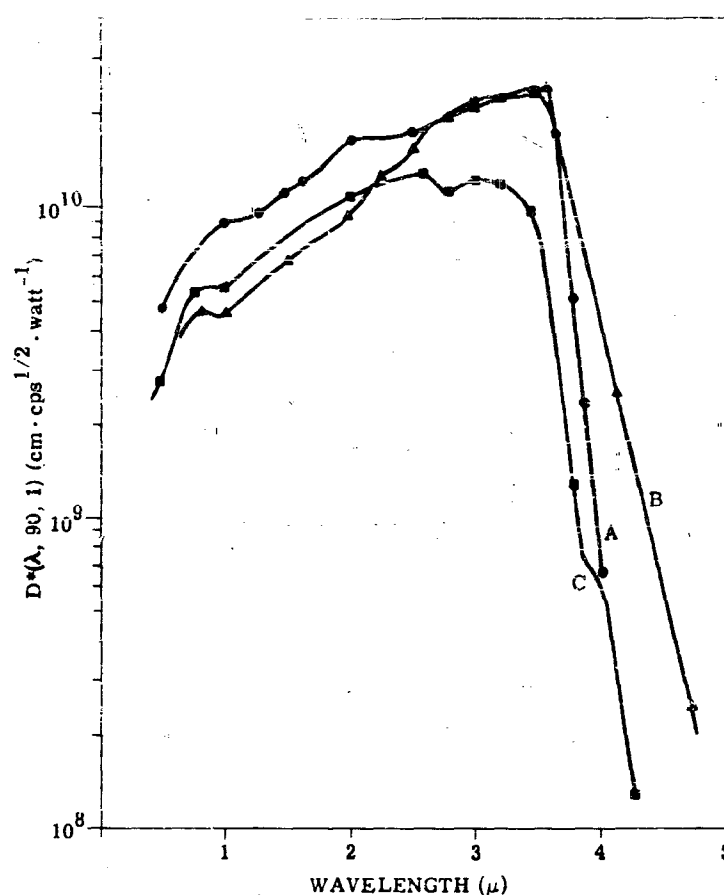


FIGURE 5-75. ABSOLUTE SPECTRAL RESPONSE OF Te

relative response remains unchanged. Therefore, the detectivity would increase by a factor of 2. A similar treatment of cell B would lead to an increase in detectivity by a factor of 4. This factor of 4 would place cell B only a factor of 5 from the theoretical limit of detectivity. The theoretical limit is calculated by assuming that all the noise is caused by the random arrival of photons from a 300°K background. This value is $5 \times 10^{11} \text{ cm}\cdot\text{cps}^{1/2}\cdot\text{watt}^{-1}$.

Figure 5-76 is a histogram of 20 detectors constructed from crystals grown by the vapor-phase method. These cells represent the early tellurium detector work at WRL. The number of cells is

TABLE 5-12. SUMMARY OF INAS DATA

Mfr.	Cell Area (mm ²)	Cell Number	Blackbody Response			Spectral Peak (μ)	Cell Temp. (°C)	Dark Resistance (ohms)
			NET (50°K, 90, 1) (w/cm ²)	NEP (500°K, 90, 1) (watts)	D* (500°K, 90, 1) (cm·cps ^{1/2} ·w ⁻¹)			
WRL	0.17	UM 59	4.7×10^{-3}	7.1×10^{-11}	1.3×10^9	3.6	-195	20
N-H	0.8	MH 38	1.7×10^{-8}	3.3×10^{-10}	5.1×10^8	2.6	-195	450
M-H	4.3	MH 117	$4. \times 10^{-9}$	1.9×10^{-10}	1.1×10^9	3.5	-195	2400

Cell Number	Response: Spectral Peak			Cell Noise (af = 5) (μv)	Data Source	Time Constant (μsec)
	NET (2, 90, 1) (2 pk' 90, 1) (w/cm ²)	2 pk' 90, 1) (2 pk' 90, 1) (watts)	D* (2 pk' 90, 1) (cm·cps ^{1/2} ·w ⁻¹)			
UM 59	2.2×10^{-9}	3.7×10^{-12}	2.5×10^{10}	1090	1	120
MH 38	4.7×10^{-10}	1.3×10^{-11}	1.3×10^{10}	150	2	49
MH 117	2.1×10^{-10}	9.0×10^{-12}	2.3×10^{10}	300	3	20

1. Properties of Photoconductive Detectors, NOLC Report Number 438, Navy Ordnance Laboratory, Corona, Calif., January 1959 (CONFIDENTIAL).
2. Properties of Photoconductors, NOLC Report Number 535, Naval Ordnance Laboratory, Corona, Calif., August 1960 (CONFIDENTIAL).
3. Properties of Photoconductors, NOLC Report Number 527, Naval Ordnance Laboratory, Corona, Calif., August 1960 (UNCLASSIFIED).

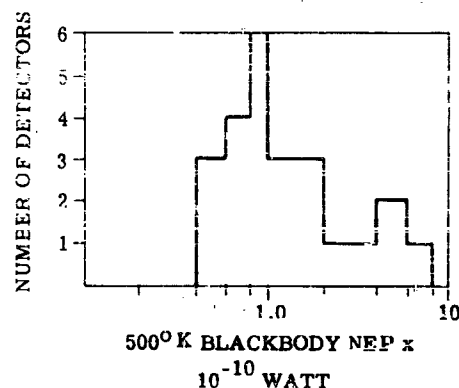


FIGURE 5-76. BLACKBODY NET DISTRIBUTION FOR 1/2 x 1/2-MM Te DETECTORS

plotted as a function of $NEP(500^{\circ}K, 90, 1)$. All the cells had sensitive areas of $1/2 \times 1/2 \text{ mm}^2$. D^* is related to NEP by the expression,

$$D^*(500^{\circ}K, 90, 1) = \frac{\sqrt{A} \sqrt{\Delta f}}{NEP(500^{\circ}K, 90, 1)}$$

Therefore, the best $D^*(500^{\circ}K, 90, 1)$ value recorded was about $1.3 \times 10^9 \text{ cm} \cdot \text{cps}^{1/2} \cdot \text{watt}^{-1}$. This corresponds to a peak $D^*(\lambda_{pk}, 90, 1)$ of $2.1 \times 10^{10} \text{ cm} \cdot \text{cps}^{1/2} \cdot \text{watt}^{-1}$. For tellurium the relationship between peak D^* and $D^*(500^{\circ}K)$ is

$$D^*(\lambda_{pk}, 90, 1) = 16 \times D^*(500^{\circ}K, 90, 1)$$

The degradation of D^* due to intense thermal backgrounds has not been determined conclusively as yet; however, preliminary results¹² indicate that D^* degrades by a factor of 5 for background levels of about 10^{-3} effective watts/cm². Effective implies that only those background photons are considered which cause band-to-band transitions in the tellurium detector.

¹²T. Limperis and W. Wolfe, Institute of Science and Technology of The University of Michigan.

In summary, the advantages of tellurium are:

- | | |
|-------------------------------|------------------------------------|
| (1) large quantum efficiency | (3) relatively short time constant |
| (2) advanced state of the art | (4) a propitious spectral response |

The quantum efficiency is high since tellurium is an intrinsic detector (i.e., photons produce charge carriers via band-to-band transitions). The high refractive index, however, leads to a reflectivity of about 50%. This loss can be overcome by antireflection coating.

The value of detectivity for typical commercially available tellurium detectors is 5×10^{10} $\text{cm} \cdot \text{cps}^{1/2} \cdot \text{watt}^{-1}$. This is only a factor of 10 from the theoretical limit, which implies an advanced state of the art.

A typical time constant is about 60 μsec , which is relatively short and indicates a satisfactory information capacity, for some applications.

Figure 5-77 shows the tellurium-detector spectral response located at a minimum of the spectral-emission curve for a clear summer daytime sky (Reference 5-113). This, coupled with the fact that the atmosphere has an infrared window between 3.3 and 4.1 μ , makes tellurium an interesting detector material for some infrared system applications.

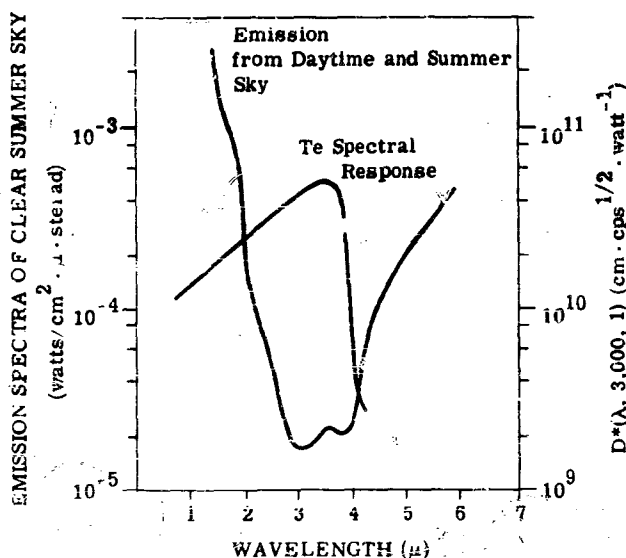


FIGURE 5-77. Te RESPONSE AND SKY EMISSION vs. WAVELENGTH

5.6. INDIUM ARSENIDE, by Thomas Limperis

Indium arsenide is an intermetallic semiconductor formed from elements in the third and fifth column of the periodic table. It has a zinc blende structure (Reference 5-114) with a forbidden band gap small enough to allow band-to-band absorption in the near-infrared window (2-5 μ). For the past three years, the Research Division of Philco Corporation has been active in developing an uncooled infrared quantum detector from this material. The characteristics of this detector are presented in detail later in this section.

5.6.1. ABSORPTION. The room temperature absorption spectrum has been determined by Oswald and Schade (Reference 5-115) by measuring the transmission and reflection from a single crystal of InAs with resistivity of approximately 10^{-3} ohm-cm. The results are presented in Figure 5-78. This spectrum indicates an optical band gap of 0.33 eV. The increase in absorption at wavelengths longer than 4.0 μ is due primarily to photon absorption by free carriers.

5.6.2. REFRACTIVE INDEX. The refractive index as a function of wavelength is presented in Figure 5-79. These data were also obtained by Oswald and Schade (Reference 5-115). They indicate a refractive index of around 3.2 in the region of 4 to 15 μ .

5.6.3. BAND GAP. The forbidden band was determined in two ways. First, the position of the absorption edge yields what is referred to as an optical band gap (or band gap determined by optical measurement). This value, as stated above, is around 0.33 eV at room temperature. The forbidden

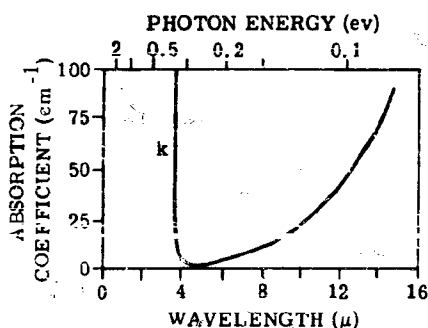


FIGURE 5-78. ABSORPTION COEFFICIENT OF InAs. Resistivity = 10^{-3} ohm-cm.

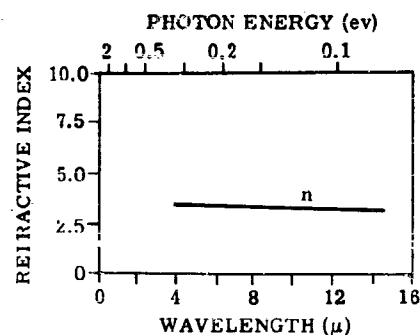


FIGURE 5-79. REFRACTIVE INDEX OF InAs. Resistivity = 10^{-3} ohm-cm.

band was also determined by measurements of the temperature dependence of resistivity. This investigation by Folberth et al. (Reference 5-116) yielded a value of 0.45 ± 0.02 ev at 0°K .

The temperature dependence of the forbidden band was determined by Oswald (Reference 5-117). He found that it followed the relationship $E_g = 0.45 - 3.5 \times 10^{-4}T$, where T is the sample temperature in degrees Kelvin. The room-temperature band gap calculated from the resistivity measurements is 0.35 ev, which is in good agreement with the optical measurement reported above.

The variation of bandwidth with temperature is shown in Figure 5-80, and the absorption spectra at different temperatures are presented in Figure 5-81. These data were taken using an indium arsenide crystal with a 2.5×10^{-3} -ohm-cm resistivity.

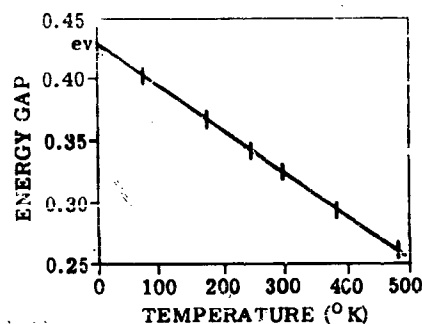


FIGURE 5-80. ENERGY GAP VS. TEMPERATURE FOR InAs

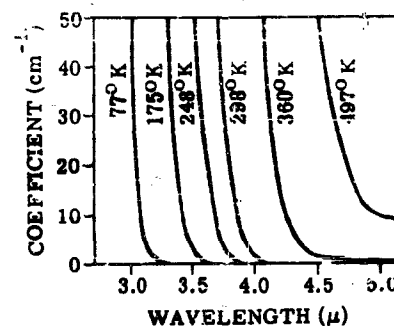


FIGURE 5-81. ABSORPTION SPECTRUM OF InAs WITH TEMPERATURE AS A PARAMETER

5.6.4. SPECTRAL RESPONSE. Detectors prepared from this material are operated in the photovoltaic mode, using a p-n junction. There are three fabrication methods investigated by Philco for the preparation of indium arsenide p-n junctions. They are;

- (1) Alloying of dopant to form a p-n junction.
- (2) Alloying of a chemically deposited dopant to form a junction
- (3) In-diffusion of dopant to form a junction.

The first involves heating a region of the n-type semiconductor base material to its melting temperature. A quantity of p-type dopant, either cadmium or zinc, is dissolved in the melted region, and the material is refrozen.

The second method utilizes a temperature below the melting point. A dopant, or solvent containing the dopant, is used to dissolve a layer of the n-type material, which is cooled so that most of the solvent material is rejected from the freezing volume leaving a p-type layer on the surface.

The in-diffusion method consists of heating the In or As base material in an atmosphere of cadmium or zinc allowing the dopant to diffuse into the surface. The formation of p-n junction by out-diffusion is done by heating the semiconductor in a high vacuum to a temperature just below its melting point. The impurity atoms diffuse to the surface of the sample and then evaporate. If the rate of evaporation is adjusted properly a junction will form.

In each of the methods just described a p-type layer is formed on the n-type base material. These layers are approximately 0.0065 inch thick. Leads are attached to the two surfaces, and a photovoltage is generated when photons of the proper wavelength are absorbed in the indium arsenide. The spectral characteristics of this photovoltage are dependent upon the p-type material used in the fabrication. For comparison, the spectral response of a zinc alloy and a cadmium-diffused cell are presented in Figures 5-82 and 5-83, respectively. The spectral response curve for an out-diffused InAs cell is the same as

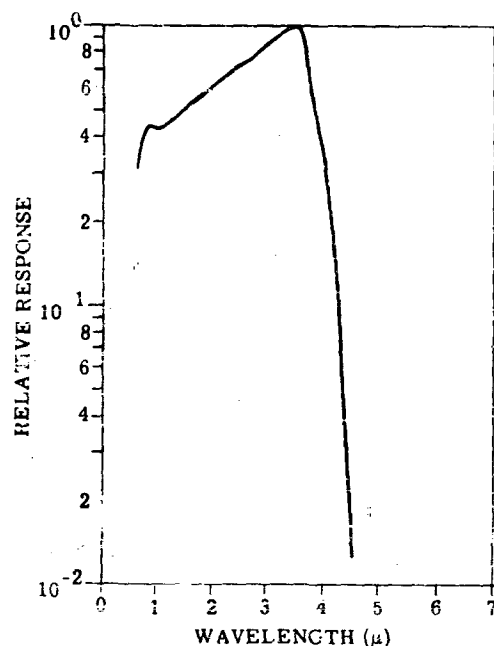


FIGURE 5-82. RELATIVE SPECTRAL RESPONSE OF InAs (Zn ALLOY)

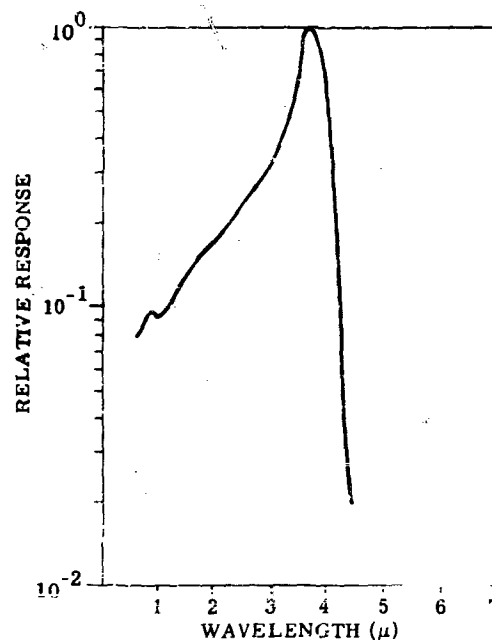


FIGURE 5-83. RELATIVE SPECTRAL RESPONSE OF InAs (Cd DIFFUSED)

for a zinc-alloyed sample. These cells were manufactured by Philco, and their characteristics were measured by NOLC (Reference 5-110).

5.6.5. TIME CONSTANT. The time constant of these detectors is less than $2\ \mu\text{sec}$. This value was determined from the data published by Philco in their series of progress reports and from the four detectors sent to NOLC by Philco for cell testing.

Interestingly enough, no detectable change in time constant occurs when cooling the cell to dry-ice temperature.

5.6.6. RESISTANCE. Since the photovoltaic mode is always used, the dark resistances reported in the literature are either front resistance, R_f , back resistance, R_b , or dynamic resistance, R_d . NOLC reports the dynamic resistance. The average value of dynamic resistance for the four cells reported was 25 ohms. This is a very low input resistance for any preamplifier, and consequently transformer coupling is required. The transformers used by NOLC were UTCHA 103A's which have a 2.5-ohm primary. Upon cooling the cell to dry-ice temperatures, the dynamic resistance increases to a value above 20,000 ohms.

Average values of the front and back resistance (determined from the Philco data) are: $R_f \approx 2.0$ ohms, and $R_b \approx 40$ ohms. The production models today have dynamic resistances between 200 and 400 ohms.¹³

The dependence of cell resistance upon the level of background irradiance has not been reported up to the time of this report.

5.6.7. NOISE. The noise voltage spectrum for a typical cell is presented in Figure 5-84. The $1/f$ noise component is predominant out to about 80 cps, after which the significant contribution is shot noise. Since the time constant is so short, the radiation may be chopped anywhere from 80 cps to around 100 kcps without degrading the signal-to-noise ratio; however, beyond this point, the response decreases with increasing frequency, and consequently a degradation in D^* results.

5.6.8. DETECTIVITY. Thirty-seven room-temperature InAs detectors have been reported to date, all constructed by Philco. They include detectors prepared by the three methods of fabrication discussed in Section 5.6.4. Of these, 33 were reported in their periodic progress reports, while the

¹³Private communications with P. Cholet.

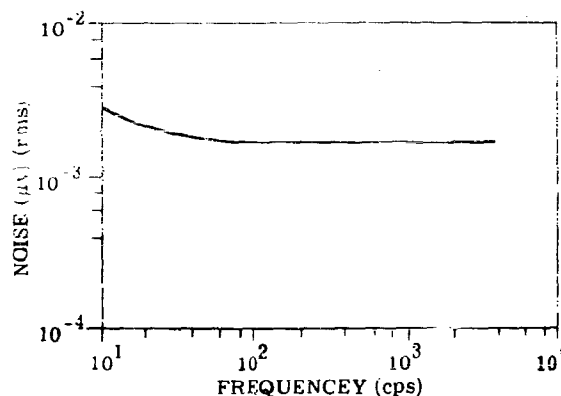


FIGURE 5-84. NOISE SPECTRUM FOR A TYPICAL InAs CELL

other four detectors were tested at NOLC. The average value of D^* (500°K , 750, 1) was $0.8 \pm 0.5 \times 10^8 \text{ cm} \cdot \text{cps}^{1/2} \cdot \text{watt}^{-1}$. This corresponds to a D^* (λ_{pk} , 750, 1) of $1.6 \times 10^9 \text{ cm} \cdot \text{cps}^{1/2} \cdot \text{watt}^{-1}$.

The best cell of the group had a D^* (λ_{pk} , 750, 1) of $3.6 \times 10^9 \text{ cm} \cdot \text{cps}^{1/2} \cdot \text{watt}^{-1}$. Cholet (Reference 5-118)¹⁴ states that with improved construction techniques, D^* (λ_{pk} , 750, 1) should increase by a factor of 6, or the average cell D^* (λ_{pk} , 750, 1) would become about $10^{10} \text{ cm} \cdot \text{cps}^{1/2} \cdot \text{watt}^{-1}$. The sensitive areas of these cells range in size from 0.25 mm^2 to 7.0 mm^2 .

The temperature dependence of D^* is illustrated in Figure 5-85. It is apparent that an optimum operating temperature exists near the temperature of dry ice. The D^* value at this optimum temperature is better by a factor of three than the D^* measured at 300°K .

Attempts at immersion have been made by Philco in the following way: the sensitive element was immersed in Q dope (polystyrene) and a sapphire lens was attached. The spectral response of this unit showed a strong absorption band around 3.5μ caused by the polystyrene. Preliminary measurements with low-melting ternary glasses as an immersion medium have given excellent results; however these data have not yet been published.

¹⁴According to private communications with Dr. Cholet, the average D^* (λ_{pk} , 800, 1) of today's InAs cell is about $5 \times 10^9 \text{ cm} \cdot \text{cps}^{1/2} \cdot \text{watt}^{-1}$.

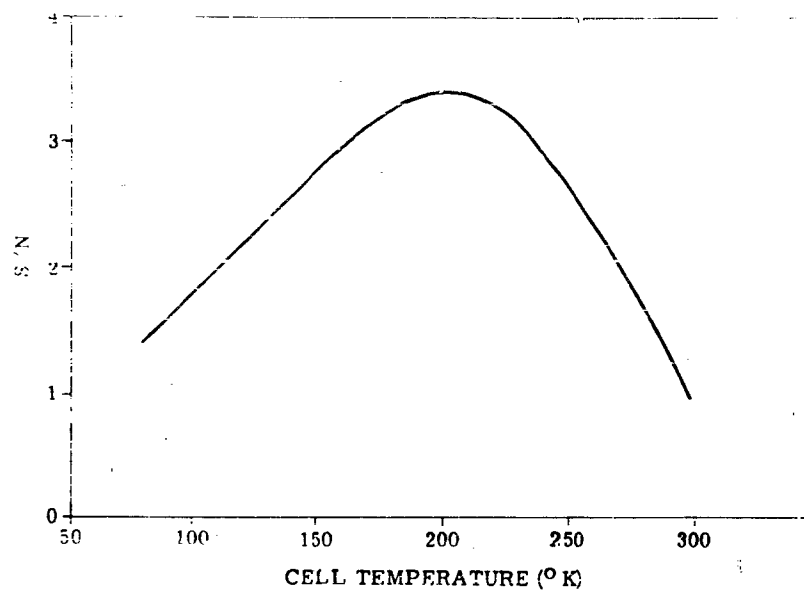


FIGURE 5-85. S/N RATIO VS. CELL TEMPERATURE

5.7. INDIUM ANTIMONIDE. by Joseph Mudar, Thomas Limperis, and William L. Wolfe

5.7.1. INTRODUCTION. Until the early 1950's, the emphasis on infrared photodetector development was centered on thin, polycrystalline films of the lead salts, PbS, PbSe, and PbTe. The advancement of solid-state physics, particularly semiconductors, led to the successful development of a number of techniques for the preparation of pure, synthetic, single crystals. These crystals were considered as potential infrared detectors. Shive (Reference 5-119) described such detectors made of germanium in 1950. However, the spectral response was limited to the intrinsic absorption region of Ge, namely wavelengths shorter than 1.75μ .

There are two obvious ways to extend the spectral response of bulk detectors to longer wavelengths. The first is to add impurities which introduce allowed electron energy levels in the forbidden gap, and the second is to choose materials which have a smaller intrinsic band gap. The impurity approach has been used extensively with Ge, and is described earlier in this report. The choice of other materials which have appropriate band gaps has led to detectors fabricated from Te, InAs, InSb, and GaAs. InSb, one of the most interesting of all semiconductors, because of its unusual properties, is the subject of this section. It is one of the intermetallic compounds made up of elements from column III and column V of the periodic table. Many of its properties are similar to the properties of its neighbors in column IV, (e.g., Si, Ge, and Sn). Since In and Sb are in the same period as Sn, InSb should have many properties similar to Sn—and it does.

Welker (References 5-120 and 5-121) made extensive measurements on the electrical, optical, and mechanical properties of single-crystal InSb. These measurements showed that some properties of the material have extreme values. (For instance, the electron mobility is very high— $80,000 \text{ cm}^2 \cdot \text{volt}^{-1} \cdot \text{sec}^{-1}$ —at 300°K .)

5.7.2. PHYSICAL PROPERTIES. Indium antimonide has a gray, metallic appearance, very much like tin. It crystallizes in the zinc-blende structure, has a melting temperature of 523°C at 1 atmosphere, and a specific gravity of 5.78 at room temperature. It exists only as a solid under standard conditions of temperature and pressure; in the molten state it is an ideal solution of In and Sb.

5.7.3. OPTICAL PROPERTIES. The optical absorption has been measured by Moss, Smith, and Hawkins (Reference 5-122). They measured the external transmittance of a number of very thin slices of a single crystal of pure material. Their results are shown in Figure 5-86. The absorption edge (defined as the point of maximum slope) is seen to be 6.94μ at room temperature. This corresponds to 0.175 eV for the band gap.

The position of the absorption edge is strongly dependent upon the temperature and the concentration of n-type impurity.

The apparent optical energy gap of indium antimonide as a function of electron concentration (as calculated by Kaiser and Fan in Reference 5-123) is shown in Figure 5-87. It is noted that for concentrations below 10^{17} cm^{-3} , the room-temperature absorption limit lies at 0.18 eV or 7μ , implying absorption transitions that are intrinsic in nature. For extrinsic carrier concentrations varying from 10^{17} cm^{-3} to $5 \times 10^{18} \text{ cm}^{-3}$, the absorption edge moves from 0.18 eV to approximately 0.50 eV, which corresponds to a wavelength shift from 7.0μ to 2.5μ . This behavior is anomalous; in most semiconductors, impurity centers decrease the optical energy gap and therefore shift the absorption edge to longer wavelengths. This unusual behavior is explained by Burstein (Reference 5-124), who postulates that lower states of the conduction band are progressively filled by electrons, so that absorption transitions can only take place to the higher, empty, conduction-band states.

The variation of the optical energy gap with temperature might best be understood by examining the band structure as a function of lattice spacing, which is shown in Figure 5-88. The normal lattice

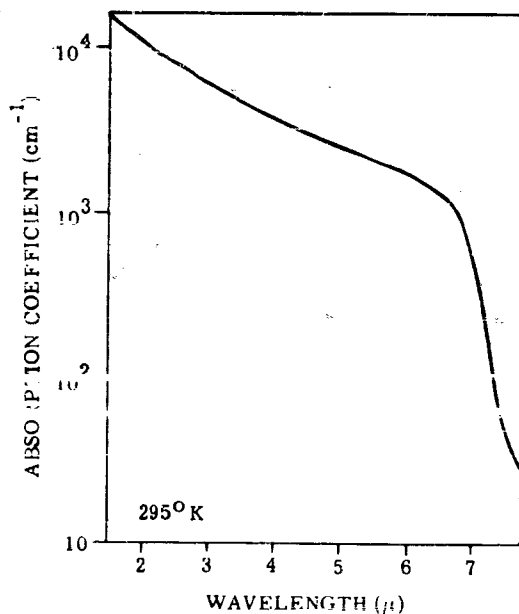


FIGURE 5-86. ABSORPTION IN InSb

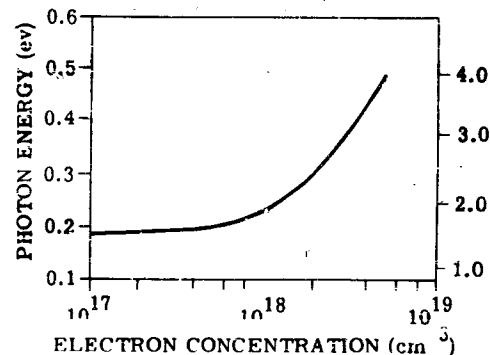


FIGURE 5-87. APPARENT OPTICAL ENERGY GAP OF InSb AS A FUNCTION OF ELECTRON CONCENTRATION

spacing is that spacing which exists when the material is at room temperature. As the temperature decreases, the lattice spacing decreases, thereby yielding an increased value for the energy gap. Also, there is a narrowing of the valence and conduction bands due to an electron-lattice interaction which also yields a higher value for the energy gap. The net result of these phenomena is shown in Figure 5-89. At room temperature the energy gap is 0.175 ev. In the temperature range from 300°K to 100°K the change is linear with a slope of -3.3×10^{-4} ev/°K (Reference 5-100, p. 230). Below 100°K the energy gap is essentially constant, changing only 0.05 ev for a ΔT of 100°K.

Measurements of the refractive index of very thin single crystals of InSb with a carrier concentration less than 10^{16} cm⁻³ have been made by Moss, Smith, and Hawkins (Reference 5-122). Moss has subsequently constructed a theoretical curve on the basis of dispersion theory. Both the experimental and the theoretical curves are shown in Figure 5-90.

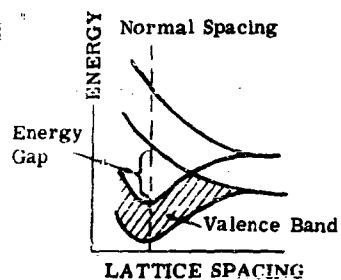


FIGURE 5-88. BAND STRUCTURE VS. LATTICE SPACING

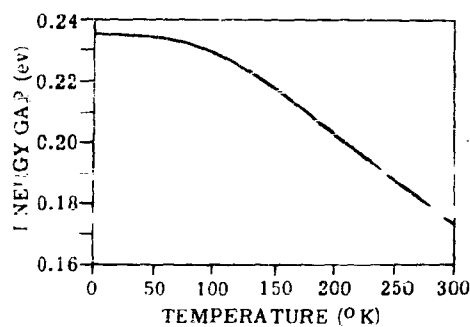


FIGURE 5-89. ENERGY GAP AS A FUNCTION OF TEMPERATURE FOR InSb

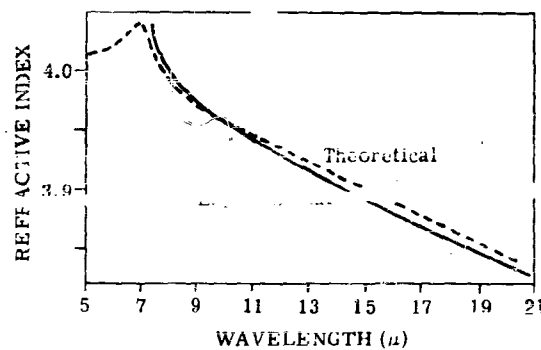


FIGURE 5-90. REFRACTIVE INDEX OF InSb

5.7.4. INDIUM ANTIMONIDE PHOTODETECTORS. Single crystals of indium antimonide are used in several ways to detect infrared photons. The first and perhaps the most widely used is the photovoltaic mode. Here, incoming photons are incident on or in the vicinity of a p-n junction of InSb, and the resulting charge carriers generate a photovoltage. The second mode, photoelectromagnetic, employs single crystals of InSb immersed in a magnetic field. The infrared photons cause band-to-band transitions, and the resulting charge carriers are separated by the magnetic field, thus generating a signal voltage. In the third mode, the change in conductivity is monitored. In this case, incident photons produce hole-electron pairs which alter the crystal's conductivity, and this is detectable as a change in voltage. The spectral response of these cells is related directly to the intrinsic band gap of InSb.

Impurity-activated crystals of InSb have been reported on by Blunt (Reference 5-125) in 1958 and recently by Engeler (Reference 5-126) and Smith (Reference 5-127). These detectors include InSb doped with Au, Ag, and Cu. An extremely long wavelength, impurity-activated detector employing n-type impurities which lie close to the conduction band has been reported by Smith. The spectral response of these cells depends upon the ionization energy of the impurity level. The detector types mentioned above are described in detail in the following sections.

5.7.4.1. The Photovoltaic Detector. There are two different types of photovoltaic detectors. The first (historically) was constructed by pulling an InSb boule in the usual manner, but at an appropriate time a large quantity of p-type impurity was introduced. Thus, a bar which has a relatively sharp transition from n-type material to p-type material results. This is appropriately called a grown junction (more often referred to simply as a junction). The other type of photovoltaic detector is a diffused-junction cell. These cells are prepared by heating an n-type sample until a thin p-type layer is formed on the surface. This may also be accomplished by diffusing p-type impurities such as zinc or cadmium into the surface of a piece of n-type InSb. The detection mechanism is the same in both grown and diffused cases; however, there is a considerable difference in cell geometry.

For both the grown junction and diffused-junction types, the signal-to-noise ratio may often be optimized by applying a reverse bias to the p-n junction. The relationship between signal, noise, and signal-to-noise ratio with the applied bias current level for a typical detector is presented in Figure 5-91. In some instances, the optimum detectivity is obtained at zero bias. Besides increasing the signal-to-noise ratio, back biasing also increases the absolute level of signal and noise voltage. This eases the problem of low-noise preamplifiers.

The photovoltaic detectors have a theoretical limit of detectivity which is larger by a factor of $\sqrt{2}$ than the PEM or photoconductive detectivities. This factor comes from the fact that background

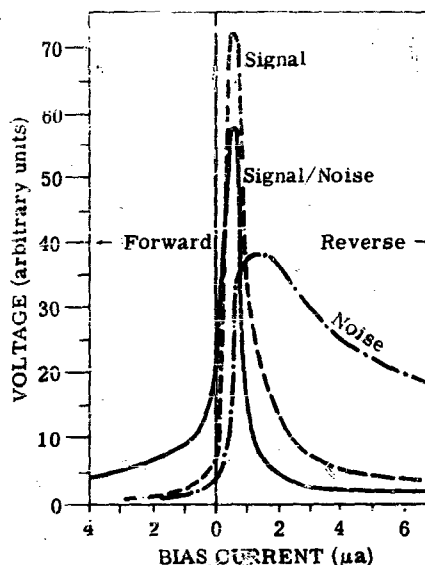


FIGURE 5-91. S/N RATIO VS. BIAS CURRENT FOR LAS CELL NO. PV-52

noise, which is the ultimate limiting noise source in detectors, manifests itself as both generation and recombination noise in the PEM or photoconductive detectors, but only as a generation noise in the photovoltaic detector. The net effect is a $\sqrt{2}$ -higher noise in PEM or photoconductive detectors (see Chapter 3 for a detailed discussion of noise).

5.7.4.1.1. Grown Junction (Photovoltaic). The principle of the grown junction is illustrated in Figure 5-92. A potential gradient is produced at the junction of the p- and n-material. When radiation is incident on the bar, electron-hole pairs are generated, and, by the process of diffusion, these charge carriers approach the electric field at the junction. This field causes the holes to be swept across the junction into the p-type region, and the electrons are swept into the n-type region, producing a photovoltage between the leads. The sensitive area is defined by the width of the junction (usually about 50 μ), and the breadth of the bar. Extremely small sensitive areas may be obtained by this construction technique. These long thin sensitive areas are ideally suited for some scanner applications.

Chicago Midway Laboratories (now LAS, Laboratories for Applied Science, The University of Chicago) initiated (Reference 5-128) the work on grown-junction detectors and reported the characteristics of many cells fabricated in this way.

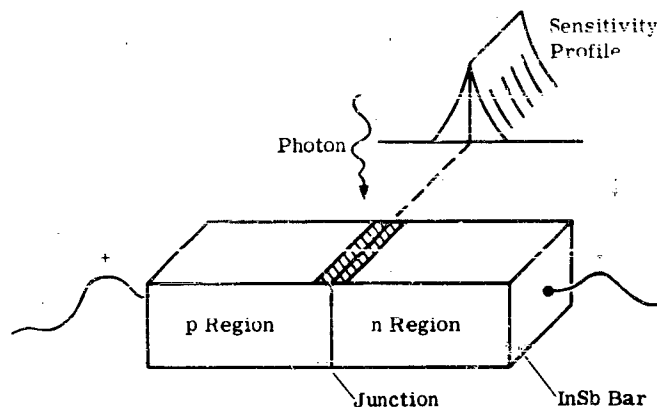


FIGURE 5-92. GROWN JUNCTION

5.7.4.1.1.1. Noise Spectra. The three grown-junction detectors manufactured by LAS and measured by NOLC (Reference 5-129) had considerably different noise voltage spectra (see Figure 5-93). They all had a $1/f$ component; however, the frequency at which this component became insignificant was different for each detector. Two of the detectors, PV-51 and PV-52, which had an optimum back bias of about 2.5 volts, displayed a $1/f$ component out to 1000 cps where the noise became white. The white noise is probably shot noise (see Chapter 3 for a detailed discussion of noise). The third detector, PV-20, had a $1/f$ noise power spectrum out to the limit of the measurement (10^4 cps). Interestingly enough, detector PV-20 had a zero optimum back bias.

5.7.4.1.1.2. Spectral Response. A typical spectral response curve (Reference 5-130) for liquid-nitrogen-cooled, InSb, grown-junction detectors is shown in Figure 5-94. The long-wavelength cutoff is about 5.7μ , which agrees nicely with what one might predict from the band gap. The departure from the approximate saw-tooth configuration which one associates with quantum detectors is possibly due to a "disturbed" (Reference 5-131) layer which forms on the junction and is caused by the etching solution.

5.7.4.1.1.3. Time Constant. The time constant of this detector is generally less than $2 \mu\text{sec}$. This means that maximum responsivity exists out to chopping frequencies of about 10^5 cps. Beyond 1000 cps, the noise is white for the back-biased detectors, consequently no increase in signal-to-noise ratio can be expected for chopping frequencies beyond this point. At frequencies higher than 10^5 cps, the responsivity begins to degrade due to time-constant considerations, and thus an optimum chopping frequency for this detector type would be between 1000 cps and 10^5 cps.

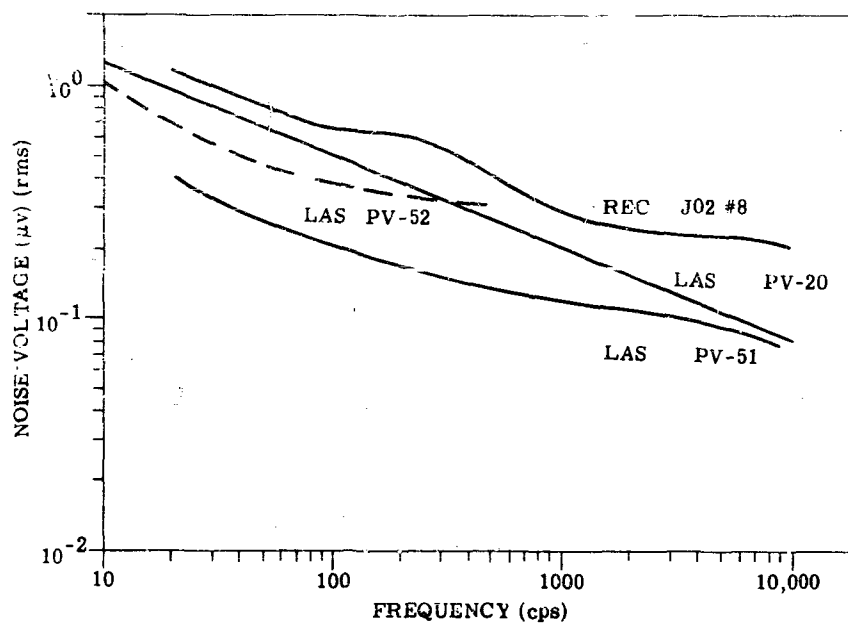


FIGURE 5-93. NOISE SPECTRA OF GROWN-JUNCTION InSb DETECTORS

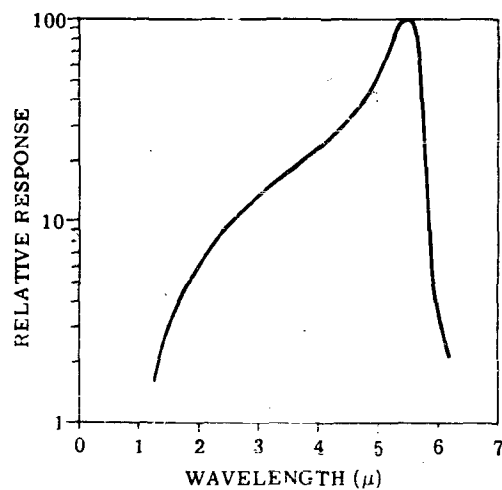


FIGURE 5-94. SPECTRAL RESPONSE OF A GROWN-JUNCTION InSb DETECTOR

5.7.4.1.1.4. Impedance. For junction-type detectors the impedance must be referred to as a back, forward, or dynamic impedance. The latter is defined as

$$Z_d \triangleq \frac{\Delta E}{\Delta I}$$

where $\Delta E/\Delta I$ is simply the slope of the rectification curve (E vs. I). An average value of the dynamic resistance determined from the reported data is about 41 kohms.

5.7.4.1.1.5. Detectivity. Difficulties are encountered in associating a D^* value with a grown-junction cell. The reason for this is the peculiar sensitivity contour (Figure 5-95) which presents a problem in defining the detector area. One can see by the figure that the breadth of the junction may be considered as large as 100μ . However, the junction breadth is often defined as the distance between the points where the relative response falls to 37% of the maximum value.

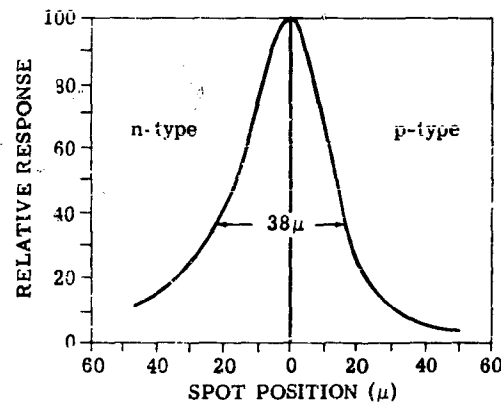


FIGURE 5-95. SENSITIVITY PROFILE ACROSS p-n JUNCTION OF A TYPICAL GROWN-JUNCTION DETECTOR. Infrared spot diameter $\approx 25 \mu$.

Table 5-13 is a list of the detectors and their characteristics which was published by LAS and NOLC. It is interesting to note that 11 of the cells have two entries in the table, one for the results of measurements in the unbiased condition, and the other for measurements in the back-biased condition. This is illustrated in the histogram in Figure 5-96. The shaded area represents detectivity values obtained on the back-biased cells and the blank squares represent the unbiased detectors. Little can be inferred from this histogram since only 28 cells are listed; however, indications are

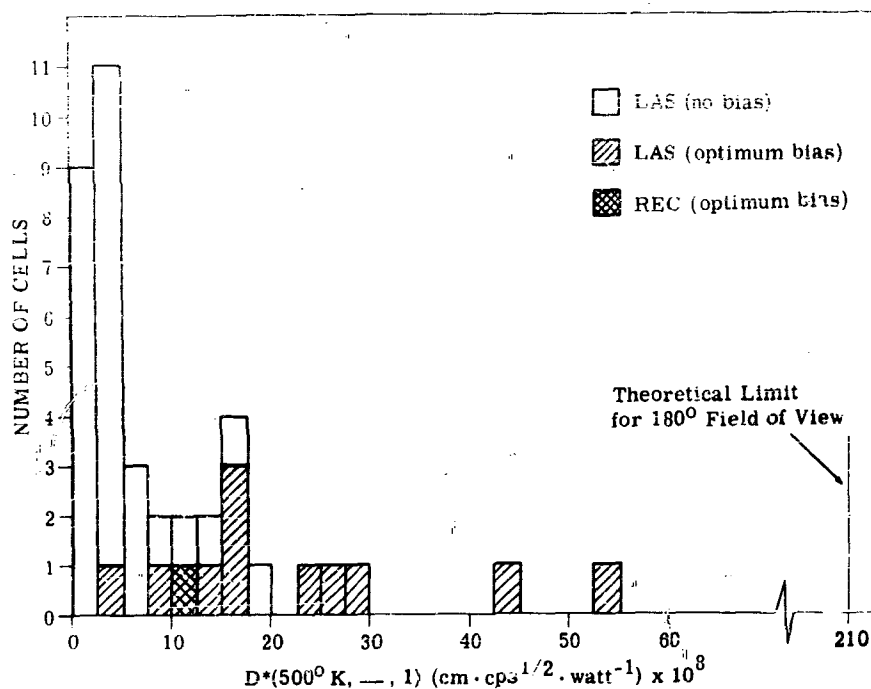


FIGURE 5-96. HISTOGRAM OF GROWN-JUNCTION CELLS

that the average D^* value of the back-biased detectors exceeds the average D^* value of the unbiased cells by about a factor of 5. The highest $D^*(500^\circ\text{K}, 90, 1)$ was from a back-biased cell which had a value of 5.4×10^9 (a factor of about 4 from the theoretical limit of detectivity).

The effect of increasing background temperature on the detectivity of grown-junction cells has not been determined as yet. Measurements of this type have been made on the diffused-junction cells. These data are described in the photovoltaic diffused-junction section.

Commercial manufacturers of grown-junction photovoltaic detectors are Radiation Electronics Corporation, Polan Industries Inc., and the Crosley Division of the Avco Corporation.

5.7.4.1.2. Diffused Junction (Photovoltaic). The formation of a p-type surface on an n -type InSb slab was discovered by Goldberg at LAS early in 1956. The p-type surface was produced by heating the slab to 450°C in a vacuum. The resulting p-n junction proved to be highly photosensitive at 77°K . The mechanism of signal generation by incident radiation for diffused-junction photovoltaic

detectors is identical to the signal-generation mechanism of grown-junction detectors. Over the past few years the diffused-junction detector has become the more popular of the two. There are two reasons for this: first, the diffused junction detector is not restricted to a line configuration as in the grown-junction detector. For example, diffused-junction detector areas of 0.25 mm^2 to 36 mm^2 are readily available from the manufacturers today. Second, the method of manufacture is more adaptable to large-scale manufacturing techniques.

5.7.4.1.2.1. Spectral Response. A typical spectral-response curve is shown in Figure 5-97. This response is essentially that of a quantum detector having a peak at 5μ and a cutoff wavelength at 5.3μ , compared to a grown-junction cell which has a peak at 5.5μ and a cutoff wavelength at 5.7μ . This difference is due to long-wavelength radiation being absorbed so deep in the crystal that carriers produced recombine before diffusing back to the junction region of the diffused junction.

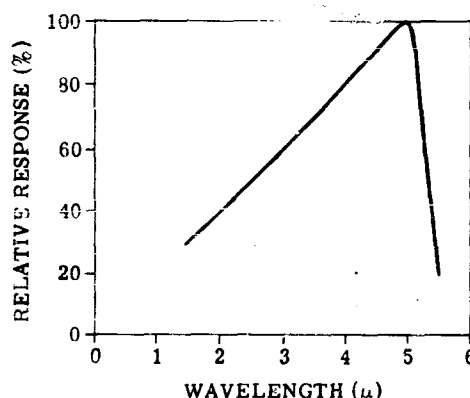


FIGURE 5-97. TYPICAL SPECTRAL RESPONSE FOR DIFFUSED-JUNCTION CELLS

5.7.4.1.2.2. Time Constant and Frequency Response. Since the time constant of InSb detectors is of the order of $1 \mu\text{sec}$ or less, the frequency spectrum of the responsivity should be flat out to at least 10^5 cps . However, since the capacitance of the detector is of the order of 10^{-10} F , the detector should increase with chopping frequency until the detector is in the white-noise spectrum.

5.7.4.1.2.3. Noise. Two noise voltage curves are shown in Figure 5-98. Curve A was selected from data published by NOLC and is typical of the noise spectrum of early diffused-junction detectors. The

predominant noise source appears to follow a $1/f^n$ law where n varies from 0.3 to 0.5. Recently, however, Levenstein (Reference 5-47) and Beyen et al. (Reference 5-132) have reported measurements on several InSb diffused-junction detectors with detectivities which were about a factor of 1.2 below the theoretical limit at chopping frequencies of 900 cps. Curve B is a noise-spectrum curve associated with these recent detectors and shows the white-noise spectrum beginning at about 500 cps.

As shown in Table 5-14, the cell noise voltage ranges in value from 1.1 to 200×10^{-9} volts. Such small noise voltages require very careful preamplifier design (Reference 5-133). Back biasing provides some help on this score by increasing the detector impedance.

5.7.4.1.2.4. Cell Impedances. Cells can be made having a wide range of impedances. The majority of the cells reported had dynamic impedances in the 500-ohm to 1000-ohm range. Currently produced cells have impedances in the 1000-ohm to 10,000-ohm¹⁵ range, depending on cell area.

5.7.4.1.2.5. Detectivity. The magnitude of the photovoltaic signal will depend on the number of hole-electron pairs generated and the number of these pairs that are separated before they recombine. Decreasing the recombination rate will, therefore, increase the signal voltage. The recombination

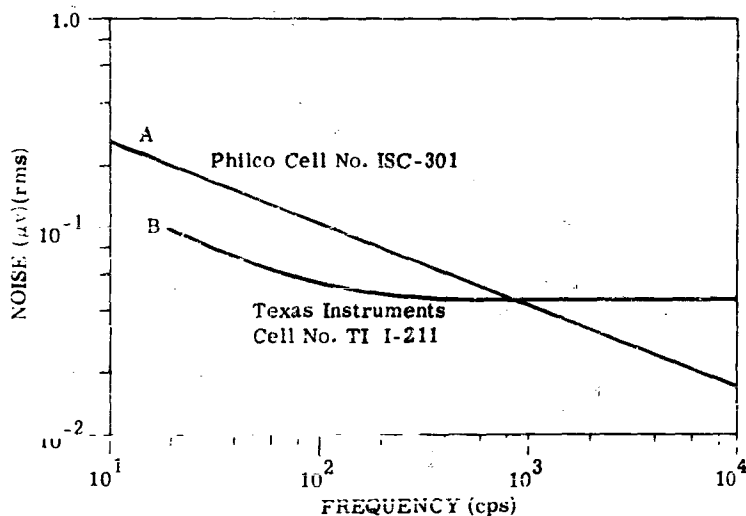


FIGURE 5-25. InSb PHOTOVOLTAIC DIFFUSED-JUNCTION NOISE SPECTRUM

¹⁵Private communications with Werner Beyen.

that takes place in the bulk of the surface layer can be reduced by reducing the thickness of the surface layer. Recombination at the surface can be reduced by proper etching and cleansing techniques.

The detectivity is also a function of the initial impurity content of the bulk material. Philco Corporation reports on optimum impurity doping of about 5×10^{15} impurities, cm^{-3} .

Since the InSb room-temperature energy band gap is 0.18 eV, photovoltaic detectors must be cooled to decrease the number of thermally generated hole-electron pairs and thereby establish the junction in order to obtain high detectivities. Very little is gained in cooling below 77°K .

Boeing Aircraft Company has performed a study of photosaturation effects on infrared quantum detectors (Reference 5-134). This work was done to determine the degradation of system performance due to aerodynamic heating of domes in infrared seeking missiles. The responsivity and noise of various detectors were measured as a function of intensity of background radiation. The background radiation was measured in units of effective watts/ cm^2 . This effective flux density is obtained by multiplying the spectral power density of the saturating source by the normalized spectral response of the cell. The degradation of normalized detectivity of an InSb diffused-junction photovoltaic detector is shown in Figure 5-99. This degradation is due entirely to an increase in noise level. The responsivity remained constant over this flux range.

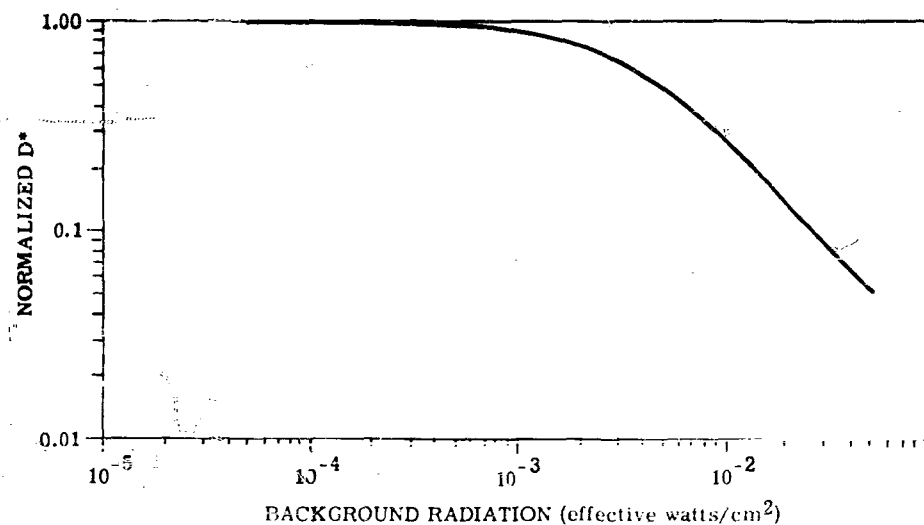


FIGURE 5-99. D^* VS. BACKGROUND RADIATION IN DIFFUSED-JUNCTION CELLS

Table 5-14 is a compilation of the data on InSb diffused-junction detectors reported by NOLC, TI, Philco, and Syracuse University.

The number of cells in a given detectivity range vs. detectivity are plotted in histogram form in Figure 5-100. The highest D^* (500°K, —, 1) value reported was $2.1 \times 10^{10} \text{ cm} \cdot \text{cps}^{1/2} \cdot \text{watt}^{-1}$ for a Philco Corporation detector measured at Syracuse University. This cell apparently has an angular field of view of 130°. Normalizing this D^* value to a 180° field of view places the detectivity of this cell at only a factor of 1.2 (or 20%) from the theoretical limit. The histogram shows a mode at $D^* = 2 \times 10^9 \text{ cm} \cdot \text{cps}^{1/2} \cdot \text{watt}^{-1}$ or about a factor of 10 from the theoretical limit. The average detectivity is $3.7 \times 10^9 \text{ cm} \cdot \text{cps}^{1/2} \cdot \text{watt}^{-1}$. Ratios of D^* (500°K, —, 1)/ D^* (λ_{pk} , —, 1) were in a narrow

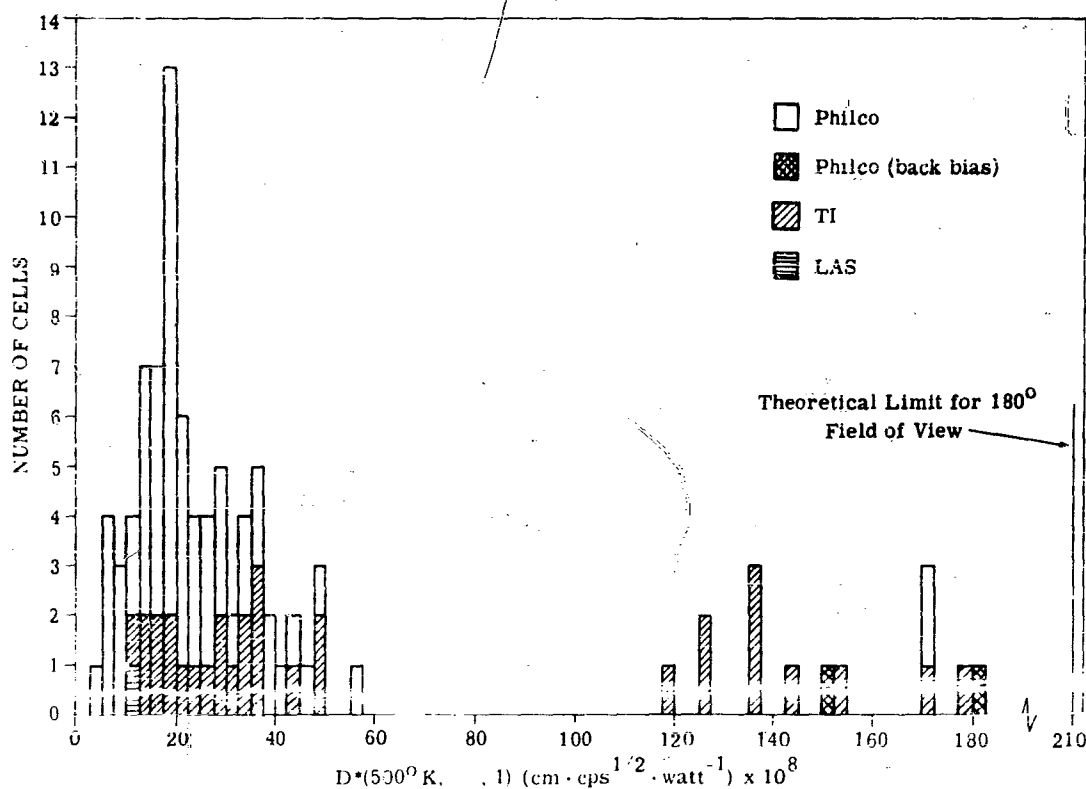


FIGURE 5-100. HISTOGRAM OF DIFFUSED-JUNCTION CELLS

CONFIDENTIAL

[illegible]

TABLE 5-14 (Continued)

[illegible]

[illegible]

3. Final report on development of high sensitivity *infected* (see title). Report Number N 27-115 (Final). P. Washington, Pa., November 1959 (UNCLASSIFIED).
4. Final Report on Director's Program of Research on *Chlamydia* (see title). Columbia University, New York, New York, 1960 (UNCLASSIFIED).
5. Laboratory Manual for the *Chlamydia* (see title). Department of Health, Education & Welfare, Public Health Service, Washington, D.C., 1960 (UNCLASSIFIED).
6. J. J. Bowers, G. B. Brown, H. D. Adams, and L. S. Sacks. Laboratory Detection Report—1 and 2nd Workshop on *Chlamydia*. *Trans Am Soc Trop Med Hyg*, Vol. 35, 1965 (UNCLASSIFIED).

[illegible]

range of about 5.0 with a maximum of 5.4. Only the D^* ratios of cells showing a quantum-detector-type spectral response were considered in these statistics. Present-day manufacturers of this detector can furnish cells with D^* (500°K, —, 1) values of 5×10^9 . Higher detectivities are furnished at an increased price.

Commercial manufacturers of the diffused-junction, photovoltaic, indium antimonide detector are Texas Instruments and Philco Corporation.

5.7.4.2. Photoconductive Detectors. The increase in electrical conductivity caused by radiation incident on the crystal is the mechanism utilized in photoconductive detectors. The direct effect of this incident radiation is an increase in the number of mobile charge carriers in the crystal. If an impinging photon has energy greater than the energy difference between the highest point of the filled valence band and the lowest point of the vacant conduction band, then there is a high probability that the absorbed photon will create a hole-electron pair. Both the hole and the electron may contribute to the increase in conductivity.

Shortly after Welker's original work on the compounds formed by elements in columns III and V of the periodic table, Avery et al. (Reference 5-135) demonstrated that InSb had photoconductive properties out to 7μ at room temperature. Goodwin (Reference 5-136) demonstrated that excellent cooled detectors could be made from InSb which were sensitive out to 5.5μ . Due to the very short carrier lifetime in InSb it was previously felt that this material would be unsuitable for photoconductive detectors because of the small signal voltage. This signal voltage was a factor of 10 smaller than that observed in photovoltaic InSb. However, the noise level at frequencies sufficiently high to be out of the $1/f$ region is about a factor of 10 lower than the noise level in photovoltaic detectors at the same frequency. This results in a comparable S/N ratio. Photoconductive InSb detectors now compare very favorably with photovoltaic detectors. They have detectivities as high as D^* (500, 1080, 1" = $1 \times 10^{10} \text{ cm}^2 \cdot \text{cm}^{-1} \cdot \text{watt}^{-1}$, or a factor of 1.5 from theoretical limit (Reference 5-137). Commercial detectors are now available which are operable in a temperature range from 77°K to room temperature (Reference 5-138).

All detectors have been made from grown single crystals of InSb. To obtain the purity required, the individual constituents, In and Sb, must be zone-refined as well as the InSb compound. Due to the small energy band gap in InSb, a large number of electron-hole pairs are thermally generated at room temperature. The conduction will be dominated by these intrinsic carriers for impurity concentrations of less than $10^{16} \text{ atoms} \cdot \text{cm}^{-3}$. Therefore, impurity measurements for values lower than 10^{16}

atoms cm^{-3} must be made at lower temperatures. This is usually accomplished by making liquid-nitrogen Hall measurements.

Slices cut from these boules are lapped, polished, and etched to the desired thickness. They can be as thin as $4\ \mu$ (Reference 5-137). Contacts are usually soldered to the ends and protected before etching.

5.7.4.2.1. Spectral Response. Typical spectral response curves for 77°K , 193°K , and 300°K are shown in Figure 5-101. The 77°K curve is for a Syracuse University detector and is similar to the photovoltaic response curve having a peak at about $5\ \mu$ and a cutoff wavelength at about $5.5\ \mu$. The 193°K curve is for a Texas Instruments detector operating at solid CO_2 temperature. The increase in operating temperature results in a spectral-peak shift to about $6\ \mu$. The 300°K curve is based on data from a Mullard Limited of England ORP-10 detector. This curve shows a peak at $6.5\ \mu$ with a cutoff wavelength at about $7.3\ \mu$.

5.7.4.2.2. Frequency Response and Time Constant. Although no curves of signal voltage vs. chopping frequency were found in the literature, LAS reports a flat frequency response out to about 75 kcs (Reference 5-138). Due to the short time-constant characteristic of InSb the frequency response should be flat out to at least this frequency. Practically all of the detectors reported had a time constant of less than $1\ \mu\text{sec}$. However, Syracuse researchers (Reference 5-139) discuss the occurrence of two time constants: one of less than $1\ \mu\text{sec}$, the other several microseconds. Figure 5-102 shows a response to a square radiation pulse with two decay slopes appearing.

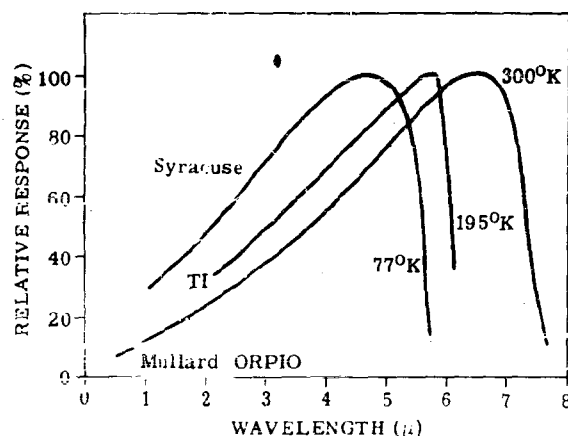


FIGURE 5-101. SPECTRAL RESPONSE OF InSb PHOTOCONDUCTIVE CELLS

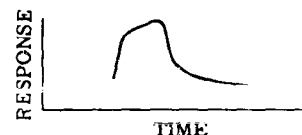


FIGURE 5-102. RESPONSE OF InSb TO A SQUARE RADIATION PULSE. Two decay modes appear.

5.7.4.2.3. Noise. A typical noise spectrum is shown in Figure 5-103. The main contribution appears to be $1/f$ noise out to 10^3 cps. Since these noise voltages are extremely small (of the order of 10^{-9} to 10^{-8} volt), great care must be devoted to the associated electronics to insure that the system is detector-noise limited. Since the signal voltage does not vary with the chopping frequency in the $1/f$ region, chopping at a frequency of about 10^3 cps should result in maximum signal-to-noise ratio and consequently maximum detectivity.

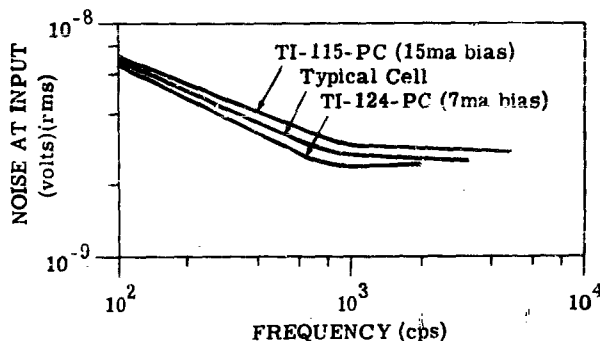


FIGURE 5-103. NOISE SPECTRUM OF PHOTOCONDUCTIVE InSb

5.7.4.2.4. Cell Resistance. The majority of cells reported indicate that the impedances may be divided into two groups: low-impedance cell produced by TI (10-100 ohms), and high-impedance cells made by LAS (1-10 kohm). The higher impedances of the LAS cells may be attributed to two factors.

- (1) A lower impurity concentration (about 7×10^{14} impurities/cm³), therefore a higher resistivity material (Reference 5-140).
- (2) The LAS cells were operated at 77°K compared with 193°K operation by TI.

5.7.4.2.5. (Confidential) Detectivity. As described above, there are two types of InSb photoconductive detectors, which are called low-impedance and high-impedance cells. Low-impedance cells are optimized for performance at 193°K; high-impedance cells are optimized for performance at 77°K. The ranges of values are given above. It is interesting to note that detectors with impedances as high as 40 kohm have been reported (Reference 5-141). These cells were constructed from material with an impurity content of about 10^{12} cm⁻³. High-impedance cells of this type can be manufactured with large thicknesses, since the signal voltage will not be shorted by the high resistance

bulk. This leads to a mechanically rigid cell which is amenable to mass production. On the other hand the low-impedance cell must have a thickness of approximately 10μ in order to maximize the S/N ratio.

The temperature dependence of detectivity is quite different for the two detector types. This is shown in Figure 5-104, where the S/N ratio is plotted as a function of reciprocal temperature. The low-impedance detector data were taken from a Texas Instruments progress report (Reference 5-142), while the high-impedance data were taken from a Syracuse University report (Reference 5-141). The figure indicates a rather important point: the S/N ratio of thin (or low-impedance) detectors remains relatively high for temperatures between 80°K and 200°K . This means that the low-impedance cells can be operated at dry-ice temperature without serious degradation of the noise equivalent power. Syracuse University reports a decrease in detectivity by a factor of 6 when their low-impedance detector is operated at solid CO_2 temperature instead of at liquid-nitrogen temperature.

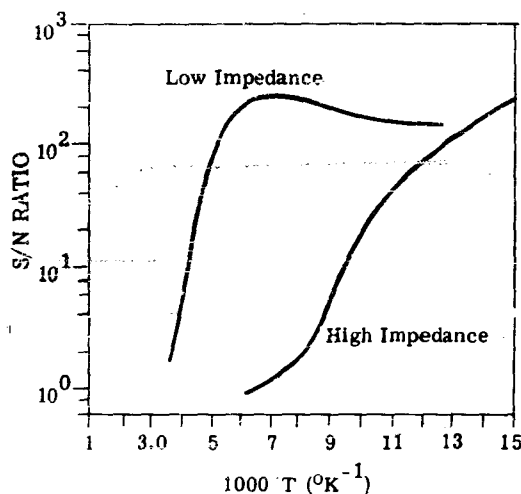


FIGURE 5-104. S/N RATIO VS. TEMPERATURE FOR HIGH-AND LOW-IMPEDANCE CELLS

Commercial cells which are made to operate adequately at dry-ice temperatures are available today. In general, these low-impedance cells also have a higher S/N ratio at liquid-nitrogen temperatures than their high-impedance counterparts.

The significant advantage of the high-impedance cell is that the generated signal and noise voltages are larger than in the case of the low-impedance cells. In fact, this was the reason for their development. These higher voltages and higher impedances ease the problem of selecting appropriate electronics to insure that the system is detector-noise limited. Table 5-15 lists the photoconductive detectors reported in the literature along with their measured parameters. The highest detectivity reported for a cell operated at 193°K is $D^*(500^\circ\text{K}, 840, 1) = 1.2 \times 10^9 \text{ cm} \cdot \text{cps}^{1/2} \cdot \text{watt}^{-1}$, which is about a factor of 12 from the theoretical limit. The highest detectivity reported for a cell operated at 77°K is $D^*(500^\circ\text{K}, 1000, 1) = 10^{10} \text{ cm} \cdot \text{cps}^{1/2} \cdot \text{watt}^{-1}$, which is about 38% down from the theoretical limit for 180° field of view. The detectivity at the wavelength for which the spectral response is a maximum is about a factor of 6 greater than 500°K blackbody detectivity for liquid-nitrogen-cooled detectors. $D^*(500^\circ\text{K}, \text{---}, 1)$ and $D^*(\lambda_{\text{pk}}, \text{---}, 1)$ values for 9 cells were listed. $D^*(\lambda_{\text{pk}}, \text{---}, 1) / D^*(500^\circ\text{K}, \text{---}, 1) = 6.1$ for the largest $D^*(\lambda_{\text{pk}}, \text{---}, 1)$ value, and $D^*(\lambda_{\text{pk}}, \text{---}, 1) / D^*(500^\circ\text{K}, \text{---}, 1) = 5.2$ for the smallest $D^*(\lambda_{\text{pk}}, \text{---}, 1)$ value. The average value is 5.7.

The optimum bias currents for the high-impedance cells are in the range of 30-300 μa . For the low-impedance cells, larger values of bias currents (5-35 ma) were required for optimum operation. Figure 5-105 shows the detectivity of these cells in histogram form. Nothing specific can be said about detectors operated at 77°K other than their detectivities range in values from $2 \times 10^8 \text{ cm} \cdot \text{cps}^{1/2} \cdot \text{watt}^{-1}$ to $10^{10} \text{ cm} \cdot \text{cps}^{1/2} \cdot \text{watt}^{-1}$. The detectors operating at 193°K have detectivities grouped about

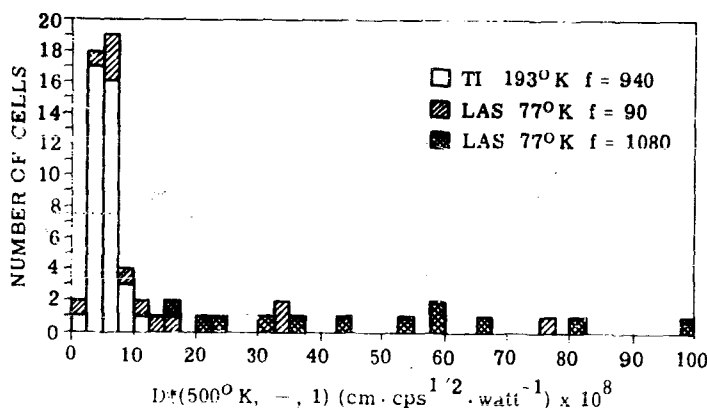


FIGURE 5-105. HISTOGRAM OF PHOTOCONDUCTIVE CELLS
Confidential

$5 \times 10^8 \text{ cm} \cdot \text{cps}^{1/2} \cdot \text{watt}^{-1}$. Commercial manufacturers of photoconductive indium antimonide detectors are:

- (1) Mullard Electronics Products, Ltd.
- (2) Radiation Electronics Corporation
- (3) Texas Instruments Incorporated
- (4) Minneapolis-Honeywell Regulator Company
- (5) Block Associates, Inc

5.7.4.3. PEM Detectors. Detection of radiation by the PEM effect has certain advantages over photoconductive and photovoltaic methods. Cooling of PEM detectors is not required; therefore, in InSb, the long-wavelength cutoff is extended to about 7μ . This also simplifies detector design by eliminating the dewar systems which employ infrared window materials; of course, a magnetic field must be supplied. PEM detectors are operated without a bias current, thus eliminating this as a noise source.

Briefly, the PEM effect can be explained by the following mechanism. Photons impinging upon semiconductor crystals are absorbed at or near the surface and create hole-electron pairs. The excess concentration of these mobile carriers near the irradiated surface leads to a diffusion current for both electrons and holes. The current direction is toward the opposite unirradiated surface. A magnetic field normal to the diffusion current will deflect the electrons and holes in opposite direction as shown in Figure 5-106. The excess concentration of these carriers at the electrodes A and B gives rise to the signal voltage.

Shortly after Welker's initial work on InSb, Karnick et al. (Reference 5-143) demonstrated that this compound could be used as an uncooled PEM detector. Due to its high carrier mobility and short lifetime it was shown that InSb is a particularly favorable material for PEM detectors.

A successful manufacturing technique has been to cement a thin slice of single crystal to a glass plate. The slice is then lapped and polished down to about 25μ . Detector elements of the desired dimensions are cut from the crystal, with the glass backing retained to give strength and rigidity. Leads are attached and the element is given a final etch to obtain the desired dimensions. The element is then fastened between the pole pieces of a permanent magnet. The detector need not be hermetically sealed, since operation in the atmosphere does not adversely affect performance.

TABLE 5-15. InSb-CELL DATA (PHOTOCONDUCTIVE)
Confidential

Site	Year	Altitude (m)	Latitude (°N)	Longitude (°E)	Area (km²)	Population (1000)	Vegetation	Climate	Soil	Water	Land Use	Notes	
1	1955	112	11° 12' N	103° 12' E	100	100	Forest	Humid	100	100	100	100	
2	1955	112	11° 12' N	103° 12' E	100	100	Forest	Humid	100	100	100	100	
3	1955	112	11° 12' N	103° 12' E	100	100	Forest	Humid	100	100	100	100	
4	1955	112	11° 12' N	103° 12' E	100	100	Forest	Humid	100	100	100	100	
5	1955	112	11° 12' N	103° 12' E	100	100	Forest	Humid	100	100	100	100	
6	1955	112	11° 12' N	103° 12' E	100	100	Forest	Humid	100	100	100	100	
7	1955	112	11° 12' N	103° 12' E	100	100	Forest	Humid	100	100	100	100	
8	1955	112	11° 12' N	103° 12' E	100	100	Forest	Humid	100	100	100	100	
9	1955	112	11° 12' N	103° 12' E	100	100	Forest	Humid	100	100	100	100	
10	1955	112	11° 12' N	103° 12' E	100	100	Forest	Humid	100	100	100	100	
11	1955	112	11° 12' N	103° 12' E	100	100	Forest	Humid	100	100	100	100	
12	1955	112	11° 12' N	103° 12' E	100	100	Forest	Humid	100	100	100	100	
13	1955	112	11° 12' N	103° 12' E	100	100	Forest	Humid	100	100	100	100	
14	1955	112	11° 12' N	103° 12' E	100	100	Forest	Humid	100	100	100	100	
15	1955	112	11° 12' N	103° 12' E	100	100	Forest	Humid	100	100	100	100	
16	1955	112	11° 12' N	103° 12' E	100	100	Forest	Humid	100	100	100	100	
17	1955	112	11° 12' N	103° 12' E	100	100	Forest	Humid	100	100	100	100	
18	1955	112	11° 12' N	103° 12' E	100	100	Forest	Humid	100	100	100	100	
19	1955	112	11° 12' N	103° 12' E	100	100	Forest	Humid	100	100	100	100	
20	1955	112	11° 12' N	103° 12' E	100	100	Forest	Humid	100	100	100	100	
21	1955	112	11° 12' N	103° 12' E	100	100	Forest	Humid	100	100	100	100	
22	1955	112	11° 12' N	103° 12' E	100	100	Forest	Humid	100	100	100	100	
23	1955	112	11° 12' N	103° 12' E	100	100	Forest	Humid	100	100	100	100	
24	1955	112	11° 12' N	103° 12' E	100	100	Forest	Humid	100	100	100	100	
25	1955	112	11° 12' N	103° 12' E	100	100	Forest	Humid	100	100	100	100	
26	1955	112	11° 12' N	103° 12' E	100	100	Forest	Humid	100	100	100	100	
27	1955	112	11° 12' N	103° 12' E	100	100	Forest	Humid	100	100	100	100	
28	1955	112	11° 12' N	103° 12' E	100	100	Forest	Humid	100	100	100	100	
29	1955	112	11° 12' N	103° 12' E	100	100	Forest	Humid	100	100	100	100	
30	1955	112	11° 12' N	103° 12' E	100	100	Forest	Humid	100	100	100	100	

[illegible]

Journal of Small Area Indian Antismoking Cells, Report Number 100, 1993, pp. 1-14.

Dr. J. C. P. Jones, for the development of Small Area Isotonic-Antimicrobial Cells, is a member of the staff of the University of California, Los Angeles, California 90024.

1955-9, Laboratory for Applied Science, The University of Cambridge, Cambridge, England.

March 1959 (CONFIDENTIAL).
de Intersect Detective, Seventeenth Quarterly Progress Report.

[illegible]

Journal of the American Statistical Association, Vol. 53, No. 282, 1958, pp. 1-12.

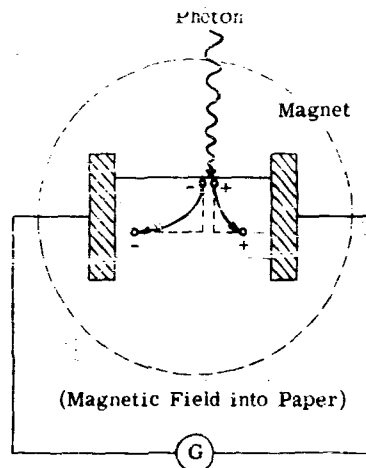


FIGURE 5-106, SCHEMATIC REPRESENTATION OF THE PEM EFFECT

5.7.4.3.1. Spectral Response. A room-temperature spectral-response curve is shown in Figure 5-107. This curve is essentially that of a quantum detector having a peak at about 6.0μ and a cutoff wavelength slightly beyond 7μ .

5.7.4.3.2. Time Constant and Frequency Response. The time constant is less than $1\mu\text{sec}$.

5.7.4.3.3. Noise. A typical noise spectrum curve is reported by NOLC and is shown in Figure 5-108. If the equipment used to measure the signal is a high-impedance device, the detector signal can be considered to be an open circuit voltage. Since these detectors are operated without a bias current, the noise components are $1/f$ for low frequencies ($f < 100$ cps), and Johnson noise for higher frequencies. According to theory, generation-recombination noise should be negligible since it is a function of the mean value of the current.

5.7.4.3.4. Cell Impedances. All of the cells reported had low impedances, ranging from 4.5 ohms to 90 ohms.

5.7.4.3.5. Detectivity. One of the controllable parameters in obtaining an optimum detectivity is the cell thickness d . From a theoretical view point the response should vary as $1/d$, while the noise should vary as $1/\sqrt{d}$. Therefore, the signal-to-noise ratio should vary as $1/\sqrt{d}$. These

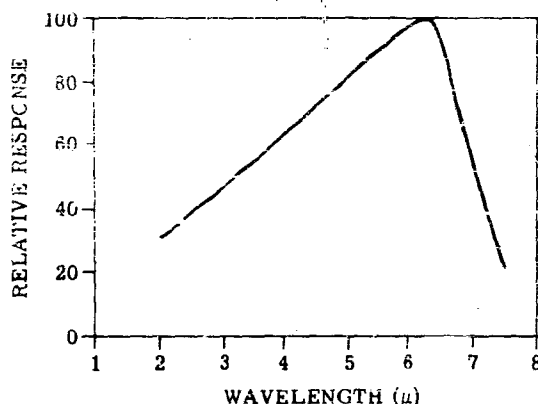


FIGURE 5-107. TYPICAL SPECTRAL RESPONSE OF AN InSb PEM CELL at 300°K

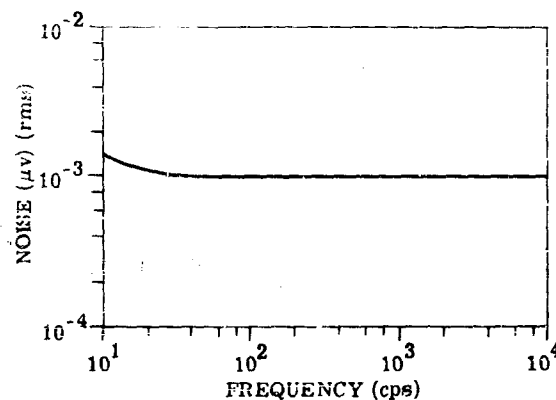


FIGURE 5-108. NOISE SPECTRUM FOR PEM CELLS

relationships hold down to the absorption length of radiation in the material. For InSb this is from 1μ to 10μ . Optimum cell performance should, therefore, result for thicknesses of the order of $1-10\mu$. Since signal strength is a linear function of magnetic field strength, the latter should be as large as possible, consistent with practical detector geometry. Table 5-16 lists the PEM detectors reported in the literature along with their measured parameters. A histogram of these cells is given in Figure 5-109. All of the $D^*(500^\circ\text{K}, -, 1)$ values lie in a region from 10^7 to 6×10^7 $\text{cm} \cdot \text{cps}^{1/2} \cdot \text{watt}^{-1}$, with the majority of the $D^*(500^\circ\text{K}, -, 1)$ values in the 2.5×10^7 to 5×10^7 $\text{cm} \cdot \text{cps}^{1/2} \cdot \text{watt}^{-1}$ region. These values are about a factor of 500 from the theoretical limit. The highest detectivity reported is $D^*(500^\circ\text{K}, -, 1) = 5.6 \times 10^7$ $\text{cm} \cdot \text{cps}^{1/2} \cdot \text{watt}^{-1}$ by LAS, which is a factor of about 300 from the theoretical limit for a 180° field of view. Ratios of $D^*(500^\circ\text{K}, -, 1)/D^*(\lambda_{pk}, -, 1)$ were fairly consistent with the majority of the cells having ratios from 2.8 to 3.3. The average ratio for the cells listed was 3.1. Using this relationship, one has $D^*(\lambda_{pk}, -, 1) = 3D^*(500^\circ\text{K}, -, 1)$. Private communications with cell manufacturers have indicated that $D^*(500^\circ\text{K}, -, 1)$ values of 6.0×10^7 $\text{cm} \cdot \text{cps}^{1/2} \cdot \text{watt}^{-1}$ are guaranteed and that the best cells measured to date have $D^*(500^\circ\text{K}, -, 1)$ values of about a factor of 2 higher.

Commercial manufacturers of PEM indium antimonide detectors are:

- (1) Minneapolis-Honeywell Regulator Company
- (2) Radiation Electronics Corporation
- (3) Texas Instruments Incorporated

TABLE 5-16. InSb-CELL DATA (PEM)

No.	Series	Area (cm ²)	20°K Blackbody Response			500°K Reactivity Response			Cell Noise (10 ⁻³ cps)	Internal Noise (10 ⁻³ cps)	Cell Temp. (°C)	Cell Area (cm ²)
			$\frac{V}{A}$ (10 ⁻³ V/cm ²)	$\frac{V}{A}$ (10 ⁻³ V/cm ²)	$\frac{V}{A}$ (10 ⁻³ V/cm ²)	$\frac{V}{A}$ (10 ⁻³ V/cm ²)	$\frac{V}{A}$ (10 ⁻³ V/cm ²)	$\frac{V}{A}$ (10 ⁻³ V/cm ²)				
1	CM1	0.54	2.815	1.20	0.971	9.5	13.0	0.140	5.4	4.0	3.4	1
2	CM2	2.81	2.160	50.20	0.279	7.0	210.0	0.072	5.6	50	3.0	1
3	CM3	3.26	2.010	6.10	0.279	5.1	219.0	0.072	9.5	90	3.1	1
4	CM4	2.2	1.207	20.40	0.558	4.16	89.0	0.158	2.6	80	3.0	1
5	CM5	3.299	4.290	12.07	0.451	3.87	43.2	0.1354	4.52	65	3.0	1
6	CM6	1.4	3.200	45.00	0.282	11.0	153.0	0.0789	26	26	3.0	2
7	CM7	1.8	1.400	25.00	0.536	4.1	73.0	0.179	33	33	3.0	2
8	CM8	1.6	1.800	30.00	0.423	6.0	96.0	0.132	68	68	3.0	2
9	CM9	3.0	1.800	54.00	0.120	5.7	170.0	0.102	41	41	3.0	2
10	CM10	0.40	1.000	30.00	0.18	19.0	94.0	0.074	1.0	9.5	29	3
11	CM11	0.65	5.400	25.00	0.49	15.0	67.0	0.099	1.85	8.8	29	3
12	CM12	1.43	3.760	53.70	0.228	12.5	179.0	0.0877	0.62	4.7	30	3
13	CM13	1.0	1.180	31.80	0.316	9.5	95.4	0.103	0.61	1.5	29	3
14	CM14	2.9	3.340	38.50	0.44	4.47	134.0	0.13	1.59	5.5	30	5
15	CM15	0.58	4.52	26.2	0.23							
16	CM16	0.84	3.76	31.6	0.29				0.75	4.3	30	5
17	CM17	0.60	3.07	18.4	0.42				0.84	8.2	30	5
18	CM18	0.81	3.47	28.1	0.32				2.00	25.0	30	5
19	CM19	0.50	4.04	20.2	0.35				0.94	10.0	30	5
20	CM20	0.45	4.11	18.6	0.26				1.80	24.0	30	5
21	CM21	0.80	3.80	28.5	0.31				0.89	8.8	30	5
22	CM22								2.34	40.0	30	5

- Properties of Photo Inductive Detector, NCLC Report Number 387, Naval Ordnance Laboratory, Corona, Calif., November 1957 (CONFIDENTIAL).
- Improved Infrared Detector Program, Quarterly Interim Progress Report Number CML-57-TN-P118-5, Chicago Midway Laboratories, The University of Chicago (Chicago, Ill., August 1957) (CONFIDENTIAL).
- Properties of Photo Inductive Detector, NCLC Report Number 525, Naval Ordnance Laboratory, Corona, Calif., August 1960 (CONFIDENTIAL).
- Properties of Photo Inductive Detector, NCLC Report Number 390, Naval Ordnance Laboratory, Corona, Calif., December 1957 (CONFIDENTIAL).
- Properties of Photo Inductive Detector, NCLC Report Number 438, Naval Ordnance Laboratory, Corona, Calif., January 1959 (CONFIDENTIAL).
- W. H. R. Adams, L. H. Adams, and L. Sloan, *Proc. IRE*, 1960, Vol. 48, No. 1, p. 59.

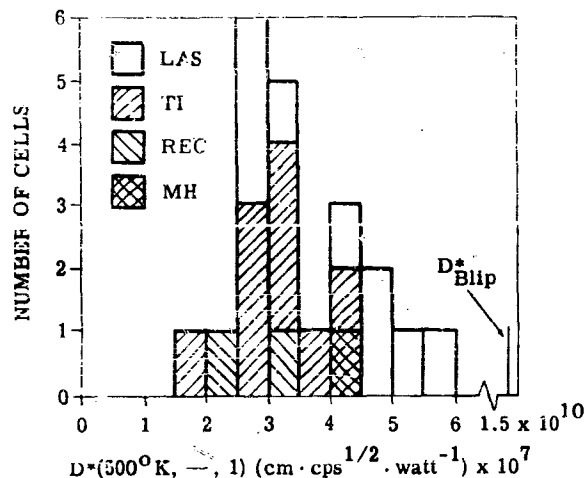


FIGURE 5-109. HISTOGRAM OF D^* VALUES FOR PEM DETECTORS

5.7.4.4. Impurity-Activated InSb Detectors. There are presently two approaches to preparing extrinsic InSb detectors. The first depends upon the addition of known amounts and types of impurities to the parent lattice, and the second utilizes the impurity levels which exist in high-purity InSb crystals. These high-purity crystals have donor concentrations of about $4 \times 10^{14} \text{ cm}^{-3}$.

In the first case, the introduced impurities change the electronic structure in the immediate vicinity of the impurity in the crystal. This change results in the introduction of allowed electron energy states in the forbidden band. Figure 5-110 is a simple band picture of InSb along with the allowed electron energy states introduced by copper, silver, and gold. The numbers adjacent to these energy states refer to the separation (in electron volts) between the level and the valence band (E_v). Blunt (Reference 5-144) determined the energy levels of Cu in the InSb lattice by measuring the conductivity and Hall coefficient of doped samples as functions of temperature. Photoconductivity measurements were also made on these prototype detectors. D^* values shown in Table 5-17 ($T = 5^\circ\text{K}$) were calculated from Blunt's data. It should be noted that no effort was made to optimize the NEP when constructing these cells. Hall data and resistivity measurements were the primary objective.

The levels introduced by Ag, Au, and Cu were determined by Engeler (Reference 5-126). The measurements on the Cu levels agree with those of Blunt. Measurements on prototype InSb: AuII (implying the second level of gold in the InSb lattice) detectors have been reported by Borrellio et al. (Reference 5-78).

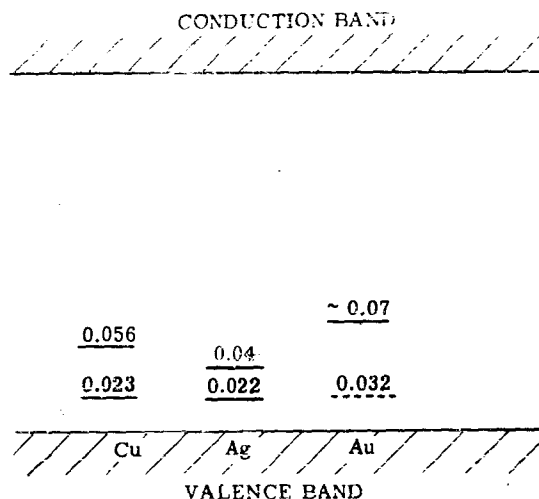


FIGURE 5-110. INDUCED IMPURITY LEVELS IN InSb

TABLE 5-17. D^* VALUES CALCULATED FROM BLUNT'S DATA

Cell No.	Copper Impurity Level (ev)	$D^*(\lambda_{pk}, 450 \text{ cps, 1})$ (cm · cps ^{1/2} · watt ⁻¹)
C-51	0.023	3×10^8
C-68B-3	0.058	2×10^7

Another method of constructing impurity-activated InSb detectors is simply to take high-purity InSb (about 10^{14} cm^{-3} donor impurities) and utilize the impurity centers which introduce allowed electron energy levels in the forbidden band (quite close to the conduction band). If the impurity concentration is greater than 10^{13} cm^{-3} , the impurity centers will lie close enough to each other to interact and produce a number of degenerate states. In this situation it is extremely difficult to depopulate the extrinsic electrons from the conduction band by cooling the sample. However, if a magnetic field is applied, the interaction between impurity centers decreases and the ionization energy will be increased. Consequently, a detector may be fabricated from this material with an extrinsic long-wavelength cutoff corresponding to the ionization energy. The ionization energy is a function of the size of magnetic field employed. Putley (Reference 5-145) reports a laboratory sample of n-type InSb which exhibits a minimum detectable power per unit bandwidth of about $5 \times 10^{-10} \text{ watt}$

at 0.5-mm, 5×10^{-11} watt at 2-mm, and 10^{-10} watt at 4-mm wavelengths. The sample dimensions were $0.5 \times 0.5 \times 1.0$ cm. Indium electrodes were applied to 0.5×1.0 cm² faces. The magnetic field was applied at right angles to the direction of current flow and of the incident radiation. Patley and Smith (Reference 5-146) report a response out to 2 mm for a similar-type detector.

These impurity-activated InSb detectors are in a very early stage of development and little can be said about their characteristics except for the spectral response, which is of course determined by the ionization energy. Indications are, however, that the InSb:AuII detector will provide a high-impedance detector in the 6- μ region. The second type of cell mentioned above should prove valuable as a detector of electromagnetic radiation in the spectral region between infrared and microwaves.

5.8. REFERENCES

- 5-1. R. A. Smith, F. E. Jones, and R. P. Chasmar, The Detection and Measurement of Infrared Radiation, Oxford at the Clarendon Press, 1957, p. 298.
- 5-2. J. H. Molitor, R. R. Sexauer, and D. A. Jerde, Photosaturation of Infrared Detectors: I. Effects on PbS, Reference Number PAD/APS-8b/0058, Boeing Airplane Co., Seattle, Wash., February 1958 (CONFIDENTIAL).
- 5-3. J. H. Molitor and R. R. Sexauer, Photosaturation of Infrared Detectors: II. Effects on Photovoltaic InSb, Reference Number PAD/APS 8b/0059, Boeing Airplane Co., Seattle, Wash., April 1958 (CONFIDENTIAL).
- 5-4. J. H. Molitor and R. R. Sexauer, Photosaturation of Infrared Detectors: III. Effects on Au-Doped Ge, Reference Number PAD/APS-8b/0059, Boeing Airplane Co., Seattle, Wash., August 1959 (CONFIDENTIAL).
- 5-5. J. H. Molitor, Photosaturation of Infrared Detectors: IV, Reference Number S-7870-7401, Boeing Airplane Co., Seattle, Wash., July 1959 (CONFIDENTIAL).
- 5-6. T. P. Merritt, Proc. IRIS, 1956, Vol. 1, No. 2.
- 5-7. H. Steele and D. Owens, Effects of Radiation on PbS IR Detectors and IR Optics, Boeing Airplane Co., Seattle, Wash., October 1957.
- 5-8. E. W. Kutzscher, Proc. IRIS, 1956, Vol. 1, No. 2.
- 5-9. Development of IR Guidance for Small Air-to-Air Missiles, Quarterly Progress Report Number 8, Avion Division, ACF Industries, Inc., Paramus, N. J., September 1958 (UNCLASSIFIED).
- 5-10. E. W. Kutzscher, Proc. IRE, September 1959, Vol. 47, No. 9.
- 5-11. R. R. Bilups and W. L. Gardner, Proc. IRIS, 1961, Vol. 6, No. 2.
- 5-12. R. J. Cashman, Development of Sensitive Lead Sulfide Photosensitive Cells for Detection of Intermediate Infrared Radiation, Report Number OSR05998, Northwestern University, Evanston, Ill.
- 5-13. L. Sosnowski, J. Starkiewicz, and O. Simpson, "Lead Sulfide Photoconductive Cells," Nature, 1947, Vol. 159, p. 818.
- 5-14. R. J. Cashman, Proc. IRE, September 1959, Vol. 47, No. 9, pp. 1470-1471.
- 5-15. W. N. Arnquist, Proc. IRE, September 1959, Vol. 47, No. 9, p. 1420.
- 5-16. T. S. Moss, Proc. Phys. Soc. (London), 1953, Vol. B66, p. 993.
- 5-17. F. Fischer, B. Gudden, and M. Tren, Physik. Z., 1938, Vol. 39.
- 5-18. W. W. Scanlon and G. Lieberman, Proc. IRE, May 1959, Vol. 47, No. 5, p. 910.
- 5-19. H. Wilman, Proc. Phys. Soc. (London), 1948, Vol. A60.
- 5-20. L. Roth, dissertation, Erlangen, 1938.
- 5-21. T. S. Moss, Proc. IRE, 1955, Vol. 43, pp. 1869-1881.
- 5-22. Feltynowski, et al., Bull. Acad. Sci., Poion, 1954, Vol. C 13, No. 2, p. 389.
- 5-23. W. Paul, D. A. Jones, and R. V. Jones, Proc. Phys. Soc. (London), 1951, Vol. B64, p. 528.

- 5-21. W. W. Scanlon, Phys. Rev., 1953, Vol. 92, p. 1573.
- 5-25. A. Rose, E. S. Rittner, and R. L. Petritz, Photoconductivity Conference, Wiley, New York, N. Y., 1956.
- 5-26. A. Rose, Proc. IRE, December 1955, Vol. 43, pp. 1850-1869.
- 5-27. J. N. Humphrey and R. L. Petritz, Phys. Rev., 1957, Vol. 105, p. 1736.
- 5-28. J. C. Slater, Phys. Rev., 1956, Vol. 103, p. 1631.
- 5-29. R. H. Harada and H. T. Minden, Phys. Rev., 1956, Vol. 102, p. 1250.
- 5-30. R. L. Petritz, Phys. Rev., 1956, Vol. 104, p. 1508.
- 5-31. A. F. Gibson, Proc. Phys. Soc. (London), 1952, Vol. B65, p. 378.
- 5-32. A. M. Clark and R. J. Cashman, Phys. Rev., 1952, Vol. 85, No. 6.
- 5-33. Handbook of Chemistry and Physics, 39th ed., Chemical Rubber Publishing Co., Cleveland, O., 1959.
- 5-34. S. S. Ballard, K. A. McCarthy, and W. L. Wolfe, Optical Materials for Infrared Instrumentation, Report Number 2389-11-S, Willow Run Laboratories, The University of Michigan, Ann Arbor, Mich., January 1959 (UNCLASSIFIED).
- 5-35. D. G. Avery, Proc. Phys. Soc. (London), 1954, Vol. B67, p. 2.
- 5-36. Infratron Lead Sulfide Photoconductors, Technical Bulletin No. 2, Infrared Industries, Inc., Needham Heights, Mass., November 1958 (UNCLASSIFIED).
- 5-37. Kodak Ektron Detectors for the Infrared, Technical Brochure, Eastman Kodak Co., Rochester, N. Y., April 1960 (UNCLASSIFIED).
- 5-38. A. B. Naugle, V. R. Allen, and A. J. Cussen, Properties of Photoconductive Detectors, NOLC Report Number 365, Naval Ordnance Laboratory, Corona, Calif., April 1957, p. 12 (CONFIDENTIAL).
- 5-39. S. C. Freden and R. S. White, Phys. Rev. Letters, 1959, Vol. 3, No. 9.
- 5-40. J. A. Van Allen, Report of the Space Science Board of the National Academy of Science, Natural Research Council, Chap. VII, "Physics of Fields and Energetic Particles in Space," February 1960.
- 5-41. R. L. Petritz, Proc. IRE, September 1959, Vol. 47, No. 9, p. 1465.
- 5-42. E. D. McAlister, The Dependence of Sensitivity on Time Constant in Photoconductive Detectors, NAVORD Division, Eastman Kodak Co., Rochester, N. Y., 1956.
- 5-43. A. B. Naugle and A. J. Cussen, Properties of Photoconductive Detectors, NOLC Report Number 349, Naval Ordnance Laboratory, Corona, Calif., May 1957 (CONFIDENTIAL).
- 5-44. A. J. Cussen, Characteristics of Photoconductive Detectors, NOLC Report Number 144, Naval Ordnance Laboratory, Corona, Calif., February 1958 (UNCLASSIFIED).
- 5-45. D. G. Avery, Proc. Phys. Soc. (London), 1953, Vol. B66, p. 134.

- 5-46. G. J. Koch, Status of Photoconductive Cell Development, Progress Report for Quarter January 1, 1955 to April 1, 1955, Eastman Kodak Co., Rochester, N. Y., April 1955 (CONFIDENTIAL).
- 5-47. H. Levinstein, Interim Report on Infrared Detectors, Physics Report Number 104-2, Syracuse University, Syracuse, N. Y., April 1960.
- 5-48. A. F. Gibson, Proc. Phys. Soc. (London), 1952, Vol. B55, p. 318.
- 5-49. W. W. Scanlon and G. Lieberman, Proc. IRE, September 1959, Vol. 47, No. 9.
- 5-50. W. W. Scanlon and G. Lieberman, Proc. IRE, October 1959, Vol. 47, No. 10.
- 5-51. T. Limperis and W. L. Wolfe, Proc. IRIS, 1960, Vol. 5, No. 4, p. 141.
- 5-52. W. G. Pfann, J. Metals, 1952, Vol. 4, p. 747.
- 5-53. S. Kyropoulos, Z. Anorg. Chemie., 1926, Vol. 154, p. 308.
- 5-54. W. C. Dash and R. Newman, Phys. Rev., 1955, Vol. 99, p. 1151.
- 5-55. L. Johnson and H. Levinstein, Phys. Rev., 1960, Vol. 117, p. 1191.
- 5-56. J. Bardeen, F. J. Blatt, and L. H. Hall, Photoconductivity Conference at Atlantic City November 1954, Wiley, New York, N. Y., 1956.
- 5-57. G. Dresselhaus, A. F. Kip, and C. Kittel, Phys. Rev., 1955, Vol. 98, p. 368.
- 5-58. R. N. Dexter, H. J. Zeiger, and B. Lax, Phys. Rev., 1955, Vol. 104, p. 637.
- 5-59. H. B. Briggs and R. C. Fletcher, Phys. Rev., 1952, Vol. 87, p. 1130.
- 5-60. H. B. Briggs and R. C. Fletcher, Phys. Rev., 1953, Vol. 91, p. 1342.
- 5-61. W. Kaiser, R. J. Collins, and H. Y. Fan, Phys. Rev., 1953, Vol. 91, p. 1380.
- 5-62. M. Lax and E. Burstein, Phys. Rev., 1955, Vol. 97, p. 39.
- 5-63. R. J. Collins and H. Y. Fan, Phys. Rev., 1954, Vol. 93, p. 674.
- 5-64. W. Kohn, Solid State Physics (ed. F. Seitz and D. Turnbull), Academic Press, New York, N. Y., 1957, Vol. 5.
- 5-65. E. Burstein and W. Nottingham, Photoconductivity Conference, Wiley, New York, N. Y., March 1949.
- 5-66. W. C. Dunlap, Phys. Rev., 1953, Vol. 91, p. 1282.
- 5-67. W. C. Dunlap, Phys. Rev., 1955, Vol. 97, p. 614.
- 5-68. W. C. Dunlap, Phys. Rev., 1955, Vol. 100, p. 1628.
- 5-69. G. Morton, E. E. Hahn, and M. L. Schultz, Photoconductivity Conference at Atlantic City, November 1954, (ed. R. G. Breckenridge), Wiley, New York, N. Y., 1956.
- 5-70. R. Newman and W. W. Tyler, Solid State Physics (ed. F. Seitz and D. Turnbull), Academic Press, New York, N. Y., 1958, Vol. VIII.
- 5-71. K. M. VanVliet, Proc. IRE, 1958, Vol. 46, p. 1004.
- 5-72. A. U. MacRae and H. Levinstein, Phys. Rev., 1960, Vol. 119.

- 5-73. P. Bratt, W. Engeler, H. Levinstein, A. U. MacRae, and J. Pehek, Infrared Physics, 1961, Vol. 1.
- 5-74. F. Burstein, J. W. Davison, F. E. Bell, W. J. Turner, and H. G. Lipson, Phys. Rev., 1954, Vol. 93, p. 69.
- 5-75. G. Picus and S. F. Jacobs, Conference of International Committee for Optics, Stockholm, August 1959.
- 5-76. S. J. Fray and J. F. C. Oliver, J. Sci. Instr., 1959, Vol. 36, p. 195.
- 5-77. P. Bratt, W. Engeler, H. Levinstein, J. Pehek, and C. Stannard, Proc. IRIS, June 1960, Vol. 5, No. 4, p. 15.
- 5-78. S. Borello, W. Engeler, H. Levinstein, and C. Stannard, Proc. IRIS, April 1961, Vol. 6, No. 2.
- 5-79. H. Stohr and K. Klemm, Z. Anorg. u. Allgem. Chem., 1939, Vol. 241, p. 305.
- 5-80. A. Levitas, C. C. Wang, and B. H. Alexander, Phys. Rev., 1954, Vol. 95, p. 846.
- 5-81. E. R. Johnson and S. N. Christian, Phys. Rev., 1954, Vol. 95, p. 560.
- 5-82. F. Herman, Phys. Rev., 1954, Vol. 95, p. 647.
- 5-83. R. Braunstein, A. R. Moore, and F. Herman, Phys. Rev., 1958, Vol. 109, p. 695.
- 5-84. G. A. Morton, M. L. Schultz, and W. E. Harty, RCA Rev., December 1959, Vol. XX, No. 4.
- 5-85. M. L. Schultz, J. I. Gittleman, W. E. Harty, and G. A. Morton, Proc. IRIS, March 1958, Vol. 3, No. 1.
- 5-86. K. S. Ling, Impurity Activated Alloy Infrared Detectors, Third Quarterly RCA Progress Report, Electron Tube Division, Radio Corp. of America, Harrison, N. J., January 1960 (UNCLASSIFIED).
- 5-87. W. L. Eisenman and A. B. Naugle, Properties of Photodetectors, NOLC Report Number 527, Naval Ordnance Laboratory, Corona, Calif., August 1960 (UNCLASSIFIED).
- 5-88. R. Machol, J. Phys. Chem., 1958, Vol. 62, p. 361.
- 5-89. F. C. Brown and A. M. MacMahon, International Critical Tables, McGraw-Hill, New York, N. Y., 1929, p. 208.
- 5-90. W. W. Coblentz, Bulletin Number 14, National Bureau of Standards, Washington, D. C., 1918.
- 5-91. J. Czochralski, Z. Phys. Chem., 1917, Vol. 93, p. 219.
- 5-92. P. W. Bridgeman, Proc. Am. Acad. Arts Sci., 1925, Vol. 60, p. 305.
- 5-93. J. von Weidel, Z. Naturforsch., 1954, Vol. 9A, p. 697.
- 5-94. R. C. Keezer, unpublished data, Institute of Science and Technology, The University of Michigan, Ann Arbor, Mich.
- 5-95. T. J. Davis, J. Appl. Phys., 1957, Vol. 28, p. 1217.
- 5-96. J. J. Loferski, Phys. Rev., 1954, Vol. 93, p. 707.

- 5-97. K. C. Normua and J. S. Blakemore, "Optical Absorption in Tellurium," presented to American Physical Society, New York, N. Y., January 1960.
- 5-98. T. S. Moss, Proc. Phys. Soc. (London), 1952, Vol. B65, p. 62.
- 5-99. L. J. Neuringer, Phys. Rev., 1955, Vol. 96, p. 1185.
- 5-100. T. S. Moss, Optical Properties of Semiconductors, Academic Press, New York, N. Y., 1959.
- 5-101. J. R. Reitz, Phys. Rev., 1957, Vol. 105, p. 1233.
- 5-102. T. S. Moss, Photoconductivity in the Elements, Butterworth, London, 1952.
- 5-103. P. A. Hartig and J. J. Loferski, J. Opt. Soc. Am., 1954, Vol. 44, p. 17.
- 5-104. R. S. Caldwell, Optical Properties of Tellurium and Selenium, Supplement to Sixth Quarterly Report, Department of Physics, Purdue University, Lafayette, Ind., January 1958 (UNCLASSIFIED).
- 5-105. T. S. Moss, Proc. Phys. Soc. (London), 1949, Vol. A62.
- 5-106. T. Fukuroi, S. Tanuma, and E. S. Tohisawa, Sci. Rep. Res. Inst., Tohoku University, A1. 365, 1949.
- 5-107. G. L. Suits, Proc. IRIS, June 1958, Vol. 3, No. 2, p. 105.
- 5-108. C. D. Butter and L. D. McGlaughlin, Proc. IRIS, 1960, Vol. 5, No. 3.
- 5-109. A. P. de Carvalho, C. R. Acad. Sci., Paris, 1957, Vol. 244.
- 5-110. W. L. Eisenman and A. B. Naugle, Properties of Photodetectors, NOLC Report Number 525, Naval Ordnance Laboratory, Corona, Calif., August 1960 (CONFIDENTIAL).
- 5-111. J. M. Pernet and A. B. Naugle, Properties of Photoconductive Detectors, NOLC Report Number 438, Naval Ordnance Laboratory, Corona, Calif., January 1959 (CONFIDENTIAL).
- 5-112. D. E. Edwards, Ultimate Sensitivity and Practical Performance of the Tellurium Photoconductive Detector, Report Number 2900-129-R, Willow Run Laboratories, The University of Michigan, Ann Arbor, Mich., December 1959 (UNCLASSIFIED).
- 5-113. W. R. Fredrickson et al., Infrared Spectral Emissivity of Terrain, Interim Development Report Number 2, Syracuse University, Syracuse, N. Y., July 1957.
- 5-114. T. S. Liu and E. A. Peretti, Trans. Am. Soc. Metals, 1953, Vol. 45, p. 677.
- 5-115. F. Oswald and R. Schade, Z. Naturforsch., 1954, Vol. 9A, p. 611.
- 5-116. O. G. Folberth, O. Madelung, and H. Weiss, Z. Naturforsch., 1954, Vol. 9A, p. 954.
- 5-117. V. F. Oswald, Z. Naturforsch., 1955, Vol. 10A, p. 927.
- 5-118. P. H. Cholet, Proc. IRIS, August 1960, Vol. 5, No. 4, p. 161.
- 5-119. J. A. Shive, Bell Labs. Rec., 1950, Vol. 28, p. 8.

- 5-120. D. H. Welker, Z. Naturforsch., 1952, Vol. 2A, p. 744.
- 5-121. D. H. Welker, Z. Naturforsch., 1953, Vol. 8A, p. 248.
- 5-122. T. S. Moss, S. D. Smith, and T. F. D. Hawkins, Proc. Phys. Soc. (London), 1957, Vol. B70, p. 176.
- 5-123. W. Kaiser and H. Y. Fan, Phys. Rev., 1955, Vol. 98, p. 985.
- 5-124. E. Burstein, Phys. Rev., 1954, Vol. 93, p. 632.
- 5-125. R. E. Blunt, Proc. IRIS, 1959, Vol. 3, No. 2.
- 5-126. W. Engeler and H. Levinstein, Optical Society of America meeting, March 1961.
- 5-127. R. A. Smith, "Photoconductivity in Semiconductors having a Small Forbidden Energy Gap," presented at the International Conference on Semiconductor Physics, Prague, September 1960.
- 5-128. G. R. Mitchell, A. E. Goldberg, and S. W. Kurnick, Phys. Rev., 1955, Vol. 97, p. 239.
- 5-129. A. B. Naugle, V. R. Allen, and A. J. Cussen, Properties of Photoconductive Detectors, NOLC Report Number 387, Naval Ordnance Laboratory, Corona, Calif., November 1957 (CONFIDENTIAL).
- 5-130. F. F. Rieke, Improved Infrared Detector Programs, Quarterly Interim Report, Chicago Midway Laboratories, The University of Chicago, Chicago, Ill., August 1956 (CONFIDENTIAL).
- 5-131. F. F. Rieke, Improved Infrared Detector Programs, Quarterly Interim Report, Chicago Midway Laboratories, The University of Chicago, Chicago, Ill., March 1957 (CONFIDENTIAL).
- 5-132. W. J. Beyen, G. R. Pruett, H. D. Adams, and L. Sloan, Proc. IRIS, 1960, Vol. 5, No. 4, p. 99 (CONFIDENTIAL).
- 5-133. G. R. Pruett and R. L. Petritz, "Detectivity and Preamplifier Considerations for InSb Photo-Voltaic Detectors," Proc. IRE, September 1959, Vol. 47, No. 9.
- 5-134. H. N. Ritland, Photosaturation of Infrared Detectors, Boeing Airplane Co., Seattle, Wash., 1959 (CONFIDENTIAL).
- 5-135. D. G. Avery et al., Proc. Phys. Soc. (London), 1954, Vol. B67, p. 761.
- 5-136. D. W. Goodwin, J. Sci. Instr., 1957, Vol. 34, p. 367.
- 5-137. F. F. Rieke, Development of Small Area Indium Antimonide Cells, Quarterly Progress Report, Chicago Midway Laboratories, The University of Chicago, Chicago, Ill., September 1959.
- 5-138. F. F. Rieke, Development of Small Area Indium Antimonide Cells, Final Report, Chicago Midway Laboratories, The University of Chicago, Chicago, Ill., March 1960.
- 5-139. H. Levinstein, Interim Report on Infrared Detectors, Physics Report Number 103-8, Syracuse University, Syracuse, N. Y., May 1959 (UNCLASSIFIED).

- 5-140. F. F. Rieke, Development of Small Area InSb Cells, Report Number LAS-QR-P155-14, Chicago Midway Laboratories, The University of Chicago, Chicago, Ill., November 1959 (CONFIDENTIAL).
- 5-141. P. Bratt, W. Engeler, H. Levinstein, A. MacRae, and J. Pehek, Germanium and Indium Antimonide Infrared Detectors, Final Report, Syracuse University, Syracuse, N. Y., February, 1960.
- 5-142. W. J. Beyen and G. R. Pruett, The Study of InSb Infrared Detectors, Thirteenth Quarterly Progress Report, Texas Instruments Incorporated, Dallas, Tex., October 1959.
- 5-143. S. W. Kurnick, A. J. Strauss, and R. N. Zitter, Phys. Rev., 1954, Vol. 94, p. 1791.
- 5-144. R. F. Blunt, Proc. IRIS, 1958, Vol. 3, No. 2, p. 31.
- 5-145. E. H. Putley, Impurity Photoconductivity in n-Type InSb, to be published.
- 5-146. E. H. Putley and R. A. Smith, Proc. IRIS, January 1961, Vol. 6, No. 1, p. 81 (CONFIDENTIAL).

6 UNUSUAL DETECTORS

Gwynn H. Suits, Thomas Limperis, and William L. Wolfe

The infrared detectors described in considerable detail in the preceding chapter employ photo-voltare, photoconductive, or photoelectromagnetic phenomena to transduce the infrared signal into an electrical output. These transducing processes are by no means the only ones available to the infrared physicist. In the past few years several new processes which merit discussion have been mentioned in the literature. These are:

- (1) The infrared image-position indicator
- (2) Detectors based on microwave techniques
- (3) Detectors based on optical-pumping techniques

None of these detectors have yet been produced in sufficient quantity to permit a comprehensive examination of their limitations or advantages. The information that follows is therefore based upon limited data and theoretical considerations of the processes involved.

6.1. THE IMAGE-POSITION INDICATOR

In 1957, Wallmark (References 6-1 and 6-2) reported a method for determining the position of a small spot of light on a detector surface. He shows that a diffused-junction photodetector produces a voltage difference between two points on its surface. This lateral voltage is dependent on the distance of the light spot from the electrodes. The voltage is a result of the lateral photoeffect, described as follows: when radiation strikes the surface of a junction, as shown in Figure 6-1, hole-electron pairs are generated. As is the case in conventional photovoltaic detectors, the holes move to the p-type region and electrons to the n-type region (see Chapter 3). If the conductivity of the p-region is much larger than that of the n-region, the holes will quickly become uniformly distributed throughout the p-region. Meanwhile, the electrons will have moved only slightly. Thus, some of the holes which have migrated far from the initial disturbance will cross the junction into the n-region, thereby creating a potential difference between themselves and the electrons, which have moved but little from the spot of light. A current will then flow until charge neutralization occurs. The flow of current causes a potential difference V , a function of the resistivity (ρ) of the material and the lateral

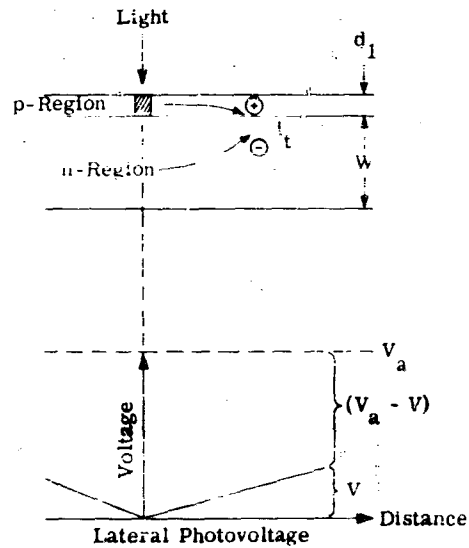


FIGURE 6-1. LATERAL PHOTOEFFECT

current density (J_t):

$$V = - \int_0^x \rho J_t dx \quad (6-1)$$

The transverse photovoltage (voltage across the junction) at the point of illumination is given as V_A . For points away from the illuminated region, the transverse potential will be $V_A - V$. The transverse current density, J_t , may be calculated from conventional junction theory (Reference 6-3).

$$J_t = J_s \left\{ \exp \left[\frac{q}{kT} (V_A - V) \right] - 1 \right\} \quad (6-2)$$

where J_s is a constant
 q is the charge
 k is Boltzmann's constant
 T is the absolute temperature

The relationship between transverse current density and the lateral potential V may be obtained by setting the divergence of the electron current density in the n-layer equal to the density of the cur-

rent crossing the junction.

$$\nabla^2 V = -\rho J_s / W \quad (6-3)$$

where W is the thickness of the n-region. When Equation 6-2 is substituted into Equation 6-3, there results

$$\nabla^2 V = -\frac{\rho J_s}{W} \left\{ \exp \left[\frac{q}{kT} (V_A - V) \right] - 1 \right\} \quad (6-4)$$

Consider the simple case of one dimension (the x direction),

$$\frac{d^2 V}{dx^2} = -\frac{\rho J_s}{W} \left\{ \exp \left[\frac{q}{kT} (V_A - V) \right] - 1 \right\}$$

and by integration

$$\frac{dV}{dx} = \left\{ \frac{2\rho J_s kT}{qW} \left[\exp \frac{q}{kT} (V_A - V) + \frac{q}{kT} V + K \right] \right\}^{1/2} \quad (6-5)$$

where K is the integration constant. From the boundary condition: $\left(\frac{dV}{dx}\right)_{x=0} = 0 = (\rho J_s)_{x=0}$ and $V = 0$ at $x = 0$, the constant of integration is solved for, and $V(x)$ is found to be

$$V \sim \sqrt{2\rho J_s} x \quad (6-6)$$

In order to determine the position of the light spot in two dimensions, four electrical contacts are needed as shown in Figure 6-2. Equation 6-4 then becomes

$$\frac{d^2 V}{dx^2} + \frac{d^2 V}{dy^2} = -\frac{\rho J_s}{W} \left\{ \exp \left[\frac{q}{kT} (V_A - V) \right] - 1 \right\}$$

The solutions V_x and V_y , according to Allen et al. (Reference 6-4) are

$$V_x = \frac{\rho I}{2\pi W} \ln \frac{r_1}{r_2} \quad (6-7)$$

and

$$V_y = \frac{\rho I}{2\pi W} \ln \frac{r_3}{r_4} \quad (6-8)$$

where I is the total photocurrent

r_i is the distance from the light spot to the i -th electrode

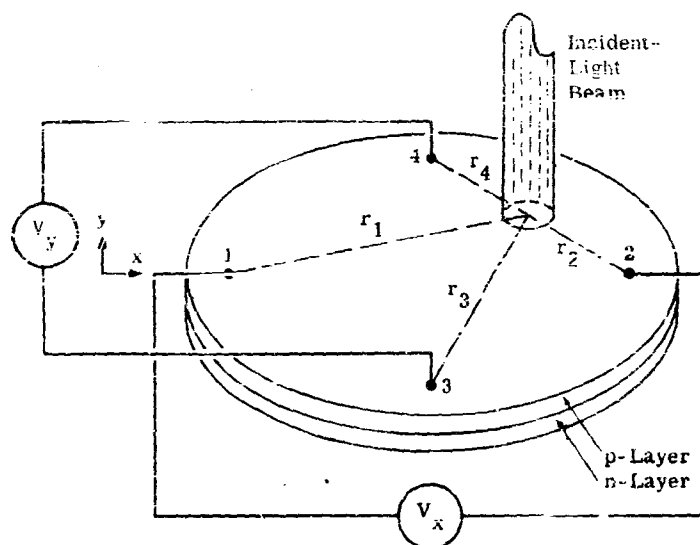


FIGURE 6-2. SPOT-POSITION LOCATION IN TWO DIMENSIONS

These expressions for V_x and V_y agree with experimental data (Reference 6-4) as shown in Figure 6-3. The zero position represents a spot located at the center of the detector surface. The relationship between V_x and V_y with spot position is approximately linear (deviating from a linear function by no more than 10%) between plus and minus one-half the distance between the center and the electrodes.

The early work on spot-position indicators described by Wallmark was accomplished with germanium p-n junctions. EOS (Electro-Optical Systems, Inc.) and Philco have been active in developing an infrared image tracker of the sort described above. The EOS cell, called the RRT (radiation tracking transducer), is made of an uncooled silicon p-n junction. Its spectral response peaks at 0.9μ , which is characteristic of intrinsic silicon. Both Philco and EOS have prototype indium antimonide image-position indicators with detection capabilities out to 6μ .

The EOS silicon RRT has a time constant of about $6 \mu\text{sec}$. Its dynamic impedance ranges from 0.7 to 7.0 kohm. The noise spectrum is flat from 300 cps to 10^4 cps with an rms value in the white region of 1.55 times the thermal noise due to the dynamic impedance. Resolution of angular position of a radiation source is better than 0.1 second of arc. The noise equivalent power (defined as that light-spot power located 0.25 cm from the center which yields unity signal to noise ratio), is about 2×10^{-10} watt for 1-cps bandwidth and a 25°C cell temperature.

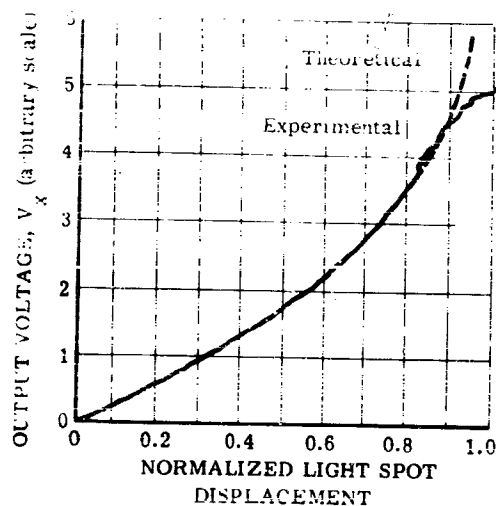


FIGURE 6-3. VARIATION OF V_x WITH SPOT POSITION

Detectors of this type should see extensive application in tracking and guidance, computers, and data processing.

6.2. INFRARED DETECTORS BASED ON MICROWAVE TECHNIQUES

Researchers at General Bronze Electronics (Reference 6-5) and Conovar of the Air University (Reference 6-6) have found that microwave cavities, which utilize semiconductor dielectrics, have electrical characteristics depending on the free charge-carrier concentration in the dielectric material. An infrared detector system employing this phenomenon was developed by General Bronze Electronics. It utilizes an infrared-sensitive semiconductor simultaneously illuminated with infrared and microwave energy. The variation of incident infrared energy is sensed as a complex impedance change in a high Q microwave cavity (Figure 6-4). The microwave energy reflected by the cavities are combined 180° out of phase in the output arm; therefore, if the system is balanced (the reflected waves from the cavities have the same amplitude and phase), no power is coupled to the output arm. Since the phase and amplitude of the reflected waves is dependent upon the complex impedance of the dielectric material, incident radiation upon one of the dielectrics will produce a different signal in the output arm, a function of the intensity of the incident infrared energy. The waveform in the output arm will have a microwave carrier (10 kmc is presently used) with an envelope frequency

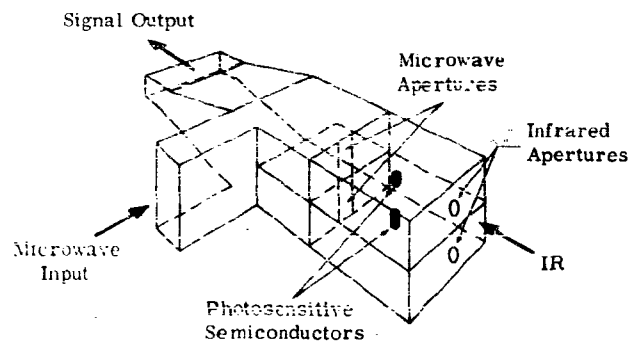


FIGURE 6-4. GENERAL BRONZE INFRARED DETECTOR

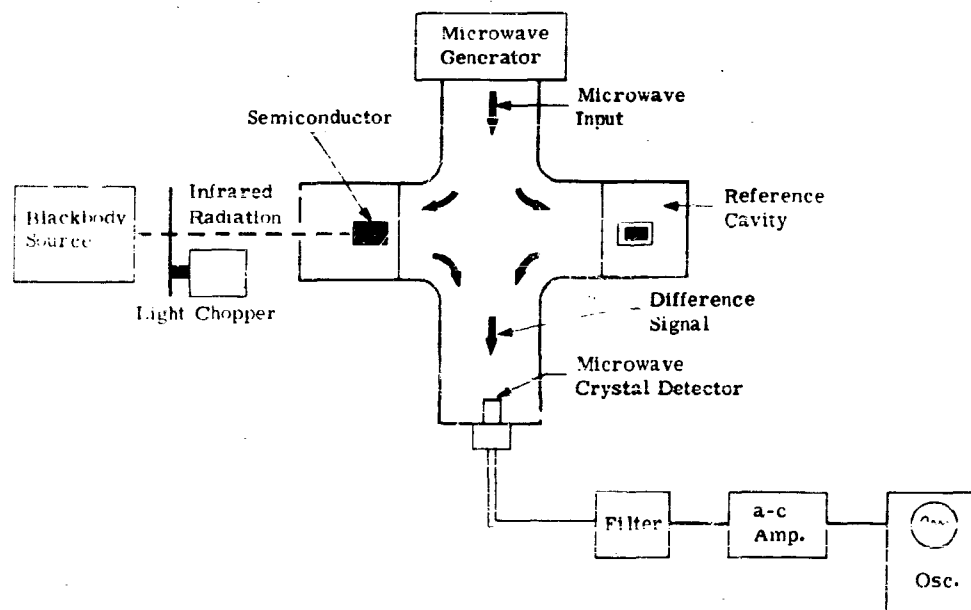


FIGURE 6-5. BLOCK DIAGRAM OF TEST SETUP

equivalent to the radiation chopping frequency. This signal is detected by a microwave crystal detector and fed into an amplifier. Figure 6-5 shows a block diagram of a test setup for this system.

Several advantages of this type of system are immediately apparent. The absence of electrical contacts on the semiconductor means a reduction in $1/f$ noise component. Also the fact that no d-c bias circuitry is used insures a large system bandwidth, limited only by the lifetime of the charge carriers in the semiconductor. For semiconductors with carrier lifetimes of 1.0 second or less, system bandwidths of about 1 mc/s are realizable. This large system bandwidth can be put to good advantage in infrared, high-resolution, reconnaissance, and mapping systems.

The primary disadvantages of systems of this type are their considerable bulk and the difficulty in using necessary cryogenic equipment for cooling the detector element. The bulk is mainly caused by the microwave pump and the necessary microwave plumbing. When long-wavelength detection is desired, semiconductor materials with small band gaps must be used, and they require cooling to decrease the number of thermally generated charge carriers. Cooling, however, cannot be accomplished easily when the semiconductor is mounted in a small, sensitive, microwave cavity. At present, cooling in the prototype systems is accomplished by immersing both cavities in an open tank of liquid nitrogen — an awkward method for field use. Improvements in cooling efficiency may be expected, but they will most likely be at the expense of system bulk.

Up to the present time only gold-doped germanium and indium antimonide have been used as detector elements. Noise equivalent powers of about 5×10^{-10} watt have been reported for Ge:Au. Assuming that this measurement was corrected to one-cycle bandwidth, and using the infrared aperture as the detector area, one obtains a value of

$$D^*(500^\circ\text{K}, 900, 1) = 5 \times 10^8 \text{ cm} \cdot \text{cps}^{1/2} \cdot \text{watt}^{-1}$$

The typical photoconductive $9\text{-}\mu$ Ge:Au detector available commercially has a $D^*(500^\circ\text{K}, 900, 1)$ of about 4×10^9 . This indicates that the General Bronze Detector in its present form is down about a factor of 8 in D^* from the average value. It should be pointed out, however, that no effort was made to enhance the poor absorption characteristic which is associated with impurity-activated germanium. In conventional detectors using Ge:Au, the sensitive element is housed in a highly reflective chamber to insure multiple transmittals of the infrared photons through the element, thereby effectively increasing the absorption.

Further development of this detector should provide a valuable component to our infrared reconnaissance and scanning systems designers.

6.3. OPTICAL-PUMPING TECHNIQUES

6.3.1. AMPLIFICATION BY STIMULATED EMISSION. The advent of the Maser has suggested to many researchers the possibility that a similar amplification or even a detection process may be applicable to infrared radiation. Maser (Microwave Amplification by Stimulated Emission of Radiation) action is made possible by the inversion of the population of electrons in different energy levels of a material. The inversion is performed by "pumping" energy into a material by shining radiation of frequency higher than the frequency of the radiation to be detected or amplified. Figure 6-6 shows diagrammatically three possible energy levels of a material. First, radiation which has energy sufficient to cause transitions from level one to level three is shown on the material. This pumping action may be described by

$$hf_{1,3} + e_1 = e_3 \quad (6-9)$$

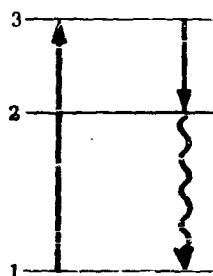


FIGURE 6-6. POSSIBLE ENERGY LEVELS

Then the electrons in level three make a transition to level two; the transition is accompanied by the emission of low-energy quanta:

$$e_3 = e_2 + hf_{3,2} \quad (6-10)$$

The system is then in a metastable state. When signal photons are incident, they cause the following reaction

$$hf_{1,2} + e_2 = e_1 + 2hf_{1,2} \quad (6-11)$$

If the system had not been made metastable by the pumping process, the reaction would have been

$$hf_{1,2} = e_1 + e_2 \quad (6-12)$$

The difference is due to the fact that in the metastable condition there are too many electrons in state two, and too few in state one; thus, the e_2 electrons make the transition.

One might think of the signal photon $hf_{1,2}$ as a catalyst, performing the function of increasing the probability of electron transitions from state two to state one. For, without $hf_{1,2}$, the final reaction occurring with low probability would have been

$$e_2 \rightarrow e_1 + hf_{1,2}$$

The new photon in Equation 6-11 must have the same phase as the catalyst photon.

These reactions have been applied to microwave detection and amplification by considering the energy levels available in different crystals and gases, and the competing or associated processes which contribute to the noise of the system.

Because the electrons of any material are bound to the nuclei or ion cores, they are also subject to interference from them. In a solid material this influence occurs by means of the electrostatic and magnetic coupling between the lattice atoms, and the electronic system which holds the lattice atoms together. In a gas, the interference is due to collisions between gas atoms and between gas atoms and the container wall. Since the Maser action depends upon the measurable increase in the stimulated emission due to the catalyst photon. It is important that the electron motions involved in transitions between energy levels be sufficiently isolated from the rest of the motions of the atomic system in order to avoid the overpowering influence of the rest of the atomic system in inducing transitions. The most successful Maser system, currently, makes use of the magnetic moment associated with the electron spin and orbital momentum, because in some materials these motions are relatively independent of the other crystalline and gas motions.

6.3.1.1. Bandpass. One of the disadvantages — and at the same time, advantages — of the Maser is that it tends to be a narrowband device. It works on the basis of the absorption of photons by bound electrons which change from one discrete energy state to another. The width of the spectral line associated with the two energy states will determine the spectral width of the system. Further, if the Maser is to be relatively noise free, the transition which corresponds to the stimulated radiation should be isolated from the rest of the motions in the material.

Although the Maser tends to be a narrowband device, there are theoretically no less than three techniques available by which the spectral band may be broadened. By analogy to electric circuit design, the basically high-Q system can be loaded with losses, thereby decreasing the effective quality

factor. Two or more high-Q resonant systems can be coupled tightly to each other, causing the resulting resonant curve to be considerably broader than either of the original ones. There is, of course, a limit to both of these techniques at which maser action will no longer be possible. A third technique utilizes an ensemble of isolated high-Q circuits which are not closely coupled, but which are stagger-tuned to a number of nearly equal frequencies. The "woofer-tweeter" systems of audio systems are common examples of this approach. The difficulty lies in obtaining a number of masers with response at the frequencies required.

6.3.1.2. Infrared Applications of the Maser Principle. It is preferable at this stage of the discussion to discard the term Maser, and replace it with the term Iraser. The concepts are exactly the same: radiation of frequency corresponding to the 1-3 transition is shone on the detector material; electrons make a transition from level one to level three; then from three to two with the emission of low-energy photons; and then from two to one as the signal radiation falls on the detector. Of course, $f_{1,2} = c/\lambda_{1,2}$ is now about 10^{14} cps, and the energy difference $hf_{1,2}$ is about 0.4 ev. The pumping energy must be considerably greater than 0.4 ev, probably that obtained in the visible part of the spectrum. Accordingly, rather than spin-moment energies, the levels associated with impurity levels and fluorescence in solids must be used. This is exactly what has been done in the case of the ruby Laser, which radiates rather than detects radiation (L stands for light): the pumping frequency is essentially that of green light (although white-light sources are used for convenience), and the emitted light is deep red, a wavelength of about 0.69μ .

6.3.1.3. Threshold Signal Limitations. The primary limit to the detectivity of any infrared detector is the fluctuation in the arrival of signal photons. However, this is a characteristic of the radiation and not the detector. All detectors operate exactly alike when they are limited by this photon noise. It is therefore important to investigate the limiting noise mechanism in the Iraser and see how it compares in absolute value with photon noise. The limiting mechanism, neglecting contributions from the circuit elements, is spontaneous emission. It is inherent in all quantum amplifiers of the Maser type. Spontaneous emission is a result of electrons in level two making a transition to level one when signal photons are not incident on the detector.

Spontaneous emission has been discussed by Weber (Reference 6-7) who derived an expression for the equivalent temperature (T_e) of spontaneous emission noise. This temperature is defined as

that positive temperature of a black background which emits noise equivalent to the spontaneous emission. It is expressed as

$$T_e = \frac{hf}{k} \ln 2 \quad (6-13)$$

where k is the Boltzmann constant. For frequencies up to about 10^{11} cps ($\lambda = 0.5$ mm), T_e is less than 28°K , and at a frequency 4×10^{14} ($\lambda = 0.8 \mu$) T_e becomes $18,000^\circ\text{K}$. It is apparent from this analysis that equivalent noise temperatures in the infrared region render the Iraser impractical for infrared detection unless target temperatures are much higher than $18,000^\circ\text{K}$.

It should be pointed out, however, that Equation 6-13 was derived assuming that the number of quanta per radiation oscillator (N) followed Bose-Einstein statistics,

$$N = \frac{1}{e^{hf/kT} - 1}$$

However, this relationship holds for $hf \ll kT$. For wavelengths shorter than 10μ , $hf > kT$ and Bose-Einstein statistics do not provide an accurate picture.

Schawlow and Townes (Reference 6-8) have shown that directional selection effectively decreases the spontaneous emission. This is true since spontaneous emission radiates into an infinite distribution of modes, while stimulated emission radiates into relatively few modes. This concept has been applied only to Lasers and not to the infrared-detection problem.

The conclusion is that infrared detectors employing the maser principle will suffer severely from noise due to spontaneous emission. Should innovations render the Iraser practical, the engineer still faces the problem of having an extremely narrowband device.

For further reference, the reader should consult the works of Gelinas (Reference 6-7), Whittke (Reference 6-9), Schawlow and Townes (Reference 6-8), and Bloembergen (Reference 6-10). In addition, excellent bibliographies and reviews are contained in publications of the Trionics Corporation (Reference 6-11) and the Jet Propulsion Laboratory of the California Institute of Technology (Reference 6-12).

6.3.2. QUANTUM COUNTERS. It is possible to construct quantum mechanical amplifiers without spontaneous emission noise (References 6-7 and 6-13). However, they are not Masers per se, since the output is not a result of stimulated emission. They are essentially quantum counters. Figure 6-7 shows a typical energy-level diagram for such a device. The separation between the ground state E_1

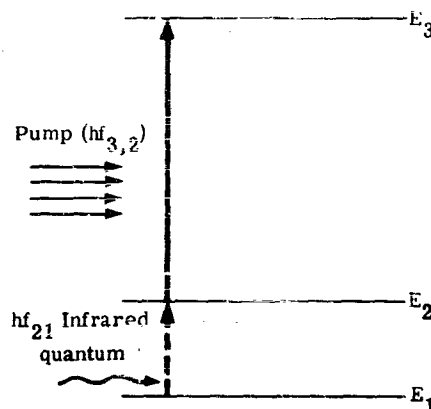


FIGURE 6-7. ENERGY-LEVEL DIAGRAM FOR AN INFRARED QUANTUM COUNTER

and level E_2 is such that $hf_{1,2} \gg kT$. This is to insure that very few electrons are thermally excited from the E_1 level to E_2 . When no infrared photons are incident, no output will occur since level E_2 is unpopulated. When an infrared photon is absorbed it causes a transition from level one to level two. The pumping frequency then produces a further transition to the E_3 level, provided the pumping intensity produces transitions at a faster rate than the radiationless decay or than the spontaneous emission from level E_2 back to the ground state.

Spontaneous emission from level E_3 to E_2 will lead to resonance, since on its decay from E_3 to E_2 , it may be repumped to E_3 again. Thus several quanta $hf_{3,2}$ may be re-emitted for each incident infrared quantum. The emitted radiation may be separated from the pumping flux by the use of polarization or direction of propagation.

Devices similar to this one are being developed at Harvard University, The Johns Hopkins University, and the University of Maryland.

6.4. REFERENCES

- 6-1. J. T. Wallmark, Proc. IRE, April 1957, Vol. 45, pp. 474-483.
- 6-2. J. T. Wallmark, Electronics, July 1957, Vol. 30, pp. 165-167.
- 6-3. W. Shockley, Electrons and Holes in Semiconductors, Van Nostrand, New York, N. Y., 1950, p. 316.
- 6-4. D. Allen, I. Weiman, and J. Winslow, "Radiation Tracking Transducers," presented to the Fourth IRE Instrumentation Conference, November 1959 (UNCLASSIFIED).

- 6-5. Technical Proposal for Infrared Detector Development Program, The General Bronze Corp., Garden City, N. Y., April 1958 (UNCLASSIFIED).
- 6-6. J. C. Conovar, Masters Thesis, "An Infrared Detector Utilizing a Microwave Resinator," Institute of Technology, Air University, August 1959 (UNCLASSIFIED).
- 6-7. J. Weber, Rev. Mod. Phys., July 1959, Vol. 31, No. 3, p. 681.
- 6-8. A. L. Schawlow and C. H. Townes, Phys. Rev., December 1958, Vol. 112, No. 6, pp. 1940-1949.
- 6-9. J. P. Wittke, Proc. IRE, March 1957, Vol. 45, pp. 291-316.
- 6-10. N. Bloembergen, Phys. Rev., October 1956, Vol. 104, No. 2, pp. 324-327.
- 6-11. Infrared Sensor Development, Final Report on Contract AF 33(616)-5895, Trionics Corp., Madison, Wis., March 1960 (UNCLASSIFIED).
- 6-12. Literature Search No. 57: MASERS, Jet Propulsion Laboratory, California Institute of Technology, Pasadena, Calif., 15 February 1960 (UNCLASSIFIED).

Appendix A TEST PROCEDURES

Sol Nudelman

The purpose of this appendix is to describe the experimental test program required to provide the necessary descriptive and evaluative information for proper detector usage. The information provided is extensive. It is the responsibility of the engineer to interpret properly and to use as much of this information as is required for the design of his infrared system. Most of the experimental detail supplied here is descriptive of the facilities and procedures established at the Naval Ordnance Laboratory, Corona (Reference A-1), and Syracuse University (Reference A-2). These facilities have been sponsored by the services to provide up-to-date quantitative measurements on all types and kinds of photodetectors, with the philosophy that experimental procedures undertaken and data provided be in the spirit of a standards laboratory. The following experimental information is required.

1. Optimum bias in the case of a photoconductive-type detector.
2. Noise spectrum.
3. Response to a blackbody, usually set at 500°K .
4. Spectral dependence in terms of
 - (a) Relative response
 - (b) Absolute response.
5. Time constant or frequency response.
6. Sensitivity contour.

From these data are obtained the various figures of merit listed in Table A-1.

A.1 DETERMINATION OF NEP

The circuitry used for measurement of noise and of signal response to a blackbody, and for the determination of optimum bias, is shown in block form in Figure A-1. The important components of this circuitry are the infrared source, the preamplifier, and a wideband harmonic analyzer. The source is a blackbody emitter, with precision temperature controls. A standard condition used to-day in test procedures is to make measurements with a blackbody set at a temperature of 500°K . The source is mechanically modulated by a disc-type chopper. Generally, this chopper is arranged

TABLE A-1. FIGURES OF MERIT

Figure of Merit	Definition	Units
NEI	$NEI = HV_N / V_S$	Noise equivalent input (watts/cm ²)
$NEP = P_n$	$NEP = HV_N A / V_S$	Noise equivalent power (watts)
Jones's	$S = \frac{NEP}{A^{1/2}} \left(\frac{f}{\Delta f} \right)^{1/2}$	Jones's (watts/cm)
D^*	$D^* = \frac{\sqrt{A \Delta f}}{NEP}$	The detectivity normalized to unit area and unit bandwidth (cm · cps ^{1/2} · watt ⁻¹)
S_1	$S_1 = \frac{V_S}{HE} \left(\frac{r_C + r_L}{4r_C r_L} \right)^2$	Specific sensitivity (cm ² /watt)

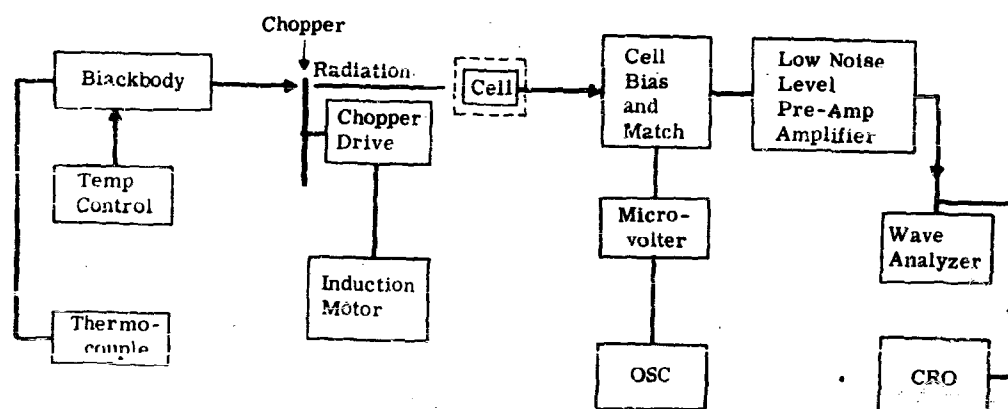


FIGURE A-1. BLOCK DIAGRAM OF SYSTEM TO MEASURE NEP

with two speeds to provide radiation modulated at 90 cps and 900 cps. This chopped radiation causes a similarly modulated electric signal to be generated in the detector system, amplified, and measured with the harmonic wave analyzer. The wave analyzer is also used to determine the noise level by obtaining a reading when the detector is shielded from the chopped radiation.

The signal and noise for a photoconductive detector are determined as a function of bias voltage. The bias current is varied, with signal and noise voltage determined for different values of the current. For most detectors chopping frequency in this case is not significant in that optimum bias does not change appreciably with modulating frequency. Figure A-2 shows a typical bias graph with plots

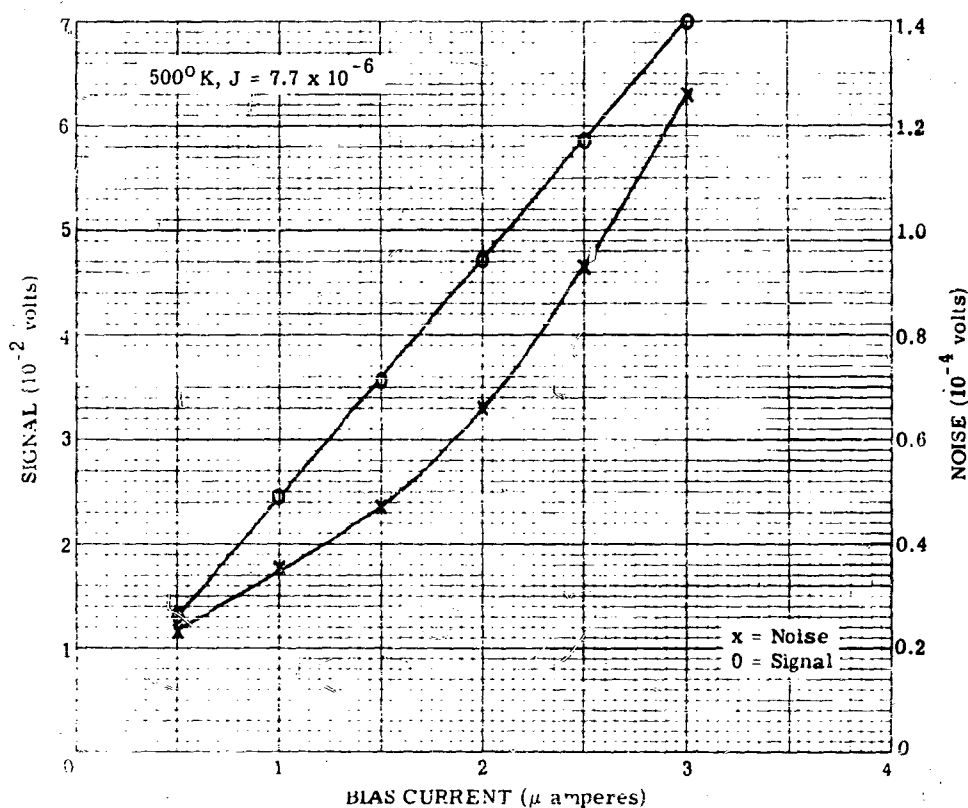


FIGURE A-2. DETERMINATION OF OPTIMUM BIAS

of signal and noise, versus bias current. This graph is typical of those supplied by the Naval Ordnance Laboratory, in which the radiation at 1.1 μ from a helium source is used for the signal measurement. The optimum bias point is determined from this graph and used in all subsequent measurements. Typical circuitry of the cell bias and match box shown in Figure A-1 is drawn schematically in Figure A-3. Two sets of input leads are shown from the detector to the match box. One set is used for photoconductive detectors where bias currents are needed and the other for non-current-carrying photovoltaic and PEM detectors. Photovoltaic- and PEM-type cells are usually tested by connecting them to the preamplifier through a transformer. This is because they have been low impedance devices. In particular, indium antimonide and indium arsenide are typical of such detectors. It is desirable to use a transformer whose impedance can be varied. This is important to insure that the equivalent noise input resistance of the preamplifier be transformed to an impedance lower than the impedance of the detector being tested. Another advantage of satisfying noise considerations is that maximum power can be transferred.

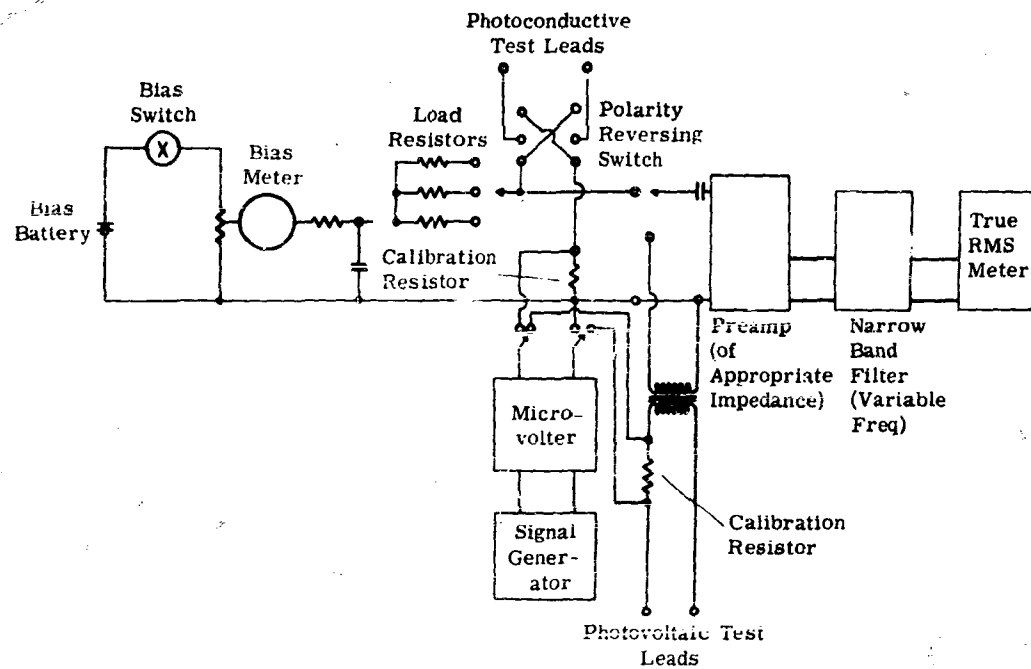


FIGURE A-3. TEST CIRCUITRY FOR INFRARED DETECTORS

The simplest kind of circuitry associated with the photoconductive detector is shown in Figure A-4(a) and consists simply of a bias battery supply in series with the photoconductive detector and a load resistor. The signal is taken off the load resistor and fed through a capacitor to a preamplifier. The voltage across the load resistor is given by

$$V_L = V \frac{r_L}{r_L + r_C} \quad (\text{A-1})$$

The change in voltage across the load resistor produced by the action of radiation is attained by differentiating this equation with respect to the resistance of the cell. Then it follows that

$$V_S = V \frac{r_L r_C}{r_L + r_C} \cdot \frac{\Delta r_C}{r_C} \quad (\text{A-2})$$

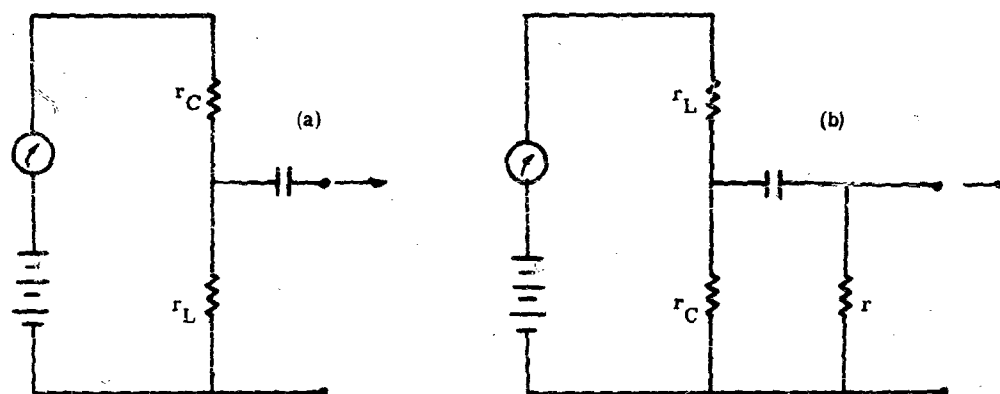


FIGURE A-4. PHOTOCONDUCTIVE DETECTOR CIRCUITS

The signal voltage V_S is symmetrical with respect to the load resistor and to the cell or detector resistance so that the same signal voltage can be picked off the photoconductor or the load resistor. When the load resistance is much larger than the detector resistance, a constant bias current condition prevails. Maximum signal voltage is obtained when the load resistance equals the detector resistance, while extended frequency response is obtained for small values of load resistance. This latter requirement usually appears when high-resistance fast detectors are dealt with. In this situation capacitive effects become important, and, in order to match the response time capability of the detector, it is necessary to use a small load resistor, resulting in reduced signal amplitude but flat frequency response over a wider frequency range.

response time capability of the detector, it is necessary to use a small load resistor, resulting in reduced signal amplitude but flat frequency response over a wider frequency range.

A modification of this simple circuit is shown in Figure A-4(b). It involves placing a d-c load resistor in series with the detector and an a-c load resistor across the detector through a coupling capacitor. The output is fed to the preamplifier from the a-c load resistor. The effect of this type of circuitry is to permit varying the load resistor to the preamplifier without influencing the biasing current of the photoconductive detector. This is important in attaining the optimum bias current. One would like to retain this condition and yet have the flexibility of varying the load resistor to the preamplifier for an independent control on frequency response.

In making any noise-limited measurements, it is important that the preamplifier noise be less than the detector noise. There are two types of noise to consider with respect to the preamplifier: (1), an effective series noise; (2), an effective parallel noise.

The series noise is experimentally determined by shorting the input to the preamplifier and noting the signal voltage at its output. The parallel noise is determined by opening the circuit input and recording the noise level. Then, starting with large resistances, a sequence of resistances of decreasing value is placed across the input to the preamplifier and the output noise is noted. These resistances are then reduced to a point where a change in the noise output from the open circuit condition of the preamp is recorded. Detector resistance is then maintained below this value. The resistance of the detector must provide a noise greater than the preamplifier noise. This condition is equivalent to the resistance of the detector, being larger than the series resistance of the preamplifier, but less than the shunt resistance. This condition is a sensible one. If two resistors are placed in series, the effective noise is the sum of the noise from the two resistors. If one is much larger than the other, then its noise predominates. When two resistors are placed in parallel, the effective resistance is that of the smaller resistance, and correspondingly the dominant noise is that which is associated with the smaller resistor. Therefore, the shunt resistances that may be incorporated in the preamplifier input, together with any other shunt resistance across the detector, must always be larger than the detector resistance. This requirement becomes difficult when one is forced to deal with very high impedance detectors, usually significantly higher than 15 or 20 megohms. Otherwise the problem of shunt noise is not serious, and one usually finds that the series noise requires the most caution.

The primary purpose of measuring signal and noise voltages with the equipment of Figure A-1 is to determine the photodetector noise equivalent power. This power can be determined if the

radiation power density from the blackbody falling on the detector is known. To calculate this value, it is necessary to start with the Stefan-Boltzmann law given by

$$W = \epsilon \sigma_s (T^4 - T_0^4) \quad (A-3)$$

where W = radiant emittance, or radiant power per unit area emitted from a surface, T and T_0 are the absolute temperatures of the radiating body and background respectively, ϵ is the emissivity, and σ_s is the Stefan-Boltzmann constant. The power density H from a source of radiance N at a distance x to the detector is the detector irradiance

$$H = N \cdot \frac{A_s}{\lambda^2} = \frac{w}{\pi} \cdot \frac{A_s}{\lambda^2} \quad (A-4)$$

where A_s is the source area, N is the radiant flux emitted by the source per unit area per unit solid angle and is equal to w/π . For a circular source aperture of diameter D_s , the power density is

$$H = \frac{w}{\pi} \cdot \frac{\pi D_s^2}{4\lambda^2} = \frac{w}{\pi} \frac{A_s}{\lambda^2} \quad (A-5)$$

and therefore NEP is given by

$$NEP = \frac{HA_d}{V_S/V_N} = \frac{w}{4} \left(\frac{D_s}{\lambda} \right)^2 \frac{V_N}{V_S} A_D \quad (A-6)$$

The gain of the circuitry used to determine NEP is checked with an oscillator and a microvolter connected to the input of the preamplifier. The noise bandwidth of the system is determined by measuring the Johnson noise generated in a wire-wound resistance as

$$\Delta f = \sqrt{2}/4kTr \quad (A-7)$$

where k is the Boltzmann constant, T is the absolute temperature, and r is the resistance. The signal to-noise ratio of a detector at a given bias current is generally independent of the load resistance. However, as shown by Equation A-2, the signal voltage, and correspondingly the noise voltage, are a function of the load resistor. Since different applications may require different load resistors, a

listing of detector signal and noise measurements must include the value of the load resistance used in making the measurements.

A.2. TIME CONSTANT

A knowledge of a detector's speed of response is of great importance to the system designer. In conjunction with noise spectra, it tells him at what frequencies he may operate the detector and still retain a sufficient signal for his purposes. He may also then select the frequency which will optimize the signal-to-noise ratio for his system's performance. Speed of response information is usually provided in one of two forms. They are (1), a plot of response versus frequency from which a detector time constant can be estimated, and (2), the photodecay characteristic after removal of a photoexcitation source. Information of type (1) is generally obtained by amplitude modulation of radiation from an infrared source irradiating the detector and varying the frequency of modulation, while type (2) is obtained by observing the signal wave shape of the photodetector response to periodic pulses of light. Systems for making measurements to provide the two types of information are described below.

A.2.1. FREQUENCY RESPONSE. This measurement is usually made with a metallic-disc light chopper. The disc is ringed with slits spaced symmetrically so that the separation distance between slits equals a slit's width.

The modulation frequency is given by the spinning rate of the disc multiplied by the number of slits in the disc. The higher the frequency of modulation required, the higher the spinning rate, and/or the greater the number of slits cut in the disc. Increasing the number of slits results in slits of decreasing width (for any one size disc), until eventually an optical system is required to image down the infrared source onto the slit. The radiation passing through the slits is then focused onto the detector. For low-frequency operation, sinusoidal modulation can be obtained by proper selection of the chopper opening (Reference A-3).

Corona determines the frequency response by using a variable-speed chopper, giving a frequency range of 100 to 40,000 cps. Radiation from a Nernst glower is sinusoidally modulated by the chopper and is usually filtered by a selenium-coated germanium window. The signal from the detector is measured by putting the output of a cathode follower and a preamplifier into the y-axis input of an oscilloscope. An incandescent tungsten source is simultaneously modulated by the chopper and activates a photomultiplier whose signal is fed into a preamplifier and a tachometer; the latter's output is proportional to frequency and is put on the X-axis of the oscilloscope. The oscilloscope display

is photographed as the chopper slows down from its maximum speed. Syracuse University, using a wheel cut with 1400 circular holes spinning at a rate of 10,000 rpm, obtains a maximum chopping frequency of 240,000 cps. This equipment uses a glow bar as the light source and an As_2S_3 lens to focus the source onto the slit. For photodetectors whose response can be described by

$$V_S = \frac{V_0}{\sqrt{1 + (\omega\tau)^2}} \quad (\text{A-8})$$

this high-frequency chopping rate permits an evaluation of time constants as short as 0.5 μsec . Typical frequency response data reported from NOLC are shown in Figure A-5.

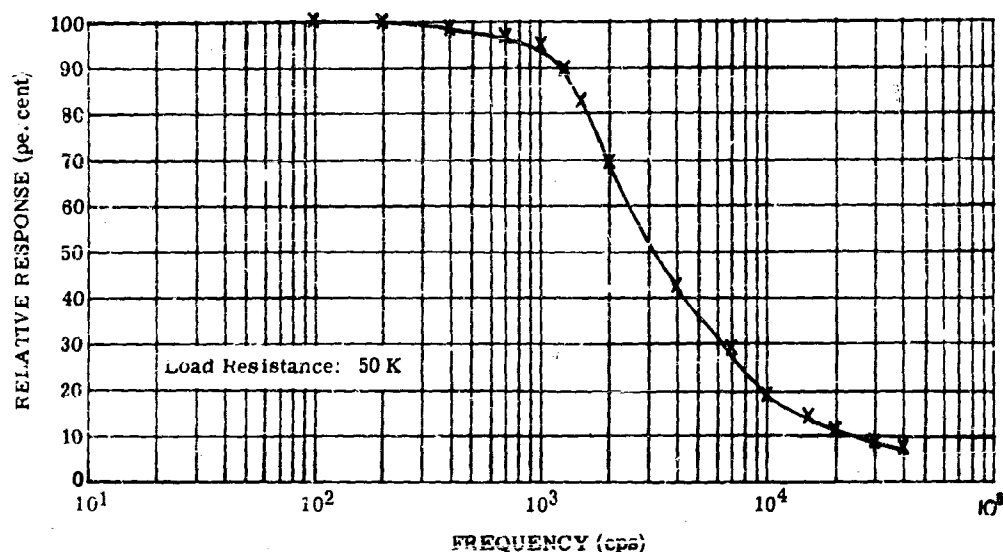


FIGURE A-5. DETECTOR FREQUENCY RESPONSE

A.2.2. PULSE RESPONSE. Another approach to the measurement of speed of response of the detector is a direct measurement of the decay or rise characteristics of the detector. For detectors with slow response and high sensitivity it is fairly easy to design a mechanical light chopper with sufficient speed so that the dynamic characteristics measured belong to the photodetector and not to the chopper. However, when one is forced to deal with photodetectors whose response times are less than 1 μsec , and where the signal is noise limited, then it becomes increasingly difficult to make this

measurement using normal procedures. To measure the decay or rise characteristics of the detector requires a light source whose rise or fall time is of the order of $1/10$ the time that is to be measured. Optical spinning mirror systems can provide such rapid rise-and-fall light-pulse time. A rather simple arrangement is shown in Figure A-6. A collimated beam of light is deflected by a rotating mirror. At distance X away from the mirror a decollimating mirror is placed, which focuses the infrared radiation on the detector. The rise time of the light pulse is the time it takes the leading edge of the pulse to fill the decollimating mirror, and the fall time is the time required for the trailing edge of the light beam to move off of that same mirror. The velocity with which the light ray moves across this mirror is given by the distance between the spinning mirror and the decollimator, multiplied by the angular velocity of the spinning mirror. The rise time and decay time, assuming a symmetrical light pulse, are then both equal, and equal to the width of the decollimator divided by the velocity. Obviously, by making X sufficiently large, the rise and fall times can be made shorter, but generally at the expense of decreasing intensity at the detector. The energy may be increased by the use of a cylindrical mirror which compresses without affecting its width. Light pulses with rise and decay times of the order of 50 nsec have been generated with this technique, using a mirror spinning at 10,000 rpm.

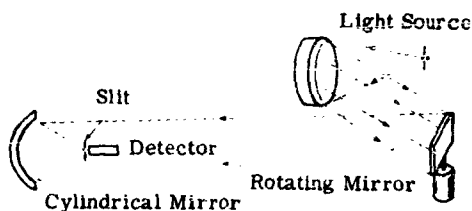


FIGURE A-6. SIMPLE SPINNING MIRROR FOR PERIODIC LIGHT-PULSE GENERATION

Another useful spinning mirror technique is that described by Garbuny (Reference A-4). The method consists of surrounding a rotating multisided mirror by a set of stationary mirrors (see Figure A-7). This assembly is so adjusted that the collimated light from the source is repeatedly reflected between the central and the stationary mirror plane. Each face of the mirror rotating with angular velocity ω adds 2ω to the rotational speed of the emerging light beam. If D is the width of a slit in the image plane and is less than the width of the light beam ϕ , the rise time and the fall time of the pulse are given by

$$\tau_r = \frac{D}{2N\omega X} \quad (\text{A-9})$$

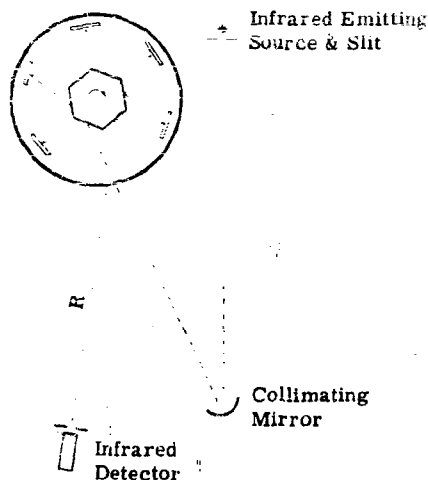


FIGURE A-7. SPINNING MIRROR SYSTEM FOR PERIODIC LIGHT-PULSE GENERATION IN THE MILLIMICROSECOND TIME DOMAIN

and the first part of the pulse.

$$\tau_d = \frac{\delta - 2D}{2N\omega X} \quad (A-10)$$

where N is the number of faces on the rotating mirror and X its distance from the image. By using a multisided spinning mirror to obtain high tangential velocities, it is possible to substantially reduce the radial distance from the spinning mirror to the detector over that required in Figure A-6. Using mirror optics for collimating the light source permits any infrared emitter to be used. With a 0.5-mm detector, a spinning mirror rotation rate of 10,000 rpm, $X = 1$ meter, and $N = 6$, rise times of 30 μsec are readily available. Using a turbine-drive motor system to spin the mirror, rotating speeds as high as 3000 rps can be obtained so that pulse rise and decay times of less than 1 μsec become readily possible.

Often in pursuing a research and development program on detectors, it is necessary to observe in detail the wave shape of the photoresponse to a light pulse. These observations often have to be made in the noise-limited condition. Examples of such cases are: (1) the examination of fractional

microsecond signals from high impedance generators such as gold-doped germanium. The measurement technique here requires the a-c loading of the detector (see Figure A-4b) with a low enough resistance to provide flat frequency response over the spectrum of interest. (2) The examination of fractional microsecond signals from low-impedance generators such as the InSb detector. This measurement is difficult because the noise level of a wideband preamplifier is higher than that of the detector. (3) The reproduction of low-level signals caused by low-level radiation sources. This is the case for wavelength-dependent measurements.

A device has been developed which makes measurement in these cases readily possible. The device applies a sampling technique and integration (or averaging) to the direct measurement of the shape of periodic noise limited waveforms. This may be compared to the usual coherent detector which can be used to measure the amplitude of fixed-frequency sine waves. In both cases the response time and bandwidth are determined by a simple RC integrator and the bandwidth narrowed at the expense of recording time. The operation of the wave-shape recorder can be described with reference to Figure A-8. The signal wave shape is periodic, triggered in the same manner that would be required for good high-speed oscillographic reproduction, while the noise is random in nature. The interval Δt represents an on-time of an electronic switch, during which the signal and noise voltage is fed directly into an integrator. By sampling successive intervals and averaging, it is possible to reduce the noise-voltage fluctuation observed at the integrator output without affecting the signal level. Quantitatively, the noise-voltage fluctuations are reduced by $1/\sqrt{N}$, where N is the number of observations made during an average measurement. The signal-to-noise voltage ratio is then improved by the square root of N . If Δt is made small compared to the signal transient time and is slowly and uniformly retarded in time with respect to signal onset, an accurate chart record of the signal wave shape may be produced (Reference A-5).

The circuit for the device is shown in Figure A-9, and is similar to the box-car circuit used in radar. Its components include a driven blocking oscillator activated by positive trigger pulses, an electronic switch, an integrator, a cathode follower and a recorder. The driven blocking oscillator provides a pulse to close the electronic switch. The switch connects the input of the integrator to the signal plus noise voltage occurring during Δt . During the off-time, the capacitor of the integrator will maintain its potential until the next on-time when a new signal plus noise level is sampled. To avoid signal attenuation, the output of the integrator is connected to a cathode follower and no continuous d-c current is allowed to flow. Since the purpose is to permit operation with signal-to-noise ratios less than unity, long integration times are required which are compatible with chart recorders.

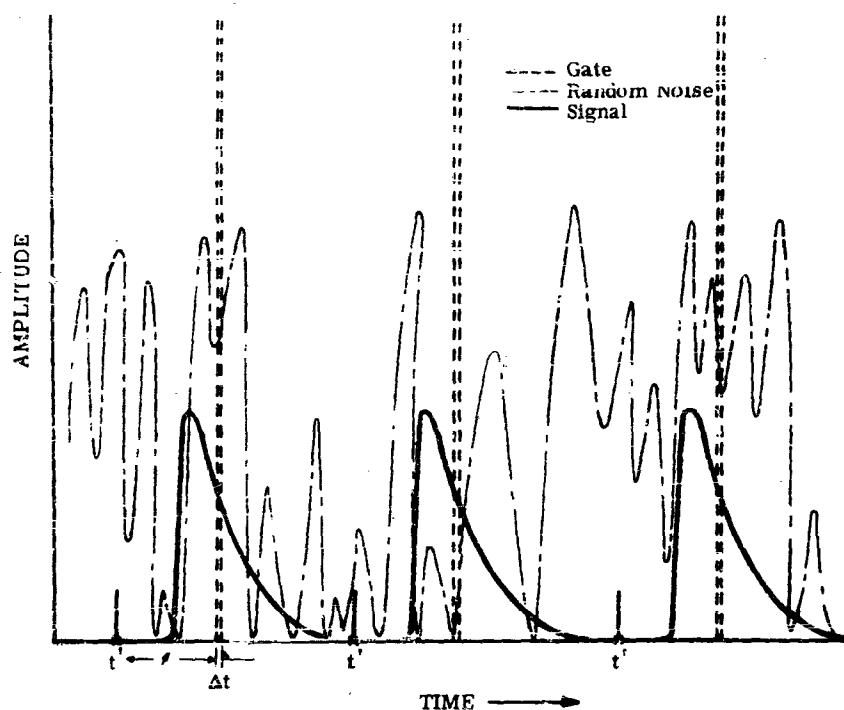


FIGURE A-8. SIGNAL, NOISE, AND GATE RELATIONSHIP IN WAVE-SHAPE RECORDER

A block diagram of a complete experimental arrangement for photon-excited signals is shown in Figure A-10. It is necessary that the signal of interest and the on-time switch be made to accurately follow some time reference. Two systems are shown which meet this requirement. The first system is used when the light sources available are capable of being driven by an electric signal such as a CRO lamp or electro-optic shutters. The sequence of events can then be demonstrated from a noise-free reference pulse provided by a stable oscillator.

The second system is used when mechanical light modulators such as spinning mirrors and rotating choppers are necessary. Now the reference pulse cannot be supplied by an external source, but must be generated by the modulator itself. This can be done by causing a light source to excite a fast photodetector such as a photomultiplier prior to excitation of the photodetector of interest. In both systems, if a variable delay is provided with respect to the reference, the electronic on-time switch may be slowly and uniformly retarded in time and a chart recording of the complete voltage

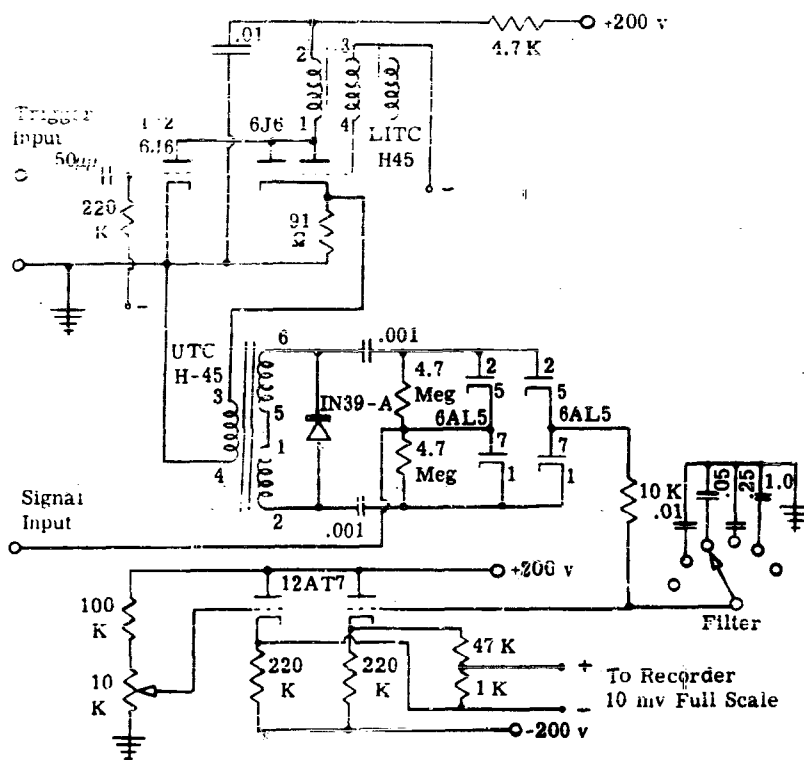


FIGURE A-9. SCHEMATIC OF WAVE-SHAPE RECORDER

waveform will be produced. Using the Garbuny spinning mirror, noise-reduction improvement by a factor of 300, with 50-msec light pulses has been achieved (Reference A-5).

A.3. SPECTRAL RESPONSE

Measurements of the wavelength dependence of infrared photodetectors are generally made with an experimental setup such as that illustrated in Figure A-11. The measurement is made with a constant energy irradiation at the detector by monitoring the output from the exit slit of the monochromator with a thermocouple throughout the spectral range of measurement. This may seem like a strange procedure considering that the photodetectors described here are photon counters rather than energy detectors. However, to make the measurement at constant photon densities requires a reference photodetector flat in response over an extended infrared wavelength region. Such detectors are not

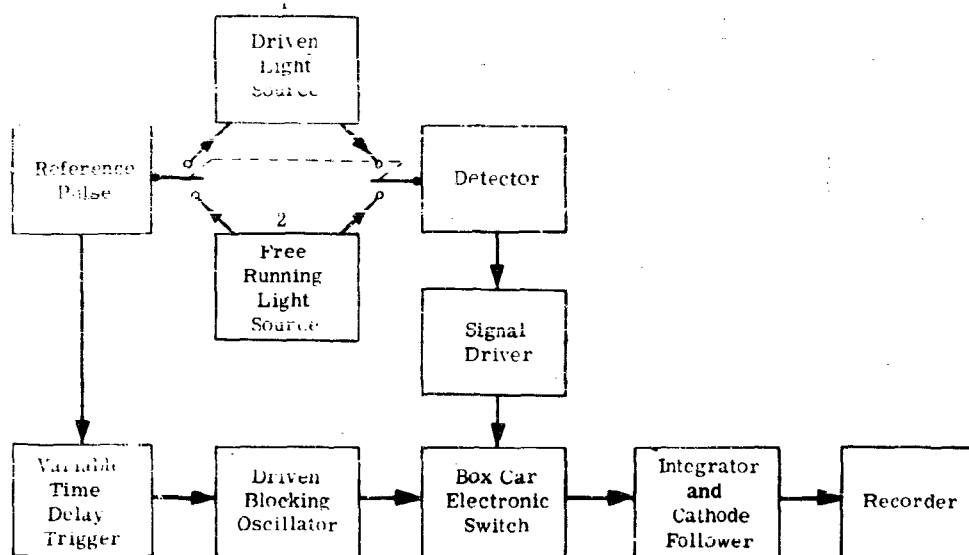


FIGURE A-10. BLOCK DIAGRAM OF WAVE-SHAPE RECORDER

yet available. Thermocouples, however, are flat over the wavelength region of interest here, and therefore are readily applicable to this kind of measurement. The result of this procedure is to obtain wavelength-dependent curves that are sawtoothed in appearance rather than flat topped. This is expected, as explained in Section 3.4. Two monochromators are in normal use at Corona; one, a Leiss double monochromator, has CaF_2 prisms, giving a range from 0.6 to 8μ , and the other, a Perkin-Elmer model 98, has NaCl prisms, giving a range from 2 to 15μ .

The energy flux from the exit slit is kept at a constant value over that portion of the spectrum used by comparing the flux at each wavelength with the thermopile or thermocouple response. This comparison arrangement can be accomplished within the monochromator or with an external arrangement. As the wavelength output is changed, the energy falling on the thermocouple is raised or lowered to an arbitrary value by opening or closing the entrance slit of the monochromator, with the middle and exit slits usually remaining fixed. Once this level is set, the energy flux is allowed to fall onto the detector and the response is then obtained. A typical relative response curve from Corona is shown in Figure A-12. Generally, the chopping rate of the light input to the monochromator is 10 to 13 cps, compatible with the response characteristics of the thermocouple. However, since most

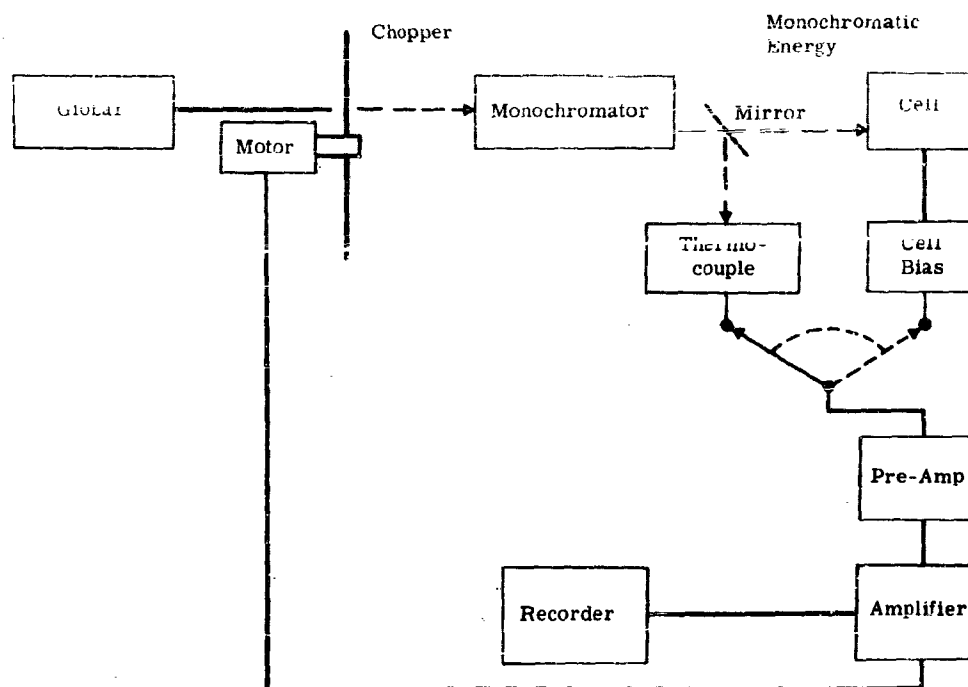


FIGURE A-11 . BLOCK DIAGRAM OF SYSTEM TO MEASURE DETECTOR RESPONSE

photodetectors show considerable improvement of NEP at higher chopping rates, it is advantageous when possible to modulate the spectral radiation at frequencies in the order of a few hundred cycles per second. At Syracuse, the chopper is operated at 208 cps, and the detector signal is measured by feeding it through a filter of 30 cps bandwidth tuned to 208 cps, a preamplifier, and a vacuum-tube voltmeter. At the low chopping frequency, the detector signal is fed directly into the amplifying system of the monochromator.

Along with the measured relative spectral response curve, it is important that the detector user be provided with an absolute calibration sufficiently universal so that the spectral dependencies of figures of merit, such as NEI, NEP, and D^* , can be readily derived. The information available from the measurements of NEP and relative spectral response, and the theoretical law for blackbody spectral radiation distribution are sufficient to provide the absolute calibration.

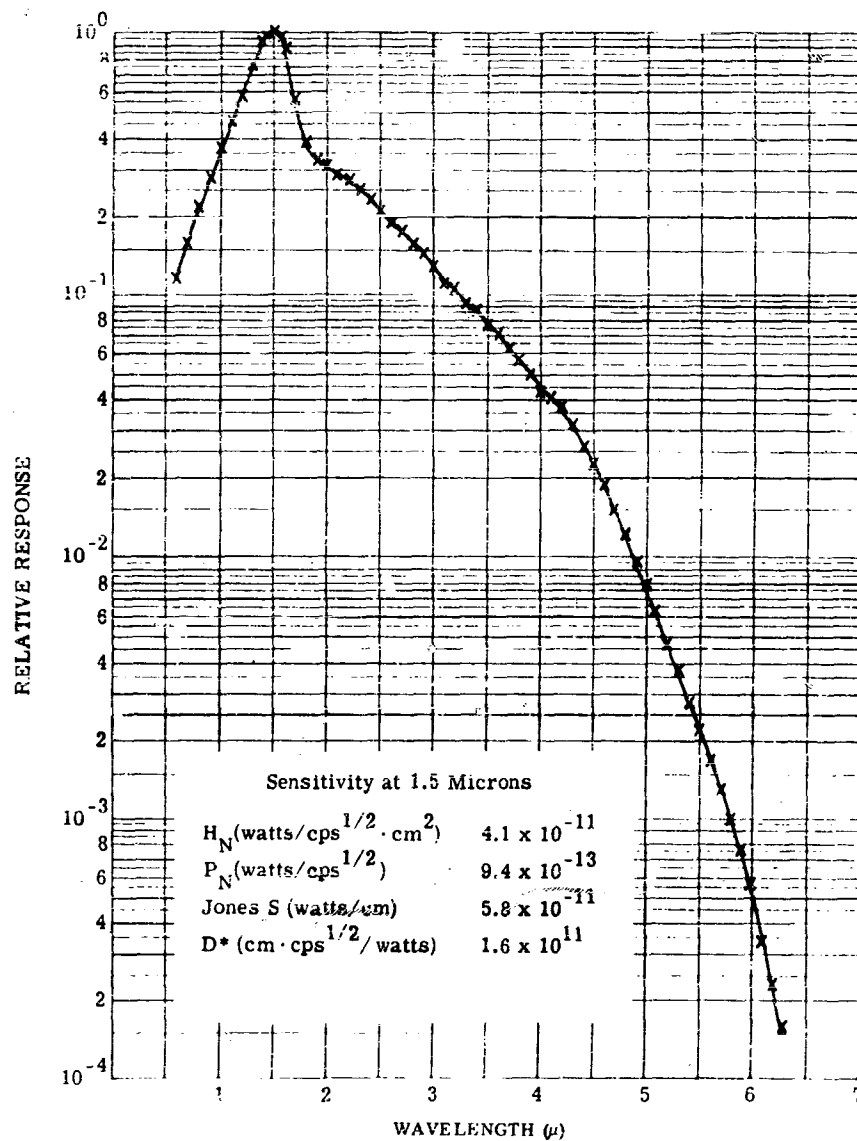


FIGURE A-12. DETECTOR RELATIVE SPECTRAL RESPONSE

The noise equivalent power is defined by

$$NEP = \frac{P}{V_S/V_N} = \frac{V_N}{\gamma_T} \quad (A-11)$$

where $P = H \cdot A$, $\gamma_T = \frac{V_S}{P}$, γ_T is the responsivity of the detector to a blackbody (usually set at 500°K), and P is the radiation power falling on the detector.

Since this is a blackbody measurement, the responsivity is determined in an absolute manner, and represents an average value taken over the spectral range of sensitivity of the photodetector. In Figure A-13, the averaged absolute value of the responsivity is shown (C), together with the blackbody spectral radiation curve (A), and a plot of the relative spectral photoresponse of the detector (B). It is clear that one can provide an absolute scale corresponding to curve C, but it still has to be determined where curve B should be placed with respect to this scale. When curve B is properly placed

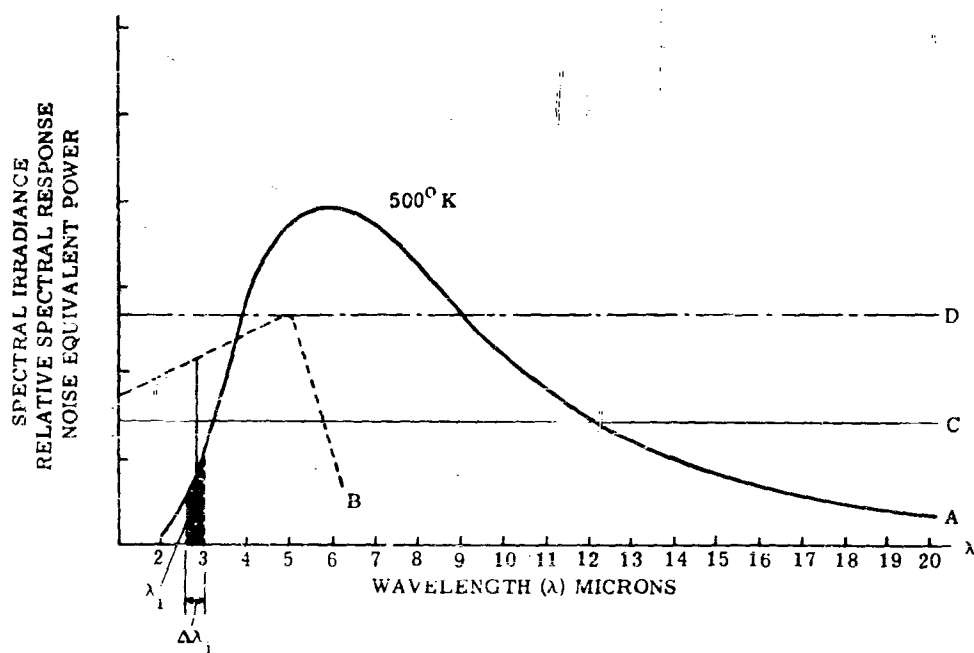


FIGURE A-13. DETERMINATION OF ABSOLUTE SPECTRAL RESPONSE

on the scale corresponding to an absolute calibration, the product

$$\sum_{i=0}^{\infty} \gamma_{a, \lambda_i} \cdot \Delta P_{\Delta \lambda_i}$$

where γ_{a, λ_i} is the absolute response and $\Delta P_{\Delta \lambda_i}$ is the power in the bandwidth $\Delta \lambda$ centered at λ_i , summed over the wavelength of detector spectral sensitivity, equals the signal voltage obtained in the NEP measurement, and therefore also the averaged absolute responsivity curve C.

The quantity needed for calibration is the absolute value of the spectral response determined at the "peak" of curve B. To arrive at this value, assume that another (unknown) photodetector response curve (D) is flat (a black detector), and passes through the peak of our photodetector curve B. The ratio of the signal voltages generated by these two different detectors is given by

$$\xi = \frac{V_r}{V_{BB}} = \frac{\sum_{i=0}^{\infty} \gamma_{r, \lambda_i} P_{\lambda_i} \Delta \lambda_i}{\sum_{i=0}^{\infty} \gamma_{BB, \lambda_i} P_{\lambda_i} \Delta \lambda_i} = \frac{\sum_{i=0}^{\infty} \gamma_{r, \lambda_i} P_{\lambda_i} \Delta \lambda_i}{\gamma_{BB, \lambda_i} \sum_{i=0}^{\infty} P_{\lambda_i} \Delta \lambda_i} \quad (A-12)$$

If one normalizes, taking $\gamma_{BB, \lambda_i} = 1$

$$\xi = \frac{\sum_{i=0}^{\infty} \gamma_{r, \lambda_i} P_{\lambda_i} \Delta \lambda_i}{\sum_{i=0}^{\infty} P_{\lambda_i} \Delta \lambda_i} \quad (A-13)$$

The denominator is simply the blackbody radiation energy falling on the black photodetector of unit response, while the numerator provides a smaller number representing the signal voltage derived from our photodetector. Obviously the numerator is smaller than the denominator, and ξ represents an effectiveness factor indicating how close the average response of B comes to that of the black detector D.

The absolute value of the averaged spectral response C, as noted earlier, is a quantity obtained in the NEP measurement. Therefore an absolute determination of the peak spectral response can now be obtained by dividing the responsivity value from the NEP measurement by the effectiveness factor. Similarly, this procedure provides an absolute spectral dependence for the other figures of merit.

To calculate the effectiveness factor, the expression for ξ is simplified to

$$\xi = \frac{\sum_{i=0}^{\infty} r_i \lambda_i H_{\lambda_i} \Delta \lambda_i}{\sum_{i=0}^{\infty} H_{\lambda_i} \Delta \lambda_i} \quad (\text{A-14})$$

where $P_{\lambda} = H_{\lambda} A$ and H_{λ} is the radiant power per unit wavelength at the wavelength λ , for the blackbody used in the measurement (here taken at 500°K). However, a correction to the expression for γ must be considered. In practice the experiment performed to determine NEP involves using chopped radiation from a 500°K blackbody source. However, the chopper generally is a black mechanical spinning disc whose temperature is about 300°K (room temperature). Therefore the a-c signal response is actually the result of the detector's looking alternately at 500°K and 300°K sources, and not simply at a 500°K source against a background of absolute zero. The detector is then actually sensitive to the shaded portion of the radiant power, shown in Figure A-14. The effectiveness factor

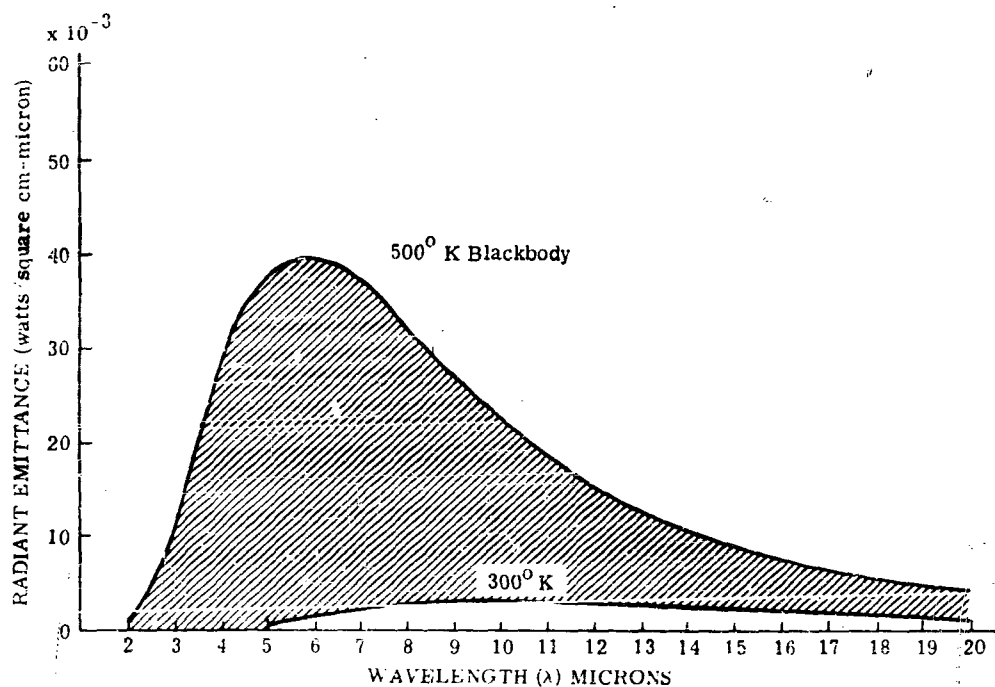


FIGURE A-14. BLACKBODY SPECTRAL RADIANT EMITTANCE

should then more properly be expressed as

$$\xi = \frac{\sum_{i=0}^{\infty} \left(H_{\lambda_i}^{500^\circ} - H_{\lambda_i}^{300^\circ} \right) \gamma_{r_i \lambda_i} \Delta \lambda_i}{\sum_{i=0}^{\infty} H_{\lambda_i}^{500^\circ} \Delta \lambda_i - \sum_{i=0}^{\infty} H_{\lambda_i}^{300^\circ} \Delta \lambda_i} \quad (\text{A-15})$$

The denominator is determined from the Stefan-Boltzmann law (see Equation A-3)

$$W = \sigma_s T^4 - T_0^4$$

where σ_s is the Stefan-Boltzmann constant, and T and T_0 are 500°K and 300°K , respectively. The quantity H is therefore the power exposure responsible for the detector signal response, and is a constant. The "power fraction" given by

$$F_{\lambda_i} = \frac{\left(H_{\lambda_i}^{500^\circ} - H_{\lambda_i}^{300^\circ} \right) \Delta \lambda_i}{H} \quad (\text{A-16})$$

where $H_{\lambda_i}^{500^\circ} \Delta \lambda_i$ is the radiant power within the bandwidth $\Delta \lambda_i$ at the center wavelength λ_i , can now be used in the determination of ξ , since

$$\xi = \sum_{i=0}^{\infty} F_{\lambda_i} \cdot \gamma_{r_i \lambda_i}$$

The power fraction may be calculated at different wavelengths, either by the use of a radiation slide rule or the tables of A. N. Lowan and G. Blanch (Reference A-6). A table can then be prepared to evaluate ξ , as shown by Table A-2.

Once the effectiveness factor is calculated, the peak value of NEP or D^* can readily be computed, since

$$\text{NEP}_{\lambda, \text{peak}} = \text{NEP}_{\text{BB}} \cdot \xi$$

or

$$D^*_{\lambda, \text{peak}} = \frac{D^*_{\text{BB}} \left(500^\circ \right)}{\xi}$$

as shown in Table A-2.

TABLE A-2. EVALUATION OF $D^*_{\lambda, \text{peak}}$

$$D^*(500^\circ\text{K}, 900 \text{ cps}) = 7 \times 10^9 \text{ cm-cps}^{1/2} \text{-watt}^{-1}$$

$$\text{Cell response factor (K)} = \frac{D^*(500^\circ\text{K}, 900 \text{ cps})}{\sum (\text{Energy Fraction} \times \text{Relative Response})} = \frac{7 \times 10^9}{20} = 3.5 \times 10^8$$

Wavelength Interval (μ)	Energy Fraction (500°K Blackbody)	Relative Response (Mid-Interval)	Energy Fraction x Relative Response	$D^* = K$ (Relative Response)
1-1.5	7×10^{-6}	20		$.7 \times 10^{10}$
1.5-2.0	3.7×10^{-4}	32		1.1×10^{10}
2.0-2.5	.0032	44	0.1	1.5×10^{10}
2.5-3.0	.012	55	0.7	1.9×10^{10}
3.0-3.5	.024	66	1.6	2.3×10^{10}
3.5-4.0	.038	84	3.2	2.9×10^{10}
4.0-4.5	.050	90	4.5	3.1×10^{10}
4.5-5.0	.058	80	4.6	2.8×10^{10}
5.0-5.5	.062	55	3.4	1.9×10^{10}
5.5-6.0	.063	30	1.9	1.1×10^{10}
6.0-6.5	.061			
6.5-7.0	.058			
7.0-7.5	.054			
7.5-8.0	.050			
8.0-8.5	.045			
8.5-9.0	.041			
9.0-9.5	.037			
9.5-10.0	.033			
10.0-10.5	.029			
10.5-11.0	.027			
11-12	.045			
12-13	.035			
13-14	.029			
14-15	.022			
15-16	.019			

TABLE A-2. (Continued)

wavelength Interval (μ)	Energy Fraction (500°K Blackbody)	Relative Response (Mid-Interval)	Energy Fraction x Relative Response	D* = K (Relative Response)
16-17	.015			
17-18	.013			
18-19	.011			
19-20	.0084			
20-22	.015			
22-24	.0097			
24-26	.0072			
26-28	.0038			
28-30	.0029			

Σ Sum: 20.0

A.4 NOISE SPECTRUM

The noise-voltage spectrum is obtained with the system described in Section A.1. However, the light source is removed, and the noise voltage is obtained by simply reading the voltage at the wave analyzer. A typical plot of noise spectrum is shown in Figure A-15.

A.5 SENSITIVITY CONTOURS

If a microscopic spot of light is projected onto the surface of a photodetector, and the photoresponse recorded as a function of the spot's position, it is found that the photoresponse generally changes with the spot's position. The surface of the detector is thus rarely uniform in its photoresponse. The film detectors (lead compound family) are the worst offenders in this regard. If a graph of photoresponse versus light-spot position is made, and points of equal photoresponse are linked together, the resultant plot provides a "sensitivity contour," illustrated by Figure A-16 for a PbSe detector.

The experimental arrangement at Corona to obtain sensitivity contours uses a microtable which allows the cell to be moved a small measured amount. The table is linked through a system of gears to a plotting table which gives up to a 36/1 increase in the scale. The exciting radiation is from an

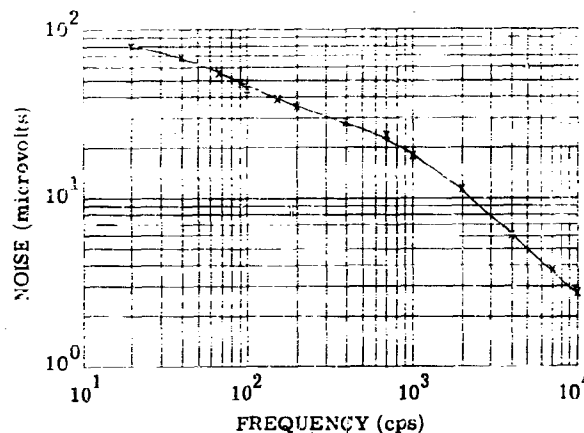


FIGURE A-15. DETECTOR NOISE SPECTRUM

incandescent tungsten bulb chopped at 90 cps and is passed in reverse through a microscope so that a spot 0.066 mm in diameter is focused on to the detector. As the detector is moved beneath this radiation, the relative response at 10 percent intervals is noted on the plotting table. Lines connecting equal points of sensitivity are then drawn to obtain a plot such as in Figure A-14. This light-probe technique is also important for its utility in fundamental research programs on detector materials, where it is used in studies of diffusion length, time constant, and mobility (Reference A-7).

Contours of the sensitive area of a photodetector are of principal concern when the optical system associated with the detector does not utilize the full area. Also, they are important in determining an averaged evaluation of the surface area for substitution in the expression for D^* .

A.6 GENERAL COMMENTS

A summation of data necessary to evaluate a detector is shown in Figure A-17, which consists of a typical data sheet from an NOLC report. Notice that the data for blackbody and spectral response are followed by sets of three numbers in parentheses. These numbers represent quantities which have essentially become standards for rating infrared detectors. The notation $D^*(500, 90, 1)$ under blackbody response means that the test blackbody was operated at 500°K, the radiation from the blackbody was amplitude modulated at a frequency of 90 cps, and the bandwidth of the evaluation was normalized to 1 cps. For $D^*(\lambda, 90, 1)$ under spectral response, λ refers to the wavelength at which detector

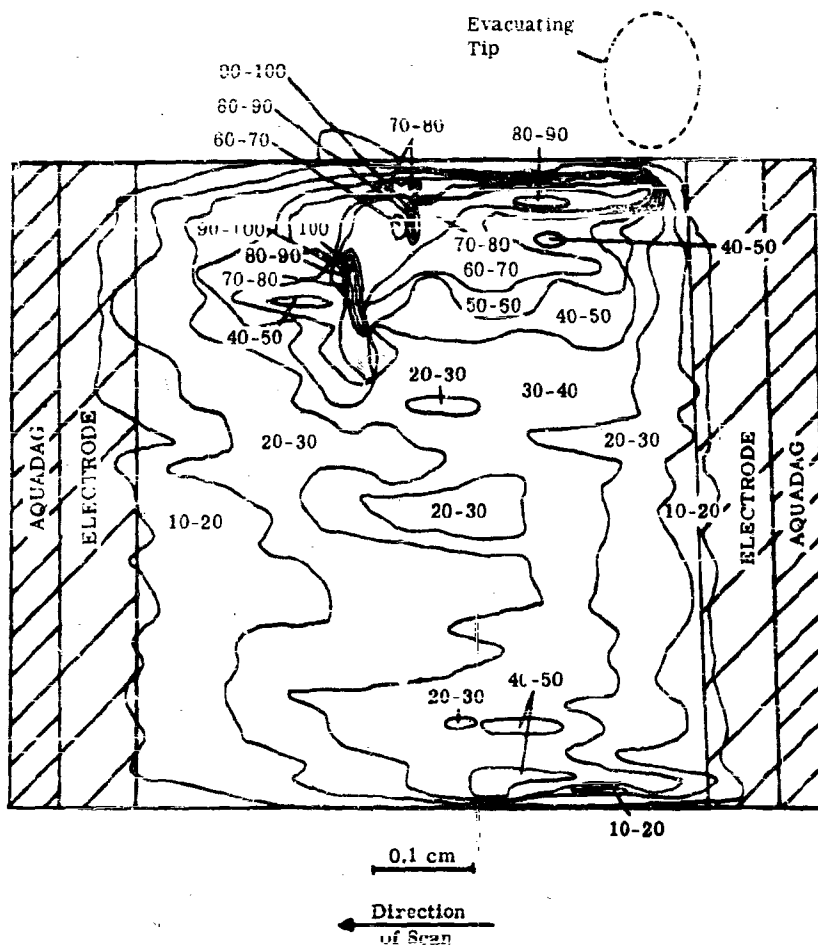


FIGURE A-16. DETECTOR SENSITIVITY CONTOUR

response is a maximum, while the other numbers mean the same as above. The quantities H_N and P_N refer to detector noise equivalent irradiance and NEP, respectively.

A quantity denoted as "Jones' S" appears in the table and merits discussion. The term was suggested by R. C. Jones (Reference A-8) early in the development of infrared photoconducting detectors. Refer to Equation 4-52, separating out the factors of frequency, bandwidth, and area: it follows that the detectivity in the excess-noise-limited case is proportional to the square root of the frequency,

CELL SENSITIVITY		CONDITIONS OF MEASUREMENT	
500°K blackbody response		Chopping frequency (cps)	90
H_N (watts $\text{cps}^{1/2} \cdot \text{cm}^2$)		Bandwidth (cps)	5
(500, 90, 1)	4.5×10^{-9}	Humidity (%)	23.5
(500, , 1)	Cell temperature (°C)	-195
P_N (watts/ $\text{cps}^{1/2}$)		Dark resistance (ohms)	5.2×10^6
(500, 90, 1)	1.0×10^{-10}	Dynamic resistance (ohms)	...
(500, , 1)	Load resistance (ohms)	5.5×10^6
Jones S (watts/cm)		Transformer	...
(500, 90, 1)	6.5×10^{-9}	Cell current (μ amps)	1.5
(500, , 1)	Cell noise (μ volts)	47
D^* (cm $\cdot \text{cps}^{1/2}$ /watt)		Blackbody flux density (μ watts/ cm^2 , rms)	7.7
(500, 90, 1)	1.5×10^9		
(500, , 1)		
Spectral peak (μ)	1.5		
Response at spectral peak			
H_N (watts/ $\text{cps}^{1/2} \cdot \text{cm}^2$)			
(λ , 90, 1)	4.1×10^{-11}		
(λ , , 1)		
P_N (watts $\cdot \text{cps}^{1/2}$)			
(λ , 90, 1)	9.4×10^{-3}		
(λ , , 1)		
Jones S (watts/cm)		CELL DESCRIPTION	
(λ , 90, 1)	5.8×10^{-11}	Type: Ge (AuSb doped)	
(λ , , 1)	Angular field of view: approx. 110°	
D^* (cm $\cdot \text{cps}^{1/2}$ /watt)		Window: sapphire	
(λ , 90, 1)	1.6×10^{11}	Method of preparation: crystal	
(λ , , 1)	Area (cm^2): 2.25×10^{-2}	
Effective time constant (μ sec)	8.1×10^1		
DATA SHEET NO. 675			
PHILCO CORP., CELL NO. 1207			

FIGURE A-17. A TYPICAL DATA SHEET

and inversely proportional to the square root of the product of area and bandwidth. It follows that the quantity defined as

$$\text{Jones' } S = \sqrt{f/D^*}$$

is a quantity independent of the frequency of a measurement and therefore useful for evaluating intrinsic detectivity. The development of infrared detectors, however, has advanced to a state where $1/f$ noise limitations have been reduced to the point where this concept is no longer useful. It is incorrectly used when applied to any of the other types of noise limitations. Jones has recommended that Jones's be discontinued as a means of rating detectors. This probably will happen in the near future.

Finally, as a generally useful report, which covers much of infrared detection technology, see Reference 9.

A.7 REFERENCES

1. R. F. Potter, J. M. Pernet, and A. B. Naugle, Proc. IRE, 1959, Vol. 47, p. 1503.
2. P. Bratt, W. Engeler, H. Levenstein, A. MacRae, and J. Pehek, Final Report on Ge and InSb Infrared Detectors, Syracuse University, under Air Force WADD Contract Nr. AF 33(616)-3859, February 1960.
3. R. B. McQuistan, J. Opt. Soc. Am., 1953, Vol. 48, p. 63.
4. M. Garbuny, T. P. Vogt, and J. R. Hansen, Rev. Sci. Instr., 1957, Vol. 28, p. 828.
5. S. Nudelman and J. T. Hickmott, Bull. Am. Phys. Soc., 1959, Ser. 2, Vol. 4, 153.
6. A. N. Lowan and G. Blanch, J. Opt. Soc. Am., 1940, Vol. 30.
7. Methods of Experimental Physics, K. Lark-Horovitz, V. A. Johnson and L. Marton eds., Academic, New York, 1959, Vol. 6B, p. 352.
8. R. C. Jones, Rev. Sci. Instr., 1953, Vol. 24, p. 1035.
9. W. J. Beyen, P. R. Bratt, H. W. Davis, L. F. Johnson, H. Levenstein, and A. V. MacRae, Final Report on Germanium and Lead Telluride Detectors, Syracuse University, under Air Force WADC Contract AF 33(616)2221, February 1957.

Appendix B
IMMERSION LENSES for INFRARED INSTRUMENTS

William L. Wolfe and John Duncan

B. 1. INTRODUCTION

Many infrared instrument applications require large-aperture, high-speed, optical systems. The straightforward approach to this problem is careful design and painstaking manufacture of precious surfaces—which often must be aspheric. But the straightforward technique has engineering limitations, e.g., maximum obtainable size of refractive elements, and stress and temperature problems with very large reflectors. The requirement for volume and weight reduction imposed by space applications is also an influential factor. Accordingly, optical designers have come upon the idea of using small field lenses in contact with detectors. These lenses provide an engineering advantage over larger optical systems—and provide an additional advantage when used in an already large, high-speed system. The usual arrangement has been a hemispherical button which provides a gain proportional to the refractive index (Reference B-1). One of the authors of this appendix (W. W.) suggested some time ago that some improvement might be obtained by the use of the aplanatic surface of a hemisphere. More recently, it has been shown that the gain for the aplanatic case is proportional to n^2 .¹ This appendix presents a more thorough investigation of the problem.

There are two general cases for which the gain should be calculated: (1) sources which are small compared to the entrance window of the optical system, and (2) sources which are large compared to or about the same size as the entrance window. It also is important to specify whether the gain is obtained by changing the position of the detector assembly in the optical system (keeping the detector size constant) or by changing the detector size, keeping the position fixed. Finally, the gain will depend upon the configuration of the lens itself. Only the hemisphere and aplanatic hyperhemisphere are considered here.

¹ This result was obtained by Eric Wormser and John Strong and indicated in a private communication.

The inclusion of all these parameters in the analysis requires consideration of eight cases. These cases are listed below:

- I. Point Source
 - A. Constant-Area Detector
 1. Aplanatic lens
 2. Hemispherical lens
 - B. Constant-Position Detector
 1. Aplanatic lens
 2. Hemispherical lens
- II. Extended Source
 - A. Constant-Area Detector
 1. Aplanatic lens
 2. Hemispherical lens
 - B. Constant-Position Detector
 1. Aplanatic lens
 2. Hemispherical lens

B. 2. DEFINITION OF GAIN

Since infrared, immersion, optical systems are the sole subject of this paper, the gain can be defined as the ratio of the output of an infrared detector which is immersed to the output of an unimmersed detector. The useful output of a detector may be specified as the signal-to-noise ratio S/N generated by a given input power P . This can be written in terms of the detectivity D :

$$S/N = PD$$

Thus the gain G is

$$G = \frac{(S/N)'}{S/N} = \frac{P'D'}{PD}$$

where primes indicate quantities describing the immersed system. The gain is equal to the ratio of the product of the incident power and the detectivity for the two cases. It has been shown that the detectivity of a detector is inversely proportional to the square root of its area (Reference B-2). Thus,

$$G = \frac{P'}{P} \sqrt{\frac{A}{A'}}$$

B.3. POINT-SOURCE CASES

If the object to be viewed is a radiating point source, and if reflection losses are ignored, the power received by an immersed detector is the same as the power received by an unimmersed detector. Then the gain is

$$G = \frac{P'}{P} \sqrt{\frac{A}{A'}} = \sqrt{\frac{A}{A'}}$$

If the detector area is not changed (Cases IA1 and IA2), there is no gain. If the immersion lens is used so that the area of the detector can be decreased, the gain will equal the ratio of the square roots of the detector areas. For the aplanatic lens (Case IB1) this ratio is n^2 , or

$$G = n^2$$

This relationship can be obtained through the following considerations (Figure B-1). A spherical lens of refractive index n and radius r is placed in air (of refractive index 1). Then two hypothetical spheres are constructed concentric with the spherical lens, one with radius nr , one with radius r/n . The lens then has the property that all rays which would have intersected the outer sphere at B (e.g., AB) now intersect the inner sphere at C. Furthermore, the image is aplanatic—it has no spherical or comatic aberration. The properties of such a sphere are further described in the literature (References B-3 to B-5). It is easy to see that if chords are good approximations to arcs the ratio of the linear dimensions of the images of the optical system is given by CE/BF . Further, the triangles DEC and DBF are similar; thus

$$\frac{CE}{BF} = \frac{DC}{DB} = \frac{r/n}{rn} = \frac{1}{n^2}$$

The linear dimensions of the detectors have the ratio $1:n^2$; the areas have the ratio $1:n^4$. So the gain is

$$G = \sqrt{\frac{A}{A'}} = \sqrt{n^4} = n^2$$

For the hemispherical case with constant area (Case IA2) there is no gain, as noted above for Cases IA. If the area is changed (Case IB2), the magnification expressions for a single spherical surface can be used. The result is

$$G = \sqrt{\frac{A}{A'}} = \sqrt{n^2} = n$$

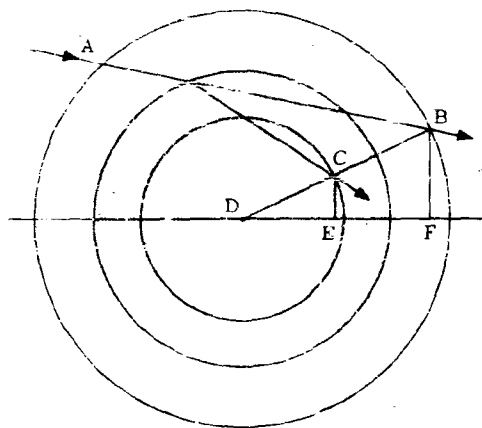


FIGURE B-1. APLANATIC SPHERE

B.4. EXTENDED-SOURCE CASES

Next, the extended-source cases may be considered. For an extended source, the radiance divided by the square of the refractive index is constant. Thus

$$G = \frac{P'D'}{PD} = \frac{N'A'\omega'D'}{NA\omega D} = \frac{\omega'n^2}{\omega} \sqrt{\frac{A'}{A}}$$

where ω is the solid angle of the optical system. For constant area (Cases IIA1 and IIA2), the gain is proportional to the ratio of the solid angles of acceptance and n^2 . These angles can be determined as follows: the angle ω is the area of the principal optical element divided by the focal length squared. When the immersion lens is introduced, the angle ω' is the area of the image of the principal optical element formed by the immersion lens divided by the distance of the image from the focal plane. Consider Figure B-2. The image of the optical element h is h' . The object and image distances are o and i , respectively. Then from two expressions for magnification it is possible to write

$$\frac{h'}{h} = \frac{i}{o + r}$$

Thus

$$\frac{\omega'}{\omega} = \left[\frac{h' \cdot (o + r)}{h \cdot i} \right]^2 = \left(\frac{r}{o + r} \right)^2 = \left(\frac{f}{d} \right)^2$$

where $d = o + r$. Thus for Case IIA1,

$$G = \left(\frac{nf}{d + r/n} \right)^2$$

and for Case IIA2,

$$G = \left(\frac{nf}{d} \right)^2$$

The problem then is to determine d . Refer to Figure B-3. The equation of the edge ray is

$$y = -\frac{h}{f}x + h$$

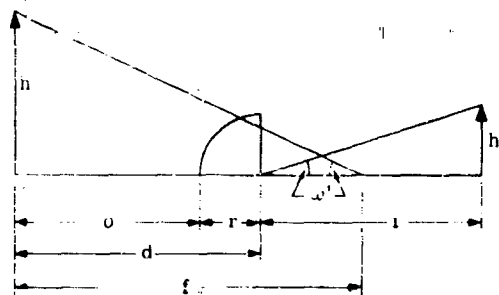


FIGURE B-2. SOLID-ANGLE GEOMETRY

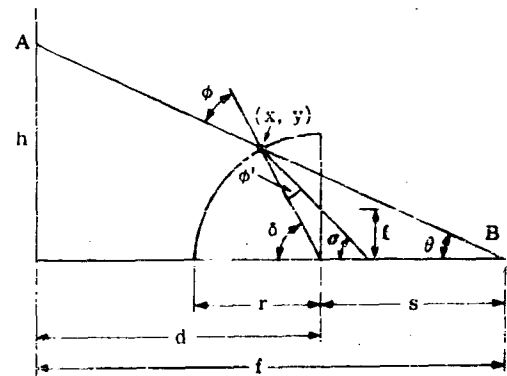


FIGURE B-3. IMMERSION-LENS GEOMETRY

where h is the semidiameter of the principal optical element and f is its focal length. The equation for the immersion lens is

$$(x - d)^2 + y^2 = r^2$$

Other relationships can be obtained from the geometry; an explicit equation for d might be derived, but it would not be very useful because of its complexity. However, one can also assume reasonable values for f , h , r , n , and d , and solve for the detector height l . These calculations require: (1) simultaneous solution of the two equations above for specific values of f , h , r , n , and d ; (2) determination of $\delta = \tan^{-1} \left[\frac{(y)}{d - x} \right]$; (3) determination of $\phi = \delta - \alpha$; (4) calculation of $\phi' = \sin^{-1} \left[\frac{(\sin \phi)}{n} \right]$ and calculation of $\sigma = \delta - \phi'$; and (5) calculation of $l = y + (x - d) \tan \sigma$. These computations can

also be done graphically. The results of the graphical computations are shown in Figure B-4. Figure B-4 is a graph of detector height as a function of position of the immersion lens for an $f/\sqrt{3}/2$ system (chosen close to $f/1$ but so that the half angle is 30°). All values of the parameters have been normalized to the radius of the immersion lens.

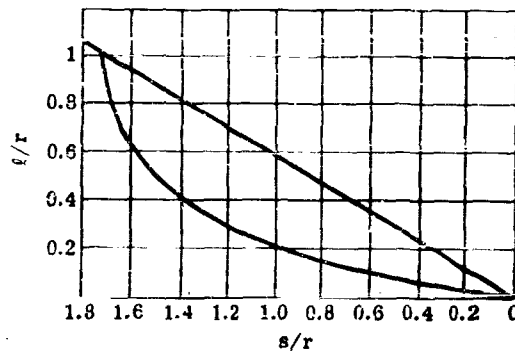


FIGURE B-4. DETECTOR HEIGHT VS. DISTANCE FROM ORIGINAL FOCAL POINT

The graphical computations were obtained in the following way. From Figure B-3 it can be seen that

$$\frac{l}{\sin \phi'} = \frac{r}{\sin \left[\frac{\pi}{2} + (\delta - \phi') \right]}$$

$$l = \frac{r \sin \phi'}{\cos (\delta - \phi')}$$

The second useful relation is Snell's law for a material of refractive index n in air. This is

$$\sin \phi' = \frac{1}{n} \sin \phi$$

These two equations can be solved simultaneously to obtain l as a function of δ for given n and ϕ (i.e., $\delta - \theta$). The solution for $\phi = 30^\circ$ and $n = 4$ is plotted in Figure B-5. The coordinates are normalized to the radius of the immersion lens. The equation of the edge ray is

$$y = -x \tan \theta + h$$

which can be used to find the position for the lens in the system. The x coordinate of the intersection

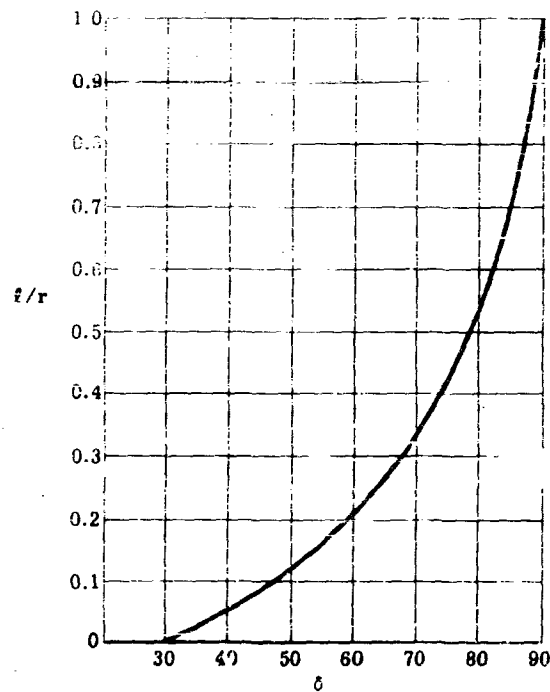


FIGURE B-5. NORMALIZED DETECTOR HEIGHT VS. ANGLE :

of the ray with the lens is

$$x = \frac{-r \sin \delta + h}{\tan \theta}$$

If d is the distance from the entrance aperture to the back surface of the immersion lens,

$$d = x + r \cos \delta$$

$$d = \frac{h}{\tan \theta} + r \left(\cos \delta - \frac{\sin \delta}{\tan \theta} \right)$$

The focal length of the original optical system is

$$f = h / \tan \theta$$

Thus

$$d = f + r \left(\cos \delta - \frac{\sin \delta}{\tan \theta} \right)$$

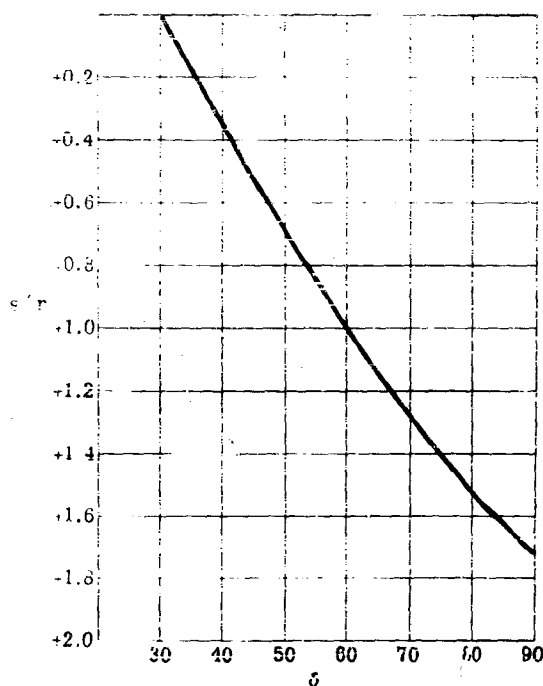


FIGURE B-6. DISTANCE OF DETECTOR SURFACE FROM ORIGINAL FOCAL PLANE VS. ANGLE δ

Figure B-5 shows the relationship of f and δ for given n and n' . Figure B-6 shows s/r as a function of δ . Thus f/r and s/r can be related by use of the two curves, and gains can be calculated. The graph can now be used to obtain the results for Cases IIA1 and IIA2.

If the position of the lens in the optical system is kept constant (Cases IIB1 and IIB2), $o + r$ or $o + r/n$ will be equal to f , and $\omega = \omega'$. Then

$$G = n^2 \sqrt{\frac{A'}{A}}$$

For the aplanatic case, the gain is 1; for the hemispherical case, the gain is n . This case also results from a requirement to keep $\omega = \omega'$.

B. 5. LIMITATIONS

In the gains derived above no losses by reflection or absorption were included. A loss factor K may be introduced:

$$K = (1 - \rho)e^{-ax}$$

where ρ is the intensity reflection coefficient, a is the absorption coefficient, and x is the geometrical path length. Because the radiation falling on the lens will probably not be incident at an angle of more than 40° , it is reasonable to approximate ρ by the Fresnel expression for normal incidence,

$$\rho = \left(\frac{n - 1}{n + 1} \right)^2$$

Thus,

$$K = \frac{4n}{(n + 1)^2} e^{-ax}$$

In most cases, the reflection losses can be reduced significantly by coatings. In regions of no absorption, K may have values of 0.9 to 1.0.

There is a limitation in the use of an immersion lens in very fast optical systems. As the speed and therefore the solid angle is increased, the marginal rays strike the lens-detector surface at more oblique angles. As the refractive index of the lens compared to that of the detector becomes larger, the critical angle also increases, and the size of the bundle which can be accepted by the lens-detector combination decreases.

Thus it can be seen that the desirable optical properties of an immersion lens are low absorption and high refractive index. However, if the refractive index of the lens is larger than that of the detector, the speed of the optical system will eventually be affected. Finally, reflection losses should be considered and reduced as much as possible. In this connection, the reflection loss at the curved front surface of the immersion lens may be considerably less than the loss at the flat surface of an unimmersed detector in a high-speed optical system.

B. 6. APPLICATIONS

Although this appendix is not concerned with properties of thermistor detectors, it is useful to review the characteristics of immersed thermistors to illustrate the results obtained by the method. (Most of the following discussion is based on an excellent review of thermistors by De Waard and Wormser, Reference B-1).

Germanium is generally used as the lens material ($n_{\text{Ge}} = 4$ through the infrared, $n_{\text{thermistor}} = 3.5$). The high electrical conductivity of germanium prevents direct immersion of the thermistor material. Since its electric operation would be impaired. Such immersion would otherwise be very desirable. Germanium has the desirable high index of refraction and the thermistor material matches it reasonably well. The critical angle becomes large and the reflection losses at the thermistor-germanium interface small. The electrical properties in this case, however, are overriding. Thus, separation layers of polyethylene, Mylar, and other plastics were used until selenium was determined to be a superior material. The selenium used was arsenic-modified amorphous selenium, also called selenium glass. It not only possesses superior optical properties—better transmission, even in thin layers, and higher refractive index—but it is also superior mechanically in a number of ways.

It should be mentioned that in the design of immersed thermistors, specific heat and thermal conductivity play an important role in the choice of lens and film material. This is because the lens is also used as a heat sink. With photoconductive detectors these considerations do not apply.

The Barnes Engineering Company has made some tests to compare the performance of immersed systems to those which did not have immersion lenses. The experimental results for hemispheres approached those predicted theoretically.

Substituted for unimmersed bolometers in Barnes 4-in. OptiTherm Radiometers, these immersed detectors have exhibited close to theoretically predicted performance. Immersed and unimmersed bolometers with identical fields of view and identical time constants compared in the radiometer system showed the immersed detector to have been better than 3 times the detectivity (signal/noise) of high quality (copper-Mylar, Type D, Figure 3-3) unimmersed units. (Reference B-1, page 60).

Further, Figure B-7 illustrates the comparison of field of view for the immersed and unimmersed detectors.

In the case of a germanium lens with a selenium film separator, a field of view approaching the theoretical limit was obtained. The critical angle is ϕ_c .

$$\phi_c = \sin^{-1} \left(\frac{2.5}{4.0} \right) = 38.5^\circ$$

In practice, a germanium convex plane spherical lens is ground and polished; a controlled-thickness selenium layer is evaporated onto the plane surface; and the thermistor detector is tamped into place. Finally a layer of selenium is evaporated onto the detector to provide insulation for the Zapon-black backing.)

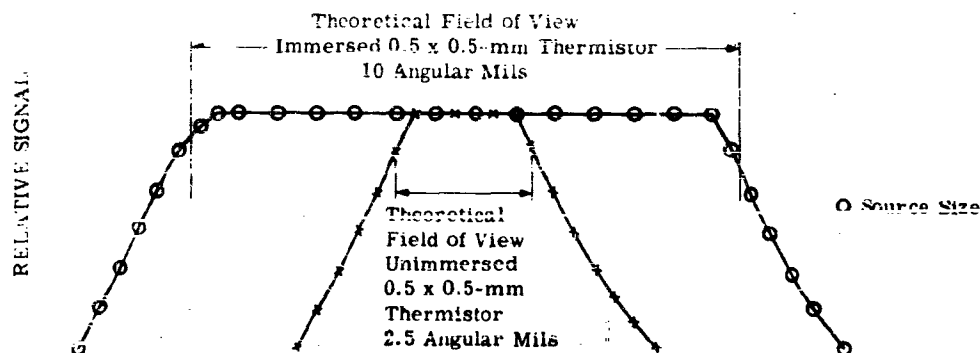


FIGURE B-7. COMPARATIVE FIELDS OF VIEW OF IMMERSSED AND UNIMMERSSED DETECTORS IN BARNES 1-INCH OPTITHERM

Immersion lenses for photoconductive detectors provide a somewhat different set of problems, although the basic theory and many of the techniques discussed for thermistor-bolometer immersion lenses still hold. A gain in linear dimension approximately equal to the refractive index squared may be obtained, so it is still advisable to use a high-index material. Electrical insulation is a significant problem, but thermal contact is no longer important. For most photoconductive detectors the field-of-view limitations imposed by critical angle considerations no longer apply. The detector material has a higher index of refraction than the immersion material, and no separator is necessary.

The Eastman Kodak Company has reported an optical gain of five when a lead sulfide cell was immersed at the center of a sphere of selenium glass (Reference B-6). (Apparently the glass is their arsenic- π doped selenium glass with an index of refraction of about 2.5 at about 2μ . Thus, since they use a hemisphere, a theoretical area gain of about 6.25 can be expected.)

The Eastman Kodak Company has also tried germanium as an immersion material (Reference B-7). Electrical shunting problems arise as with thermistors. Silicon monoxide has been used as an insulating film, but small holes in the film have caused shorting problems. They have also tried strontium titanate, titanium dioxide, and NBS experimental glass F-234 for immersion.

The immersed detectors currently made by the Eastman Kodak Company are lead sulfide deposited onto strontium titanate lenses. The theoretical area gain in this case is almost 2.3, the value of the refractive index around 2μ . Infrared Industries and the Electronic Corporation of America both report that they have been successful in not only immersing PbS on SrTiO_3 , but also in cooling the combination to liquid nitrogen temperatures.

This of course points out the additional characteristic which is desirable in materials for immersion lenses, mainly for quantum detectors: the thermal expansion of the lens should match that of the detector. The linear coefficient of the thermal expansion of lead sulfide is about twice that of strontium titanate. ($k_{\text{PbS}} = 18 \times 10^{-6}$ per degree centigrade, $k_{\text{SrTiO}_3} = 9.4 \times 10^{-6}$ per degree centigrade). One would therefore expect a certain amount of separation when the combination is cooled by approximately 50°C, although the lead sulfide film could spread out some. The combination is probably more stable when the thermal conductivity of the lens matches that of the detector. One approach might be the use of barium titanate, which has an expansion coefficient of 16×10^{-6} per degree centigrade in the temperature range considered and a high dielectric constant. Its refractive index is about the same as SrTiO_3 (~ 2.40).

B.6. REFERENCES

- B-1. R. DeWaard and E. Wormser, Thermistor Infrared Detectors, Part I, Properties and Developments, NAVORD Report Number 5495, Barnes Engineering Co., Stamford, Conn., 30 April 1958 (UNCLASSIFIED).
- B-2. T. Limperis and W. Wolfe, "A Study of the NEP Area Dependence in Film-Type Infrared Quantum Detectors," Proc. IRIS, August 1960, Vol. 5, No. 4, p. 141 (CONFIDENTIAL).
- B-3. F. Jenkins and H. White, Fundamentals of Optics, 2nd ed., McGraw-Hill, New York, N. Y., 1950, pp. 137-138.
- B-4. M. Born and E. Wolf, Principles of Optics, Electromagnetic Theory of Propagation, Interference and Diffraction of Light, 1st ed., Pergamon Press, New York, N. Y., 1959, pp. 148-149.
- B-5. P. Drude, Theory of Optics, Dover reprint, New York, N. Y., 1959.
- B-6. G. J. Koch, Status of Photoconductive Cell Development, Report Number 50, Eastman Kodak Co., Rochester, N. Y., 1 January 1955 (CONFIDENTIAL).
- B-7. J. Stanley Dunn, Status of Photoconductive Cell Development, Report Number 54, Eastman Kodak Co., Rochester, N. Y., 30 September 1955 (CONFIDENTIAL).

Appendix C COOLING DEVICES for INFRARED DETECTORS

Paul R. Barker and William L. Brown

C.1. INTRODUCTION

The operating temperatures of present-day infrared detectors range from 1.2°K in the case of impurity activated indium antimonide to 300°K for the lead salts. The proper temperature for a given detector is determined by noting the temperature dependence of the optical and photoelectric properties, and choosing that temperature which provides the best results for the system of interest. The important characteristics which depend upon temperature are detectivity, time constant, spectral response, and resistance. In some cases detectivity may be optimized by cooling with little or no sacrifice in time constant, resistance, or spectral response. Examples of this are high-impedance indium antimonide and indium arsenide, where cooling to 193°K provides optimum detectivity with little change in the other characteristics. On the other hand, the characteristics of lead sulfide are strongly dependent on temperature. Cooling causes a shift in long-wavelength threshold toward longer wavelengths, in contrast to the shift toward shorter wavelengths which is characteristic of most other materials. However, the recombination time increases with decreasing temperature, as does the resistance. The effects of temperature variation for lead sulfide (reference 1) are shown in Figures C-1 and C-2. Figure C-1 shows the variation of spectral response with temperature, and Figure C-2 presents the dependence of detectivity upon chopping frequency, with the temperature and corresponding time constant as parameters. The detector element which requires cooling is usually mounted in a vacuum flask, called a dewar, into which a cooling head may be placed. The flask is double-walled, with the detector mounted on the inner wall and an infrared-transmitting window incorporated into the outer wall. In situations where it is impractical to place the cooling head close to the detector, a highly conductive material (e.g., a ruby rod) is used as the heat-transmitting medium between the detector and the cooling head.

Several methods are available for cooling an infrared detector to the required temperature and maintaining that temperature during the desired operating time. The cooling devices derived from these methods are of four major types: (1) direct-contact coolers, (2) Joule-Thomson cryostats, (3) expansion engines, and (4) thermoelectric coolers. The first three of these are considered in detail in the next sections, followed by a brief discussion of thermoelectric coolers and other methods of cooling. Section C.6 presents some information on commercial models of coolers.

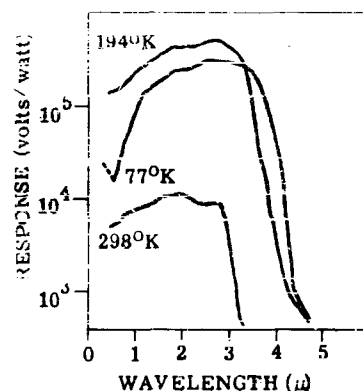


FIGURE C-1. SPECTRAL RESPONSE OF PbS DETECTORS

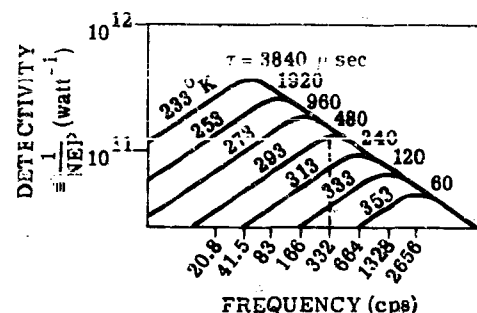


FIGURE C-2. VARIATION OF DETECTIVITY AT SPECTRAL PEAK WITH CHOPPING FREQUENCY FOR PbS, $\Delta f = 1$ cps; $A = 1 \text{ cm}^2$.

C.2. DIRECT-CONTACT COOLERS

The simplest technique for cooling infrared detectors is one in which the detector is in direct thermal contact with a supply of liquid coolant (e.g., nitrogen). A great variety of such direct-contact coolers is available, in widely varying sizes, for low-temperature applications. Nearly every major producer of infrared cooling devices makes at least one type of direct-contact cooler for infrared-detector applications.

Often the direct-contact cooler consists merely of an unpressurized supply of liquid in the detector dewar, but the systems vary up to types requiring pressure regulators, insulated supply lines, heating elements, pressurized cooling heads, and pressurized tanks. One of the more basic systems will be described first, since the simpler cooling devices are merely truncations of the basic apparatus which transfers liquid coolant from a low-pressure supply tank to the cooling head by means of a pressurized chamber (Figure C-3). The physical operation of the system is as follows. The supply valve opens, allowing liquid to flow from the supply tank into the pressurized chamber. As soon as a predetermined level is reached, the supply valve closes and the heater is turned on. The heater is controlled by a pressure sensor which is set to maintain a flow of liquid into the cooling head at a rate sufficient to replenish the liquid which boils off. Gas formed from heat exchange with the apparatus flows through the return line and out the vent port. Any excess liquid flows back to the supply tank through the return line. As soon as the liquid level in the pressurized chamber falls below a

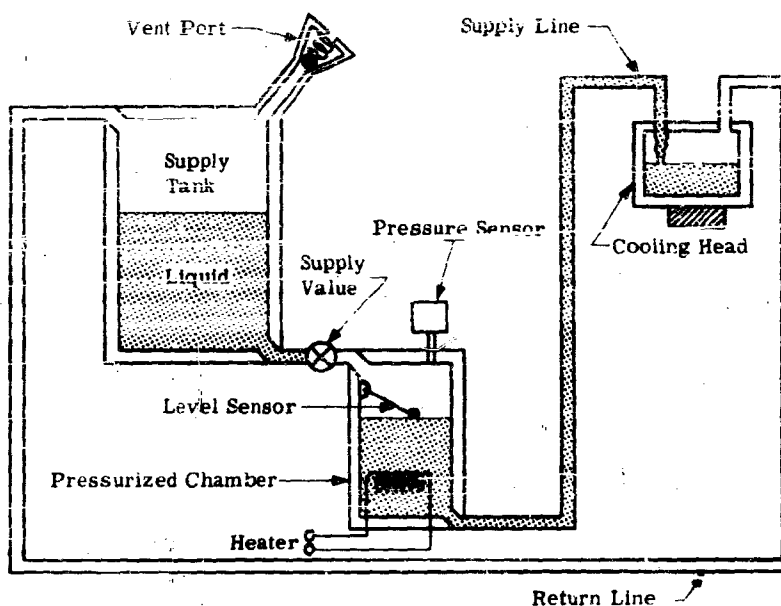


FIGURE C-3. BASIC DIRECT-CONTACT COOLING SYSTEM

certain level, the level sensor shuts the heater off and opens the supply valve, admitting more liquid from the supply tank. The process then repeats itself until the supply tank is empty.

It is evident that the above system may be simplified without seriously limiting its performance as a cooling device. The pressurized chamber, supply valve, and return line may be removed and the heater placed in the supply tank (Figure C-4). This modified system is the most common direct-contact cooling device on the market. The main problem encountered is the waste of liquid by overflow from the cooling head.

The simplest system of all may be obtained by further elimination of the supply tank, heater, and supply line, leaving only the cooling head. A limited supply of coolant may then be poured into the dewar and cooling will proceed until the liquid is completely evaporated. Such a system is quite satisfactory for laboratory usage and has been developed by some companies for use in field applications (Reference C-2).

A direct-contact liquid-helium cooler has been described (Reference C-3, page 332) in which temperatures less than 4.2°K have been maintained for relatively long periods of time. The system derives its usefulness from the fact that the saturation temperature of a substance decreases as its

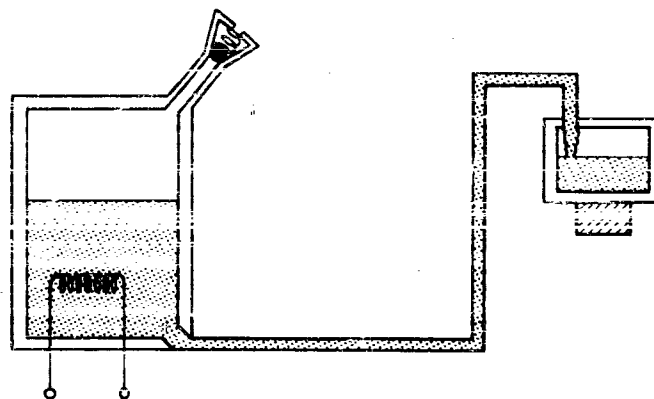


FIGURE C-4. MODIFIED DIRECT-CONTACT COOLING SYSTEM

pressure decreases (Figure C-8). Liquid helium, at atmospheric pressure and 4.2°K , is delivered through a "flash-evaporation" valve into a region of constant low pressure where part of the liquid evaporates, cooling the rest to the low-pressure saturation temperature. The temperature is controlled by regulation of the low pressure. The major limitation of the system is the size of vacuum pump required to maintain the low pressure. Ten mw of cooling at a temperature of 1.25°K were obtained with a 10 cubic-ft. minute vacuum pump which maintained the pressure at 1 mm of mercury.

C.3. THE JOULE-THOMSON EFFECT

One of the more common methods for cooling infrared detectors employs a device known as a cryostat, in which a high-pressure gas is caused to flow through a tube and expand to low pressure through an orifice at the end of the tube (Figure C-5). Cooling accompanies the expansion due to a phenomenon known as the Joule-Thomson (or Joule-Kelvin) effect. The efficiency of the device is increased by allowing heat exchange between the cooled outgoing gas and the warm incoming gas.

C.3.1. THERMODYNAMICS OF THE JOULE-THOMSON EXPANSION. The classic experiment which exemplifies the Joule-Thomson effect was first performed by William Thomson and James Joule about 100 years ago. The experiment utilized a porous plug, made of cotton, embedded in a beechwood pipe (essentially an insulator) to provide an adiabatic transition from a region of constant high pressure on one side of the plug to a region of constant low pressure on the other side. The porous plug was used instead of a small orifice because it was considered desirable to have a smooth, uniform flow in the low-pressure region so that the thermodynamic quantities would be well defined.

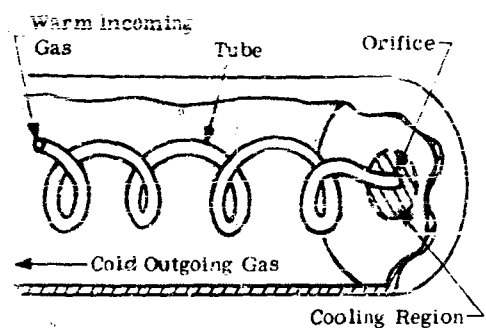


FIGURE C-5. JOULE-THOMSON COOLER

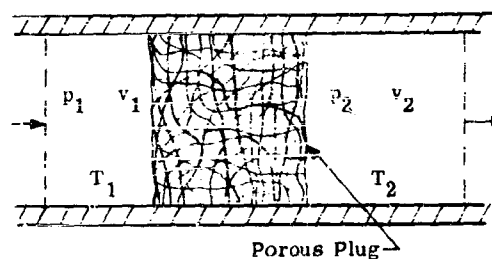


FIGURE C-6. JOULE-THOMSON POROUS-PLUG EXPERIMENT

The porous-plug experiment may be represented by the system shown in Figure C-6. After a steady-state temperature distribution is reached in the system, there is no heat transfer along the gas stream. The gas in v_1 and v_2 may be considered as one mole of gas observed before and after passing through the plug.

As the gas flows through the plug, the force $p_1 A$ acts through a distance v_1/A and the force $p_2 A$ acts through a distance v_2/A . (See Section C.8 for definitions of symbols.) The total work is therefore

$$\int dw = p_1 v_1 - p_2 v_2$$

There is no heat transfer along the gas stream nor through the pipe, and thus

$$\int dq = 0$$

The change in kinetic and potential energy is negligible, and so the first law of thermodynamics reduces to

$$\Delta u = \int dq - \int dw$$

Therefore,

$$u_1 - u_2 = -(p_1 v_1 - p_2 v_2)$$

The enthalpy is defined as

$$h = u + pv$$

By rewriting the first-law relation as

$$u_1 + p_1 v_1 = u_2 + p_2 v_2$$

it can be seen that the porous-plug experiment is a constant-enthalpy (isenthalpic) process.

It is of interest to investigate the Joule-Thomson effect from an analytical thermodynamic viewpoint. This may quite easily be done. The following relationships (Reference C-4, page 60) hold for any gas:

$$dh = T ds + v dp$$

$$ds = (\partial s / \partial T)_p dT + (\partial s / \partial p)_T dp$$

$$(\partial s / \partial T)_p = T^{-1} (\partial q / \partial T)_p = c_p T^{-1}$$

$$(\partial s / \partial p)_T = -(\partial v / \partial T)_p$$

Combining these for $dh = 0$,

$$(\partial T / \partial p)_h = c_p^{-1} [T(\partial v / \partial T)_p - v]$$

The quantity $(\partial T / \partial p)_h$ is called the "Joule-Thomson coefficient" of the gas. The temperature change in a Joule-Thomson expansion is given by

$$\Delta T = \int_{p_1}^{p_2} (\partial T / \partial p)_h dp$$

The nature of the temperature change during a Joule-Thomson expansion can be studied using van der Waals' gas equation (Reference C-4, page 55)

$$(p + av^{-2})(v - b) = RT$$

where a is a constant which relates to the cohesive forces between the molecules, b is a constant which accounts for the finite volumes of the molecules, and R is the gas constant. Neglecting second-order terms in a and b ,

$$\left(\frac{\partial T}{\partial p} \right)_h = c_p^{-1} \left(\frac{2a}{RT} - b \right)$$

van der Waals' equation, $(\partial T/\partial p)_h > 0$, when $T < (2a/bR)$. The point in an isenthalpic process at which $(\partial T/\partial p)_h = 0$ is known as the "inversion point."

$$(\partial T/\partial p)_h > 0$$

when $T < (2a/bR)$. The point in an isenthalpic process at which $(\partial T/\partial p)_h = 0$ is known as the "inversion point."

It should be emphasized that van der Waals' equation does not represent the properties of an actual gas well enough to permit an exact analysis of the Joule-Thomson effect. An example clearly illustrates this point. Careful measurements by Roebuck and Osterburg (Reference C-5, page 251) using nitrogen gas at atmospheric pressure between 93°K and 373°K yielded the empirical formula

$$(\partial T/\partial p)_h = -0.0020 + (39/T)^2 \text{ } ^\circ\text{K/psi}$$

whereas, with values of a and b from Reference C-6, van der Waals' equation gives

$$(\partial T/\partial p)_h = -0.0092 + 8.0/T \text{ } ^\circ\text{K/psi}$$

The same analysis which describes the porous-plug experiment holds for "throttling" through a valve or an orifice, as in a cryostat, since the assumptions of no heat transfer and no change in kinetic and potential energy still apply. In general, it may be said that the temperature change of a real gas under conditions of constant enthalpy depends upon the initial and final pressures and the initial temperature of the gas. The magnitude of the temperature change associated with a given set of inlet and outlet conditions may be determined from curves showing temperature as a function of pressure at constant enthalpy, as in Figure C-7.

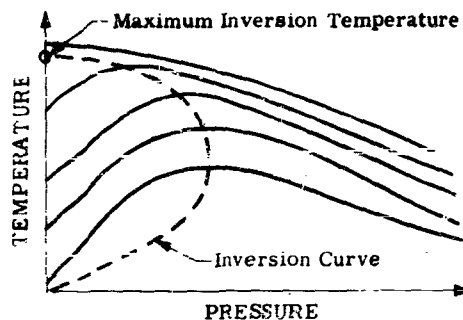


FIGURE C-7. ISENTHALPIC CURVES AND INVERSION CURVE FOR A GAS

It should be understood that expansion through an orifice is not a gradual process (i.e., is not quasi-static), so the isenthalpic curve is not the graph of the expansion process, but rather represents the locus of all equilibrium states of the gas at a certain enthalpy. Hence, when the inlet conditions correspond to a point on a certain isenthalpic curve, the outlet conditions will fall on the same isenthalpic curve, but nothing can be said about the "intermediate states" of the process.

A method of obtaining an isenthalpic curve for a gas is to allow the pressure of the gas to decrease in small steps through a series of throttling valves and measure the temperatures and pressures at each step. The points corresponding to the measured values of temperature and pressure lie on the isenthalpic curve, which reaches a maximum at its inversion point. By using several different initial temperatures and pressures, whole families of isenthalpic curves may be obtained.

The locus of all the inversion points is the inversion curve for the gas. For any initial condition (p_1, T_1) falling to the left of the inversion curve, cooling will accompany expansion to (p_2, T_2) at some point along the isenthalpic curve. If the gas is initially to the right of the inversion curve, the temperature change could be positive or negative, or there might be no change at all.

If the gas is initially above the maximum inversion temperature (Figure C-7), it will always heat up in an isenthalpic expansion. An example is compressed helium gas at 200 atmospheres and at room temperature, which is sufficiently above the maximum inversion temperature to cause a rise of 12°K upon expansion to the atmosphere.

Condensation will occur when the outlet temperature and pressure fall on the saturation curve of the gas, as at point B in Figure C-8. Note that the isenthalpic curve does not cross the saturation curve, but rather follows along it for some distance before finally rising above it again. If the outlet conditions correspond to point C in Figure C-8, re-evaporation will overcome condensation and no liquid will form.

C.3.2. JOULE-THOMSON COOLERS. The Joule-Thomson cooler is probably the most common of all infrared cooling devices. A few of its more important features will be discussed here.

The cryostat, as the Joule-Thomson cooler is usually called, is made from a length of finned tubing, coiled around a mandrel, with an orifice at the exit end of the tube (Figure C-5). A high-pressure gas enters the tube at a temperature below its maximum inversion temperature. It passes through the tube and expands at the orifice, cooling by virtue of the Joule-Thomson effect. The gas, thus cooled, passes back over the finned tubing, cooling the incoming gas. The process is carried on continuously until liquid begins to emanate from the orifice. The temperature of the cooled gas

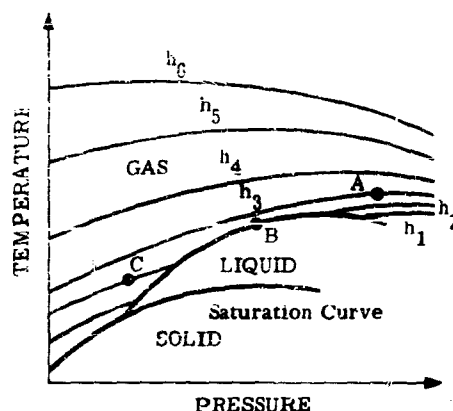


FIGURE C-8. ISENTHALPIC CURVES SUPERIMPOSED UPON PHASE DIAGRAM

is then constant, since the liquid-gas combination is a saturation state of the gas (e.g., point B, Figure C-8). This temperature is the boiling point of the gas at the exit pressure (atmospheric pressure in the case of conventional cryostats).

The finned tubing must have a very small inside diameter in order to give a large ratio of surface-area to volume and thus to provide efficient heat exchange. This narrow passageway is subject to clogging, since the extremely low temperature of the tubing causes any impurities in the gas to freeze on the surface. For this reason, it is important that extremely high-purity gas be used in the cryostat and that the cryostat itself be kept free from contamination while it is not in use.

A method of obtaining high-purity gas with little technological effort is to use a tank of liquified gas as the supply, since any contaminant which might freeze on the tube surface is automatically "frozen out" in the tank. A heater may be used in the supply tank to generate the gas at the required inlet pressure, which is typically above 1200 psi. One problem encountered with this type of supply is evaporation of the liquid during standby. However, a liquid supply is much simpler than compressed gas supplies in that it requires no elaborate filtering apparatus, and the supply tank is at a relatively low pressure and occupies much less space than a compressed gas supply with a comparable mass of coolant.

Closed-loop cryostats have been made which recycle the gas in order to provide continuous operation for long periods of time (Reference C-3, page 324, and Reference C-7). To accomplish a continuously operating cycle of this type, the expanded gas must be pressurized by a noncontaminating

compressor. Such a compressor may be built with a diaphragm (Reference C-3, page 317) or with a nonlubricated piston (Reference C-8, page 192).

C.4. EXPANSION ENGINES

When a gas is allowed to expand and do work without exchanging heat with its surroundings, its internal energy is decreased by the amount of the work, and hence its temperature drops (as can be shown by the first law of thermodynamics). As a result of the work of Collins (Reference C-9, page 157) and Kapitza (Reference C-8, page 189), it became practical to liquefy helium by the use of expansion engines. (Helium is the most difficult gas to liquefy because it has the lowest saturation temperature of any gas and because it has a very small Joule-Thomson coefficient.) The expansion processes developed somewhat independently by Collins and Kapitza used counter-flow heat exchangers to provide cooling of the helium previous to its use in the expansion engine. Kirk and Stirling later introduced a reciprocating-flow thermal regenerator (discussed below) which was developed and refined by the Philips Company (Reference C-10, page 105) for use in an air liquefier. The regenerator offers, among other advantages, some mechanical simplifications over counter-flow heat exchangers.

A miniaturized device designed specifically for the purpose of cooling small regions to extremely low temperatures was developed in the late 1950's by McMahon and Gifford, utilizing a gas operating within a closed loop (Reference C-3, page 368). This device consists of a very short stroke piston, a thermal regenerator, and a compressor, with a pair of intake and exhaust valves. A schematic diagram of the system appears in Figure C-9.

Some descriptive comments about the components of this system can provide a background for understanding its operation. The piston is utilized as a means of causing the gas to do work and thus lose internal energy. The piston has sealing rings at the top, and appreciable clearance is provided between its sides and the cylinder wall to avoid heat transfer during the cyclical motion of the piston. Both the cylinder and piston are made of poor heat conductors in order to prevent the longitudinal flow of heat in the engine.

The regenerator is a heat exchanger made of a stack of fine-wire screens enclosed in a casing. The gas flows through the screens, which are made of a metal of high thermal capacity, exchanging heat during the process. Since the flow of gas is completely turbulent in the regenerator, the heat exchange rate is very high and hence the efficiency is considerably higher than that of counter-flow heat exchangers (a factor of prime importance in the performance of the engine).

The valves are operated from the same crosshead which controls the motion of the piston. The gas flows through the exhaust valve into a compressor in which it is compressed by roughly a factor

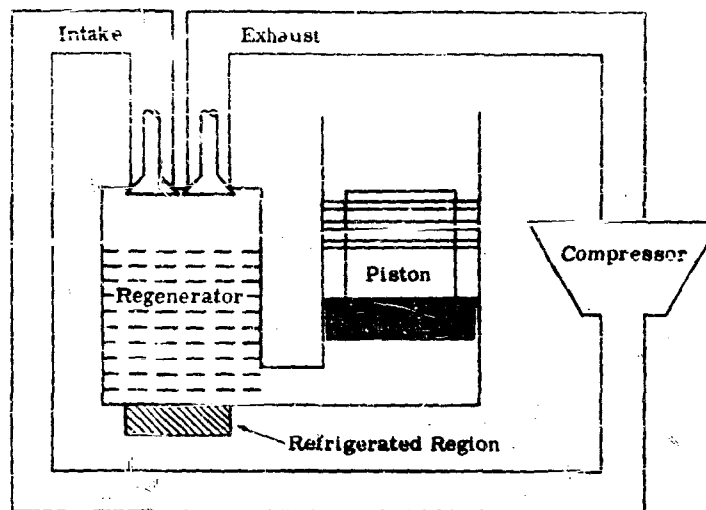


FIGURE C-9. SCHEMATIC DIAGRAM OF GIFFORD-McMAHON EXPANSION ENGINE

of 5. The gas then flows back through the intake valve into the engine, thus completing the closed loop.

The cycle through which the engine goes is essentially the Stirling cycle, and may be described as follows.

- (a) The intake valve opens. The piston is at bottom dead center as high-pressure gas enters, pressurizing the regenerator and the connective tubing (Figure C-10a).
- (b) The intake valve closes. The piston starts to recede and the gas undergoes adiabatic expansion, doing work and thus decreasing in internal energy (Figure C-10b).
- (c) The piston completes its stroke. Upon completion of the piston stroke, the exhaust valve opens and the gas expands to a low pressure. As the cooled gas passes through the regenerator, it removes heat from the screens, causing a temperature drop in the regenerator (Figure C-10c).
- (d) The piston returns to bottom dead center. The remainder of the cooled, expanded gas is forced through the regenerator and out the exhaust valve (Figure C-10d). As the gas repeatedly undergoes the cycle, the regenerator is progressively cooled until the work done by the gas exactly equals the heat flow into the system, at which point temperature equilibrium is reached.

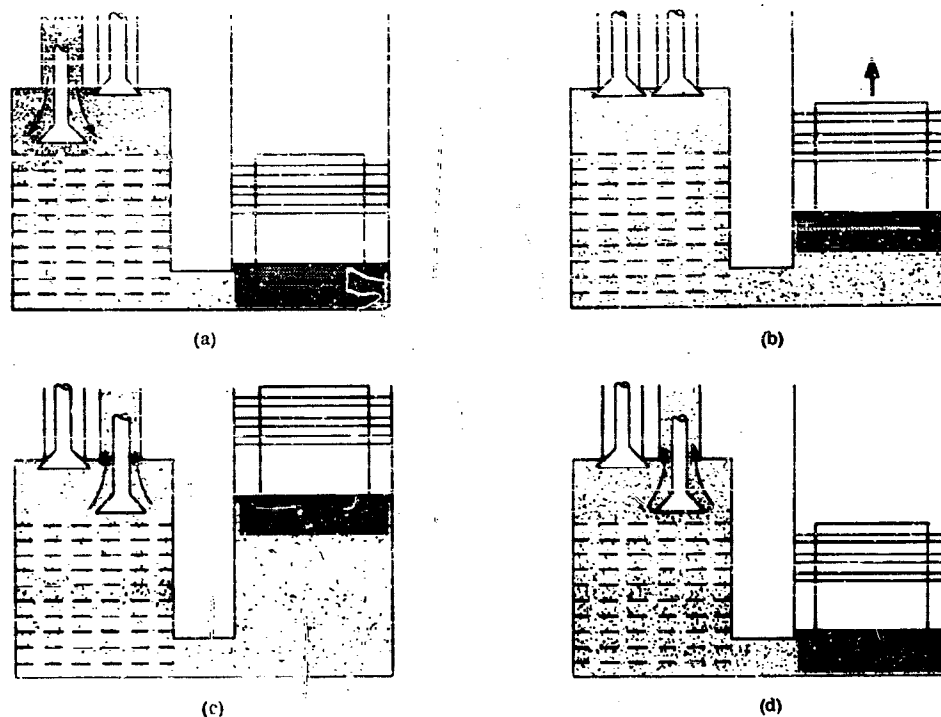


FIGURE C-10. ENGINE CYCLE. (a) First phase. (b) Second phase. (c) Third phase. (d) Fourth phase.

The developers of this engine point out that the system has two basic sources of inefficiency. The first is the "dead-air space" in the regenerator. Due to the finite volume of the regenerator, some of the gas is not exhausted at the end of the cycle. This is not a great problem, however, since the mass of unrecycled gas is small because it is at a low pressure. The second source of inefficiency is the longitudinal flow of heat in the cylinder, piston, and regenerator. Due to the large temperature gradient from the top to the bottom of the system, there is inevitably some heat flow despite the fact that the parts are constructed from poor conductors of heat. The high efficiency of the regenerator tends to compensate somewhat for the heat flow through the system.

A limiting factor in expansion-engine devices is the material from which the regenerator is fabricated. The heat capacities of most solids fall off considerably at low temperatures (Reference C-5, page 245), and consequently the ability of the solid to remove heat from the gas stream diminishes with decreased temperature. Materials such as aluminum, zinc, brass, and bronze have no

significant heat capacity below 35°K, whereas lead is able to store fair amounts of heat down to approximately 14°K. Since the maximum inversion temperature of helium gas is 23.6°K, an expansion engine with a lead regenerator may be used instead of a hydrogen cryostat to cool helium gas down to a point where it can be cooled by Joule-Thomson expansion to 4.2°K (Reference C-11).

Commercial units of the Gifford-McMahon engine (Reference C-12) use helium as the working gas and provide 0.75 watts of useful refrigeration at temperatures as low as 4.2°K, using a multistage unit with a closed-cycle Joule-Thomson circuit. Single-stage units are currently operational at 60°K, with a cooling capacity of 0.02 watt, or at 80°K with a capacity of 0.10 watt (Figure C-11). Although the rate of cooling is small, the continuous-operation feature of the closed-loop device makes this system practical for applications where high heat-dissipation rates are not essential. Systems are under development (Reference C-12) which are expected to provide 0.05 watt of refrigeration at 35°K with a single unit.

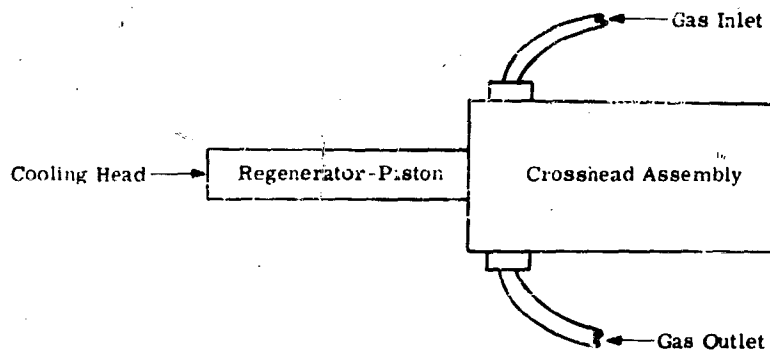


FIGURE C-11. GIFFORD-McMAHON COOLER. Scale: full size.

A developmental model of a closed cycle helium expansion engine has been built which uses no valves or compressors and is capable of producing 2.0 watts of usable refrigeration below 30°K, with a cool-down time of 10 minutes (Reference C-13, page 63). The cycle is basically the Stirling cycle, with compression and expansion both occurring within the cylinder of the engine.

C.5. OTHER METHODS OF COOLING

Cooling devices exist other than the three types previously discussed in this appendix. Among the more promising of these is one which utilizes the "reverse thermoelectric" principle known as the Peltier effect. It seems that it will eventually be feasible to make thermoelectric coolers which

will produce refrigeration at temperatures below that of liquid nitrogen, although such systems have not yet been developed. A more complete discussion of the Peltier effect and thermoelectric coolers appears in Appendix D of this report.

One method used in the laboratory to achieve temperatures near absolute zero is to cool a paramagnetic salt (a salt which becomes magnetized in the presence of an external magnetic field) by liquid helium while it is exposed to a strong magnetic field. Ordinarily the temperature of the salt would rise due to the absorption of electromagnetic energy, but the liquid helium dissipates the heat through evaporation. After a near-steady state is reached, the space surrounding the salt is evacuated to provide thermal insulation, and the magnetic field is removed. The temperature of the salt is thus reduced below liquid-helium temperature as a result of the adiabatic demagnetization of the crystals (Reference C-5, pages 271-279). However, since this technique is not continuous, it is not well suited to detector applications and hence is not considered in detail in this appendix.

A cooling apparatus was built and tested in 1946 (Reference C-14, pages 106-113) in which a compressed gas was caused to enter a cylindrical tube through a tangential nozzle, the flow inside the tube initially approximating a vortex field. As the gas traversed the tube, the flow became rotational, causing heat to flow from the gas near the axis toward the wall of the cylinder. The cooled gas near the axis was then separated from the heated gas near the wall and used as a coolant. This device was suggested as a method for producing cold air for use in mine shafts, but evidently was not developed to the extent that it could be used for cooling detectors, even though such development might be technically feasible.

C.6. COMMERCIAL COOLERS

For field applications a cooler should be light in weight and have both high efficiency and good reliability. The ease with which these qualities can be obtained depends on the type of cooler and on the required temperature. Table C-1 lists parameters of the "optimum" coolers of different types which are commercially available. In selecting the coolers to be listed an attempt was made to choose those which combine minimum weight with maximum cooling capacity and efficiency. The purpose of this table is merely to give a general idea of what can be expected from each type of cooler.

Tables C-2, C-3, and C-4¹ list specific models of commercial coolers which are now in production. Also included are a number of prototype models, some of which may eventually be put into production. Table C-2 lists direct-contact coolers. Table C-3 lists cryostats which are just cooling

¹Tables C-2, C-3, and C-4 were compiled by David Anding and John Duncan.

heads and require an external supply of gas. Table C-4 lists complete systems, which include any necessary compressors or storage tanks. Considerable effort was made to include all available coolers suitable for use with infrared detectors, but it is quite possible that there exist others which were inadvertently omitted.

TABLE C-1. PARAMETERS OF OPTIMUM AVAILABLE COOLERS

Type of Cooler	Anticipated Temperature (°K)	Power Input Required (watts)	Cooling Capacity (watts)	Availability of Cooling	Factors Affecting Reliability	Approximate Weight (lbs)
Direct-Contact Cooler	4.2-77	None (3)	0.05-10	Continuous (4)	(Excellent Reliability)	(6)
Nitrogen Cryostat	77	None (3)	1-10	On Demand (5)	Gas Purity	(6)
Cascaded Cryostat	4.2-27	None (3)	0-5	On Demand (5)	Gas Purity	(6)
Cryostat with Compressor in Closed Loop	20	600	10	On Demand	Gas Leakage, Contamination, Compressor Life	15-20
Expansion Engine	60-80	200	0.02-0.1	On Demand	Gas Leakage, Compressor Life	10-20
	40-70 (1)	200	1.5-5	On Demand	Gas Leakage	5-15
Cascaded Expansion Engine and Cryostat	4.2	1000	0.5	30-minute Cool-Down	Gas Leakage, Contamination, Compressor Life	30
Cascaded Thermoelectric Cooler	212 (2)	2.5-20	0.12-0.50	On Demand	(Excellent Reliability)	1-5

(1) Production scheduled for September 1961.

(2) More efficient junction materials are under investigation.

(3) May need small power supply for heating element and control system.

(4) Storage container filled prior to use.

(5) Based on storage capacity.

(6) Depends on storage container and operating time.

TABLE C-2. DIRECT-CONTACT COOLERS

Model	Operating Pressure	Coolant	Temp. Cooling Media	Cool-Down Time (minutes)	Standby Time (hours)	Operating Time (hours)	Power Supply (watts)	Total Weight (lb.)
Linde LNI-1	Open	Nitrogen	77°K	1.5		8.5	None	0.76
Linde LNI-2	Open	Nitrogen	77°K	0.5		22	None	1.98
Linde LNI-3	Open	Nitrogen	77°K	0.5		29	None	3.21
Linde LNI-4	Open	Nitrogen	77°K	0.5		10	None	0.67
Linde LNI-5	Open	Nitrogen	77°K	0.5		9	None	1.06
Linde LNF-2	Open	Nitrogen	77°K		Capacity 2.6 lbs Evaporation 0.9 lbs/day	Determined by flow rate	None	5.60
Linde LNF-3	Open	Nitrogen	77°K		Capacity 0.81 lbs Evaporation 0.31 lbs/day	Determined by flow rate	None	2.81
Linde LNF-4	Open	Nitrogen	77°K to 165°K		Capacity 5.7 lbs Evaporation 0.73 lbs/day	Determined by flow rate Maximum 0.3 lbs/hr	None	13.7
Linde LNF-5	Open	Nitrogen	77°K		Capacity 5.7 lbs Evaporation 0.73 lbs/day	Determined by flow rate	None	8.5
Linde LNF-6	Open	Nitrogen	77°K		Capacity 0.92 lbs Evaporation 1.47 lbs/day	Determined by flow rate	None	1.57
Linde LNF-8	Open	Nitrogen	77°K		Capacity 0.63 lbs Evaporation 0.65 lbs/day	Determined by flow rate	None	2.16
Linde LNI-11	Open	None Hydrogen Helium	20°K to 40°K		3 30 300	3 30 300	None	2.36
Linde LNI-12	Open	None	27.2°K to 40°K			8 to 4	None	5.8
SBRG LNI-E	Open	Nitrogen	77°K	< 1	24	6	None	0.0

(1) LNI models are liquid nitrogen cooled.
LNF signifies liquid nitrogen feed systems.

(2) For all models, provision can be made for remote filling when dewar installation is such that it is inaccessible for pen filling.

Position of Detector	Dimensions				Remarks
	Spout		Over-All		
	Length (inches)	Diameter (inches)	Length (inches)	Diameter (inches)	
Side mounted			4	3	Pour-filled. Cooling commences at filling. Operation in vertical position only.
Side mounted			8	3.5	Pour-filled. Cooling commences at filling. Operation in vertical position only.
Snout, side mounted	4.5	1	11	3.5	Pressure-filled through insulated line. Cooling commences at filling. Operation in vertical position.
Snout, side mounted	2.5	0.8	5.4	3.1	Pressure-filled. Cooling commences at filling.
Bottom mounted			6.9	3	Pour-filled. Cooling commences upon filling. Operation in vertical position only.
			14.5	4.5	Pressure-filled. Operated in vertical position only.
			8	3.5	Pressure-filled. Operated in vertical position only.
			13.6	7.9 x 6 25	Temperature control $\pm 3^{\circ}\text{F}$ over entire range given. Pressure-filled.
			13.5	6	Pressure-filled
Bottom mounted			6	3.5	Pour-filled. Operated in vertical position only.
			10.5	3.5	Pressure-filled at 35 psig. Operation in vertical position only.
			10.9	3.5	May be operated with any of three liquids mentioned. Pour-filled. Nitrogen shield.
			8	4.6	Temperature is pressure-controlled. Designed for cooling large mosaic detectors.
		16.25	5 x 5		

(3) At altitudes above 147,000 feet systems can be closed and vented through an absolute pressure relief valve to keep liquid from solidifying.

(4) Units custom-designed to meet customer-specified space limitations upon request.

TABLE C-3. JOULE-THOMSON CRYSTATS

MT	W. No.	Gas	Temp at Cooling Head	Cooling Capacity (watts)	Operating Pressure (psi)	Flow Rate (cc/min)	Angle (degrees)	Length (inches)	Center of Gravity (inches)	Remarks
A-20-10-10		Hydrogen	20°K ± 2°K	1.4	N ₂ 2250 H ₂ 1800	N ₂ 3.34 H ₂ 3.37		6.1 ± 2	1.4	2-stage, 1st stage, Neon gas, 1st stage, Hydrogen in second stage. Operating at pressure 2°K.
A-20-10-10		Hydrogen	20°K ± 2°K	3.4	N ₂ 1500 H ₂ 1550	N ₂ 1.94 H ₂ 1.72		6.36	3.8	2-stage, 1st stage, Neon gas, 1st stage, Hydrogen in second stage. Operating at pressure 2°K.
A-20-10-10		Hydrogen	20°K ± 2°K	4	N ₂ 2100 H ₂ 1500	N ₂ 1.10 H ₂ 1.74		6.1/2	3.2	2-stage, 1st stage, Neon gas, 1st stage, Hydrogen in second stage. Operating at pressure 2°K.
A-20-10-10		Hydrogen	20°K ± 2°K	6	N ₂ 2000 H ₂ 1500	N ₂ 1.28 H ₂ 1.74		1.1	3.4	2-stage, 1st stage, Neon gas, 1st stage, Hydrogen in second stage. Operating at pressure 2°K.
NO-1	CH-204-1	Freon A Argon N Nitrogen	192°K 80°K 77°K	0.5-1			3.08	2	0.34	Adjustable flow rate to 2.2 liters per minute at 1000 psi.
NO-2	CH-320-1	Freon A Argon N Nitrogen	192°K 80°K 77°K	0.5-1				2	0.26	Adjustable flow rate to 2.2 liters per minute at 1000 psi.
NO-3	CH-500-1	Freon A Argon N Nitrogen	192°K 80°K 77°K	0.5-1				2	1/2	Adjustable flow rate to 2.2 liters per minute at 1000 psi.
NO-4	CH-100	Hydrogen	30°K	0.5-1				2	1/2	Prototype 2-stage, 1st stage, Neon gas, 1st stage, 1st stage.
NO-5	CH-100	Nitrogen	77°K	1.0	1500	0.1	4	1.1/4	3/1	
NO-6	CH-150	Nitrogen	77°K	1.0	1500	0	4	1.3/4	0.205	
NO-7	CH-200	Nitrogen	77°K-80°K	1.0	2000	0.1	3	1/2	0.181	
NO-8	CH-200	Nitrogen	77°K-80°K	1.0	2000	0.28	3	3/4	0.171	2-stage, cascaded, 1st stage, Neon gas, 1st stage, 1st stage.
NO-9	CH-200	Hydrogen	20°K	1.0	N ₂ 1250 H ₂ 1000	N ₂ 0.18 H ₂ 0.16	3.5			3-stage, 1st stage, 1st stage, 1st stage.
NO-10	CH-200	Helium	4.2°K	1.0	N ₂ 1500 H ₂ 1500	N ₂ 0.17 H ₂ 0.19		6	1.2	All are production models. All are also used as any other of standard gas supply is applicable.

C.7 REFERENCES

- C-1. D. Jeffries, Proc. IRIS, 1958, Vol. 3, No. 1, p. 49 (SECRET).
- C-2. R. F. Rice and R. A. Trentham, Infrared Cell Cooling Systems, Memorandum Number SOL-M-22, Linde Co., Indianapolis, Ind., 15 April 1960 (UNCLASSIFIED).
- C-3. K. D. Timmerhaus (ed.), Advances in Cryogenic Engineering, Plenum Press, New York, N. Y., 1959.
- C-4. Arnold Sommerfeld, Thermodynamics and Statistical Mechanics, Academic Press, New York, N. Y., 1956.
- C-5. Mark W. Zemanski, Heat and Thermodynamics, McGraw-Hill, New York, N. Y., 1943.
- C-6. Charles D. Hodgman (ed.), Handbook of Chemistry and Physics, Chemical Rubber Publishing Co., Cleveland, O., 1956, p. 2127.
- C-7. AIResearch Closed Cycle Liquid Nitrogen Refrigeration System, AIResearch Manufacturing Divisions, Garrett Corp., Los Angeles, Calif., 6 December 1960.
- C-8. P. Kapitza, Proc. Roy. Soc. (London), 1934, Vol. A147.
- C-9. S. C. Collins, Rev. Sci. Instr., 1947, Vol. 18, No. 3.
- C-10. J. W. L. Kohler and C. O. Jonkers, Philips Tech. Rev., 1954, Vol. 16, No. 4.
- C-11. K. W. Cowans, paper presented at the winter convention of the Institute of Radio Engineers Professional Group on Military Electronics, Los Angeles, Calif., 2 February 1961.
- C-12. Integrated Infrared Detector-Cooler, Norden Division, United Aircraft Corp., Norwalk, Conn., 9 November 1960.
- C-13. Bernard Kovit, Space Aeronautics Magazine, Conover-Mast Publications, New York, N. Y., January 1961.
- C-14. R. Hilsch, Rev. Sci. Instr., 1947, Vol. 18, No. 2.

C.8. SYMBOLS

- n the enthalpy of one mole of a gas (inch-pounds/mole)
- p the pressure exerted by a gas (pounds/inch²)
- q the heat added to one mole of a gas in a thermodynamic process (inch-pounds/mole)
- s the entropy of one mole of a gas (inch-pounds/degree Kelvin-mole)
- T the absolute temperature of a gas (degrees Kelvin)
- u the internal energy of one mole of a gas (inch-pounds/mole)
- v the volume occupied by one mole of a gas (liters/mole)
- w the work done by one mole of a gas in a thermodynamic process (inch-pounds/mole)

TABLE C-4. COMPLETE SYSTEMS

Min.	Model No.	Method of Cooling	Temper. of Heat Sink	Ambient Temp. Range	Coolant	Cool Down Time	Standby Time	Operating Time	Cooling Capacity (watts)	Total Weight (lbs)
A. J. Hughes		2-stage Joule-Thomson expansion	20 ± 2 K	-100°K to -124°K	Hydrogen	1.5 min.		Continuous	1.2	15
Hughes		3-stage 2-stage adiabatic expansion with a Thomson crystal	4.2°K	55°K to 180°K	Helium	30 min.		Continuous	0.5	30
Hughes		Joule-Thomson	80°K	-85°K to -150°K	Helium	5 min.	3 years	1 min.		
Herbert H. Jones	Jan	Joule-Thomson	70°K		Nitrogen			Continuous for 18 hours	5	45
Grady		McMahon expansion engine	40°K		Helium	15 min.		Continuous	0.05	5
Arthur Little		Gifford- McMahon expansion engine	40°K to 80°K	10-150°K	Helium	5-1 min. 2-5 min.		Continuous	0.02 0.08	0.3 exclusive of compressor
Weating House	1	Joule-Thomson	98°K		Nitrogen	4.10 min.		Continuous	1-2	30
Weating House		Joule-Thomson	90°K		Nitrogen precooled by Nitrogen	15-10 min.		Continuous		30
Phelps		Expansion engine	30°K		Helium	10 min.		Continuous for 1000-2000 hours	3 at 40°K	5 exclusive of motor
Energy Systems		Thermal conduction	100°K at 100°K ambient			10 min.		Continuous	0.015	0.63
Hughes		Thermal conduction	120°K at 100°K ambient					Continuous	0.115	
Energy Systems	EX-104	Thermal conduction	100 ± 20°K at 100°K			10 min. with heat sink		Continuous	4	9.17
Energy Systems		Thermal conduction	100 ± 20°K at 100°K					Continuous	1.2	

Model	Operating Pressure (psia)	Heat Exchanger Rate (W)	Heat Exchanger				Dimensions (inches)	Remarks
			Heat Exchanger Rate (W)	Heat Exchanger Rate (W)	Heat Exchanger Rate (W)	Heat Exchanger Rate (W)		
1000	1000	1000	4.5	1.35			8 x 9 x 12	System includes compressor, absorber, and heat exchanger. A. J. Ad. products is available for use.
1000	1000		10.5	1.875			12 x 12 x 12	Heat exchanger dimensions include dewar and insulating envelope. System includes compressor, absorber, and detector cooling assembly. Heat exchangers designed for a variety of dewars.
			1.25	0.4	4.0	1.5		Operating times may be extended by using large supply reservoirs.
200	200	200	1.4	0.37			25 x 14 x 20	Heat exchanger dimensions include dewar and insulating envelope.
1	1	200	5	1.25			12 x 6 x 3	Prototype including detector cooler and helium compressor, supply cylinder.
	closed	200	0.1	2	0.22		3.25 x 1.25 x 1.25	System inclusive of everything but compressor may be operated with any supply capable of supplying helium gas at proper pressure and flow rate.
900	Closed	1500	2	0.24			8 x 9 x 12	Other from Barlow Research Center or Air Products (cryostat) are applicable. This system may be modified by the use of hydraulic power instead of electrical power. Modified system weighs 30 lbs and is 6 x 6 x 6 inches overall.
								Same as above. Neon gas is pre-cooled before its conversion temperature by liquid nitrogen.
							5 x 2 x 15	System will cool from 3 temperature from ambient to 30°K. Contains no compressors or valves. Dimensions are inclusive of everything except motor drive.
13							2.5 x 1 x 1	Cooling 20°K dimensions 0.125 x 1.25 inches. Ambient temperature refers to temperature of hot surface (T_H). Temperature of cold surface (T_C) is 10°K at ambient. ΔT is 10°K. ΔT decreases with decreasing hot surface temperature.
5							2.5 x 1 x 1	Ambient temperature refers to temperature of hot surface. T_H is temperature of hot surface. T_C is 10°K at ambient. ΔT is 10°K. ΔT decreases with decreasing hot surface temperature.
							1.2 x 1.2 x 1	Maximum temperature difference between hot surface (T_H) and cold surface (T_C) is 10°K. ΔT is 10°K. ΔT decreases with decreasing hot surface temperature.
							1.2 x 1.2 x 1	Maximum temperature difference between hot surface (T_H) and cold surface (T_C) is 10°K. ΔT is 10°K. ΔT decreases with decreasing hot surface temperature.

Appendix D Peltier Cooling

Robert H. Vought, General Electric Company

D.1. INTRODUCTION

A standard temperature-indicating thermocouple produces an emf when the two junctions between dissimilar materials are held at different temperatures. Conversely, an externally driven current in a similar thermocouple circuit will produce a temperature difference between the two junctions by absorbing heat at one junction and releasing it at the other. These phenomena illustrate the Seebeck effect and the Peltier effect, respectively. A device which utilizes the Peltier effect to transport heat from one region to another is called a thermoelectric heat pump, or Peltier heat pump, and can be used either for heating or cooling.

Until recently the Peltier heat pump was primarily a laboratory curiosity because the temperature differences which could be produced with metallic junctions were insignificant. However, during the past few years semiconductors have been developed which are capable of producing appreciable temperature differences (up to 75°K with the heat sink at room temperature). Better thermoelectric materials are being sought, and it may be expected that larger temperature differences will become feasible in the near future.

The following discussion will be concerned with the application of the Peltier heat pump to the cooling of infrared detectors. Emphasis will be placed upon those features of Peltier cooling systems which are not common to other types of cooling systems. This appendix includes a description of the physical mechanisms by which Peltier cooling is achieved, a physical and mathematical description of the typical performance of an isolated Peltier couple, a design procedure for constructing a simple Peltier cooler with prescribed characteristics, and a brief discussion of some of the problems associated with the use of Peltier couples in achieving practical cooling systems.

D.1.1. ADVANTAGES OF PELTIER HEAT PUMPS. There are compelling reasons for considering Peltier heat pumps for many problems involving refrigeration, including the cooling of infrared

detectors. The following are among the significant characteristics of Peltier heat pumps.

- (a) They are small. The lower limit on the size of Peltier couples probably will be set by the heat transfer coefficients of the heat absorbers and heat rejectors.
- (b) They are reliable. Solid-state devices, which involve no moving parts or circulating fluids, are extremely reliable and will operate continuously for long periods of time without requiring attention.
- (c) Their performance is independent of heat pumping capacity. The efficiency of a Peltier heat pump depends only on the working temperatures and material properties and is independent of the cooling capacity.
- (d) The cooling rate is controllable. With a simple current-control circuit, the rate of heat removal may be regulated continuously over a broad range in order to maintain constant temperature even though the heat load or the temperature of the heat sink may vary considerably.
- (e) The device can be used to heat or cool. A Peltier cooler can be made to serve as a heater by reversing the current. Thus it can be used under conditions where the ambient temperature is sometimes above and sometimes below the required constant temperature.
- (f) The Peltier heat pump produces no vibration and is absolutely silent.

A complete evaluation of the applicability of a Peltier cooling system to a particular problem requires an examination of the disadvantages as well as the advantages. To a considerable extent, the disadvantages of Peltier cooling result from the relative infancy of the technique. Several of the incompletely solved problems are discussed briefly in Section D.5. Present and future development of materials, fabrication techniques, and associated circuitry will certainly decrease the importance of these problems.

D.1.2. CURRENT STATE OF DEVELOPMENT OF PELTIER COOLERS. Most work which has been publicized has been concerned primarily with temperatures in a range of about 50°K on either side of room temperature. Devices which have been used, or which can be made for sale, are small and have heat pumping capacities from fractions of a watt to a few watts. Considerable effort is being expended on the development of devices with large cooling capacities, which may be used for household refrigerators and air conditioners. Standard compression-expansion coolers are still superior for these applications, but the development of more efficient materials could well make Peltier coolers economically competitive with present-day refrigeration techniques.

As will be shown later, the maximum temperature difference attainable with given materials is proportional to the square of the absolute temperature of the cold side of the couple. It would thus appear that refrigeration by Peltier coolers is impractical. However, some phenomena that are virtually nonexistent at room temperature are pronounced at low temperatures. It may be possible to exploit one or more of these for Peltier cooling at these low temperatures. Further development may provide materials and devices which will be useful at liquid-nitrogen or even liquid-helium temperatures. Near absolute zero the rate of heat pumping will be quite small, but this is true of any method of cooling. Furthermore, heat capacities in this range are very low, so it is not necessary to pump a great amount of heat to produce useful temperature differences.

D.2. DESCRIPTION OF A PELTIER COUPLE.

A brief discussion of a Peltier couple will now be given, along with a simplified physical picture of the cooling mechanism and some qualitative discussion indicating the material properties which are pertinent to Peltier cooling.

Figure D-1 is a schematic representation of a Peltier couple. The arms of the couple, n and p, represent n-type and p-type semiconductors, respectively. They are connected by metallic conductors which exhibit negligible thermoelectric effects. A current passing from an n-type material to

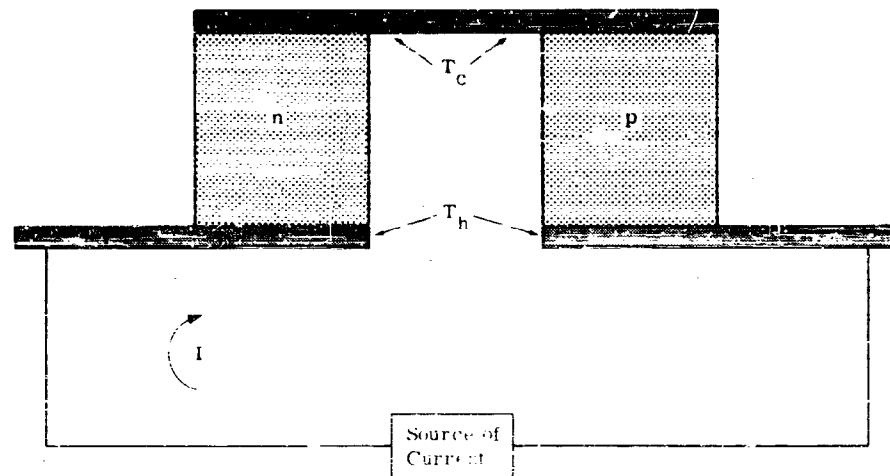


FIGURE D-1. SCHEMATIC CONSTRUCTION OF PELTIER HEAT PUMP

nonthermoelectric conductor removes heat from the conductor. On the other hand, a current passing from a p-type material to a nonthermoelectric conductor delivers heat to the conductor. In both cases, reversing the current will cause the heat to flow the other way. Thus it can be seen that the effect of a current in the direction indicated in Figure D-1 is to make the temperature of the top, T_c , lower than the temperature of the bottom, T_h .

D.2.1. QUALITATIVE EXPLANATION OF THE PELTIER EFFECT. Qualitatively, the Peltier effect can be understood with the aid of Figure D-2, which represents an energy-level diagram of a Peltier couple, with RI drops ignored. The regions labeled M_1 , M_2 , and M_3 represent metals exhibiting no thermoelectric effects, while n represents an n-type semiconductor and p represents a p-type semiconductor. Finely dotted areas represent valence bands where the energy levels are normally occupied by electrons, whereas coarsely dotted areas represent conduction bands where, in the case of semiconductors, the energy levels are normally unoccupied. The horizontal straight line through the diagram represents the Fermi level. Metal-semiconductor contacts are assumed to be nonrectifying.

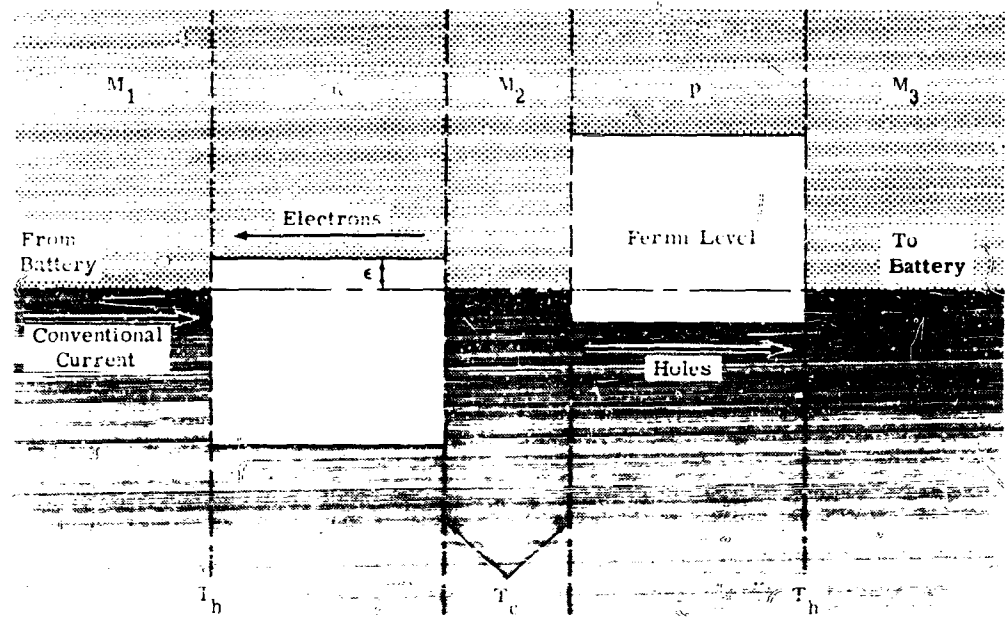


FIGURE D-2. ENERGY LEVEL DIAGRAM OF A PELTIER COUPLE

In the metals and n-type semiconductors, current is carried by electrons moving from right to left. In the p-type semiconductor, current is carried by positively charged holes moving from left to right. Consider first the passage of electrons from M_2 to n to M_1 . As electrons arrive at the M_2 -n junction, there are no available levels in the n-type materials below the bottom of the conduction band. In order to pass through n the electrons must be thermally excited up to the conduction band. Thus each electron removes from M_2 an amount of energy equal to the Fermi energy ϵ of the n-type material, where ϵ is the difference between the energy of the Fermi level and the energy at the bottom of the conduction band. (Actually, the energy required is greater, by an amount equal to the transport energy of the electrons in the n-type material.) This removal of energy from M_2 represents a removal of heat, and thus the M_2 -n junction is cooled. At the n- M_1 junction the electrons can drop back down to their original levels and thus give up heat.

Similar arguments apply to holes at the M_2 -p and p- M_3 junctions. At the M_2 -p junction an electron from the valence band of p must be excited up to the conduction band of M_2 , leaving a hole which moves toward M_3 . This represents heat removal at the M_2 -p junction. The heat reappears at the p- M_3 junction when an electron drops down to combine with the transported hole.

D.2.2. PERTINENT MATERIAL PROPERTIES. From the qualitative discussion of section 2.1 it can be seen that the rate of pumping of heat is directly proportional to the current. The constant of proportionality is known as the Peltier coefficient, π . (See Section D.8 for definitions of symbols.) It represents a potential difference which is determined by the Fermi energy plus a transport energy. Thus, for a current I the rate of pumping of heat by the Peltier effect, \dot{Q}_π , is

$$\dot{Q}_\pi = \pi I \quad (D-1)$$

The Seebeck coefficient of a couple, S , is the ratio of the thermal emf to the temperature difference which produces that emf (see Section D-1). For a single material, a quantity s , called the Seebeck coefficient of the material, can be defined in such a way that the Seebeck coefficient of any couple is given by the difference of the Seebeck coefficients of the two materials from which it is constructed,

$$S = s_2 - s_1$$

The Seebeck coefficient of a p-type material, s_p , and the Seebeck coefficient of an n-type material, s_n , must have opposite signs. Conventionally, s_p is taken as positive and s_n as negative. Thus, for a couple composed of a p-type and an n-type material, the difference $s_p - s_n$ is actually the sum of two positive numbers. In order to avoid difficulties with signs it is often convenient to use absolute

$$S = \frac{V}{T} = \frac{V_p}{T_p}$$

The Seebeck and Peltier coefficients are related by the first of the Thomson relations (Reference D-1 or D-2)

$$\pi = ST \quad (D-2)$$

It follows that

$$\dot{Q}_c = STI \quad (D-3)$$

where T is the temperature of the cold junction when the couple is used for cooling.

Evidently, then, Peltier cooling will be more effective with materials which exhibit large Seebeck coefficients. It is evident also that cooling will be more effective when the Joule heating, I^2R , is a minimum. The current, I , cannot be made small without reducing the rate of heat pumping (see Equation D-1). Therefore it is necessary to keep the resistance low, which can be accomplished by the use of material with low electrical resistivity ρ . A third important property is the thermal conductivity κ . Clearly this parameter should be kept as small as possible, since it would be of little value to pump heat from one region to another if most of it could flow back again.

Therefore, there are three parameters which serve to characterize a material for its cooling capabilities:

- S = Seebeck coefficient (volts per degree Kelvin)
- ρ = electrical resistivity (ohm-centimeters)
- κ = thermal conductivity (watts per centimeter per degree Kelvin)

These three quantities vary with temperature, and for accurate calculations the variations must be taken into account. Furthermore, variations of S with T give rise to an additional thermoelectric effect, the Thomson effect, and a rigorous treatment must take into account the Thomson heat which arises when a current and a parallel temperature gradient exist in a material for which S varies with T . However, for the purposes of this elementary discussion of Peltier cooling, S , ρ , and κ will be assumed constant over the temperature range under consideration, and hence the Thomson effect will not affect the problem.

D.2.3. FIGURE OF MERIT The three material properties S , ρ , and κ frequently appear in the same combination in discussions of thermoelectric devices. This combination is usually referred

as the figure of merit of the material and is denoted by Z , where

$$Z = \frac{S^2}{\rho\kappa} (0_K^{-1}) \quad (D-4)$$

Obviously, the larger the figure of merit, the more useful is the material for thermoelectric applications. At present, the best values of Z for semiconducting materials are slightly greater than $3 \times 10^{-3} 0_K$. (The best values for metals are of the order of $0.1 \times 10^{-3} 0_K$.) A figure of merit of $3 \times 10^{-3} 0_K$ makes it possible, for instance, to pump heat from ice to steam with a single stage device.

The figure of merit of a couple is defined by

$$Z_c = \frac{S^2}{RK} \quad (D-5)$$

where the material constants ρ and κ of Equation D-4 have been replaced by the electrical resistance R and the thermal conductance K .

The maximum possible value of Z_c for any couple composed of two given materials (Reference D-2, page 11) is given by

$$\left(\frac{S}{\sqrt{\rho_1 \kappa_1} + \sqrt{\rho_2 \kappa_2}} \right)^2 \quad (D-6)$$

It should be noted that Z_m depends only on the properties of the materials while Z_c depends also on the dimensions of the couple. Z_c approaches Z_m only under ideal conditions when the relative values of the various dimensions have been properly adjusted (see Section D-5).

If the values of ρ and κ are the same for the two arms of the couple, it can easily be seen that $Z_c = Z_m$ when the dimensions of the two arms are equal. If, in addition, the couple is made from p-type and n-type material, such that $s_p = -s_n = s$, then $Z_c = Z_m = s^2 / \rho\kappa$.

D.3. PERFORMANCE OF A Peltier Couple.

The performance characteristics of a typical couple, such as that shown in Figure D-1, will now be considered. The treatment is not intended to be an exact physical or mathematical description, but only an outline of the important features of Peltier couples. The numerical examples given are evaluated from approximate expressions, because the errors are small and the properties of the thermoelectric materials are not known with sufficient accuracy to warrant exact calculations.

It will be assumed that the couple has Seebeck coefficients s_n and s_p , electrical resistivities ρ_n and ρ_p , thermal conductivities κ_n and κ_p , total series electrical resistance R , and total parallel thermal conductance K between the ends, which are at temperatures T_c and T_h . The temperature difference, $T_h - T_c$, will be called ΔT . Figure D-3 is a sketch of the idealized Peltier couple that will be discussed. The conductor connecting the thermoelectric materials is assumed to have zero Seebeck coefficient, zero electrical resistivity, and infinite thermal conductivity. The thermal and electrical resistances at these connections are assumed to be zero. The validity of these assumptions will be discussed more thoroughly in Section D-5. When it is also assumed that the properties of the material are independent of temperature, it is possible to give a complete description of the equilibrium performance of the couple. It will be shown that s_n , s_p , R , K , and T_c completely define the maximum temperature difference attainable with this particular couple. However, this is not necessarily the maximum temperature difference attainable with the materials from which the couple is constructed.

There are four quantities of interest: the pumping current I , the heat-pumping rate Q , the temperature difference ΔT , and the coefficient of performance ϵ (to be defined later). Only two of these are independent. However, there are generally two conditions which are of greatest interest, namely, the pumping of the maximum amount of heat and the most efficient pumping of heat. Each of these

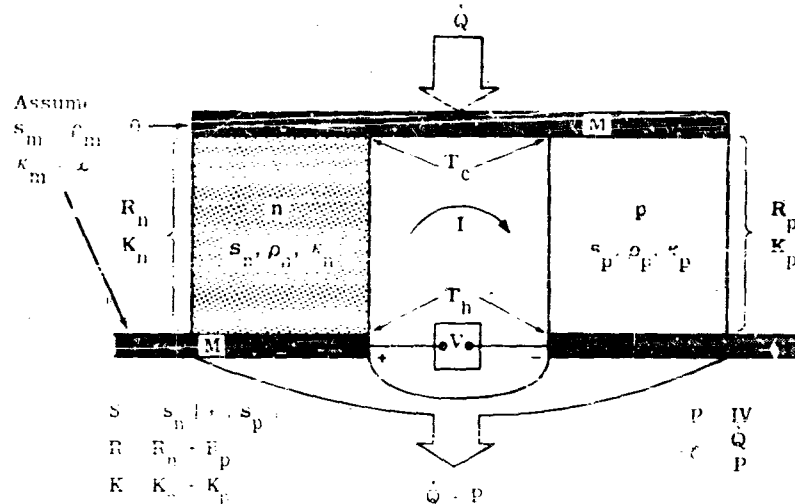


FIGURE D-3. PELTIER COUPLE WITH NOTATION AND DEFINITIONS

which, as far as the magnitude of the current is equal for a given couple, the heat-pumping capacity and coefficient of performance can be represented as functions only of ΔT and T_c .

HEAT BALANCE AT THE COLD JUNCTION. In the couple shown in Figure D-3, the current passing from *n* to *M* to *p* will remove heat from *M*. Using the arguments given in the discussion in Section D.2.1, the rate of heat removal by the Peltier effect is $\dot{Q}_p = (s_p T_c I - s_n T_c I) = ST_c I$.

It can also be shown that the uniform generation of joule heat throughout the thermoelectric material results in a flow of heat to each of the junctions at the rate $\dot{Q}_j = \frac{1}{2} I^2 R$. (It is assumed that there is no heat transfer through the sides of the thermoelectric arms.) Finally, the heat conducted back to the cold junction from the hot junction is $\dot{Q}_f = K \Delta T$.

At equilibrium, the difference between the flow of Peltier heat, \dot{Q}_p , from the cold junction and the flow of joule heat, \dot{Q}_j , and conducted heat, \dot{Q}_f , to the cold junction represents the rate, \dot{Q} , at which the couple pumps heat. Thus,

$$\dot{Q} = \dot{Q}_p - (\dot{Q}_j + \dot{Q}_f) = ST_c I - \frac{1}{2} I^2 R - K \Delta T \quad (D-7)$$

Because of the power dissipated in the thermocouple (*P*) during the heat-pumping process, $\dot{Q} + P$ watts must be rejected at the hot junction for \dot{Q} watts absorbed at the cold junction.

D.3.2. MAXIMUM RATE OF HEAT PUMPING. The current which produces the maximum rate of heat pumping is easily obtained by maximizing \dot{Q} (by setting $\frac{\partial \dot{Q}}{\partial I} = 0$). The result is that the current for maximum steady-state heat pumping, $I_{\dot{Q}}$, is

$$I_{\dot{Q}} = ST_c / R \quad (D-8)$$

which is proportional to the temperature of the cold junction and independent of the load or temperature difference. The maximum rate of heat pumping is obtained by substituting Equation D-8 into Equation D-7. The result is

$$\dot{Q}_m = \frac{1}{2} \frac{S^2 T_c^2}{R} - K \Delta T \quad (D-9)$$

If the cold junction is insulated so that no heat is absorbed from its surroundings, ΔT will rise to the maximum value that this couple can provide, ΔT_m . Thus,

$$\Delta T_m = \frac{1}{2} \frac{S^2 T_c^2}{RK} \quad (D-10)$$

The figure of merit of the couple, Z_c , may then be defined as

$$Z_c = S^2 / RK \quad (D-11)$$

The maximum temperature difference that this couple can maintain is therefore

$$\Delta T_m = \frac{1}{2} Z_c T_c^2 \quad (D-12)$$

With optimum design, a couple made of the same materials can maintain a temperature difference ΔT_M given by

$$\Delta T_M = \frac{1}{2} Z_M T_c^2 \quad (D-13)$$

where Z_M is defined by Equation D-6. In general, ΔT_m is slightly less than ΔT_M .

Equations D-9 and D-10 show that the rate of heat pumping may be written as

$$\dot{Q}_m = K(\Delta T_m - \Delta T) = K \Delta T_m \left(1 - \frac{\Delta T}{\Delta T_m} \right) \quad (D-14)$$

which decreases linearly from $K \Delta T_m$ at $\Delta T = 0$ to 0 at $\Delta T = \Delta T_m$.

The coefficient of performance, ζ , is defined as

$$\zeta = \dot{Q} / P \quad (D-15)$$

where P is the power required to pump heat at the rate \dot{Q} , and given by

$$P = IS \Delta T + I^2 R \quad (D-16)$$

$$= 2K \Delta T_m \left(1 + \frac{\Delta T}{T_c} \right) \quad (D-16')$$

By combining Equations D-14, D-15, and D-16', one finds the coefficient of performance for maximum heat pumping to be

$$\zeta_{\dot{Q}} = \frac{1}{2} \left(1 - \frac{\Delta T}{\Delta T_m} \right) \left(1 - \frac{\Delta T}{T_h} \right) \quad (D-17)$$

This has a maximum value of 1/2 and decreases to 0 when $\Delta T = \Delta T_m$.

Some of them it is now possible to obtain:

- The maximum no-load temperature difference, ΔT_m , from Equation D-12.
- The current required for maximum cooling, I_Q , from Equation D-8.
- The amount of heat pumped, \dot{Q}_m , for a given ΔT , from Equation D-14.
- The coefficient of performance, $\zeta_{\dot{Q}}$, for a given ΔT , from Equation D-17.

The nomographs to be presented later enable these values to be determined quickly in terms of the temperatures, material parameters, and dimensions. "Typical" values of \dot{Q}_m , $\zeta_{\dot{Q}}$, and I_Q , for material constants somewhat less than the best attainable are presented in Figure D-4.

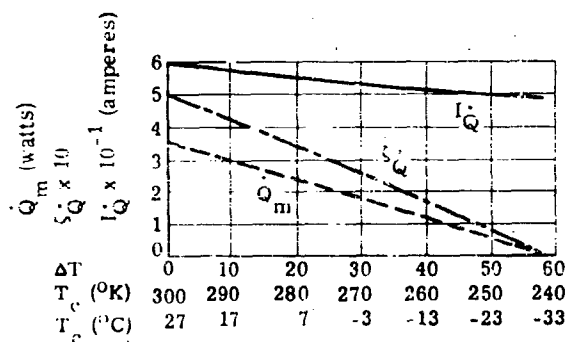


FIGURE D-4. MAXIMUM RATE OF HEAT PUMPING, CURRENT REQUIRED FOR MAXIMUM HEAT-PUMPING CAPACITY, AND COEFFICIENT OF PERFORMANCE FOR MAXIMUM HEAT PUMPING AS FUNCTIONS OF T_c (OR ΔT) FOR $T_h = 300^\circ\text{K}$. The couple is made from cubes 1 cm on a side with $s_p = -s_n = 200 \mu\text{V}/^\circ\text{K}$, $\rho_n = \rho_p = 10^{-3} \text{ ohm-cm}$, and $\kappa_n = \kappa_p = 20 \text{ mw/cm}^\circ\text{K}$.

D.5.3. MAXIMUM EFFICIENCY. Another useful operating condition is that of maximum efficiency. The expression for the current required for maximum efficiency may be obtained by maximizing the coefficient of performance with respect to current, using Equations D-7, D-15, and D-16. The result obtained shows that the current giving maximum coefficient of performance, I_c , is

$$I_c = I_Q \frac{\Delta T}{\Delta T_m} \quad \text{A} \quad (\text{D-18})$$

where A is a factor of order unity, and the relation

$$A = \frac{T_c - \sqrt{T_c^2 + 2T_c \Delta T_m + \Delta T \Delta T_m} - 1}{2T_c + \Delta T} = 1 - \frac{T_m - \Delta T}{2T_c} \quad (D-19)$$

Therefore,

$$I_p = I_Q \frac{\Delta T}{\Delta T_m} \quad (D-20)$$

Note that for constant T_c the current for maximum heat pumping, I_Q , is constant and the current for maximum efficiency, I_ζ , varies almost linearly with ΔT .

From Equation D-7 and D-8 the rate of heat pumping is found to be

$$\dot{Q}_\zeta = K \Delta T \left(2A - \frac{\Delta T}{\Delta T_m} A^2 - 1 \right) \quad (D-21)$$

where A is defined by Equation D-19 and is nearly unity, so that

$$\dot{Q}_\zeta = K \Delta T \left(1 - \frac{\Delta T}{\Delta T_m} \right) \quad (D-22)$$

This may be written in terms of the maximum heat pumping rate as

$$\dot{Q}_\zeta = \dot{Q}_m \frac{\Delta T}{\Delta T_m} \quad (D-23)$$

and will be zero for $\Delta T = 0$ and $\Delta T = \Delta T_m$, with a maximum at $\Delta T = \Delta T_m/2$, where $\dot{Q}_\zeta = \frac{1}{2} \dot{Q}_m$.

The maximum coefficient of performance, from Equations D-21, D-18, D-16, and D-15, becomes

$$\zeta_m = \frac{1}{2} \left(2 - \frac{1}{A} - \frac{A \Delta T}{\Delta T_m} \right) \left(\frac{\Delta T}{T_c} + \frac{A \Delta T}{\Delta T_m} \right)^{-1} \quad (D-24)$$

and again, since A is nearly unity, this simplifies to

$$\zeta_m = \frac{1}{2} \left(1 - \frac{\Delta T}{\Delta T_m} \right) \left(\frac{\Delta T}{\Delta T_c} + \frac{\Delta T}{\Delta T_m} \right)^{-1} \quad (D-25)$$

This may be written as

$$\zeta_m \approx \frac{\Delta T_m}{\Delta T} \cdot \frac{1}{2} \left(1 - \frac{\Delta T}{\Delta T_m} \right) \left(1 - \frac{\Delta T}{T_h} \right) \left(1 - \frac{\Delta T_m - \Delta T}{T_h} \right)^{-1} \quad (D-26)$$

which from Equation D-17, is very nearly

$$\zeta_m \approx \frac{\Delta T_m}{\Delta T} \cdot \zeta_Q \quad (D-27)$$

Note that two approximations are used in arriving at this simple form. The exact expression given by Equation D-24 can be approximated by Equation D-25, since A is very nearly unity. Equation D-26 is merely Equation D-25 written in a different form. Finally, Equation D-26 is written as Equation D-27 by assuming that

$$\Delta T_m - \Delta T \approx T_h$$

The ratio $\Delta T_m / \Delta T$ is seen to be very nearly the ratio of the coefficients of performance for maximum cooling rate and maximum efficiency. Figure D-5 shows the values of ζ_m , I_ζ , and \dot{Q}_ζ when the couple used for Figure D-4 is used under conditions of maximum coefficient of performance. The curves were obtained using Equations D-20, D-23, and D-27. For very small ΔT , Equation D-26 was used instead of Equation D-27.

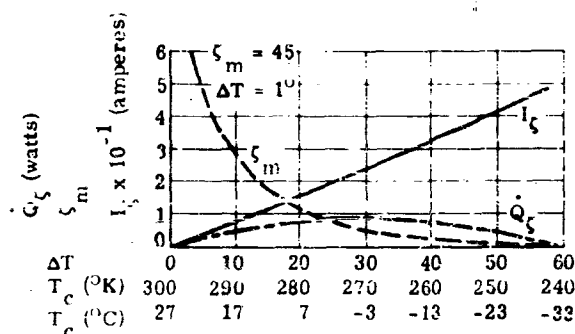


FIGURE D-5. MAXIMUM COEFFICIENT OF PERFORMANCE, CURRENT REQUIRED FOR MAXIMUM COEFFICIENT OF PERFORMANCE, AND HEAT-PUMPING RATE FOR MAXIMUM COEFFICIENT OF PERFORMANCE FOR THE COUPLE

OF TYPE D-1, $T_h = 300^\circ \text{K}$.

Analytic expressions for Q and ϵ are not difficult to obtain in simple form for other values of current. Some idea of the way in which Q and ϵ vary with current and temperature difference may be obtained from Figure D-3, where Q and ϵ are plotted against I with ΔT as a parameter. Again, the numbers refer to the couple used for Figures D-4 and D-5.

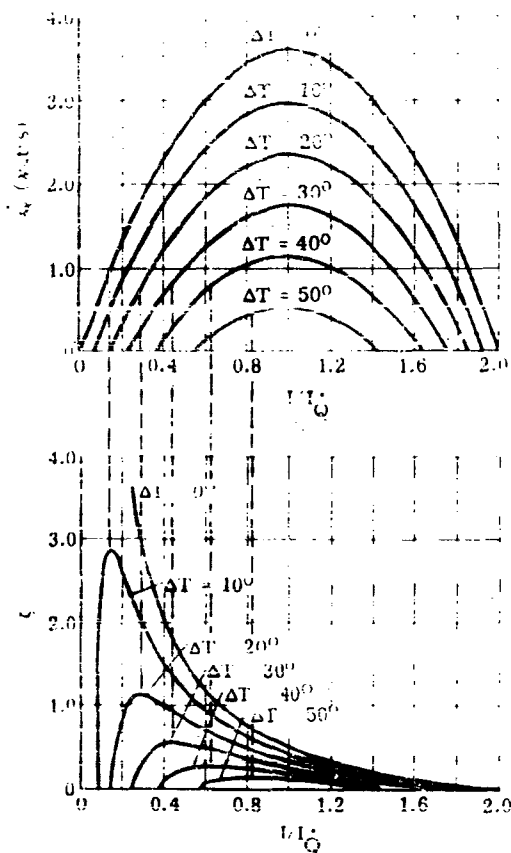


FIGURE D-3. RATE OF HEAT PUMPING AND COEFFICIENT OF PERFORMANCE AS FUNCTIONS OF CURRENT FOR VARIOUS TEMPERATURE DIFFERENCES.
 $T_h = 300^\circ\text{K}$

The nomographs were prepared by R. L. Thompson, General Electric Company.

D-4. DESIGN OF A Peltier COUPLE

In the preceding discussion, the performance of a Peltier couple of given properties and dimensions was analyzed. The task of determining the dimensions of a Peltier couple to provide a prescribed performance is not so straightforward. However, since one of the attractive features of Peltier cooling is the possibility of designing a device which will fulfill the specific requirements of a particular task with minimum space and, perhaps, minimum input power, it would be desirable to be able to determine the size and required input power before final system designs are completed. The nomographs presented here (Figures D-7 to D-16) were constructed with this objective in mind. Since some quantities must be determined by compromising among several different parameters, there is no unique cooler for a particular requirement. For instance, a single couple using a given current and voltage may be replaced by two couples using half the current but twice the voltage. Other compromises will become evident as the discussion progresses.

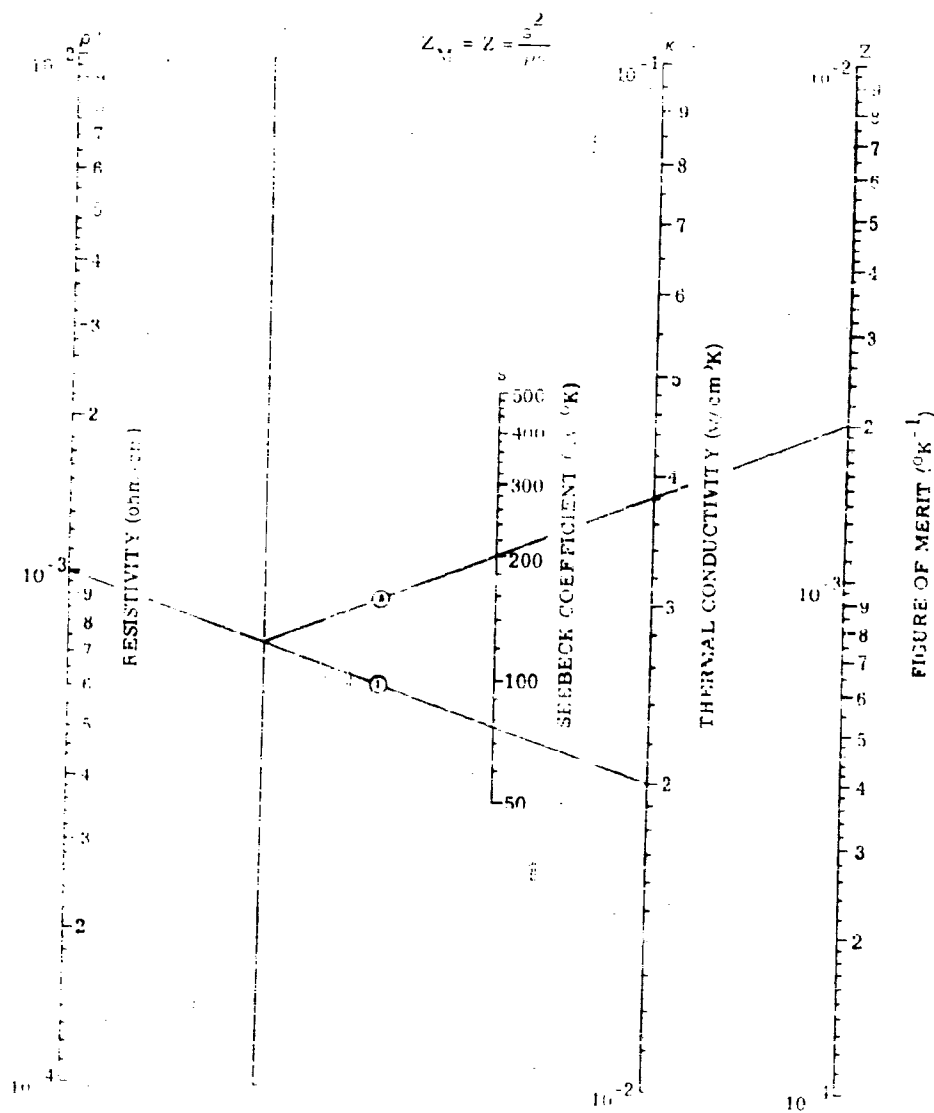


FIGURE D-7. NOMOGRAPH

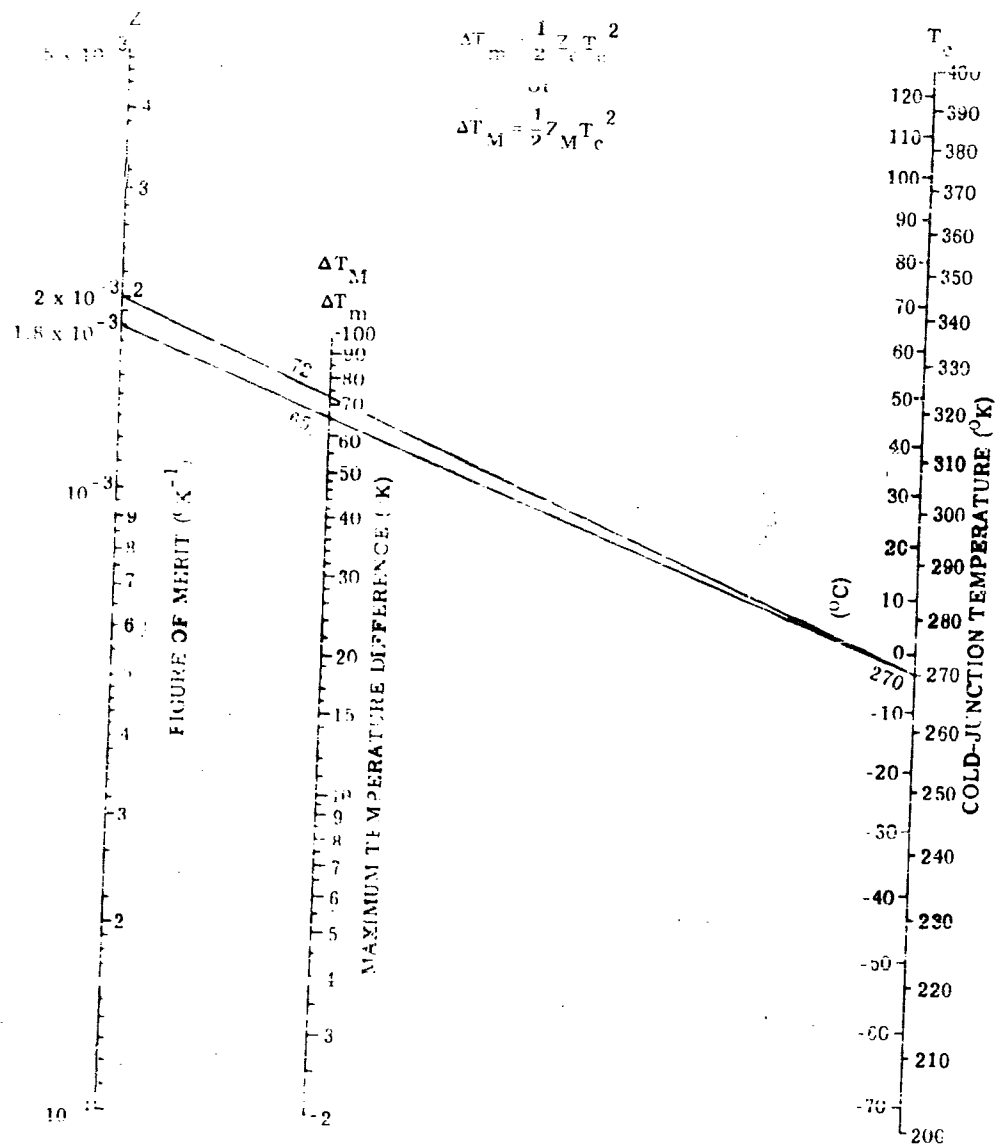


FIGURE D.8. NOMOGRAPH II

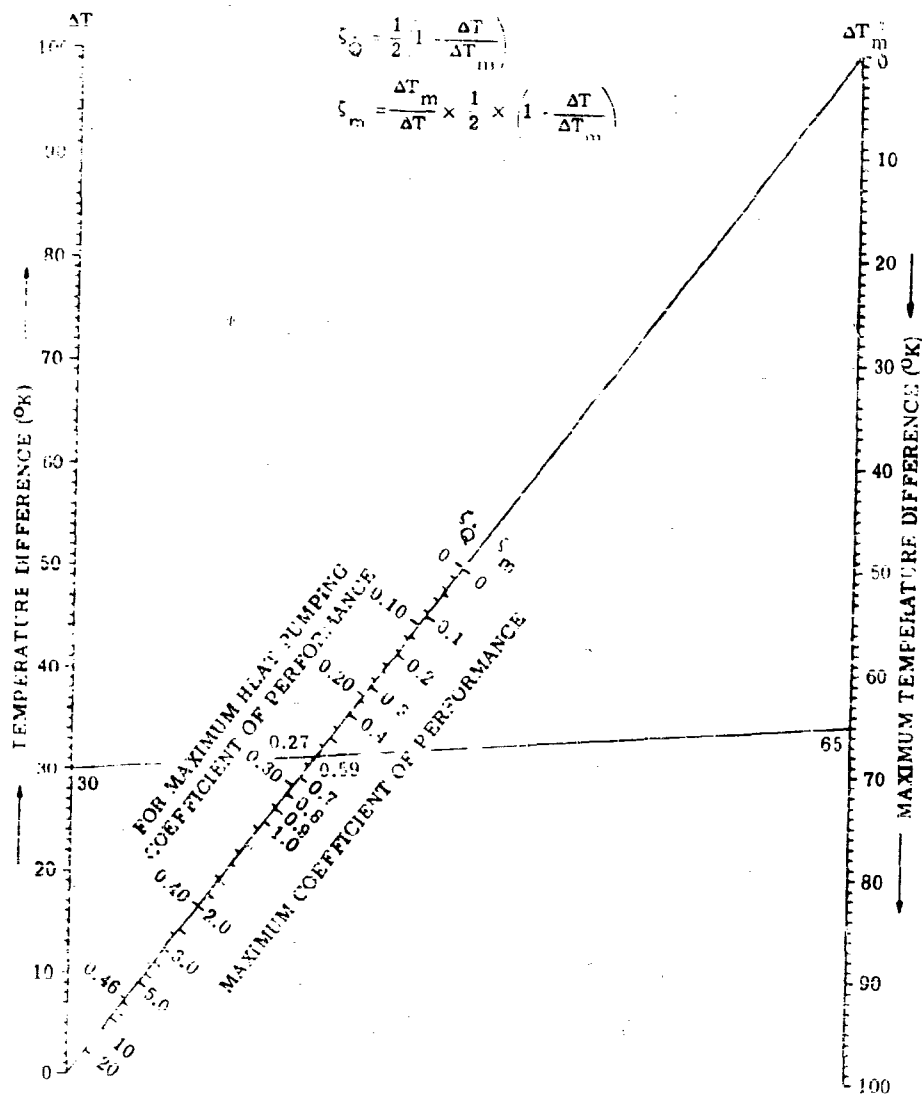


FIGURE D-9. NOMOGRAPH III

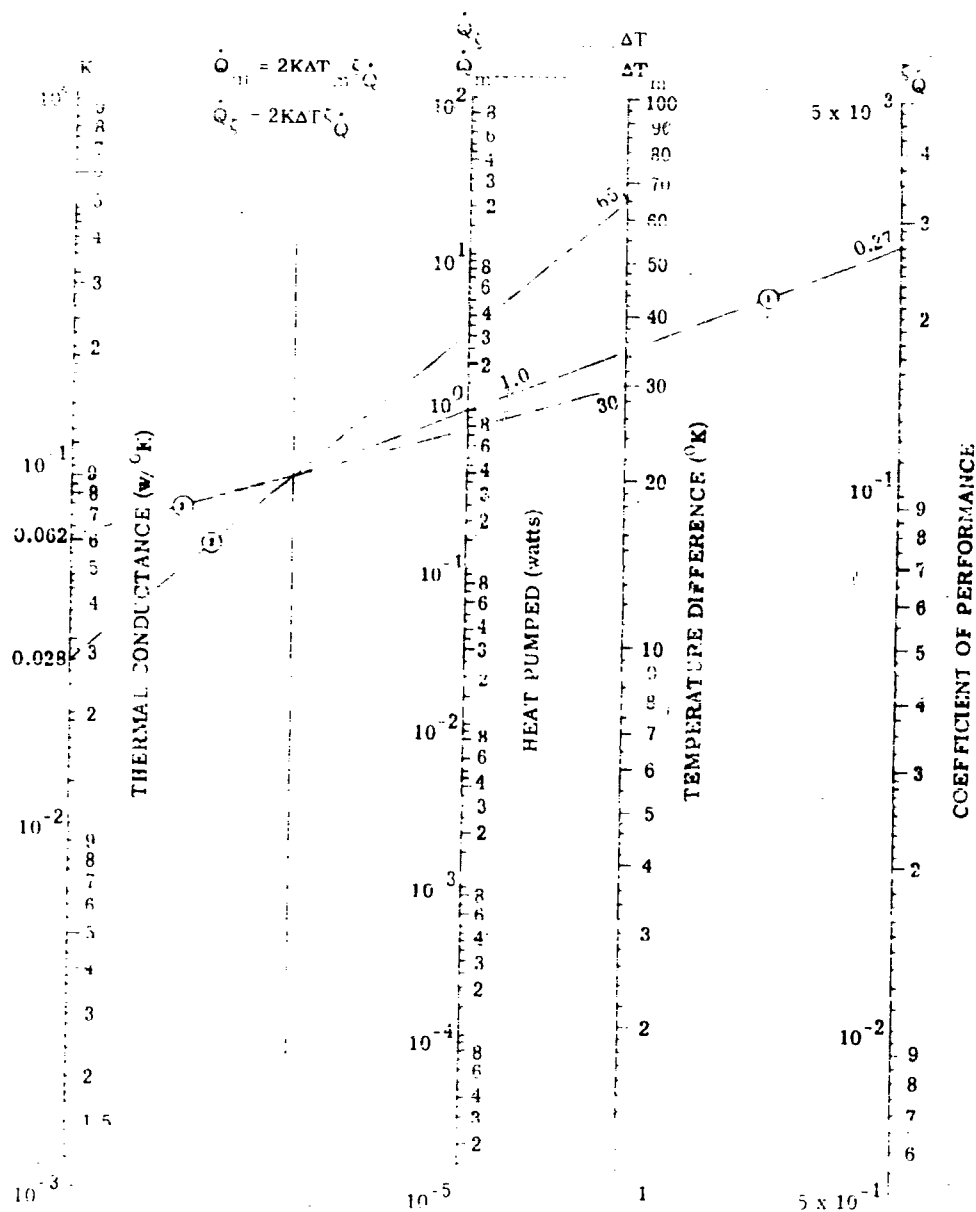


FIGURE D-19. NOMOGRAPH IV

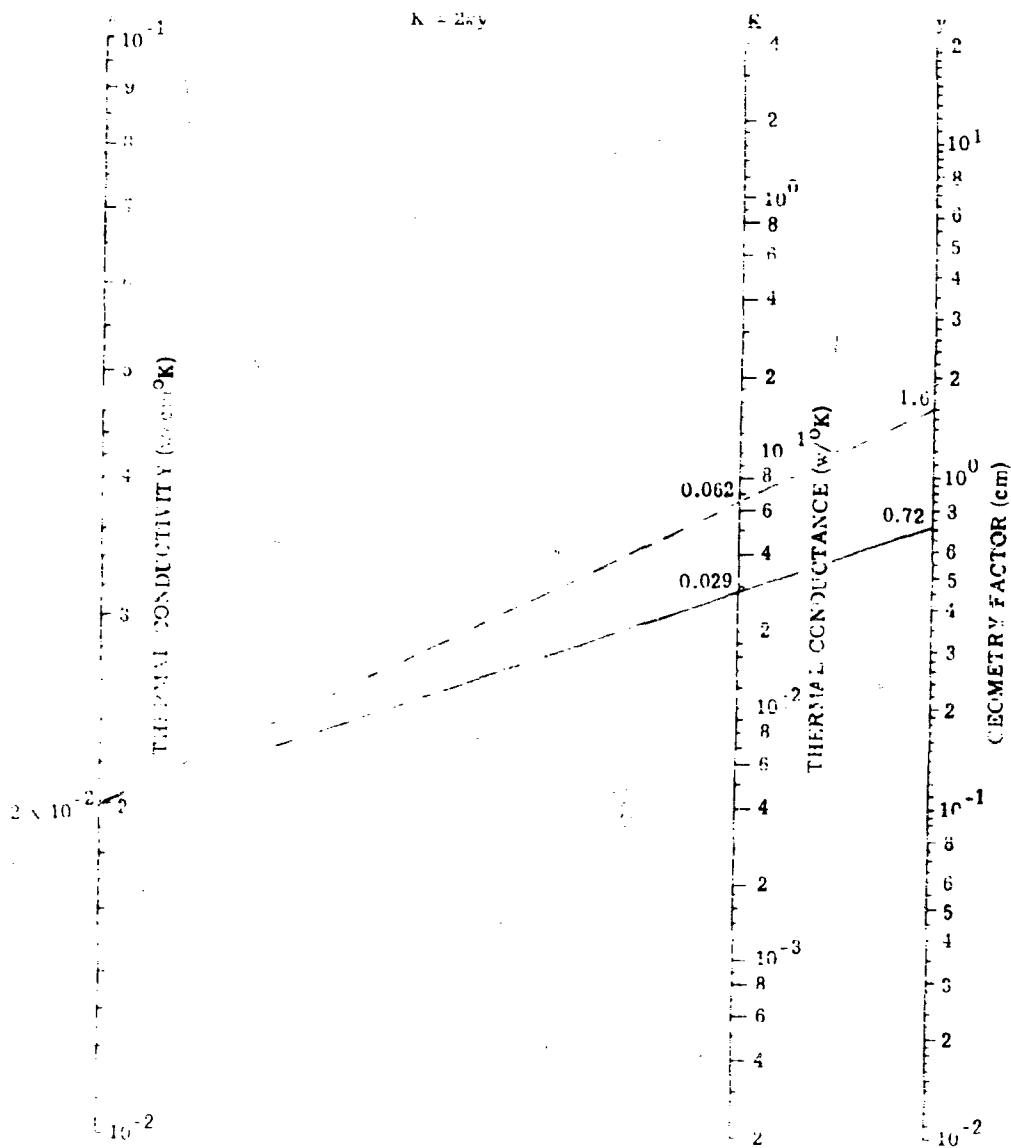


FIGURE D-11. NOMOGRAPH V

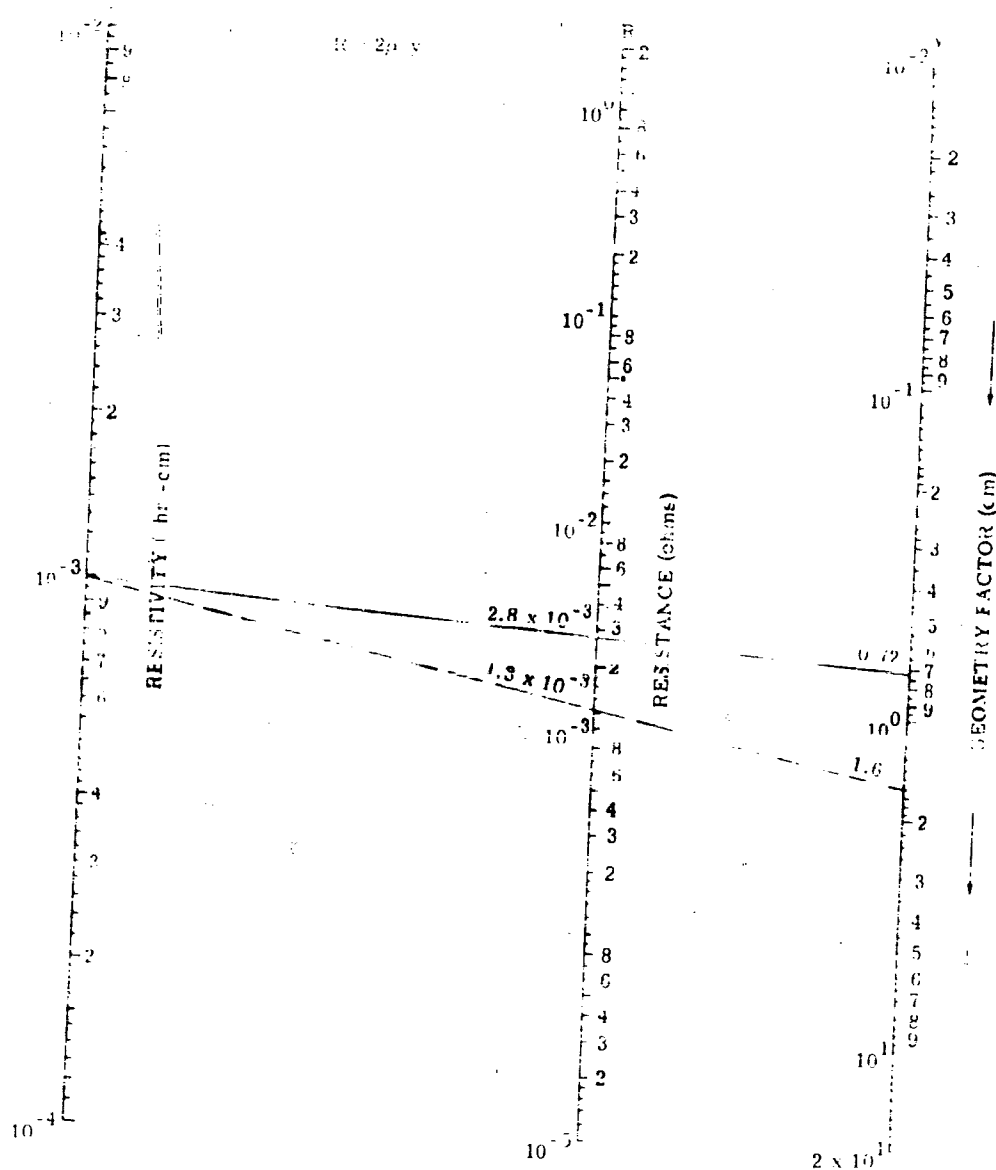
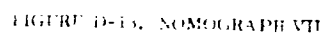


FIGURE 10-11. LOG-LOG GRAPH



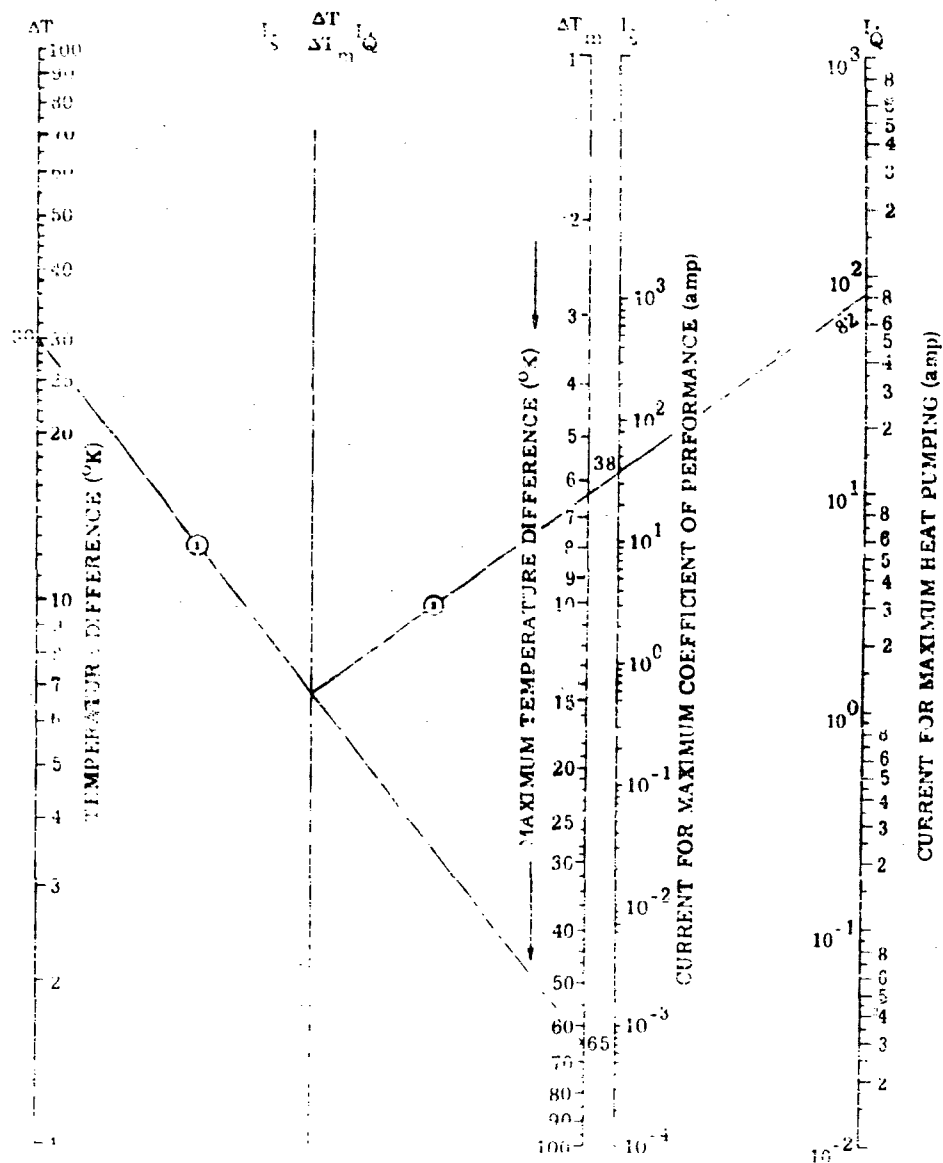


FIGURE D-11. NOMOGRAM D-11

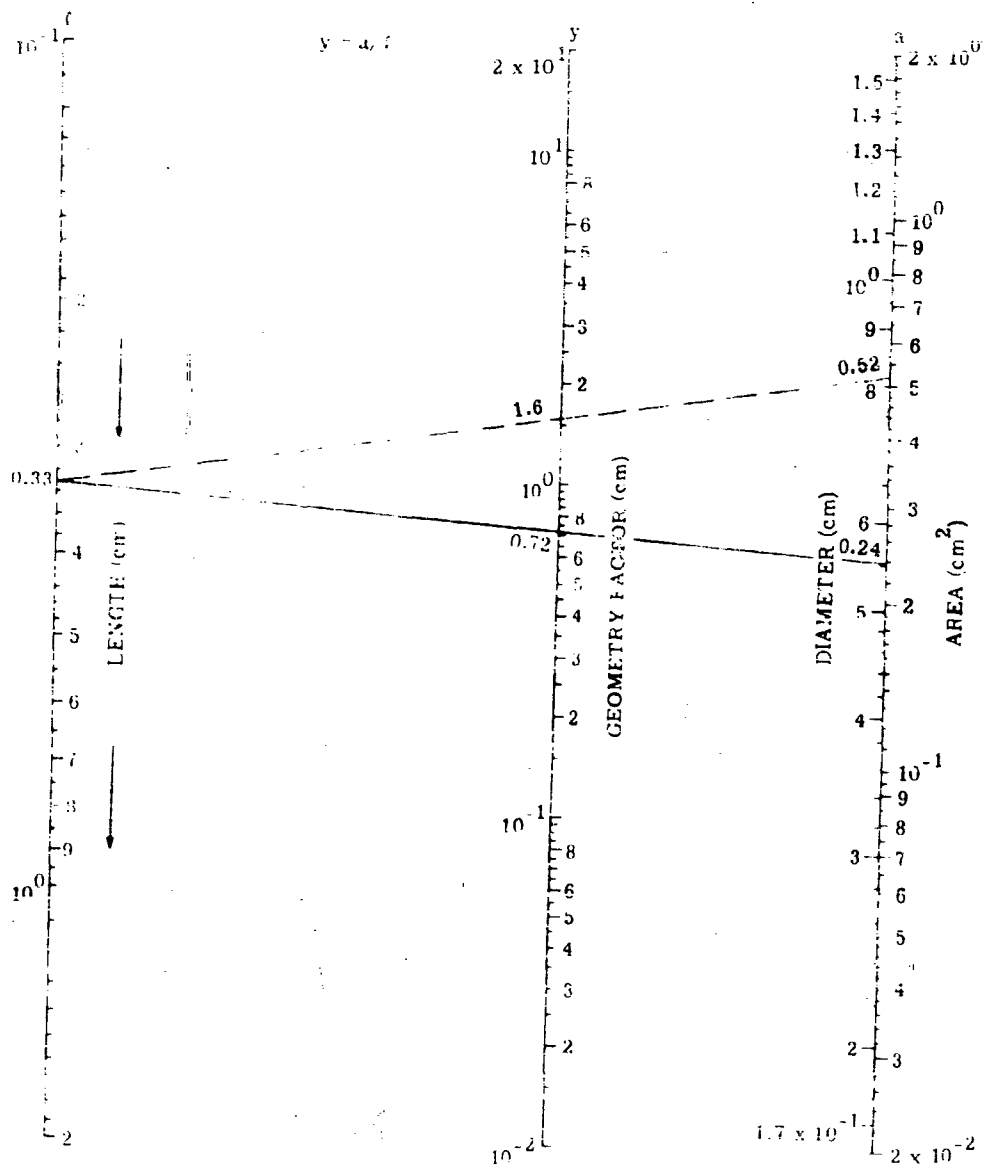


FIGURE 6-10. NOMOGRAPH IX

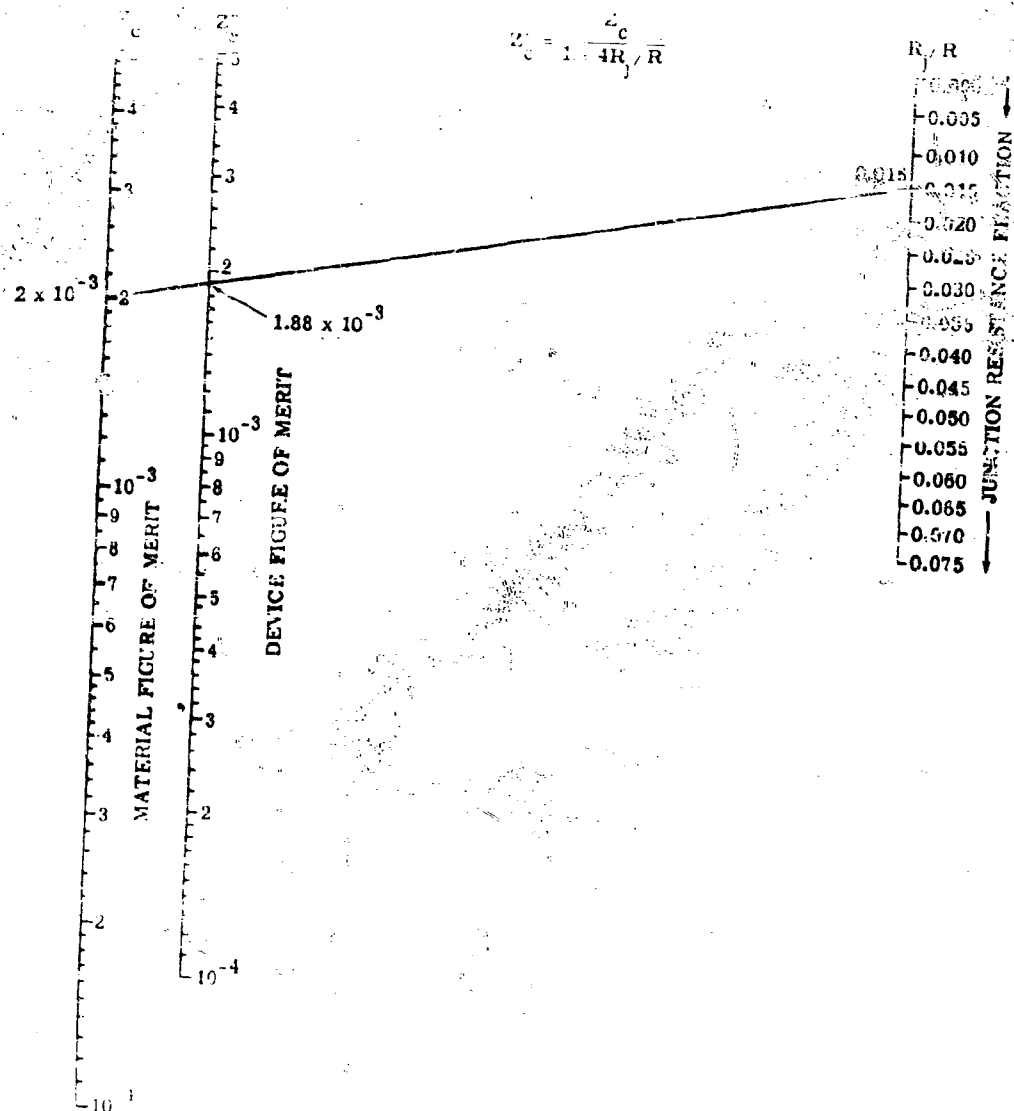


FIGURE D-1. NOMOGRAPH X

The nomographs have rather general applicability to problems of cooling. The examples which will be worked out with the use of the nomographs are quite similar to the "typical" couple used as an illustration in Section D-3. The examples are based on the same material properties given in Figure D-4; these properties are conservative for commercially available bismuth telluride (one of the better thermoelectric materials). The examples involve relatively small heat loads, and apply to temperatures within 20°K of 273°K. The nomographs have been made for wide ranges of material parameters and heat loads, and cover the temperature range from 200°K to 400°K. Accompanying each of the nomographs is the equation which was used in constructing it. It should be recalled that these are approximate expressions. However, they are adequate for the preliminary design of a Peltier cooler.

D.4.1. STATEMENT OF THE PROBLEM. To illustrate the use of the nomographs, a typical problem will be considered. It will be assumed that in order to maintain an infrared detector at a given temperature, T_c , heat must be removed at a given rate, \dot{Q} . This heat is to be discharged to a higher temperature, T_h . It may be desired to do this with the smallest possible heat pump, regardless of power requirements, or to do it most efficiently (i.e., with the highest possible coefficient of performance). It will be assumed that $s_p = s_n$, $\rho_p = \rho_n$, and $\kappa_p = \kappa_n$. The problem of optimum design when these equalities do not hold will be discussed in Section D-5. It should be noted that nomographs I, V, and VI apply only when the equalities do hold. It will be assumed further that the cold junction is to be maintained at 270°K and the hot junction at 300°K, with a heat flow of 1 watt at the cold junction. (See Figure C-2 for an indication of the detectivity which might be obtained with a lead sulfide detector at 270°K.)

The procedure to be followed is first to determine ΔT_m from the parameters of the materials, and ΔT from the given temperatures. This immediately gives the coefficient of performance, either for maximum heat pumping or for maximum efficiency. The values of ΔT , ΔT_m , and the given heat load determine the necessary thermal conductance which, with the specific thermal conductivity, determines the ratio of area to length. This ratio also yields the required resistance and current. Next, the length must be determined from considerations of convenience in fabrication and of contact resistance (see Section D-5). It is then a straightforward matter to determine the cross-sectional areas, volumes, masses, and other desired data for the steady-state operation of the cooler.

A flow diagram indicating the procedures for calculating design parameters of a Peltier cooler is shown in Figure D-17. This diagram is included to illustrate the dependence of the performance and design of the device upon specific material properties and application requirements.

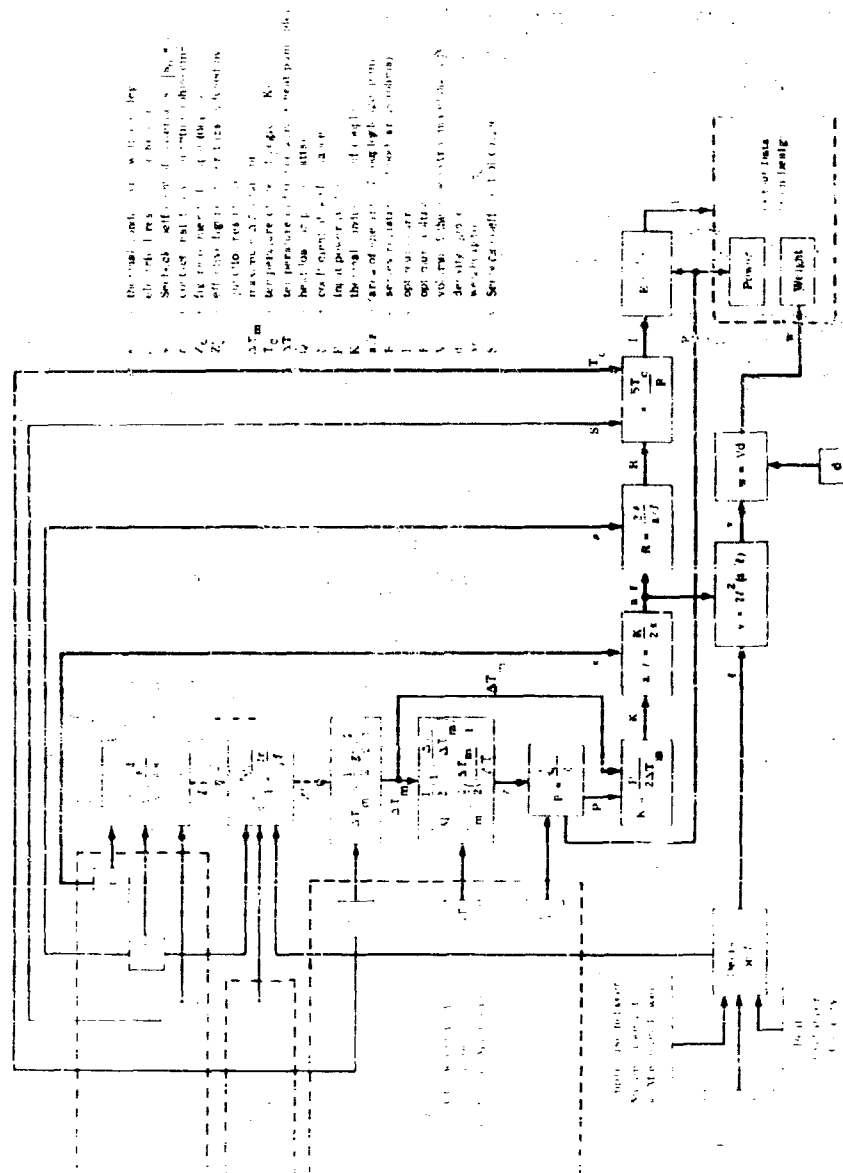


FIGURE D-17. FLOW DIAGRAM FOR DESIGN OF PELTIER COOLER

D.4.2. NOMOGRAPHS FOR MAXIMUM HEAT PUMPING. A couple which operates at maximum coefficient of performance can be constructed for a given couple temperature. This temperature is indicated on each nomograph by the lines constructed for this example from the material properties given in Figure D-4. In Figure D-4, the lines for $\Delta T_c = 30^\circ\text{K}$ and $\Delta T_m = 65^\circ\text{K}$ are first connected by a straight line. The inner section of this line with the vertical dashed line is then connected by a straight line with the appropriate value of S . This line intersects the figure-of-merit scale at $2 \times 10^{-3}/^\circ\text{K}$, the figure of merit for a couple of optimum design.

Nomograph II, representing Equation D-13, now shows that for $T_c = 270^\circ\text{K}$, $\Delta T_m = 72^\circ\text{K}$. That is, if the assembled couple took full advantage of the capability of the materials, it could maintain a 72°K temperature difference with no load. With a little foresight regarding contact resistances and convenience of construction, it will be conservatively assumed that the effective figure of merit of the couple will be 10% lower than this. The figure of merit of the couple is therefore $Z = 1.8 \times 10^{-3}/^\circ\text{K}$, and, from Nomograph II, $\Delta T_m = 65^\circ\text{K}$.

In order to obtain the coefficient of performance, it is noted that Equation D-17 can be closely approximated by

$$\epsilon_Q = \frac{1}{2} \left(1 - \frac{\Delta T}{\Delta T_m} \right) \quad (\text{D-28})$$

This is the equation from which Nomograph III was constructed. The effect of using this approximation may be seen on Figure D-4 by comparing the actual curve for ϵ_Q (Equation D-17) with a straight line between its end points (Equation D-28). From Nomograph III, it is determined that, for $\Delta T = 30^\circ\text{K}$ and $\Delta T_m = 65^\circ\text{K}$, the coefficient of performance for maximum heat pumping is $\epsilon_Q = 0.27$.

The thermal conductance of the couple can be related to known quantities by combining Equations D-14 and D-28 to give

$$\dot{Q}_m = 2K\Delta T_m \epsilon_Q \quad (\text{D-29})$$

which is represented by Nomograph IV. With $\epsilon_Q = 0.27$, $\Delta T_m = 65^\circ\text{K}$, and $\dot{Q}_m = 1$ watt, it is found that $K = 0.028$ watt $^\circ\text{K}$ is the required thermal conductance of the cooler. This is the total thermal conductance through both arms of the couple.

The total thermal conductance of both arms of the heat pump is related to the thermal conductivity by $K = 2\gamma/\Delta L$, where γ is called the geometry factor and is equal to the ratio of the cross-sectional area of each arm to its length (i.e., $\gamma = A/L$). Thus the thermal conductance determines γ . For $K = 0.028$ watt $^\circ\text{K}$ and $\Delta L = 0.5 \times 10^{-2}$ watt $^\circ\text{K}$, it is found from Nomograph V that $\gamma = 0.70$ cm. The value of

the electrical resistance of both the two arms, since $R = 2\rho l/A$. With $\rho = 10^{-3}$ ohm-cm and $l = 0.16$ cm, Nomograph VI gives $R = 2.8 \times 10^{-3}$ ohms.

The current for maximum cooling is now given by Equation D-8 or Nomograph VII. With $S = 100$ μ V/K, $T_c = 270$ °K, and $R = 2.8 \times 10^{-3}$ ohms, it is found that $I_Q = 38$ amp. The same cooling effect can be achieved by using a current of 19 amp through two couples which are thermally in parallel and electrically in series, or by using 38 μ n amp through a couple thermally in parallel and electrically in series. The use of n couples requires that the geometry factor of each couple be $1/n$ times the area-to-length ratio of the single or the original couple.

The above data constitute all the necessary electrical and thermal information about the steady-state operation of the device. It should be noted, however, that, although the area-to-length ratio of the arms has been fixed, the size has not yet been established. This indicates that a very large device could do no better than an extremely small one. However, the degree of miniaturization possible with such a device is limited, primarily due to contact resistances and fabrication techniques. For example, if the contact resistance at the cold junction is limited to 1% of the total resistance, then Z_c and ΔT_m are within 6% of their ideal values (see Section D.5.3). Allowance was made for this effect by taking $Z_c = 0.9 Z_M$. For a contact resistance on the order of 10×10^{-6} ohm-cm², the arms of the couple must be at least 0.33 cm in length. Using this length, Nomograph IX gives an area of 0.24 cm². The total area of thermoelectric material is therefore 0.16 cm², regardless of the number of couples used in parallel.

D.4.2. NOMOGRAPHS FOR MAXIMUM COEFFICIENT OF PERFORMANCE. If it is desirable to design the cooler which is most economical of power rather than most compact, the required parameters can be determined, with a slightly different procedure, from the previously mentioned nomographs plus Nomograph VIII. On Nomograph III, the lower scale is used instead of the upper one. On Nomograph IV, $1/Z_c$ is used on the right-hand scale but now the two central scales are used for $Q_c = 1$ watt and ΔT , rather than Q_m and ΔT_m . The resultant thermal conductance will, in general, be larger for the most efficient couple than for the most compact couple. Nomographs V and VI are used as before, but with the new value of thermal conductance they give different values for the geometry factor g and the electrical resistance R .

The current for maximum coefficient of performance is given by Equation D-20 or Nomograph VIII. The I_Q used in this calculation is the current for maximum heat pumping but is not the value of 38 amp determined earlier for the most compact cooler. Instead, it is the value of the current at which the cooler designed for highest efficiency should be operated in order to pump heat at the fastest

rate. Its value is determined from Nomograph VII as before, using the new value of R . This current is then used in conjunction with Nomograph VI to find the values for ΔT and ΔT_m to find i_c . The length is determined as before, and Nomograph IX again gives the area of each arm (Nomograph X will be discussed in Section D 5.)

The dashed lines on the nomographs show the operations used for designing the cooler with maximum coefficient of performance, while the solid lines indicate the operations used for designing the cooler with maximum rate of heat pumping. In each case, the heat load is 1 watt and the temperature difference is 30°K.

Table D-1 summarizes the data obtained for the two coolers. It is interesting to note that the same current is required for the optimum design with the two types of operation and that the more

TABLE D-1 COMPARISON OF COOLERS DESIGNED FOR MAXIMUM COOLING RATE WITH COOLERS DESIGNED FOR MAXIMUM COEFFICIENT OF PERFORMANCE

Requirements:

Heat load = 1 watt

$T_c = 270^\circ\text{K} (-3^\circ\text{C})$

$T_h = 300^\circ\text{K} (27^\circ\text{C})$

Materials used:

$-s_n = s_p = 200 \mu\text{V}/^\circ\text{K}$

$\rho_n = \rho_p = 10^{-3} \text{ ohm-cm}$

$\kappa_n = \kappa_p = 2 \times 10^{-2} \text{ watt/cm-deg}$

Assume: Effective Z of couple = 90% of Z of material.

Maximum ratio of resistance of cold junctions to total resistance = 3%.

Junction resistivity = 10^{-6} ohm-cm^2 .

	Cooler with Maximum \dot{Q}	Cooler with Maximum ζ
Coefficient of performance (ζ)	0.27	0.59
Thermal Conductance (K) in watts/deg	0.029	0.062
Area-to-length ratio (A/l)	0.72	1.5
Electrical Resistance (R) in ohms	2.6×10^{-3}	1.3×10^{-3}
Optimum current (I) in amperes	38	38
Total Area (200 cm square junctions)	0.46	1.05
Total Volume (200 cm square junctions)	0.10	0.34

and hence volume, by a factor of ΔT . In the case of a given material, the cross-section, geometry, material, and volume are all proportional to ΔT , whereas the electrical resistance is divided by the same factor. The above graphs may be used for designing either type of cooler, it is necessary to consider the design and control. This simple dependence on the ratio ΔT can be used to derive approximate equations for the design of Section D.5.

It should be noted that the characteristics of a cooler using given materials are fixed by the heat load and the temperature difference to be maintained. For a given ΔT , the coefficient of performance is fixed and the dimensions increase linearly with the heat load. The dependence of the dimensions on ΔT for a given load is also simple. If a variable ΔT is required, the unit should be designed for the largest expected value of ΔT and then operated at lower currents for smaller values of ΔT .

D.5.2. PRACTICAL CONSIDERATIONS

The preceding discussion of device performance was dealt with a rather idealized situation. That is, the performance referred to was that of a given thermoelectric material with a given geometry. The calculated rate of heat pumping referred only to the heat removed from the junctions between the thermoelectric materials and the idealized conductor on the cold side and delivered to the junctions between the thermoelectric materials and idealized conductor on the hot side. Little mention has yet been made of a number of considerations that are of considerable importance when this heat-pumping unit is inserted into a refrigerating system. Among such considerations are: heat exchangers on the cold and hot sides, electrical and thermal resistances of the junctions between the thermoelectric materials and realistic conductors, provision of practical power supplies, and optimum geometry to take full advantage of the capabilities of the materials.

In addition, practical devices may make use of a number of identical or similar, simple couples arranged in parallel or series. Such arrangements are possible to achieve larger temperature differences, larger heat pumping capacities, greater coefficients of performance, simpler geometric forms, simpler power-supply requirements.

The present section will deal with some of these aspects of Peltier cooling, insofar as the problems involved are significantly different from the same type of problems encountered in other cooling systems.

D.5.1. OPTIMUM CROSS SECTION OF PAIRS OF COUPLES. If the n- and p-type materials do not have equal electrical resistivities and ΔT is constant, then a couple with equal dimensions

for the two arms will not perform as well as a couple made from these same materials but with properly-adjusted dimensions. This can be readily ascertained by setting up the correct conditions for a minimum for Z to be as large as possible, and showing that RK is not a minimum if the arms have equal dimensions but different properties. The figure of merit of the couple,

$$Z = \frac{(\frac{1}{R_n} + \frac{1}{R_p})^2}{(R_n + R_p)(\frac{1}{K_n} + \frac{1}{K_p})} \quad (D-30)$$

would in general be less than the material figure of merit in Equation D-5. They are equal, and maximum, in the case of the material potentialities, only if the dimensions are adjusted to minimize RK , the denominator of Equation D-30. This optimization requires that

$$\frac{a_n/l_n}{a_p/l_p} = \frac{(\frac{1}{R_n} + \frac{1}{R_p})^2}{\frac{1}{\rho_p \kappa_n}} \quad (D-31)$$

where a and l are the cross-sectional area and length, respectively, of the arms distinguished by the subscripts n and p .

It has been shown (Reference D-30) that significant variations from this optimum ratio are not too serious. For instance, with arms of equal length, the ratio a_n/a_p may be as much as 50% larger or smaller than the optimum value without producing more than a 4% decrease in the effective figure of merit. For Bi_2Te_3 and its alloys with related compounds, the optimum ratio of areas is quite near to unity, and the use of equal areas, which is convenient for fabrication, does not represent a significant sacrifice of potential performance.

D-2. HEAT EXCHANGERS. The general problem of getting the heat to the cold junction from the volume or mass to be cooled, and from the hot junction out to the heat sink, is not significantly different from the analogous problem for other cooling systems. One aspect of the problem, however, is quite different. This results from the fact that the volume of thermoelectric material that carries the heat from the cold to the hot side can be so compact that the heat-rejecting surfaces are very close to the region being cooled. This introduces unusual, but not fundamentally new, features into the problems of insulation and heat transfer. To take full advantage of the possible compactness of the thermoelectric heat transfer material, in the design of coolers or heat sinks should be considered, and the design of the heat transfer elements, and the heat transfer elements.

15. JUNCTION RESISTANCES. Contact and junction resistances of conducting conductors, and of junctions between materials, must be considered in the practical design. The waste heat generated in the electrical conductors can also be kept in heat sink of the heat-rejecting thermocouple. Since the resistivity of copper conductors is three orders of magnitude lower than that of the thermoelectric materials. However, the effect of junction resistances may be significant, particularly at the cold junction, since heat generated there effectively adds to the heat load. The hot junction resistance is not so important since it results in heat generated immediately next to the heat-rejecting surface.

The heat generated in the cold junction resistance R_j is $I^2 R_j$, and simply adds to the joule-heat term of Equation D-7, which describes the heat balance at the cold side of the couple. Thus with two junctions, each of resistance R_j , on the cold side of a couple whose resistance is R , the joule heat to be removed from the cold junction is $(1/2)I^2(R + 4R_j)$. The effective resistance of the couple for cooling purposes is then $R + 4R_j$, so that the effective figure of merit is

$$Z'_c = \frac{S^2}{(R + 4R_j)K} = Z_c \left(1 + \frac{4R_j}{R}\right)^{-1} \quad (D-32)$$

Values of Z'_c for a given Z_c and R_j/R may be found using Nomograph X.

In order for Z'_c to be greater than some minimum fraction of Z_c , so that the junction resistance will not decrease performance more than a specified amount, a minimum length for the cooler arms is determined from the surface resistivity r of the junction. In terms of r , which has the units ohm-cm², the resistance of one contact of area a is r/a . Since $R = 2\rho L/a$,

$$4R_j/R = 2r/\rho L \quad (D-33)$$

Equation D-32 is then $Z'_c = Z_c(1 + 2r/\rho L)^{-1}$. Hence, for a specified performance of a couple made from materials with a given ρ , the ratio r/L must remain constant. Thus, as further reduction of contact resistances is attained, the minimum length of the arms may be decreased. Since the volume of the arm is aL or yL^2 , and y is fixed for a given requirement (see Section D.4.2), the required volume of thermoelectric material decreases with the square of the contact resistance.

Junction resistances cannot be calculated and are difficult to measure. At present, resistivities of the order of 10×10^{-6} ohm-cm² are considered as good. With a material resistivity of 10^{-3} ohm-cm, this would give 2.1 as the minimum percentage decrease in Z caused by contact resistance. With 10^{-4} ohm-cm, this gives the figure used in Section D.4.2.

Thermal resistances of contacts and conductors cannot be treated as analytically, or measured as conveniently, as electrical resistances. Quantitatively, the effect of these thermal resistances is to increase the necessary temperature difference between the hot and cold junctions. However, since the film of joining material at a junction is usually very thin, and therefore has a high thermal conductance, the temperature drop introduced is small compared to that appearing across the heat exchangers.

In terms of the coefficient of performance ζ , the rate of heat flow across the hot junction is $Q_h (1 + 1/\zeta)$. Thus the effect of thermal resistance is more serious at the hot junction than at the cold junction where the rate of heat flow is Q_c . If the two junctions have similar thermal contacts, the temperature drop across the thermal resistance at the hot junction will be greater than that at the cold junction by the factor of $1 + 1/\zeta$.

D.5.4. RIPPLE EFFECTS WITH RECTIFIED A.C. It should be noted that all currents entering into the calculations of Section D.3 are direct currents. Any alternating component of current would produce joule heating but would pump no heat. The provision of steady direct currents at the impedance levels required for Peltier couples is not a commonly encountered problem. Transformers, rectifiers, and, particularly, filters are discouragingly bulky for currents of, e.g., tens of amperes delivered at tenths of a volt. Thermoelectric generators would be ideally suited for Peltier coolers, since the impedance of such a generator would be comparable to the impedance of the cooler.

When rectified a.c. is used for power, the sacrifice of performance introduced by imperfect filtering is relatively easy to calculate. The quantities of importance are the root-mean-square current, I_{rms} , which determines the joule heat, and the average value of the current, $I_{\text{d-c}}$, which determines the amount of heat pumped. These are frequently related through a form factor, F , defined as

$$F = \frac{I_{\text{rms}}}{I_{\text{d-c}}} \quad (\text{D-34})$$

The form factor is easily determined from two readings: one on a d-c ammeter, and the other on an a-c ammeter of the type which reads true rms current.

If the basic equations of Section D.3 are written with I_{rms} in each of the joule-heat terms and with $I_{\text{rms}}/F = I_{\text{d-c}}$ in each of the Peltier heat terms, the resulting equations describing the performance are quite similar to the original equations. In each equation where S appears it should be replaced by S/F , and where ΔT_m occurs it should be replaced by $\Delta T_m F^2$. In fact, since ΔT_m is proportional to S^2 , the replacement of S by S/F is all that is necessary. This is what should be expected for the form factor, since it is a multiplicative factor. This combination occurs in

the heat pumping term of Equation D-7, and in representing the work done against the thermal emf in Equation D-15.

By substituting S, F for S in the equations of Section D-3, it can be shown that the performance parameters for nonsteady currents (denoted by asterisks) are related to those for steady currents (without asterisks), as follows:

$$\frac{\Delta T_m}{\Delta T_m} = \frac{1}{F^2}$$

$$\frac{Q_m^*}{Q_m} = \frac{1}{F}$$

$$\frac{I_m^*}{I_m} = F$$

(D-55)

$$\frac{C_m^*}{C_m} = \frac{Q_m^*}{Q_m} = \left(1 - F^2 \frac{\Delta T}{\Delta T_m}\right) \left(1 - \frac{\Delta T}{\Delta T_m}\right)^{-1}$$

$$\frac{C_m^*}{C_m} = \frac{Q_m^*}{Q_m} = F^{-2} \left(1 - F^2 \frac{\Delta T}{\Delta T_m}\right) \left(1 - \frac{\Delta T}{\Delta T_m}\right)^{-1}$$

In using the convenient relationships in Equation D-55 for relating performance with "rippled" to performance with pure d-c current, it must be understood that the currents with asterisks are rms values. Therefore, they are larger (by the factor F) than the values read on a d-c ammeter which might be used to measure the current. This means that if a d-c ammeter is used to measure the current with and without ripple, the ratio of the readings for currents which give maximum heat pumping would be $1/F^2$, and the ratio of the readings for currents giving maximum coefficient of performance would be unity.

The curves in Figure D-18 show the effect of the form factor on ΔT_m and on the optimum currents I_m and I_m^* . The curves in Figure D-19 show the effect on the coefficient of performance for maximum heat pumping and on the heat pumping rate when operating most efficiently, while Figure D-20 indicates the effect on the maximum heat-pumping rate and on the maximum coefficient of performance. It should be noted that easily achievable filtering produces form factors less than 1.01. For example, a sinusoidal ripple of 40% (i.e., peak-to-peak amplitude a-c component = 40% of average value) gives a form factor = 1.01. Even with $\Delta T/\Delta T_m$ as large as 0.3, this amount of ripple

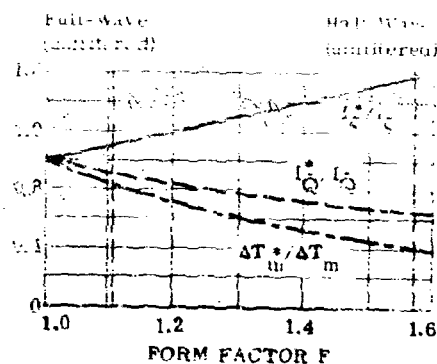


FIGURE D-18. FORM-FACTOR DEPENDENCE OF OPTIMUM CURRENTS (I^* AND I_m) AND MAXIMUM TEMPERATURE DIFFERENCE (ΔT_m)

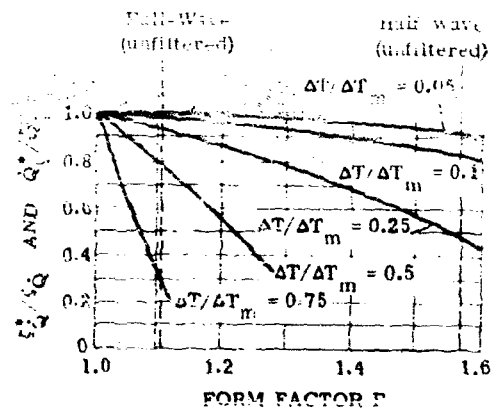


FIGURE D-19. FORM-FACTOR DEPENDENCE (FOR DIFFERENT $\Delta T/\Delta T_m$) OF COEFFICIENT OF PERFORMANCE AT MAXIMUM HEAT PUMPING (ϵ^*) AND HEAT PUMPING RATE AT MAXIMUM COEFFICIENT OF PERFORMANCE (\dot{Q}_m)

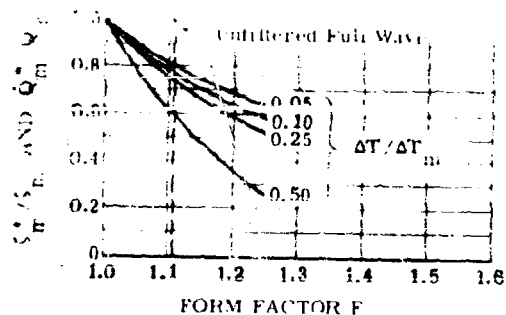


FIGURE D-20. FORM-FACTOR DEPENDENCE (FOR DIFFERENT $\Delta T/\Delta T_m$) OF MAXIMUM HEAT-PUMPING RATE (\dot{Q}_m) AND MAXIMUM COEFFICIENT OF PERFORMANCE (ϵ_m)

Decreases the maximum heat-pumping rate and the maximum coefficient of performance by less than 10%. If the amplitude of ripple is held to 10% or less, all performance losses are less than 1%.

D.5.3. TRANSIENT EFFECTS. A quantitative treatment of the performance of a thermoelectric couple operating under nonequilibrium conditions is beyond the scope of the present discussion. However, a few qualitative remarks may be made concerning sudden changes in heat load or current.

The time required for a change to occur depends upon the heat capacities and thermal conductivities of all the materials involved, as well as on the heat-transfer coefficients. A cooling device which pumps heat at an equilibrium rate of 20 watts could handle a load of 20 watts for 10 seconds on the cold side with temperature change of less than 1° if the nonthermoelectric components on the cold side had a heat capacity of 25 calories/ $^{\circ}$ K. This heat capacity corresponds to that of about 250 grams of copper.

Doubling the cooling current doubles the rate of heat removal by the Peltier effect (\dot{Q}_p of Equation D-7). Thus, since the arrival of joule heat at the cold side is slowed down by the thermal diffusivity of the arms of the couple, the net cooling rate is temporarily increased. In fact, Stillbans and Fedorovich (Reference D-4) have shown that doubling the optimum steady-state cooling current through a previously balanced couple will produce, for a short time, a temperature difference more than 25% greater than the maximum no-load steady-state temperature difference.

Evidently, then, an increased load and an increased current, applied simultaneously for a short time, tend to compensate for each other. This suggests the possibility of maintaining a constant temperature difference almost equal to ΔT_m by using a control circuit to vary the cooling current when short-duration overloads occur, even though a steady overload of comparable magnitude would make it impossible to maintain such a large temperature difference.

"Short time" as used here is a relative term, dependent upon factors such as the thermal diffusivities and the heat capacities. The same factors also determine the time required to attain the desired temperature difference when the cooler is initially turned on. An indication of this cool-down time may be obtained from consideration of the Peltier cooler of Figure D-4, which reaches more than half its possible temperature difference in less than a minute when operated at the current for maximum heat pumping. Increasing the current over this value can decrease the cool-down time considerably.

D.5.6. THERMALLY PARALLELED COUPLES. Two identical Peltier couples placed thermally in parallel will pump twice as much heat at the same temperature difference and with the same coefficient of performance as will one of them alone, provided the currents are equal. Normally they

would be connected in series electrically, requiring twice the voltage and twice the power of one couple. Similar statements apply to a cooling system in which a large number of couples are placed in parallel thermally and in series electrically.

If thermal contact with the cooled region is made through a material that is an electrical conductor, or if the cooled object is an electrical conductor, precautions must be taken to avoid electrical contact with the cooled ends of the couples which are all at different electrical potentials. Very thin insulating foils or films will serve adequately, without much increase in thermal resistance, for the relatively low voltages involved.

Appreciable input voltages could be used in cases where the couples are arranged in large banks. Similarly, a couple of large cross-sectional area, requiring a large current, could be replaced by n couples each having $1/n$ times the area of the original one and requiring $1/n$ times the current, thus making it possible to use more conventional power supplies. This, of course, entails additional fabrication problems because of the increased number of couples. Since coolers for infrared detectors do not normally require large banks of couples, further discussion of such devices will not be given here.

D.5.7. THERMALLY CASCADED COUPLES. Peltier couples may be placed in **series thermally** (i.e., cascaded) for two purposes: (1) to achieve a high coefficient of performance for a given heat load at a given temperature difference or (2) to achieve a temperature difference greater than can be achieved with a single couple. These two are not entirely unrelated, the limit on the coefficient of performance being related to the limit on the maximum temperature difference (see Equations D-17 and D-26).

As was pointed out previously, the coefficient of performance of a Peltier couple is independent of the size or capacity of the couple. It may be expressed in terms of ΔT_m , ΔT , and T_h , as shown by Equations D-17 and D-26. Thus, it is possible to discuss the improvement in performance by cascading without considering the current, voltage, heat load, etc.

The expression for the over-all performance of a cooler consisting of n stages of Peltier couples can be derived easily. The heat load, Q_1 , of stage i plus the power to run it, P_i , both contribute to the heat load, Q_{i+1} , of the next higher temperature stage, which requires power P_{i+1} . The total heat input of the last stage is equal to the heat load of the first stage plus the total power input to the stages. A straightforward manipulation results in the following expression for the over-all

Equation (D-26) can be written

$$\zeta = \left[\left(1 + \frac{1}{\zeta_1} \right) \left(1 + \frac{1}{\zeta_2} \right) \dots \left(1 + \frac{1}{\zeta_n} \right) - 1 \right]^{-1} \quad (D-26)$$

In particular, for a two-stage device,

$$\zeta_{1,2} = \left[\left(1 + \frac{1}{\zeta_1} \right) \left(1 + \frac{1}{\zeta_2} \right) - 1 \right]^{-1} \quad (D-27)$$

The results obtained from the use of a two-stage cooler may be illustrated by the following example. A single-stage cooler, made from materials such that $Z_c = 2 \times 10^{-3} \text{ } ^\circ\text{K}^{-1}$ (as in Figure D-9) and operating between 200°K and 300°K is replaced by two stages, each operating with $\Delta T = 20^\circ$. When the currents are adjusted for maximum efficiency, the coefficients of performance are 0.30 for the single stage cooler and 0.42 for the two-stage cooler. However, if the currents are adjusted for maximum heat pumping, the coefficients are 0.18 for the single stage cooler and only 0.05 for the two-stage cooler.

Further improvement could be obtained by adding a third stage, but for the above example the improvement is small (about 10%). In general, the improvement for two stages is greatest when $\Delta T / \Delta T_m$ is nearly unity. When $\Delta T / \Delta T_m \ll 1$, a multistage device is the only way to remove heat from the cold junction under steady-state operation.

The preceding discussion has referred primarily to cascaded systems in which the objective is to improve efficiency with a given temperature difference. If the principal objective is to obtain a large temperature difference between the cooled region and the heat sink, each stage can be operated, independently, at nearly its maximum temperature difference, thereby giving $\Delta T_m = \Delta T_{m1} + \Delta T_{m2} + \dots + \Delta T_{mn}$ for n stages. Since operation with $\Delta T = \Delta T_m$ is inefficient, successive stages at higher temperatures must be designed to pump rapidly increasing amounts of heat. It should be borne in mind that ΔT_m is different for each of the successive stages even if constant material properties are assumed, because of the dependence of ΔT_m on the square of the absolute temperature of the cold junction.

In considering the design of multistage coolers, it is clear that it would be undesirable to supply power to each stage separately through copper leads from a power supply at a temperature of approximately 300°K . The thermal losses through the leads and the thermal insulation between stages,

introduced by the required electrical insulation, would both constitute sources of inefficiency. Avoiding these difficulties would require the design and fabrication of a network of unequal thermoelectric elements which would allow the optimum currents to be supplied to each arm of each stage from the adjacent stages. The network of Figure D-21 represents such a design, with direct thermal and electrical connections between adjacent stages. The area to length ratio of each arm can be determined from a model design similar to those used in calculating the optimum geometry for a single couple with arms consisting of materials with unequal properties (see Equation D-30). Here, however, the problem is complicated by the fact that the currents in the arms of each couple are unequal.

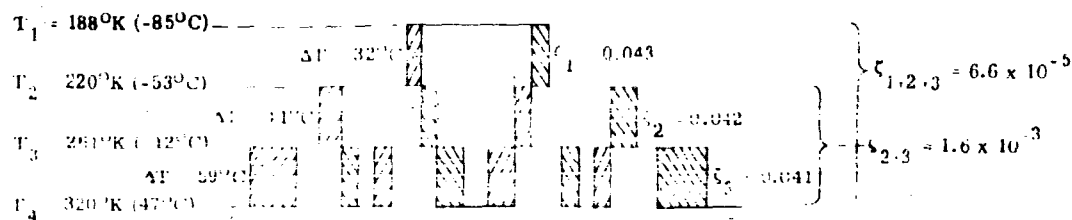


FIGURE D-21. CASCADED COUPLES WITH AREA TO LENGTH RATIO APPROXIMATELY 0.9 FOR EACH STAGE.

In the design of Figure D-21, it is assumed that the figure of merit of each element is 2×10^{-2} $^{\circ}\text{K}$, and that the current for maximum heat pumping is used. Also, each stage is designed so that $\Delta T_1 / \Delta T_2 = 0.9$. The resulting temperatures of the junctions and coefficients of performances are indicated on the diagram of the figure. Although the total temperature difference is 132°K, the over-all coefficient of performance is only 6.6×10^{-5} . Thus the system would require 1500 watts of electrical power to pump heat from 186°K to 326°K at the rate of 0.1 watt. It should be noted, however, that the same objective could be accomplished with a power of only 50 watts by the use of ten stages operating at optimum efficiency. Furthermore, the use of materials with a figure of merit of 4×10^{-3} would reduce the requirements to 6 watts and six stages.

D.6. PELTIER COOLER FOR GUNSIGHT DETECTOR

The first reported application of Peltier cooling to temperature control of an operational infrared detector was described by Kasch at the seventh meeting of the Eastern Section of IRIS in Philadelphia, 21 February 1964. Using materials considerably inferior to those presently available, sufficient heat was removed from the Peltier cooler of an AN ASO-14 gunsight to improve its operational detectivity to 1000 times that of the uncooled device, and to reduce the infrared loss, and the which

the system was placed in an environment such that large amounts of heat had to be removed to keep the cell at low temperature. Improved design of the infrared system itself would make possible much greater temperature stability and cooling components and with less power required.

The exploded view of the lens, detector, insulation, cooler, and backing plate is shown in Figure D-22. The cooler and insulation fit into a space that was available in the lens and detector housing of the original uncooled system. The Peltier cooler proper is shown in Figure D-23 and can be seen to consist of 13 couples, which are arranged in series electrically and in parallel thermally. The use of 13 couples instead of a single section of area of 2.16 cm^2 per arm rather than a single 4 cm^2 couple was dictated by the 5-amp power supply.



FIGURE D-22. EXPLODED VIEW OF DETECTOR AND COOLER

The materials used had a figure of merit of less than 1×10^{-3} and gave $\Delta T_m = 25^\circ$. With a ΔT of 25°C , the heat pumped was about 3 watts and the coefficient of performance about 0.15. The current was chosen to give maximum rate of heat pumping.

The effect of the cooler on the over-all performance of the gunsight is shown in Figure D-24. The ratio of the detectivity of the detector after it is cooled to the detectivity at ambient temperature is called the improvement factor. The improvement factor for range is the square root of this. The cooler was turned on at 1:00 and, as time elapsed, the temperature of the detector decreased and the detectivity increased. When the cooler had been operating for 90 minutes the detectivity of the detector was 1.8 times the ambient temperature value. The temperature of the detector at this time was not measured. This improvement in detectivity corresponds to a 65% improvement in range.

Thus the use of a Peltier cooler in a system which was not originally designed for cooled detectors produced a substantial improvement in performance. However, it should be borne in mind that

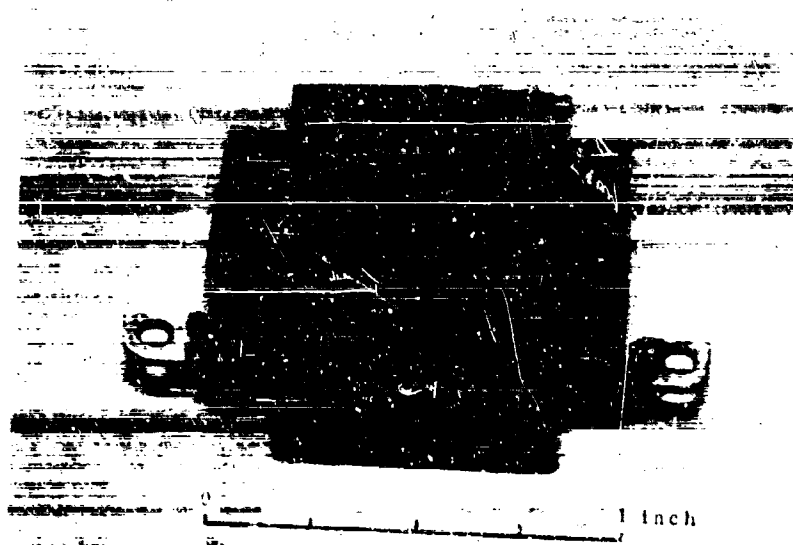


FIGURE D-23. PELTIER COOLER FOR GUNSIGHT DETECTOR

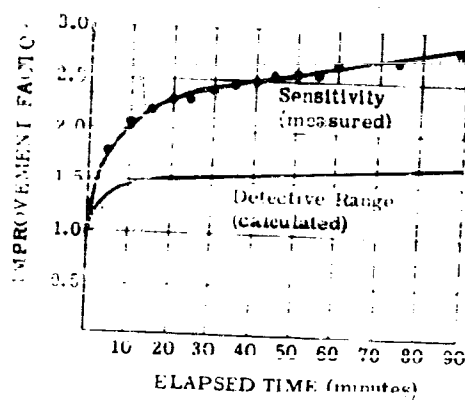


FIGURE D-24. PERFORMANCE ENHANCEMENT OF AN ASG-11 INFRARED GUNSIGHT DUE TO PELTIER COOLER

much greater than the heat load. A thermoelectric system designed to provide thermal insulation of the detector, for the purpose of minimizing thermal rates of change, provides a lower temperature, but the induced power and bias heating are negligible compared to the heat absorbed from the surroundings. Even there is no insulation.

Materials are now available with zT values two to three times higher than the values for the materials used in this device. Improved soldering and fabrication techniques also will allow smaller, lighter, more efficient coolers to be built.

The inherently small heat loads on thermally insulated detectors make multistage cooling a very attractive extension of existing technology. Much lower controlled temperatures with a compact, rugged, efficient device seem very feasible.

D7. REFERENCES

- D-1. E. E. Jaeger, *Phys. Rev.*, 1958, Vol. 107, page 538.
- D-2. H. J. Goldsmid, *Applications of Thermoelectricity*, Wiley, New York, N. Y., 1960.
- D-3. L. S. Stul'baum, *Sov. Phys. Tech. Phys.*, 1958, Vol. 3, p. 238.
- D-4. L. S. Stul'baum and N. A. Fedorovich, *Sov. Phys. Tech. Phys.*, 1958, Vol. 3, p. 460.

D8. SYMBOLS

A	cross-sectional area of thermoelectric arm
F	form factor, ratio l_{rms}/d
I	current through Peltier couple (usually pure d-c)
I_Q	current producing maximum heat pumping
I_z	current producing maximum coefficient of performance
I_{d-c}	average value of fluctuating current
I_{rms}	root-mean-square value of fluctuating current
j	subscript referring to junction between thermoelectric material and conductor
k	subscript referring to cooling heat
K	thermal conductance
l	length of thermoelectric arm
m	subscript denoting maximum value
M	subscript denoting material property
P	electrical power required to operate a Peltier couple
Q	heat-pumping rate
Q_c	rate of heat transfer by Peltier effect

Q_c	rate of heat flow at cold junction resulting from Peltier effect in the Peltier couple
Q_j	heating effect at cold junction resulting from thermal conduction through Peltier couple
Q_m	maximum heat pumping rate
Q_{m0}	heat pumping rate when coefficient of performance is maximum
r	contact resistivity
R	electrical resistance
R_j	electrical resistance of junction
S	Seebeck coefficient of a material (frequently referred to as "thermoelectric power")
S_c	Seebeck coefficient of a couple
T	absolute temperature
α	product of cross-sectional area, a , divided by length, l , of thermoelectric arm
Z	figure of merit of a couple of specified dimensions
Z_c	effective figure of merit of a couple when the effect of junction resistance is included
ΔT	temperature difference across a Peltier couple
ΔT_m	maximum steady-state temperature difference that a Peltier couple can produce with no thermal load
β	dimensionless coefficient of performance - ratio of heat load to electrical power required to operate the Peltier couple
β_m	maximum coefficient of performance
β_{m0}	coefficient of performance when heat pumping rate is maximum
κ	thermal conductivity of thermoelectric material
ρ	Peltier coefficient
ρ_s	specific resistivity of thermoelectric material

Appendix E SEMICONDUCTING MATERIALS

Thomas Linperis, John Duncan, and David Anding

The infrared detector designer often is faced with the task of perusing the properties of known semiconductors and choosing one with the proper physical, optical, photoelectric, and mechanical characteristics for detector fabrication. In order to determine which semiconductor will do the job best, it is necessary to conduct a detailed literature search, and often the properties of promising semiconductors must be determined experimentally. For convenience, therefore, tables of semiconductors with band gaps conducive to detection in the infrared spectrum have been compiled. The tables list the materials, their energy gaps, and the temperature at which the measurements were made. An extensive reference list is included to provide access to the archival literature.

TABLE E-1. ELEMENTS

Material	Energy Gap (eV)	Material Form*	Temperature (°K)	Reference
As	1.20	SC	300	1
As	1.35	SC	300	2
As	0.73	Film	300	3
Ge	0.72	SC	300	4,5
Ge	0.68	SC	300	6
Ge	0.74	SC	300	1
P (black) (p)	0.33	PC	400	7
P (black) (p)	0.57	PC	300	7
P (red)	1.5	PC	300	1
B	1.08	SC	300	1
B	1.4	PC	300	8
Si (gray)	0.1	Film	300	9
Si (gray)	0.12	Film	300	9
Se	1.6	SC	300	1
Si	1.05	SC	300	10, 11
Si	1.1	SC	300	6
Si	1.1	SC	350	11
Si	1.15	SC	300	1

TABLE 1-1. (continued).

Material	Energy Gap (eV)	Material Form	Temperature (°K)	Reference
Se	0.38	SC	300	1
Se	0.38	SC	273	12
Se	0.38	SC	300	13
Te	0.32	SC	300	14
Te	0.32	SC	300	15
Te	0.35	Film	195	16
Te	0.35	SC	300	1

*SC = single crystal; PC = polycrystalline.

TABLE 1-2. BINARY COMPOUNDS

Compound	Energy Gap (eV)	Material Form	Temperature (°K)	Reference
Ag ₂ O	0.83	SC	300	17
Ag ₂ S	0.92	SC	300	18
Ag ₂ Se	0.075	SC		19
Ag ₂ Te	0.4		300	20
Ag ₂ Te	0.95	Film	55	21
AlAs	2.4	SC	300	22
AlSb (n)	1.55	PC	300	23
AlSb (p)	1.55	SC	300	23
AlSb	1.55	SC	300	24
AsSb	1.65	SC	300	22, 25
AsSb	1.60	SC	300	6
As ₂ Se ₃	1.0	PC	300	25
As ₂ Se ₃	1.6	PC		26
As ₂ Te ₃	1.0	SC	300	27, 26
Bi ₂ S ₃	1.25		300	28
Bi ₂ S ₃	1.3	PC	300	26
Bi ₂ Se ₃	0.35	SC	300	24, 26
Bi ₂ Te ₃	0.15	SC	300	24, 26
Bi ₂ Te ₃	0.15	SC	300	29
Ca ₂ Pb	0.40			30, 31
Ca ₂ Si	1.90			32, 31, 30
Ca ₂ Si	0.90			32, 31, 30

TABLE E-2 (Continued)

Material	Band-gap eV	Material	Temperature °K	Reference
Cd _{0.8} As _{0.2}	0.6	SC	300	33, 22
Cd _{0.9} As _{0.1}	0.5	SC	300	32
Cd _{0.9} As _{0.1}	0.4	SC	195	28
Cd _{0.8} P _{0.2}	0.5-0.6	SC	300	32
CdS	0.46		300	34
CdSe	1.8	SC	300	35, 24
CdSe	1.75	PC	300	36
CdTe	1.45	SC	300	24, 35, 37
CdTe	1.55	SC	300	38
CoSb ₂	0.2			39
CoSb ₃	0.5			39
Cr ₃ Bi	0.55			31
Cr ₃ Sb	0.8	Film	77	32, 40
Cr ₃ Sb	1.0			31
Cr ₃ Sb	1.1	Film	300	41
Cu ₂ O (p)	0.25		300	42
Cu ₂ Te	1.02	Film	45	21
CuAs	1.45	SC	300	43
CuAs	1.4	SC	300	43
CuAs	1.45	SC	300	24, 5, 6
CuAs	1.37	SC	300	44
GaP	2.4	SC	300	22
GaSb	0.71	SC	300	4, 45
GaSb	0.625	SC	300	43
GaSb	0.67	SC	300	5, 22
GaSb	0.77	SC	500	6
Ga _{0.9} Te _{0.1}	1.55	SC		46
HgS				47
HgSe	0.12			48
HgSe	0.13	SC	300	49
HgSe	0.13	SC	300	50
H ₂ Te	0.68			56
H ₂ Te	0.40	SC	300	24
H ₂ P	0.41	Film	77	33, 21
InAs	0.36	SC	300	5, 22
InAs	0.39	SC	300	5, 22
InAs			300	24
InP	1.26		300	51
InP	1.25	SC	300	5, 22

TABLE E 2 (Continued)

Material	Energy Gap (eV)	Material Form	Temperature (°K)	Reference
InP	1.27	SC	300	44
InSb	0.16	SC	300	5, 6
InSb	0.23	SC	77	52
InSb	0.16	SC	300	22
InSb	0.16	SC	300	24, 53, 54
IrSe	0.96		300	24
In ₂ Te ₃	0.94	SC	300	55
In ₂ Te ₃	1.20	SC	300	56
KSe	0.90	SC	300	32
K ₂ Se	0.80	SC	300	32
Mg ₂ Ge	0.55	SC	300	34
Mg ₂ Ge	0.60		300	24
Mg ₂ Ge	0.46	SC	300	22
Mg ₂ Si	0.62	SC	300	22
Mg ₃ Sb ₂	0.82	SC	300	34
Mg ₃ Si ₂	0.82	PC	300	57
Mg ₃ Sb ₂	0.80	SC	300	33
Mg ₃ Si ₂	0.80	SC	300	32
Mg ₂ Si (p)	0.70		300	34
Mg ₂ Si (p)	0.70	SC	300	24
Mg ₂ Si	0.22	SC	300	22
Mg ₂ Sn	0.26		300	34
Mg ₂ Sn	0.20		300	24
Mg ₂ Sn	0.18	SC	300	58
MnSe	0.07 - 0.13	SC	300	59
Mn ₂ Se	0.60	SC	300	22
Mn ₂ Te	0.77	Film	55	21
Na ₂ Se	0.82	PC		20
Pb ₂ Se	0.40	SC	300	60
Pb ₂ Se	0.44	Film	300	61
Pb ₂ Se	0.40	SC	300	24
Pb ₂ Se	0.41	SC	300	62
Pb ₂ Se	0.25	Film	300	24
Pb ₂ Se	0.20	SC	300	60, 63, 62
Pb ₂ Te	0.41	Film	224	64
Pb ₂ Te	0.28	Film	300	24
Pb ₂ Te	0.22	SC	300	60, 62
Sn ₂ Se ₃	1.05	Film	300	24
Sn ₂ Se ₃	1.05	Amorphous	77	15

TABLE E-2 (Continued)

Material	Energy Gap (eV)	Material Form	Temperature (°K)	Reference
Sb_2Te_3	1.00	SC	300	26
Sb_2Te_3	1.00	Film	55	15
Sb_2Se_3	1.30	Film	55	31
Sb_2Se_3	1.23		300	30
Sb_2Te_3	1.10	Amorphous	77	15
Sb_2Te_3	0.39		300	25
Sb_2Te_3	1.00	Film	55	21
SnSe	0.54	SC	300	65
SnTe				66
TeO_2	0.36	SC	300	37
Ti_2S	1.24			68
Ti_2S	1.10			69
Ti_2Te	0.77	Film	55	21
Ti_2Te	0.40			44
U_2Te	0.92	Film	55	21
W_2Te	0.92	Film	55	21
Zn_3As_2	0.92	Film	300	21
Zn_3As_2	0.51	SC	300	70
Zn_3As_2	0.90	SC	300	32
ZnS				71
ZnSb	0.55	SC	300	33, 27
ZnSb	0.56		300	34, 30
ZnTe	0.90	Film	55	21

TABLE E-3. TERNARY AND QUATERNARY COMPOUNDS

Material	Energy Gap (eV)	Material Form	Temperature (°K)	Reference
Ag_3AsS_3	0.2 - 1	PC		27
AgAsSe_2	0.8 - 1	PC		72
Ag_3AsSe_2	0.2 - 1	PC		27
AgAsTe_2	0.8 - 1	PC		72, 73, 74
AgBiSe_2	0.34			75
AgInSe_2	1.18			73, 74
AgInTe_2	0.66			74
As_2Se_3	0.10			26
As_2S_3	0.10			26
As_2S_3	0.2 - 1	PC		27

TABLE 3.3. CONTINUED

Material	Energy Gap (eV)	Material Form	Temperature (°K)	Reference
AgSbFe ₂	0.60			26
AgSbFe ₂	0.2 - 1	PC		27
CdSnAs ₂	0.23		300	76
CuAsS ₃	0.2 - 1	PC		27
CuAsS ₃	0.2 - 1	PC		27
Cu ₃ AsS ₄	1.00			26
CuAsS ₄	0.2 - 1	PC		27
CuFeS ₂	0.53		300	24, 74
CuFeTe ₂	0.10			77
CuInS ₂	1.20			73, 74
CuInSe ₂	0.82			73, 74
CuInTe ₂	0.90			73, 74
Cu ₃ PbAs ₄	0.6 - 1	PC		72
Cu ₃ SbS ₄	0.2 - 1	PC		27
CuSbS ₃	0.2 - 1	PC		27
Cu ₃ SbS ₄	1.00			26
CuSbSe ₂	0.2 - 1	PC		27
CuSbSe ₂	0.15	PC		75
Cu ₃ SbSe ₄	0.2 - 1	PC		27

TABLE 3.4. MIXED CRYSTALS

Material	Energy Gap (eV)	Material Form	Temperature (°K)	Reference
As ₂ S ₃ -Cu ₂ S	0.8 - 1.1			78
CdTe-FeTe	1.43 - 2.1	PC	300	20
HgTe-CdTe	0.95	"	300	38
HgTe-CdTe	0.95	"	300	48
SnTe-GeTe	0.75 - 1.15	"	300	79
Ge _{1-x} Te _x	0.75 - 1.15	"		80

TABLE 2. IMPURITY-ACTIVATED SEMICONDUCTORS

Impurity	Ionization Energy (eV)	Material	Temperature (K)	Reference
CdS:Fe	0.20		300	81
CdS:Cu	0.06	SC	175	89
CdS:Li	0.02	SC	4.2	35
CdSb:In	0.27	SC	300	82
CdSb:Sn	0.42	SC	300	82
CdTe:Ag	0.49	SC	380	35
CdTe:Cl	0.029	SC	225	37
CdTe:I	0.03	SC	4.2	35
CdTe:Li	0.27	SC	300	35
CdTe:P	0.38	SC	300	35
CdTe:Se	0.51	SC	300	35
CdTe:Sh	0.36	SC	300	35
CdTe:Te	0.2	SC		37
Ge:Ag	0.14	SC	77	1
Ge:Al	0.01	SC	77	8
Ge:As	0.01	SC	77	83
Ge:As	0.01	SC	77	81
Ge:As, Ga	0.01	SC	77	82
Ge:Au (B)	0.21	SC	77	85
Ge:Au (d)	0.27	SC	77	86
Ge:Au (p)	0.11	SC	77	87, 88
Ge:Au (n)	0.15	SC	77	86, 89
Ge:Au (p)	0.13	SC	77	90
Ge:B	0.01	SC	77	83
Ge:Cl	0.06	SC		91
Ge:Co (n)	0.31	SC	195	89
Ge:Co (p)	0.25	SC	195	89
Ge:Cu	0.04	SC	175	87, 92
Ge:Cu	0.022	SC	25	90
Ge:Cu	0.057	SC	50	93
Ge:Fe (n)	0.27	SC	175	94
Ge:Fe (n)	0.33	SC	175	91
Ge:Fe	0.24	SC	77	83
Ge:In	0.01	SC	77	83
Ge:La	0.01	SC		95
Ge:Ni (n)	0.30	SC	150	96
Ge:Ni (p)	0.22	SC	150	96
Ge:P	0.01	SC	77	83

TABLE 1. (continued)

Material	Concentration Percent	Material Form	Temperature °K	Reference
Ge-Pt	0.01	SC		95
Ge-Si	0.01	SC	77	94
Ge-Se	0.14	SC	77	1
Ge-Te	0.10	SC	77	1
Ge-Zn	0.001	SC	77	88, 97
Ge-Zn	0.001	SC	4	90
Ge-Zn	0.001	SC	77	93
Se-Br	0.13	SC		98
Si-Al	0.057			99
Si-Au	0.040			100
Si-Au (p)	0.33	SC	77	101
Si-Au (p)	0.33			99
Si-B (p)	0.010	SC		100
Si-B (p)	0.031	SC		102
Si-B (p)	0.045			100
Si-Bi	0.02	SC		1
Si-Bi	0.02	SC	77	1
Si-Fe	0.05			1
Si-Ge (p)	0.001			100
Si-In (n)	0.17			99
Si-Li (n)	0.003	SC	77	99
Si-Mn	0.53			1
Si-P (n)	0.001			99
Si-P (n)	0.01	SC		102
Si-Sb (n)	0.006			99
Si-Si	0.00	SC	77	1
Zn-Au	0.001	SC	77	103
Zn-Cu	0.001	SC	77	104
Zn-Fe-Au	0.11	SC	300	105
Ge-Si-Au	0.001	SC	300	106
Ge-Si-Au	0.12	SC	300	89
Ge-Si-P	0.11	SC	300	88
Ge-Si-Zn	0.00	SC	48	90

TABLE E.1. ORGANIC SEMICONDUCTORS

Material	Energy Gap (ev)	Material Form	Temperature (°K)	Reference
Anthracene	1.0	Film	300	107, 24
Anthracene	1.7	Powder	300	108, 24
Anthracene	1.75	Powder	300	24, 109
Anthracene	1.87	Film	300	107
N Anthracene	1.12	Powder	300	110
L Anthracene	1.34	Film	300	110
Na Anthracene	1.20	Powder	300	110
1,9,4,10 Anthradipyrromethane	0.2	Film		111
Benzoquinone	0.37	Powder		112
Na 3,4 Benzoquinoline	0.35	Powder		112
Chrysene	2.20	Film	300	107
Coronene	2.3	Powder	300	109, 24
Crystal Violet Oxalate	0.58	Film		113
Crystal Violet Sulfate	0.72	Film		113
Cyananthrone	0.20	Powder	300	24
Cyananthrone	0.20	Film	300	111
Dimethylanthracene	0.4	Powder		114
Dimethylanthracene	0.45	Powder		114
Dimethylanthracene	0.45	Powder		114
Edetate	1.3		400	109
Fluoranthrene	0.70	Powder	300	24
Fluoranthrene	0.6	Film	300	108
Fluoranthrene	0.70	Film	300	111
Fluoranthrene	1.4		450	109
Geraniol	1.9			115
Geraniol	2.0	Crystals		115
Haem	1.5	Crystals		116
Hexamethyl	2.1	Crystals		116, 117
Indanthrazene	0.6	Powder	300	24, 111
Indanthrazene	0.80	Film	300	24
Indanthrazene	0.7	Powder	300	24
Indanthrazene	0.56	Powder	300	111
Indanthrazene	0.64	Powder	300	24, 111

TABLE B.1. (Continued)

Material	Ionization Energy (eV)	Material Form	Temperature (°K)	Reference
Indene	6.64	Film	300	75
Indole	6.62	Powder	300	24, 108, 109
Indole	6.65	Film	300	75
Indole	6.72	Powder	300	24
Indole	6.80	Crystalline	425	117
Indole	6.93	Film	300	75
Indole	6.95	Powder	300	118, 109
Indole	6.98	Powder		117
Methyl				
Methyl	1.6	Film		44
Methyl				
Methyl	0.58	Film		113
Methyl				
Methyl	0.78	Film		113
Naphthalene	1.70	Film	300	107
M				
Naphthalene	1.20	Powder	300	24, 109
M				
Naphthalene	1.30	Powder	300	24, 108
Naphthalene	1.12	Powder	300	24, 108
Naphthalene	1.25	Film	300	103
Naphthalene	1.27	Film	300	107
Naphthalene	1.95	Film	300	107
Parylene-Brg	0.13	Film	100-250	119
Parylene-Brg	0.13	Powder	300	120
Phenylanthracene				
Phenylanthracene	0.50	Powder	263-293	121
Phenylanthracene	0.57	Powder	250-330	122
Phthalocyanines				
Phthalocyanine	1.60	Powder	350	123
Phthalocyanine	1.30	Powder	600	124
Phthalocyanine	1.05	Powder	600	109
Phthalocyanine	1.64	SC	250	123
Phthalocyanine	1.30	SC	350	125
Metal-free	1.20	Powder	600	124
Metal-free	1.20	Powder	300	24
Metal-free	1.20	Powder	600	109
Metal-free	1.14	Crystal	100	123, 47
Metal-free	1.70	SC	350	123, 47
Metal-free	1.75	Powder		125
Metal-free	0.45	Film	300	47
Phthalocyanine	0.26	Powder	300	117

TABLE I (Continued)

Material	Ionization Energy (eV)	Material Form	Temperature (°K)	Reference
Phenyl Anthracene (dry)	2.20	Powder	300	109
Phenyl Anthracene (moist)	1.60		350	109
Pyranthrene	1.07	Film	300	108
Pyranthrene	1.07	Powder	300	24
Pyranthrene-Br₂	0.20	Film	100-250	119
Pyranthrene-Br ₂	0.15	Powder	300	119
Pyrene	2.00	Film	300	107
Pyrene-12	0.22	Powder	300	120
5, 8, (N)-Pyridine				
1, 9, -benzanthrone	3.20	Powder	300	24, 111
benzanthrone	1.00	Powder	300	24, 111
benzanthrone	0.05-1.11	Film	300	107
Tetracene	1.60	Film		107
Violanthrone	0.84	Powder	300	108
Violanthrone-Br₂	0.20	Powder	100-250	119
Violanthrone-Br₂	0.15	Powder	100-250	119
Violanthrone	0.75-0.84	Powder		108, 24, 118
Violanthrone	0.84	Film		116

REFERENCES

1. C. Moss, Photoconductivity in the Elements, Butterworth, London, 1952.
2. C. Moss, Optical Properties of Semiconductors, Butterworth, London, 1959.
3. C. Moss, Proc. Phys. Soc. (London), 1949, Vol. A62, p. 264.
4. R. Briggs, R. E. Cummings, H. J. Hrostowski, and M. Tanenbaum, Phys. Rev., 1954, Vol. 93, p. 512.
5. H. Weber, Phys. Z., 1951, Vol. 26, p. 893.
6. H. J. Hrostowski, and M. Tanenbaum, Physica, 1954, Vol. 29, p. 1055.
7. R. W. Keyes, Phys. Rev., 1953, Vol. 92, p. 560.
8. E. S. Greider, and J. A. Gutowski, J. Appl. Phys., 1957, Vol. 28, p. 1364.
9. J. Cohen, J. Appl. Phys., 1954, Vol. 25, p. 1008.

- 353

- CONFIDENTIAL

the 1990s, the number of people in the world who are illiterate has increased from 750 million to 850 million. The number of illiterate people in the world is expected to increase to 900 million by the year 2015. The number of illiterate people in the world is expected to increase to 950 million by the year 2020. The number of illiterate people in the world is expected to increase to 1 billion by the year 2025. The number of illiterate people in the world is expected to increase to 1.1 billion by the year 2030. The number of illiterate people in the world is expected to increase to 1.2 billion by the year 2035. The number of illiterate people in the world is expected to increase to 1.3 billion by the year 2040. The number of illiterate people in the world is expected to increase to 1.4 billion by the year 2045. The number of illiterate people in the world is expected to increase to 1.5 billion by the year 2050. The number of illiterate people in the world is expected to increase to 1.6 billion by the year 2055. The number of illiterate people in the world is expected to increase to 1.7 billion by the year 2060. The number of illiterate people in the world is expected to increase to 1.8 billion by the year 2065. The number of illiterate people in the world is expected to increase to 1.9 billion by the year 2070. The number of illiterate people in the world is expected to increase to 2 billion by the year 2075. The number of illiterate people in the world is expected to increase to 2.1 billion by the year 2080. The number of illiterate people in the world is expected to increase to 2.2 billion by the year 2085. The number of illiterate people in the world is expected to increase to 2.3 billion by the year 2090. The number of illiterate people in the world is expected to increase to 2.4 billion by the year 2095. The number of illiterate people in the world is expected to increase to 2.5 billion by the year 2100.

50. J. W. Cragg, *Proc. Roy. Soc. (London)*, 1952, Vol. B65, p. 376.
51. J. W. Cragg, *Nature*, London, 1949, Vol. 169, p. 426.
52. W. W. Beaman and C. D. Harwood, *Proc. Roy. Soc. (London)*, 1950, Vol. B64, p. 410.
53. E. H. Immer, *Proc. Phys. Soc. (London)*, 1952, Vol. B65, p. 405.
54. E. H. Immer, *Proc. Phys. Soc. (London)*, 1952, Vol. B65, p. 441.
55. S. Asanabe and A. Okazaki, *Proc. Roy. Soc. (London)*, 1952, Vol. B65, p. 821.
56. K. Hoshimoto, *J. Phys. Soc. Japan*, 1952, Vol. 12, No. 12, p. 1423.
57. R. G. Breckenridge and W. R. Houston, *Phys. Rev.*, 1952, Vol. 91, p. 793.
58. W. P. Hughes and L. A. Dabridge, *Photoelectron Spectroscopy*, McGraw Hill, New York, N. Y., 1952.
59. G. F. J. Garlick, *Encyclopedia of Physics*, Springer-Verlag, 1956, Vol. 19, p. 389.
60. G. Harbeck and G. Lautz, *Abhandl. Braunschweig. phys. Wiss. Ges.*, 1956, Vol. 7, pp. 36-45.
61. W. W. Harper, E. C. Johnson, and D. J. E. Marples, *J. Phys. Chem. Solids*, 1959, Vol. 18, pp. 177-181, 181-185.
62. E. H. Wernick, K. S. Geller, and K. E. L. Hall, *J. Phys. Chem. Solids*, 1959, Vol. 18, p. 154.
63. J. W. Cragg, *Proc. Roy. Soc. (London)*, 1952, Vol. B65, p. 1100.
64. J. W. Cragg, *Proc. Roy. Soc. (London)*, 1952, Vol. B65, p. 330.
65. J. W. Cragg, *Proc. Roy. Soc. (London)*, 1952, Vol. B65, p. 94-97.
66. A. J. P. Hughes, *J. Phys. Chem. Solids*, 1959, Vol. 18, p. 277.

Received May 10, 1960
 Revised May 10, 1960
 Accepted May 10, 1960